Spring 2019

Investigating blast fume propagation, concentration and clearance in underground mines using computational fluid dynamics (CFD)

Raymond Ninnang Tiile

INVESTIGATING BLAST FUME PROPAGATION, CONCENTRATION AND CLEARANCE IN UNDERGROUND MINES USING COMPUTATIONAL FLUID DYNAMICS (CFD)

By

RAYMOND NINNANG TIILE

A DISSERTATION

Presented to the Faculty of the Graduate School of the

MISSOURI UNIVERSITY OF SCIENCE AND TECHNOLOGY

In Partial Fulfillment of the Requirements for the Degree

DOCTOR OF PHILOSOPHY

In

MINING ENGINEERING

2019

Approved by:
Nassib Aouad, Advisor
Greg Galecki
Catherine Johnson
Lana Alagha
Kelly Homan

ABSTRACT

Blasting activities using standard industry explosives is an essential component of underground hard rock mining operations. Blasting operations result in the release of noxious gases, presenting both safety and productivity threats. Overestimation of post-blast re-entry time results in production losses, while underestimation leads to injuries and fatalities. Research shows that most underground mines simply standardize post-blast re-entry times based on experiences and observations. Few underground mines use theoretical methods for calculating post-blast re-entry time. These theoretical methods, however, are unable to account for the variations in the blasting conditions. Literature review shows that: (i) there is currently no means of estimating safe blast distance (i.e., blast exclusion zone); and (ii) there is a lack of a comprehensive relationship for calculating optimal post-blast re-entry time and optimal air quantity in underground mines. An important factor associated with blast fume dilution and clearance, the fan duct discharge location, needs to be studied in details. To achieve the above goals, the computational fluid dynamics (CFD) method is used to simulate blast fume dispersion and clearance in the underground mine.

An experiment has been successfully conducted at the Missouri S&T Experimental Mine to acquire blast data to validate the proposed CFD model. Computational fluid dynamics simulation results compare favorably with blast data from Missouri S&T Experimental Mine with a coefficient of determination (R^2) of 0.97. Based on the verified CFD model, various blasting and ventilation conditions were studied. A linear relationship has been developed and validated for estimating safe blast distances. Four equations have been generated and validated to conservatively calculate optimal air quantity and post-blast re-entry time based on commonly used blasting and ventilation conditions.

ACKNOWLEDGMENTS

I am highly indebted to my advisor, Dr. Nassib Aouad, for his technical knowledge, inspiration, and support leading to the successful completion of this project. I am most grateful to him for funding my research project. I would like to thank the examining committee members: Dr. Lana Alagha, Dr. Greg Galecki, Dr. Kelly Homan and Dr. Catherine Johnson for their support. Special thanks to Dr. Catherine Johnson for helping me acquire blast data for my model validation. I am also grateful to all the faculty members of the Mining Engineering Department of Missouri S&T for the advice and assistance during my research.

To Mrs. Tina Alobaidan, Mrs. Shirley Hall, and Mrs. Judy Russell I say thank you for the role you played during my study.

Special thanks to the entire Ghanaian family here in Rolla for the encouragement and support. To Victoria my lovely wife, I say well done for the encouragement, advice, and love shown to me throughout this period.

I am extremely thankful to my family, especially my father, Mr. George Tiile for their prayers and support.

Last but not the least, gratitude goes to all who directly or indirectly helped me in one way or another during the period.

TABLE OF CONTENTS

Page

ABSTRACT …….….....iii

ACKNOWLEDGEMENTS……..... iv

LIST OF FIGURES …….....ix

LIST OF TABLES ……xii

SECTION

1. INTRODUCTION 1

1.1. BACKGROUND..... 1

1.2. STATEMENT OF THE PROBLEM 4

1.3. OBJECTIVES AND SCOPE OF STUDY..... 5

1.4. INDUSTRIAL AND ACADEMIC CONTRIBUTIONS..... 6

1.5. ORIGINALITY OF PHD RESEARCH..... 8

1.6. STRUCTURE OF PHD DISSERTATION..... 8

2. LITERATURE REVIEW 10

2.1. UNDERGROUND MINE DRILLING AND BLASTING PROCESS 10

2.2. MINING EXPLOSIVES 11

2.3. BLAST FUME AND CONSTITUENT GASES 14

2.4. UNDERGROUND MINE VENTILATION..... 16

2.5. PRINCIPLES OF COMPUTATIONAL FLUID DYNAMICS (CFD) 20

2.5.1. Governing Equations. 21

2.5.2. Reynolds Number 22

2.5.3. Laminar Flow..... 23

2.5.4. Turbulent Flow. 23

2.5.4.1. The standard k– ε model..... 24

2.5.4.2. The RNG k–ε model..... 25

2.5.4.3. The realizable k-ε model 26

2.5.4.4. Spalart–Allmaras model 27

2.5.5. Numerical Analysis..... 28

2.5.5.1. Finite volume method (FVM) 28

2.5.5.2. Finite element method (FEM) 28

2.5.5.3. Finite difference method (FDM) 29

2.6. APPLICATION OF CFD TO UNDERGROUND MINE VENTILATION..... 29

2.6.1. Dust Simulation using CFD. 30

2.6.2. Simulation of Underground Mine Fire using CFD. 34

2.6.3. Spontaneous Combustion 36

2.6.4. DPM Simulation using CFD 40

2.6.5. Methane Simulation 44

2.7. BLAST FUMES AND RE-ENTRY TIMES..... 47

2.8. SUMMARY 50

3. THEORETICAL FORMULATION AND GOVERNING EQUATIONS..... 52

3.1. MATHEMATICAL MODELING 53

3.1.1. Governing Equations 53

3.1.1.1. Turbulence modeling..... 61

3.1.1.2. Species transport..... 65

3.1.2. Finite Volume Method (FVM)..... 68

3.2. COMPUTATIONAL FLUID DYNAMICS (CFD) SIMULATION OF BLAST FUMES IN UNDERGROUND MINES 68

3.2.1. Physical Model and Meshing 68

3.2.2. Boundary and Initial Conditions 69

3.2.3. Model Setup and Numerical Solution 69

3.3. SUMMARY 71

4. CFD SIMULATION RESULTS AND DISCUSSIONS 72

4.1. MESH INDEPENDENCE STUDY 72

4.2. BLOWING AND EXHAUSTING VENTILATION SYSTEM 78

4.3. SELECTION OF APPROPRIATE GAS FOR DOWNSTREAM ANALYSIS 80

4.4. INVESTIGATING THE EFFECT OF DISCHARGE LOCATION ON BLAST FUME CLEARANCE 82

4.4.1. Case 1 82

4.4.2. Case 2. 83

4.5. ESTABLISH SAFE BLAST EXCLUSION ZONES 96

4.6. ESTABLISHING A RELATIONSHIP BETWEEN OPTIMAL AIR QUANTITY AND POST-BLAST RE-ENTRY TIME 98

4.7. SUMMARY 111

5. EXPERIMENTATION AND VALIDATION 112

5.1. MISSOURI S&T EXPERIMENTAL MINE 112

5.1.1. Calibration and Monitoring 114

5.1.2. Development of CFD Model 117

5.2. VALIDATION 120

5.2.1. Re-entry Time 120

5.2.2. Safe Blast Distance. 122

5.3. SUMMARY 125

6. CONCLUSIONS, PHD CONTRIBUTIONS AND RECOMMENDATIONS FOR FUTURE WORK..... 126

6.1. SUMMARY AND CONCLUSIONS..... 126

6.2. PHD RESEARCH CONTRIBUTIONS..... 130

6.3. RECOMMENDATIONS FOR FUTURE WORK..... 131

APPENDICES

A. EFFECT OF DISCHARGE LOCATION ON FUME CLEARANCE…….134

B. OPTIMAL AIR QUANTITIES…….153

C. EXPERIMENTATION AND VALIDATION……..159

BIBLIOGRAPHY……176

VITA……190

LIST OF FIGURES

Page

Figure 4.1. CO concentration at 1 hr for coarse mesh 74

Figure 4.2. CO concentration at 30 min for coarse mesh 74

Figure 4.3. CO concentration at 1 hr for medium mesh 75

Figure 4.4. CO concentration at 30 min for medium mesh 75

Figure 4.5. CO concentration at 1 hr for fine mesh 76

Figure 4.6. CO concentration at 30 min for fine mesh 76

Figure 4.7. CO concentrations at different times for different mesh sizes 77

Figure 4.8. Blowing ventilation system 79

Figure 4.9. Exhausting ventilation system 79

Figure 4.10. Carbon monoxide concentration after simulation 81

Figure 4.11. Nitrogen dioxide concentration after simulation 81

Figure 4.12. Carbon monoxide concentration with time 82

Figure 4.13. Discharge location of 30 m and heading length 100 m 83

Figure 4.14. Discharge location of 10 m and length 70 m 84

Figure 4.15. Discharge location of 60 m and length 100 m 84

Figure 4.16. Discharge location of 90 m and length 100 m 85

Figure 4.17. Contours representing CO concentration 86

Figure 4.18. Contours showing CO content 86

Figure 4.19. CO distribution along heading length 87

Figure 4.20. CO dispersion along heading length 87

Figure 4.21. Contours showing CO concentration 88

Figure 4.22. CO concentration along heading length 88

Figure 4.23. Variation of fume clearance with distance from heading face 89

Figure 4.24. Contours highlighting CO distribution 90

Figure 4.25. Contours representing CO concentration 91

Figure 4.26. Contours showing CO distribution 91

Figure 4.27. Contours representing CO content 92

Figure 4.28. Contours representing CO concentration 92

Figure 4.29. Contours representing CO content along heading length 93

Figure 4.30. CO content along heading length 93

Figure 4.31. CO dispersion along heading length 94

Figure 4.32. Contours demonstrating CO dispersion 94

Figure 4.33. Contours demonstrating CO concentration 95

Figure 4.34. Variation of fume clearance with distance from heading face 95

Figure 4.35. Variation of fume clearance with distance from heading face 97

Figure 4.36. Cross-sectional area of 16 m^2 and heading length 40 m 100

Figure 4.37. Cross-sectional area of 16 m^2 and heading length 100 m 101

Figure 4.38. Cross-sectional area of 20 m^2 and heading length 60 m 101

Figure 4.39. Cross-sectional area of 25 m^2 and heading length 100 m 102

Figure 4.40. Contours representing CO content 102

Figure 4.41. CO concentration along heading length 60 m and mass of 200 kg 103

Figure 4.42. Contours showing CO concentration along a heading length of 60 m and mass of 300 kg 103

Figure 4.43. CO dispersion along a heading length of 100 m and mass of 200 kg 104

Figure 4.44. CO concentration with a mass of 200 kg and airflow of 20 m^3 105

Figure 4.45. Relationship between airflow and re-entry time for a mass of 100 kg 106

Figure 4.46. Relationship between airflow and re-entry time for a mass of 200 kg..... 107

Figure 4.47. Relationship between airflow and re-entry time for a mass of 300 kg..... 108

Figure 4.48. Relationship between airflow and re-entry time for a mass of 400 kg..... 109

Figure 4.49. Relationship between airflow and re-entry time for various masses..... 110

Figure 5.1. Representation of the 34 holes schematic drill pattern..... 112

Figure 5.2. Representation of explosives and detonators loaded into holes 113

Figure 5.3. Illustration of exhaust fan at the surface..... 113

Figure 5.4. Sensor 1 location 114

Figure 5.5. Sensor readings showing variation of CO concentration with time 115

Figure 5.6. Sensor readings showing the safe time zone 116

Figure 5.7. Model geometry..... 117

Figure 5.8. CFD and experiment results at position 1 118

Figure 5.9. CFD and experiment results at position 2 118

Figure 5.10. Relationship between CFD and experimental values at position 1 119

Figure 5.11. Relationship between CFD and experimental values at position 2 120

Figure 5.12. Relationship between developed relations and CFD model values..... 122

Figure 5.13. Relationship between predictors and CFD values..... 124

LIST OF TABLES

Page

Table 2.1. ANFO Properties (Stewart, 2014) 13

Table 2.2. ANFO Explosive Noxious Gas Composition (Stewart, 2014) 14

Table 2.3. Explosive gas exposure limits (Stewart, 2014)..... 15

Table 3.1. Boundary and initial conditions used for simulation 70

Table 4.1. Nodes and computational time for the mesh sizes..... 77

Table 4.2. Input variables for CFD modeling and simulation 97

Table 4.3. Input variables for CFD modeling and simulation 100

Table 5.1. Post-blast re-entry time based on validated CFD model and the equations .. 121

Table 5.2. Safe blast distances derived using validated CFD model and the equations . 123

1. INTRODUCTION

1.1. BACKGROUND

The United States is a major mineral-producing country and a net exporter of several mineral commodities. Among the minerals produced are; gold, titanium, copper, magnesium, molybdenum, lead, palladium, platinum, silver, zinc and beryllium. The U.S. mining industry also produces significant amounts of aggregates and stones for the construction and manufacturing industry. For the United States, mining has a direct economic impact of about $600 billion annually which is about three percent of the U.S. gross domestic product (NMA, 2016). This means that the U.S. economy strongly strives on these major minerals, and commodities produced using surface and underground mining methods. Soaring demand for energy, minerals, and aggregates has led to expansions of underground mining projects, increasing drilling and blasting activities. Blasting is an essential part of the mining process and almost all forms of mining require the breaking of rocks through drilling and blasting to achieve desired fragmentation. Despite the importance of blasting to mining operations, blasting is one of the most hazardous stages in the mining process. Fumes produced from blasting activities can have severe consequences on mine workers if not properly monitored and controlled.

Blasting operations using standard industry explosives in underground mines result in the release of toxic fumes that must be controlled to ensure a safe post-blast working atmosphere. The three main gases of immediate concern to human life are carbon monoxide (CO), oxides of nitrogen (NOx / NO_2), and ammonia (NH_3). Carbon monoxide (CO) is an odorless and colorless gas that workers can be exposed to without noticing,

rendering CO gas a great threat to life. Studies show that CO is the main cause of most injuries and fatalities resulting from blast fume exposure (Stewart, 2014). Nitrogen dioxide (NO_2) has the greatest threat to life and accumulates near the floor in the absence of ventilation. Ammonia (NH_3) is colorless with a pungent smell and high-level exposure can result in irritation to the respiratory tract. Thus, mine operations typically use dilution with fresh air as one of the most effective means of controlling underground mine blast fumes. This requires that the contaminated air be removed within a reasonable time from affected areas before re-entry of workers to these working zones. One of the bottlenecks associated with fresh air dilution is to determine where to place the fan duct for effective fume clearance. The fan duct discharge location could significantly affect fume clearance, hence there is a need to establish an optimal fan duct discharge location.

Post-blast re-entry time has been identified as both a productivity problem as well as a health and safety concern in underground mining environments. Blast fume clearance may be improved by lengthy re-entry times but this can result in delayed production affecting overall productivity and efficiency. Blasting at the end of an 8-hour shift, has introduced some safety and productivity gains, since there is enough time for blast fumes to clear, but this is not the case with a 12-hour work shift (Gillies et al., 2004). Ventilation fans are allowed to run at relatively high speeds for the entire duration of shift-change resulting in increased ventilation cost. There are still major productivity, cost, health, and safety issues not addressed by these current post-blast standard operational procedures.

There are numerous incidents of over exposed workers to blast fumes and there are significant losses in production due to poor procedures for determining post-blast re-entry times (Gillies et al., 2004). A survey conducted by Gallo (1995) revealed that production

time loss in most underground mines due to delayed post-blast re-entry time can be significant since most of these mines have more than four blasts daily. Several mines relied on past experiences and observations to set post-blast re-entry times. Available traditional methods for estimating post-blast re-entry time are unable to account for the variabilities in the ventilation and blasting process. Additionally, the traditional methods offer a limited platform for calculating mine-wide fume dispersal (Stewart, 2014).

This research initiative would provide understanding into blast fume propagation in underground mines using computational fluid dynamics (CFD). This analysis would help in establishing safe blast exclusion zones immediately after blast to protect workers from blast fume poisoning. Another complicating factor to fume clearance, that is, discharge location of fresh air ducts required to clear blast fumes from blast areas is also investigated. This is aimed at developing an optimal duct discharge location or range of duct discharge locations for effective fume clearance. An attempt would also be made to establish a relationship for estimating re-entry times based on determinant variables. An additional use of the relationship developed in this study would be to help reduce ventilation cost by determining optimal air quantities based on desired post-blast re-entry times. The outlined steps above are aimed at establishing a safe, productive and cost-effective underground mine working environment. The findings of this research initiative coupled with good underground blasting practices would help reduce or eliminate the threats posed by blast fumes thereby improving the health of underground mine workers.

1.2. STATEMENT OF THE PROBLEM

The growing demand for energy, minerals, and aggregates has resulted in large-scale underground mining operations with corresponding increased drilling and blasting activities. These developments have resulted in many incidents occurring from overexposure of miners to blast fumes. There are also significant losses in production due to poor procedures for determining appropriate re-entry times after blasting. Two fatalities were reported in the Revenue-Virginius mine in Colorado in November 2013, following the exposure of 20 workers to what is believed to be carbon monoxide from blasting (Stewart, 2014). Two mine workers at Golden Star's Prestea underground mine in Ghana on December 2017 died following exposure to blast fumes (Taylor, 2018). The cause of the injuries and fatalities are attributable to inappropriate re-entry times and/or miners located within zones of high CO/NO_2 concentrations. Attaining optimal re-entry time is important as overestimation of re-entry time results in production losses, while underestimation has health and safety consequences.

Most underground mines schedule blasts at the end of working shifts with the aim of allowing enough time for blast fumes to clear without affecting production. The main challenge with this approach is that fans are forced to run at high speeds for several hours to clear the blast fumes resulting in an increased ventilation cost. It is imperative to optimize fan airflow since ventilation by fan constitutes about 35-50% (Jahir et al., n.d.) of the total energy consumption of the mine.

Moreover, attention has not been given to the best location of the fan duct despite the important role it plays in fume clearance. Miners simply place ducts at reasonable locations and set fans at arbitrary speeds hoping to get noxious gas concentrations reduced

below acceptable limits within given duration. Inappropriate duct discharge location affects fume clearance, and consequently post-blast re-entry time.

Empirical formulas based on logarithmic relationships are available for calculating post-blast re-entry time. However, these empirical relationships are not able to account for the variabilities in the ventilation and blasting process often resulting in a poor correlation to actual gas readings. Researchers have used computational fluid dynamics (CFD) to study blast fumes in underground mines with the view to capture the variations in the blasting and ventilation conditions. However, available CFD studies have overlooked an important factor to fume clearance, which is, the fan duct discharge location that is required to clear blast fumes from blast areas. Additionally, there is no relationship to estimate safe blast distance based on determinant variables. Finally, there is still a lack of a comprehensive relationship for estimating post-blast re-entry time and air quantity based on determinant variables. Thus, this research will open and advance frontiers on the use of the CFD technique to study blast fume propagation, develop an optimal range of duct discharge locations, create blast exclusion zones, and estimate optimal post-blast re-entry times in underground mines based on commonly used input parameters. Ventilation cost would also be minimized significantly by calculating optimal air quantities based on the desired post-blast re-entry times.

1.3. OBJECTIVES AND SCOPE OF STUDY

The main objective of this research is to establish a safe, productive, and cost-effective underground mine operations using computational fluid dynamics (CFD) technique.

This main objective can be accomplished by fulfilling the following specific objectives:

i. Investigate the influence of discharge location of fresh air ducts on blast fume dilution and clearance. Optimal discharge location or a range of discharge locations is developed.

ii. Establish a relationship for estimating safe blast distances. Safe blast exclusion zones are created to protect mine workers from blast fume poisoning.

iii. Develop a comprehensive relationship for estimating post-blast re-entry time and air quantity in underground mines. The established relation is also used to determine optimal air quantity based on set post-blast re-entry time, thus reducing ventilation cost.

This research initiative is limited to determining optimal post-blast re-entry time that maximizes production at minimal ventilation cost using 4-dimensional computational fluid dynamics (CFD) in ANSYS Fluent platform. The resulting theories, mathematical models and computational methodologies are, however, applicable to other aspects of underground mine ventilation such as underground fires; methane flow and explosions; gob gas flow; diesel particulate matter (DPM) propagation and control; and dust dispersion and control. Simulating various underground ventilation and blasting conditions will highlight other important variables needed to improve the established relationships, hence expanding the scope of applicability.

1.4. INDUSTRIAL AND ACADEMIC CONTRIBUTIONS

Making this research findings available to industry will serve as a step towards maintaining a safe, productive and cost-effective underground mining operations. This can

be accomplished by creating safe blast exclusion zones and estimating optimal post-blast re-entry times to prevent miners from coming into contact with high blast fume concentrations. Production delays are reduced significantly as a result of using optimal post-blast re-entry times. Estimating optimal air quantity based on the desired post-blast re-entry time minimizes underground mine ventilation cost. The blast dilution models generated can be used for predicting safe blast distance, optimal post-blast re-entry time, and optimal air quantity given various development heading arrangements, ventilation, and blasting conditions.

The new knowledge and expertise from this research would be broadly employed in understanding methane flow and explosions; diesel particulate matter (DPM) dispersion and management; gob gas flow analysis; and dust dispersion and control among others. Simulating various underground ventilation and blasting conditions will highlight other important variables needed to improve the post-blast atmospheric conditions in the underground mine.

This research effort is expected to expand frontiers and advance knowledge with the use of computational fluid dynamics (CFD) to create a safe and productive post-blast underground mine working environment. The knowledge and discoveries from this study will open new frontiers for further research initiatives using CFD. Results from CFD simulations, procedures, methods, ideas, and theories from this research would serve as base line for future research activities in related areas.

1.5. ORIGINALITY OF PHD RESEARCH

This fundamental research work is a novel effort towards providing a safe post-blast underground mine environment by developing a comprehensive relationship for estimating post-blast re-entry time. This research study is a pioneering effort towards providing understanding into the effect of the fan duct discharge location on post-blast fume clearance, subsequently developing an optimal range of duct discharge locations for effective blast fume clearance. Particularly, this study will pioneer the design of a relationship between airflow and post-blast re-entry time. Optimal air quantity is calculated based on the established relationship minimizing ventilation cost. Moreover, a relationship for estimating safe blast distance is developed. Blast exclusion zones are created based on the relationship protecting workers against blast fume poisoning.

1.6. STRUCTURE OF PHD DISSERTATION

Section 1 presents background information about underground mine blasting and associated problems. The research problem, as well as the research objectives and methodology, are outlined. Section 2 provides an extensive review of literature in the following areas: (i) underground mine drilling and blasting, (ii) Mining explosives; (iii) blast fume and constituent gases, (iv) underground mine ventilation, (v) Mathematical modeling of blast fume, (vi) application of CFD in underground mine ventilation and principles of CFD, (vii) weaknesses in the existing techniques employed in estimating post-blast re-entry time, and (viii) limitations of available studies conducted into blast fume propagation and clearance in underground mines using computational fluid dynamics (CFD). The theoretical formulation and governing equations are presented in Section 3.

Mathematical models depicting blast fume mixed with airflow in underground mine setup would be derived. CFD models that best fit the problem are selected for CFD simulations. CFD simulations and results are captured in Section 4. SOLIDWORKS® is used to design various development heading arrangements. ANSYS Fluent is used to simulate airflow and blast fumes under varying ventilation and blasting conditions. Various equations are developed based on simulation results to predict post-blast re-entry times and safe blast distances. Section 5 highlights an experiment conducted at Missouri S&T Experimental Mine to obtain data for CFD model validation. Validated CFD model is used to simulate various development heading arrangements, and blasting conditions. The simulation results are compared with results from the developed equations. Summary of the conclusions and recommendations from the research is covered in Section 6.

2. LITERATURE REVIEW

The contributions and limitations of relevant books and technical publications have been reviewed. This section will outline the summary contributions from published literature with significant impact on blast fume and computational fluid dynamics (CFD) application to underground mine ventilation. The emphasis of this review is on (i) Underground mine drilling and blasting process; (ii) Mining explosives; (iii) Blast fume and constituent gases; (iv)Underground mine ventilation system; (v) Application of CFD to underground mine ventilation; and (vi) Post-blast re-entry times.

2.1. UNDERGROUND MINE DRILLING AND BLASTING PROCESS

Drilling and blasting need to be carried out in underground mines to enable mining advancement. Development drilling and blasting are executed first to create room for production drilling and blasting. Holes to be drilled are first planned out and then marked out on the rock face for drilling. Drilling is carried out using manual or automated means. After drilling, the holes are watered to remove drill cuts before loading of explosives. The cleaned holes are filled with explosives and then connected with required detonators. After charging and tie-ups are completed, the explosives are detonated. The entire work-force is evacuated prior to blasting and can only return to the work area after blasting. The ventilation fans are activated immediately after blasting to help clear the fume and dust from the blasted area. Workers would have to wait for an appropriate time frame before they can re-enter the mine. The quantity of toxic gases produced by blasting activities can be generally affected by confinement, priming method, charge length, underground oxygen

content, and formulation of explosives (Steyn, 2013). After blast fume is cleared mucking and other underground activities can begin.

2.2. MINING EXPLOSIVES

Drilling and blasting is the use of explosives to break rock for excavation. It is mostly employed in mining, civil works, and quarries. Explosive is any substance that produces a volume of rapidly expanding gas in a very short duration (Norman, 2015). Different types of explosives with different compositions and performance properties are used in the drill and blast process. An explosive contains nitrogen, hydrogen, carbon, oxygen, and other additives. Chemical explosives can be classified as high explosives or low explosives. High or detonating explosive is characterized by high pressure development and rapid decomposition whereas low or deflagrating explosive generates low pressures at fast burning rates. Higher velocity explosive is used for breaking relatively hard rock in a process called detonation while low velocity explosive is used in soft rock breakage in a process called deflagration. Detonation is mostly associated with the passage of a high-speed shockwave through the explosive. Deflagration is the passing of a flame front through the material; gun-powders and pyrotechnics are examples of low explosive. Examples of high explosives include ammonium nitrate-fuel oil mixture (ANFO), nitroglycerin, pentaerythritol tetranitrate (PETN), dynamite, and trinitrotoluene (TNT). Low explosives include gun-powders and pyrotechnics.

Detonating explosive is subdivided into primary and secondary explosives. Primary explosive is very sensitive and detonates by ignition from impact, heat, flame, or friction. They are detonators used to trigger the explosion of the secondary explosives. Lead azide,

nitrosoguanidine, and mercury fulminate are examples of a primary explosive. Secondary explosive is less sensitive to initiation and requires a detonator. However, the secondary explosive is more powerful than primary explosive once initiated. Trinitrotoluene (TNT) is a common example of secondary explosive. Tertiary explosive otherwise called blasting agent is insensitive to shock and as a result, requires an intermediate explosive booster. Blasting agent includes dynamite, trinitrotoluene, picric acid, and nitroglycerin.

Most underground blasting activities are carried out using ammonium nitrate-fuel oil mixture (ANFO). ANFO is a bulk explosive used in metal mining, coal mining, and construction applications among others. ANFO is made up of the oxidizing component known as the ammonium nitrate and the fuel oil (Cook, 1974). ANFO is a mixture of ammonium nitrate and fuel oil and the optimum composition for ANFO is 94.5% AN and 5.5% FO by weight to maximize its energy output and reduce toxic fume production (Taylor, 2015). Optimal detonation of ANFO explosive results in the release of nitrogen, carbon dioxide, and water. However, such conditions are practically impossible to obtain in the field with blast producing toxic gases such as carbon monoxide and nitrogen oxides (NOx). ANFO is widely used as it accounts for an estimated 80% of the 2.7×109 kg (6×109 lb) of explosives used annually in North America (Edward, 2006). ANFO is preferred over other explosives because of its low cost, ease of use and high- performance characteristics. The sensitivity of ANFO however, is affected by particle size, the intimacy of mixing, composition, and density (Taylor, 2015). Granular ANFO is used in dry holes while cartridged ANFO is used in wet holes. The composition of blast fume resulting from ANFO explosive is based on moisture content and fuel oil percentage. Products of ANFO under ideal conditions and at a stoichiometric composition is expressed by Equation 1 as follows:

$$37\ NH_4NO_3 + C_{12}H_{26} = 87\ H2O + 37\ N_2 + 12CO_2 \quad (1)$$

Less Carbon Monoxide (CO) and higher Oxides of Nitrogen (NO_x) are produced with fuel oil percentages less than 6%, while higher fuel oil percentages increase CO production and decrease NO_x yield (Stewart, 2014). Table 2.1 represents the properties of ANFO used for this research.

Table 2.1. ANFO Properties (Stewart, 2014)

Ammonium nitrate	94%
Fuel oil	6%
Density (unpacked)	820 kg/m^3
Gas Volume	1.08 m3/kg (at 25^{o}c)

The composition of additional noxious gases on ANFO (Ammonium Nitrate with 6.0% fuel oil) detonation is summarized in Table 2.2. The initial concentration of CO and NO_2 used as input parameters for the CFD model in this research are 14,815 ppm (0.015) and 1,667 ppm (0.002) respectively as observed from Table 2.2.

Table 2.2. ANFO Explosive Noxious Gas Composition (Stewart, 2014)

Noxious Gases	Gas Yield (l/kg ANFO)	Conc. ppm	Gas Density (kg/m^3)
NO_2	1.8	1667	2.62
NOX(including NO_2)	3.5	3241	<2.62
CO	16	14815	1.15
NH_3	0.4	370	0.73

2.3. BLAST FUME AND CONSTITUENT GASES

Ammonium nitrate-fuel oil mixture (ANFO) combustion produces varying quantities of noxious gases such as NO_2, NO, CO and NH_3 gas depending on explosive nature and the nature of combustion. Short re-entry time to blasted areas can result in fatal exposure to these deadly gases. Some of the gases cause oxygen depletion and are termed as asphyxiates. Others cause irritation to parts of the human body and are referred to as irritants. Blasted areas need to be well ventilated and adequate time allowed for the gases to clear before re-entry of miners.

In the U.S., underground mines use thresholds published by the national institute of safety and health (NIOSH) to regulate exposure to post-blast noxious gases. The threshold limits are commonly expressed as Time-weighted average (TWA) limits, Short-term exposure (STEL) limits or Immediate danger to life and health (IDLH). The threshold limits for the various gases are summarized in Table 2.3.

Table 2.3. Explosive gas exposure limits (Stewart, 2014)

Noxious Gases		TWA (ppm)	STEL (ppm)	IDLH (ppm)
NO_2		3	5	20
CO		25	100	1200
NH_3		25	35	300

Carbon monoxide (CO) is an odorless and colorless gas produced from incomplete combustion. Some sources of CO are blasting, diesel engine equipment, and fires. Because of the features mentioned above, workers can be exposed to CO unnoticed, hence CO offers a great threat to life. CO is slightly lighter than air, flammable in oxygen, and at certain concentrations explosive in air (Taylor, 2015). CO can be trapped in muck pile for prolonged hours. Studies have shown that CO is the main cause of most injuries and fatalities caused by exposure to blast fumes.

Nitrogen dioxide (NO_2) is an irritant asphyxiate gas, dense than air, brown in color and has a sharp-sweet odor. Exposure to NO_2 causes irritation to the respiratory tract and eyes. High level NO_2 exposures can result in blistering of lungs, pulmonary oedema, pneumonia, and death. Most of the symptoms are detectable within 2 hours of the exposure. Among all the noxious gases, NO_2 has the greatest threat to life and NO_2 often accumulates near the floor in the absence of ventilation.

Ammonia (NH_3) is formed as a result of incomplete combustion of nitrogenous material. NH_3 is colorless, light gas with a pungent smell and easily avoided through smell. High level exposures can result in pulmonary oedema, and irritation to the respiratory tract.

2.4. UNDERGROUND MINE VENTILATION

Underground mine ventilation generally involves the supply of air quantities to workings to dilute and remove blast fumes, diesel particulate matter (DPM), dust, heat, and other contaminants, and to provide oxygen to workers. In the U.S., mine ventilation is mostly directed towards the control of blast fumes, diesel engine exhaust emissions control, radiations battery emissions, dust and methane control. As most underground mines in the U.S. are getting deeper, there is also the need to regulate the temperature in deep mines. To be able to operate an efficient and cost-effective ventilation system the following should be considered; the mine operations as they will impact air quality underground including blasting and equipment emissions; air permeability of the rock affected by rock fracture patterns; temperatures and moisture contents of underground rock strata; surface temperatures and humidity; the layout of the mine workings; the air quality standards required for human health and safety in the ventilated workings; and finally the cost of energy. Most mining destinations including USA have in place statutes to specify air quantities needed to dilute and eliminate contaminated air from underground workings.

Increased mineral production over the years has led to the excessive generation of dust, diesel particulate matter (DPM) and other noxious gases in underground mines with downstream consequences. Mine ventilation is vital such that improper and /or inadequate ventilation can result in decreased productivity, increased accident rates, and reduced worker efficiency. Providing fresh air to control these contaminants, maintaining a safe and healthy environment is, however, expensive accounting for about 35-50% of the total energy consumption of the mine. There is therefore the need to establish an efficient and cost-effective ventilation control solution. As a consequence, most of the underground

mines have started applying the concept of ventilation on demand (VOD). Ventilation on demand is a concept that focuses on delivering the right quantity of air to the required mine section for a required time period. Ventilation on demand (VOD) involves a real-time analysis and control system to ensure a safe working environment and to minimize energy wastage by ventilation fans. A fully automated VOD system is accomplished by having in place a reliable continuous real-time monitoring system and automatic control system for controlling devices such as fans, doors etc. This automated VOD system can be fully integrated into any ventilation model for online optimization.

The primary ventilation system is comprised of an intake for introducing fresh air, the various mine workings, and an exhaust where stale air exits the mine workings after clearing contamination. A basic combination of fans, ducts, doors, pipes, filters, cooling and heating systems makes the ventilation system. Fresh air enters the system through the intake audits and intake airshafts and pushing facilitated by means of the main fan. Booster and auxiliary fans are then used to push fresh air to the working areas via ducts and pipes. Regulators such as mine doors are also necessary for directing fresh air to only needed areas. Contaminated air including heat, toxic gases, dust, and DPM is added to the air. The contaminated air is removed from working areas through ducts and pipes by means of auxiliary exhaust fans. The contaminated air finally makes its way to the surface through audits or airshafts.

Underground mine ventilation systems are grouped into three based on the airflow direction and fan location. These are the blower system, the exhaust system, and the combined system. The blower system has the mine fan installed at the intake airshaft creating a positive mine pressure. The exhaust system has the mine fan located on top of

the return airshaft consequently creating a suction that puts the mine pressure below the atmospheric datum. The booster system (combined system) has fans on both the intake and return airshafts. With the booster system, the fan velocity is read from the discharge side of the fan (Hartman, 1992).

The advantages and disadvantages of the ventilation systems are summarized below (Tien, 1999):

The advantages of the blower system are as follows:

1. Fan only supplies fresh outside air, non-corrosive and with normal moisture content to the workings.

2. Any fire outbreak in any part of the mine is soon detected by workers.

3. The blowing system may be the only practical means of ventilation in shallow mines and areas of contiguous mining where the ground is fractured or ground cracks into abandoned mine respectively.

4. Fan unit is cheaper because of a shorter fan ducting.

5. The haulage roads and hoisting shaft stay free from ice, making it more convenient for the men in winter.

The disadvantages of the blower system are as follows:

1. Dust and dirt from outside will settle on the fan blades.

2. Methane tends to accumulate in pockets in the roof, causing explosions at times.

3. Escape routes are mostly blocked by products of combustion making fire-fighting and rescue work more tedious in times of emergencies.

4. Accumulated air contaminants converge on workmen in the slope bottom zones due to the fact that neutral air flows away from working areas.

5. Shock losses are greater since it requires a distance of 30 times the duct diameter away from the pressure jet for the air velocity to lose 90% of its original velocity.

The advantages of the exhaust system are as follows:

1. The haulage roads are kept free from dust, gas, and smoke allowing the workers to perform their tasks in fresh air.

2. Both intake airways and track entries serve as escape ways, stopping lines are well maintained.

3. When the main fan stops, underground pressure builds up to atmospheric. Gas emission from gob and the time required for gas to reach active workings are delayed due to the pressure increase.

4. During fire or explosion incidents, rescue work to runs more smoothly and quickly, since enough fresh air is supplied along haulage routes for the transportation of material and equipment to make mine repairs.

5. Greater power savings are possible in smaller mine openings. This is due to the potentially greater recovery of velocity pressure through the use of discharge expansion ducts on exhaust fans.

The disadvantages of the exhaust system are as follows:

1. Corrosive particles settle on the fan blades and corrode the fan blades as contaminated air goes through the fan reducing effective air passage area.

2. It is tougher to detect a fire in belt and track entries since the air is carried directly to the return airways.

3. Dust generated at the portals and along the haulage road contaminates the intake air stream. Also, fire in the belt and track entries can be carried to the workings.

4. Reduced temperatures in the belt slope, slope bottom, and main haulage line makes it uncomfortable to work in these areas.

Booster (combined) system:

In the combined system, it is easier to get air to otherwise difficult places. The disadvantage of this system is that neutral spots are created due to difficulty in balancing the ventilation system.

2.5. PRINCIPLES OF COMPUTATIONAL FLUID DYNAMICS (CFD)

Computational fluid dynamics (CFD) is a branch of fluid mechanics which deals with numerical simulation of fluid flow and heat transfer problems. It uses physics, numerical and computer sciences to solve and analyze problems that involve fluid flow. Computers are used to perform the calculations required to simulate the interaction of fluids and gases with complex surfaces. As part of CFD analysis, continuum governing equations are converted to discrete algebraic equations using a process called discretization. Fluid flow is governed by three main conservation laws namely conservation of mass, conservation of momentum and conservation of energy. Mathematical equations of the mentioned laws lead to the governing equations of fluid flow which could be partial differential equations or integral equations. Partial differential equations are derived by applying the governing equations to an infinite sum of fluid particles moving in the flow. The integral equations, on the other hand, are derived by applying the governing equations to a fixed volume in the flow domain. In either case, the two equations are coupled and nonlinear. In CFD, these governing equations are solved approximately on the computer using software. The software converts the governing equations to a large set of algebraic

equations using numerical methods. Current CFD methods can be used to solve relatively simple geometries to complex physics to the desired level of accuracy. Actual industrial experiments are necessary for validating CFD models.

2.5.1. Governing Equations. The Navier-Stokes equations are the basic governing equations for a viscous, heat conducting fluid. Navier- Stokes equation is a vector equation obtained by applying Newton's Law of Motion to a fluid element. The equations that make up the Navier- Stokes equation are the mass conservation equation, the conservation of momentum and the energy equation. Equations 2 to 5 show the conservation form of the partial differential governing equations, which are known as Navier–Stokes Equations (Xu et al., 2017):

Mass conservation equation (Continuity equation):

$$\frac{d\rho}{dt} + \vec{\nabla} . \rho \vec{V} = 0 \tag{2}$$

Where ρ is the density of fluid (kg/m^3); t is time (seconds); v is velocity vector (m/s).

The conservation of momentum (Newton's second law):

$$\frac{d(\rho \vec{V})}{dt} + \vec{\nabla} . (\rho \vec{V} \vec{V}) = \vec{\nabla} . P + \vec{\nabla} . \bar{\bar{\tau}} + \rho \vec{b} \tag{3}$$

Where $\bar{\bar{\tau}}$ is viscous stress tensor (Newton) given by Equation 4 for a Newtonian Fluid, $\vec{b}$ is body force, and μ is the molecular viscosity coefficient.

$$\bar{\bar{\tau}} = \mu\left(\vec{\nabla}\vec{V} + (\vec{\nabla}\vec{V})^{T}\right) - \frac{2}{3}\mu(\vec{\nabla}\vec{V})\bar{\bar{I}} \quad (4)$$

The conservation of energy (the first law of thermodynamics):

$$\frac{d\rho e}{dt} + \vec{\nabla}.(\rho e\vec{V}) = \rho\overset{*}{q} + \vec{\nabla}.(k\vec{\nabla}T) - \vec{\nabla}.(p\vec{V}) + \vec{\nabla}.(\bar{\bar{\tau}}.\vec{V}) + \rho\vec{b}.\vec{V} \quad (5)$$

Where $\overset{*}{q}$ the rate of volumetric heat addition per unit mass, T is temperature, and e is internal energy per unit mass.

2.5.2. Reynolds Number. The Reynolds number is the ratio of the inertial force to the shearing force of the fluid. The dimensionless Reynolds number is vital in the equations that describe whether fully developed flow conditions lead to laminar or turbulent flow. The heat and mass transfer in fluid systems are affected by the type of flow in a fluid. Flow will transition from laminar to turbulent flow as the Reynolds number increases. Equation 6 describes the Reynolds number for flow through the pipe (Engineering ToolBox, 2003).

$$\mathrm{Re} = \frac{\rho v D_H}{\mu} = \frac{v D_H}{\nu} = \frac{Q D_H}{\nu A} \quad (6)$$

Where:

D_H is the hydraulic diameter of the pipe (m);

Q is the volumetric flow rate (m^3/s);

A is the pipe's cross-sectional area (m^2);

v is the mean speed of the fluid (m/s);

μ is the dynamic viscosity of the fluid (Pa·s = N·s/m^2 = kg/(m·s));

ν is the kinematic viscosity of the fluid, $\nu = \mu/\rho$ (m^2/s);

ρ is the density of the fluid (kg/m^3).

2.5.3. Laminar Flow. This occurs when a fluid flows in parallel layers, with no disruption between the layers. The fluid tends to flow without lateral mixing at low velocities. There are no cross-currents perpendicular to the direction of flow and the velocity of the fluid is constant at any point in the fluid (Geankoplis and Christie, 2003). Laminar flow is characterized by high momentum diffusion and low momentum convection (Noakes and Sleigh, 2009). Laminar flow mostly occurs at lower velocities and when the fluid is very viscous. Laminar flow is characterized as smooth compared to turbulent flow. Common applications of laminar flow are the flow of air over an aircraft wing and flow of a viscous liquid through a tube or pipe. Under normal engineering conditions, flow through pipes may be regarded as laminar at Re < 2000.

2.5.4. Turbulent Flow. Turbulent flow is a flow regime in fluid dynamics characterized by chaotic changes in pressure and flow velocity (Batchelor, 2000). Turbulence easily occurs in relatively lower viscosity fluids and at higher velocities. Smoke from a processing plant and fast river flow are common examples of turbulent flow. Flows with Re > 4000 may be generally described as turbulent flow. Most flow state in underground mine ventilation are turbulent for easy and efficient dispersion and removal of contaminants at workings. A number of turbulence models have been developed to address turbulent flow problems. Below are examples of some turbulent models.

2.5.4.1. The standard k– ε model. K-epsilon (k-ε) turbulence model is the simplest and most commonly used model in the modeling of turbulent flow conditions. It is popular in industrial flow and heat transfer simulations due to its robustness, economy, and reasonable accuracy for a wide range of turbulent flows. It is a semi-empirical model whose derivation relies on phenomenological considerations and empiricism (Fluent, 2006). It is a two-equation model which gives a general description of turbulence by solving two additional transport equations (PDEs), namely the turbulence kinetic energy, k and the dissipation rate of turbulence, ε. The k-ε model improves the mixing-length model, and provides an alternative to algebraically prescribing turbulent length scales in medium to high complexity flows. The standard k- ε model is valid only for fully turbulent flows. The turbulence kinetic energy, k and the dissipation rate of turbulence, ε are represented by Equations 7 to 11 (Xu et al., 2017).

$$\frac{d(\rho k)}{dt} + \frac{d}{dx_i}(\rho k u_i) = \frac{d}{dx_i}\left[\left(\mu + \frac{\mu_t}{\sigma_k}\right)\frac{dk}{dx_i}\right] + G_k - \rho\varepsilon \quad (7)$$

$$\frac{d(\rho \varepsilon)}{dt} + \frac{d}{dx_i}(\rho \varepsilon u_i) = \frac{d}{dx_i}\left[\left(\mu + \frac{\mu_t}{\sigma_\varepsilon}\right)\frac{d\varepsilon}{dx_i}\right] + C_{1\varepsilon}\frac{\varepsilon}{k}G_k - C_{2\varepsilon}\frac{\varepsilon^2}{k}\rho \quad (8)$$

Where μ_t and G_k are given by:

$$\mu_t = C_\mu \frac{k^2}{\varepsilon} \quad (9)$$

$$G_k = \mu_t \left(\frac{du_i}{dx_j} + \frac{du_j}{dx_i} \right) \frac{du_j}{dx_i} \quad (10)$$

The model coefficients are given by:

$$(C_\mu, C_{1\varepsilon}, C_{2\varepsilon}, \sigma_K, \sigma_\varepsilon) = (0.09, 1.44, 1.92, 1.0, 1.3) \quad (11)$$

The standard k–ε model has a wide application in the modeling of underground turbulent flow.

2.5.4.2. The RNG k–ε model. The RNG k–ε model is derived using a rigorous statistical technique used in the area of RNG theory. It is similar in form to the standard k–ε model but it contains adjustments to the dissipation equation to effectively describe flows with zones of high strain. The above modification makes the model more precise and reliable for a wider class of flows than the standard k- ε model. This model works for flows with high Reynolds number as well as transitional flows with Reynolds number in the low turbulent range (Bakker, 2004). The transport equations for the RNG k- ε model are summarized in Equations 12 and 13 (Fluent, 2006):

$$\frac{d(\rho k)}{dt} + \frac{d}{dx_i}(\rho k u_i) = \frac{d}{dx_j}\left(\alpha_k \mu_{eff} \frac{dk}{dx_j}\right) + G_k + G_b - \rho\varepsilon - Y_M + S_k \quad (12)$$

$$\frac{d(\rho \varepsilon)}{dt} + \frac{d}{dx_i}(\rho \varepsilon u_i) = \frac{d}{dx_j}\left(\alpha_\varepsilon \mu_{eff} \frac{d\varepsilon}{dx_j}\right) + C_{1\varepsilon}\frac{\varepsilon}{k}\left(G_k + C_{3\varepsilon}G_b\right) - C_{2\varepsilon}\frac{\varepsilon^2}{k}\rho - R_\varepsilon + S_\varepsilon \quad (13)$$

Where,

G_k represents the generation of turbulence kinetic energy due to the mean velocity gradients;

G_b stands for the generation of turbulence kinetic energy due to buoyancy;

Y_m highlights the contribution of the fluctuating dilatation in compressible turbulence to the overall dissipation rate;

The quantities α_k and α_ε are the inverse effective Prandtl numbers for k and ε, respectively;

S_k and S_ε are user-defined source terms.

2.5.4.3. The realizable k-ε model. The realizable k-ε model differs from the standard k-ε model in two ways: (1) model contains a new formulation for the turbulent viscosity and (2) a new transport equation for the dissipation rate, ε, has been derived from an exact equation for the transport of the mean-square vorticity fluctuation. The realizable ε model accurately predicts the spreading rate of both planar and round jets. It is also likely to provide superior performance for rotational flows (Fluent, 2006). The realizable k–ε model uses a variable C_μ as shown in Equation 14 to calculate the turbulent viscosity (Xu et al. 2017):

$$\frac{1}{\mathrm{Ao} + \mathrm{As}\ \frac{\mathrm{U}^* k}{E}} \tag{14}$$

Where:

A_0 = 4.04,

$A_S = \sqrt{6}\mathrm{COS}\emptyset$,

$S_{ij} = \frac{1}{2}\left(\frac{du_i}{dx_j} + \frac{du_j}{dx_i}\right)$,

$U^* = \sqrt{S_{ij}S_{ij} + \Omega_{ij}\Omega_{ij}}$,

$\emptyset = \frac{1}{3}\cos^{-1}(\sqrt{6}W)$,

$W = \frac{S_{ij}S_{ji}S_{ki}}{\hat{s}}$,

$\hat{s} = \sqrt{S_{ij}S_{ij}}$.

Also, a new transport equation is used for the dissipation rate, as depicted by Equation 15:

$$\rho\frac{D\varepsilon}{Dt} = = \frac{d}{dx_i}\left[\left(\mu + \frac{\mu_t}{\sigma_\varepsilon}\right)\frac{d\varepsilon}{dx_i}\right] + \rho C_1 S\varepsilon - \rho C_2 \frac{\varepsilon^2}{K + \sqrt{V\varepsilon}} + C_{1\varepsilon}\frac{\varepsilon}{k} C_{3\varepsilon} G_b \quad (15)$$

2.5.4.4. Spalart–Allmaras model. The Spalart–Allmaras model is a one-equation model which solves a transport equation for the kinematic eddy turbulent viscosity. The Spalart–Allmaras model has shown good results for boundary layers subjected to adverse pressure gradients and has been designed specifically for aerospace applications involving wall-bounded flows. The model equation is provided in Equation 16 (Xu et al., 2017):

$$\frac{\overline{D}\nu_T}{\overline{D}t} = \nabla \cdot \left(\frac{\nu_T}{\sigma_\nu}\nabla \nu_T\right) + S_\nu \quad (16)$$

Where $S_{v,}$ the source term, depends on the viscosity ν, turbulent viscosity ν_T, the mean vorticity Ω, the turbulent viscosity gradient ∇V_T and the distance to the nearest wall L_w.

2.5.5. Numerical Analysis. This is concerned with all areas of the numerical solution of a problem, from the theoretical development and understanding of numerical methods to their practical execution. Numerical analysis is aimed at designing and analyzing techniques to give approximate and accurate solutions to hard problems. Numerical analysis is applied in the area of engineering, medicine, biology, and data analysis. As discussed earlier there are no analytical solutions for N-S equations because they are nonlinear partial differential equations. Averaged N-S equations referred to as Reynolds averaged Navier Stokes equations (RANS) are normally solved instead of the actual N-S equations. There are currently three (3) numerical methods available for solving RANS namely the Finite difference method (FDM), Finite-volume and Finite-element method.

2.5.5.1. Finite volume method (FVM). The basic idea here is to take a fluid domain and divide it into small bits called control volumes and then apply conservation to the control volumes. This is accomplished using the integral form of the governing equations resulting in a set of algebraic equations. The FVM is preferred over the FEM and FDM because the FVM applies conservation directly to the control volumes. The FVM can also be formulated to consider unstructured meshes making it suitable for treating complex geometries (Blazek, 2005). FVM is used in commercial CFD packages, such as FLUENT, CFX, and PHOENICS.

2.5.5.2. Finite element method (FEM). Finite element method (FEM) is used for elliptic or parabolic approximation. It involves the division of physical space into elements and the differential form transformed to integral form using the governing equations. The FEM has the advantage of using the integral form and unstructured grids making them

suitable for complex geometries. However, it is less popular for fluid analysis due to the fact that it requires much higher numerical effort compared to FVM (Blazek, 2005). Autodesk Simulation CFD uses the finite element method for its analysis.

2.5.5.3. Finite difference method (FDM). Finite difference method is applied to the differential form of the governing equations and involves the replacement of partial derivatives with a series expansion representation using a Taylor series. This method is suitable for simple and structured geometries. However, the transformation of irregularly shaped geometries introduces problems in terms of additional cross-coupling of equations, mesh generation and general convergence making it rarely used for industrial applications.

2.6. APPLICATION OF CFD TO UNDERGROUND MINE VENTILATION

Feasible control measures to reduce miner's exposure below the regulated permissible exposure limits require a good understanding of the dynamics of the underground mine ventilation air flow. CFD simulation has been widely used in mining to study diesel particulate matter (DPM), methane, airflow, fire, and dust problems. Computational fluid dynamics (CFD) models have been used to replicate the underground mine ventilation flow pattern to study flow mechanisms and as a result design systems to improve the efficiency and safety of the underground mine. CFD provides the platform for simulating and optimizing the underground mine ventilation system, thus preventing the health implications of overexposures to blast fume, diesel particulate matter (DPM), methane, dust etc. CFD simulations compared to physical experimentation are less expensive, saves time and can be applied to flow in physically restricted areas. Numerical experiments can be carried out using CFD for the purpose of determining indices otherwise

very difficult to obtain via laboratory or full-scale experiments (Xu et al., 2017). In addition to conducting virtual experiments, CFD can be used to better design physical experiments and increase effectiveness.

2.6.1. Dust Simulation using CFD. Dust produced during mining post a serious health threat to miners and a potential cause of ailments such as coal workers' pneumoconiosis and silicosis among others. Efficient control and management are required to ensure safe and productive working conditions in the mine. A CFD study to evaluate the dust suppression of a continuous miner and a roadheader was conducted by Heerden and Sullivan (1993). The dust particles are assumed to follow the flow in the flow field, and the flow path lines were used for qualitative assessment of dust movement. The model was used to evaluate dust suppression under different machine parameters and dimensions. The effect of drum rotation, water sprays, and air movers was also investigated. The model was validated by comparing with the experimental data, although no details were provided for the validation.

Ren and Balusu (2010) modeled the dust and airflow patterns in underground mines around the longwall shearer. Three dimensional CFD models were built to represent longwall faces in thin, medium and thick seams. These models comprised of a section of the full-scale coal face and the maingate, and embodied the major longwall components such as chocks, shearer, spill plate, BSL/crusher, and conveyor. Additionally, dust scrubbers, shearer clearer, venturi sprays, and curtains were incorporated into the models to investigate the effect of various dust control options. CFD simulations were carried out with a range of ventilation rates between 30 m^3/s to 80 m^3/s to establish the base airflow patterns on the longwall face. Geometry and boundary conditions of the longwall faces

were established using field information and data. Results from the base-case CFD models were calibrated and validated against field data obtained from three Australian longwalls. The effect of various controls on dust flow patterns and dust capture on longwall faces can be investigated using parametric studies involving changes in air flow rates, shearer clearer/sprays, the position of scrubbers and curtains etc.

Auxiliary ventilation in mining roadways driven with roadheaders was researched by Toraño et al. (2011). Dust flow behavior in two auxiliary ventilation systems was analyzed by CFD models. The accuracy of these CFD models was evaluated by airflow velocity and respirable dust concentrations taken in six points of six roadway cross-sections of the operating coal mine. The models predicted the airflow and dust behavior at different points in different roadways.

Mishra et al. (2018) designed an auxiliary ventilation system for effective dust dispersion in underground coal mine development heading. Dust concentrations were monitored using Grimm Aerosol Spectrometer to determine the best auxiliary ventilation parameters for effective dust dispersion in continuous miner development heading. The effects of various auxiliary ventilation parameters on dust dispersion was studied using CFD software ANSYS-Fluent 14.0. Parameters such as air velocity, ventilation duct diameter, height of duct from mine floor and setback distance of duct opening from mine face were varied in the ranges of 3–7 m/s, 0.6–1 m, 2–3 m and 5–8 m, respectively to ascertain their influence on dust dispersion. Dust dispersion under various scenarios was better understood by this study. Factors affecting dust dispersion were also identified.

Numerical simulations on airflow-dust diffusion rules with the use of coal cutter dust removal fans and related engineering applications in a fully-mechanized coal mining

face was studied by Zhou et al. (2018). The study was aimed at establishing an effective dust suppression system during coal cutting process. A novel hydraulic axial-flow dust coal cutter removal fan was developed through the combination of simulation results, experimental measurements, and field tests. High-efficiency atomization and dust-exhausting were combined in the suppression of coal dust. A small hydraulically-powered dust removal fan was developed and installed on both end faces of the coal cutter. The formed water curtain suppresses dust around the coal cutter preventing the dirty airflow from being sucked into the hydraulic fan. The contaminated air is thus cleansed through wet purification. Simulations on the variations of airflow and dust in a fully-mechanized mining face when the developed dust removal fan was operating was conducted using the Fluent software. A novel hydraulically-powered dust removal fan with small size and large air volume was developed based on results from nozzle atomization tests and numerical simulations. Simulation results indicate that high-concentration dust clusters exceeding 1000 mg/m^3 were generated 0–20 m from the leeward side of coal cutter, and then spreads to the operating space along the foot-way. Dust concentration on the leeward side of the coal cutter was minimized to below 500 mg/m^3 after using dust removal fans. The dust removal fans performed well in terms of dust suppression after application to fully-mechanized coal mining face.

Geng et al. (2018) investigated dust dispersion driven by a hybrid ventilation system in an underground mine using computational fluid dynamics (CFD). The trajectory of dispersed dust was solved individually using Euler–Lagrange method. Influence of key parameters (e.g., gas velocity and exhaust duct length) on dust dispersion characteristics along the coal roadway have been studied. Results from the study demonstrate that the

distribution of dust shows extreme non-uniformity with a higher concentration near the mining face, mainly on the exhaust side. There was a substantial decrease in dust concentrations along the axial direction of the coal roadway. Model predictions matched experimental data.

Ren et al. (2018) used computational fluid dynamics (CFD) to improve dust management at a long wall top coal caving (LTCC) face. The impact of different ventilation arrangements of respirable dust dispersion at the LTCC face, with a special focus on the airflow patterns and the aerodynamics of fugitive dust at the intersection of maingate (MG) and face was investigated using CFD. CFD code ANSYS-Fluent was used to simulate the general airflow field and the respirable dust dispersion behavior. The airflow field was predicted using the Reynolds Averaged Navier-Strokes equations with the standard k-ε turbulence model. Three-dimensional models containing critical equipment of the LTCC face (e.g., the belt conveyor, BSL, front and rear AFC, longwall chocks and shearer) were developed using ANSYS 13 Workbench. A field investigation was conducted to observe the dust propagation and obtain the necessary data for the development and validation of the base model. Further studies were conducted to evaluate the effectiveness of two different curtain configurations at MG. Results show that the main cause of high dust exposure level at the intersection of MG and face is due to the occurrence of flow separation and incorrect use of curtains. Ventilation arrangements at the MG and face entry are crucial to reducing the impact of flow separation on the dust flow patterns at the intersection. New ventilation arrangements at the MG and face entry have been proposed and evaluated to help in the overall reduction of dust exposure.

2.6.2. Simulation of Underground Mine Fire using CFD. Mine fires generally occur as a result of human error, ignition or by spontaneous combustion. Underground mine fires cause injuries, fatalities as well as infrastructural losses. Studies have been conducted aimed at preventing or minimizing the threats presented by underground mine fires. A study to determine the critical ventilation velocity required to prevent smoke reversal was conducted by Edwards et al. (1900). Such information is important for mine firefighting and rescue operations. The fire experiments were conducted in NIOSH's Pittsburgh Research Laboratory's (PRL) Safety Research Coal Mine (SRCM). The fire intensity varied from 50 kW to 300 kW depending upon the fuel tray area and the airflow in the coal mine entry. An ultrasonic airflow sensor was used to dynamically monitor upwind from the fire as an average over the entry cross-section. The smoke reversal was monitored with light obscuration monitors, ionization smoke sensors, and visual observation. Computational methods are necessary given the practical experimental limitations placed on experiments for large fire intensities. Fire Dynamics Simulator (FDS) was used in simulating six fire experiments carried out in the SRCM at PRL. A 50 m length of tunnel section was used in the simulation with the fire located 30 m downwind from the entrance. The critical velocity for the experiment is determined from the analysis of the airflow at the roof. The inlet flow becomes the critical velocity when the airflow at the roof does not extend upwind from the leading edge of the fire source. The results of the study showed good agreement between the SRCM experimentally determined critical velocity and the CFD predictions with FDS. It was also discovered that the critical velocity to prevent smoke reversal is proportional to the fire intensity to the 0.3 power.

Edwards and Hwang (1999) used computational fluid dynamics (CFD) method to model buoyancy induced Product-Of-Combustion (POC) spread from experimental fires in the National Institute for Occupational Safety and Health (NIOSH), Pittsburgh Research Laboratory (PRL), safety research coal mine. The experiments were in two-fold, the first was using computational program CFD2000 to simulate buoyant roof layer flow generated by a diesel fuel fire in a mine entry under zero airflow conditions and the second experiment was aimed at modeling the development of reverse flow conditions for a diesel fuel fire under positive ventilation conditions in a mine entry. Results from the study revealed that for fires in an entry under zero airflow condition, the predicted spread rates were above the measured values, the overestimation is because the POC was not distinguished from the airflow in the computation. There was a good qualitative agreement between the predicted and measured CO concentration when the CFD2000 program was used to model the CO generated by a hydrocarbon (C_3H_8) fire source. Predicted critical velocity for reverse flow conditions was lower than that predicted by a Froude model analysis.

Huang et al. (2001) used the CFD approach to study the flow and temperature fields in underground coal fires using a two-dimensional model based on the theory of natural convection and heat transfer in porous media. The predicted results agreed very well with the limited field data currently available based on model calculations. The results demonstrate that fractures and/or higher permeability zones created by subsidence are vital to sustaining a natural convection flow. Air enters from the lower temperature zone and leaves in the hot area in a uniform permeable stratum but the air enters in the subsided area with the higher permeability and leaves from the hot area and less permeable area in the fire front for a non-uniform permeable stratum. The study also found out that air convection

influences shallow fire more than deeper fire. Temperature fields indicate that heat transfer largely is by heat conduction in deeper fire and the impact of convection on heat transfer is enormous when the coal fire is at shallow depth.

Hansen (2018) modeled temperature distributions and flow conditions of fires in an underground mine drift using computational fluid dynamics (CFD). Two full-scale fire experiments in a mine drift were conducted and the results used to validate CFD and empirical models. Comparing CFD models with the experimental results showed that the upper level (ceiling) fire gas temperature at 35 and 50 m from the fire were well fitted. The CFD model over predicted the ceiling fire gas temperatures directly above the vehicles in one scenario and under predicted in the other case. The average fire gas temperature was over predicted by the empirical models during most parts of the fires. The CFD model under predicted the fire gas velocities at the higher section and over predicted the fire gas velocities at the lower section. Future study is still necessary for generating more experimental data for validating CFD models.

2.6.3. Spontaneous Combustion. Spontaneous combustion of coals occurs as a result of exothermic reaction followed by self-heating and then self-ignition. Spontaneous combustion continues to threaten underground coal mines in the U.S. as well as mines with appreciable levels of accumulated methane. Several research have been directed towards finding ways of minimizing the chances of spontaneous combustion occurrences. Yuan and Smith (2007) modeled spontaneous heating in longwall gob areas using CFD. A two longwall panel district using a bleeder ventilation system with a stationary longwall face was simulated using the Fluent tool. Gas flow in the longwall mine gob area was considered as a laminar flow in a porous media while the gas flow in the ventilation airways was

treated as fully developed turbulent flow. The GAMBIT software was used for producing the physical model as well as meshing for CFD simulations. Methane was included in the simulation due to the role it plays in oxygen concentration distribution in the gob. The boundary conditions and other input data for simulation were obtained from a local Pittsburgh coal seam mine. The simulation was first carried out without coal oxidation to achieve steady state flow field and gas distributions. Then, the unsteady simulation with coal oxidation was attained using the steady state solution as the initial conditions. All the boundary conditions were kept constant, and the chemical reaction term was initialized during the unsteady simulation. The effects of the coal's apparent activation energy and reaction surface area on the spontaneous heating process were also studied. Results from the study showed that spontaneous heating is mainly controlled by oxygen availability in the presence of a significant temperature rise. Also, minimizing the coal reaction surface area would strongly reduce the spontaneous combustion fire hazard.

Yuan and Smith (2008) studied the effects of coal properties on the potential for spontaneous heating in longwall gob (mined-out) areas using CFD. Gas flow and spontaneous heating in the longwall gob areas were simulated using the Fluent software. The gas flow in the longwall mine gob area was considered as a laminar flow in a porous medium while the gas flow in the ventilation airways was simulated as a fully developed turbulent flow. GAMBIT software was used for generating the physical model and mesh for the CFD simulation. FLAC was used in modeling the permeability and porosity distributions of the gob areas. Spontaneous heating of coal in gob areas was initially simulated assuming that the gob consists of only broken rocks. This was followed by the addition of the break coal layer to the bottom of the gob replacing the original broken rock

at the same location. The steady state flow field becomes affected, and unsteady when spontaneous heating occurs in the broken coal layer. Both rock and coal layers are then simulated based on the effect of the rock layer above the coal layer on the gas flow and heat transfer. Unsteady state simulations were carried out for three different US coals and the results compared with some available test results. Simulation results show that spontaneous heating hazards of different coals are strongly reliant on mine ventilation conditions and coal properties. A coal with a relatively larger minimum SHT would result in a longer induction time for spontaneous combustion. Spontaneous heating became mainly oxygen controlled when temperature rise was significant. The temperature rise was dependent on the coal reaction surface area. Larger coal particle size had the reaction surface area and the maximum temperature rise both significantly minimized. Coal oxidation had a slight effect on spontaneous heating. The spontaneous heating in the gob area is significantly influenced by the dynamic flow field created by face movement. Modeling results from this study compared favorably with available large-scale test data except for different induction time.

The CFD modeling of spontaneous heating in a large-scale coal chamber was investigated by Yuan and Smith (2009). A commercial CFD software, FLUENT was used in the study to simulate the gas flow and spontaneous heating in the coalbed chamber as well as the gas flow in two plenum areas. Darcy's law was used to treat the gas flow in the chamber as a laminar flow in a porous medium. The spontaneous heating of coal was considered as a surface chemical reaction forming on the coal surface in a porous medium. Conduction and convection are the means by which the heat generated from coal oxidation is dissipated. Oxidation products, on the other hand, are transported by convection and

diffusion. GAMBIT, from Fluent, Inc. was used for generating the physical model and mesh for the CFD simulation. The initial temperature for coal and air were both at 300 K while the boundary conditions used for the USBM test were also used for the simulations. The generic mass equation is then solved using Fluent. A steady state flow was achieved initially by simulating without coal oxidation, then the unsteady simulations with coal oxidation were executed using the steady state solution as the initial conditions. CFD simulation results are compared with results from the U.S. Bureau of Mines experiments conducted in the coal chamber for validation purposes. There were lower temperature model predictions during the early phase but responded well on the induction time for spontaneous heating. The calibrated CFD model is useful in forecasting the induction time for spontaneous heating in underground coal mines.

Effect of longwall face advance rate on the spontaneous heating process in the gob area was examined by Taraba and Michalec (2011). A three-dimensional, single-phase model with a continuously advancing longwall face has been developed. The gob longwall area was designed on the basis of the actual longwall panel operating in the Ostrava-Karviná Coal Mines (OKD, Czech Republic). The behavior of the coal to oxygen was modeled using the results mainly from the former laboratory-scale experiments with Czech bituminous coals. The fluent software was used in developing a three-dimensional, single-phase numerical model of the longwall district. GAMBIT was used to generate the mesh and the RNG k–ε model used to model the turbulent flow in the longwall and face shields. The flow in the gob area was considered as laminar. Equations of mass, momentum, energy, and species transport were utilized by the model. Oxygen and gaseous species are transported by convection and diffusion while the heat generated from coal oxidation is

dissipated by convection and conduction. Numerical simulations established the existence of a favorable zone for the advance of the spontaneous heating process. The advancing rate of the coalface strongly affected the maximum temperature reached in the favorable zone. The slower the advancing rate is, the higher the maximal temperature and the smaller the depth of the favorable zone in the gob area. When the rate drops to a certain "critical" value, spontaneous heating turns to flammable combustion of the coal. The "critical" advancing rate increased with decreasing grain size of the coal.

2.6.4. DPM Simulation using CFD. Underground miner's exposure to diesel particulate matter (DPM) is on the rise due to the increasing use of diesel-powered mining equipment. Overexposure to DPM can cause health issues such as headache, nausea, and asthma among others. Consequently, MSHA has instituted DPM regulations to help control the level of exposures. DPM dispersion study using Computational fluid dynamics (CFD) for underground Metal/nonmetal mines was carried out by Zheng and Tien (2008). The airflow pattern in an underground metal/nonmetal mine for a single heading was investigated. Identified poorly ventilated areas were categorized into three types. A single heading with a loader and truck operating in the immediate face area was considered in the study. Blowing and exhausting ventilation system were also examined. The research identified areas of poor ventilation and local ventilation control measures were assessed. DPM is distributed in a much smaller space in a blowing face ventilation system than in an exhausting face ventilation system. Also, high velocity fresh air tends to confine DPM in smaller area, thus DPM does not spread out evenly in the face area. This makes high air velocity an effective means of controlling DPM. The outlet of the tubing should be directed

downstream away from the intersection of the main entry and the single heading to avoid mixing with the return air when using the exhausting face ventilation system.

Zheng et al. (2015) used computational fluid dynamics technique to study the DPM dispersion in a dead-end entry with loading operation. The effects of various push–pull ventilation systems on DPM distribution were assessed to improve the working conditions in underground mines. The push–pull systems were short push and long pull tubing, short push and curved pull tubing, long push and curved pull tubing, and long push and short pull tubing. ANSYS Fluent CFD tool was used to solve 3-D incompressible unsteady turbulent momentum, continuity, energy equations, standard k-ε turbulent and non-reacting transport equations. The DPM dispersion pattern was evaluated using the species transport model with buoyancy effect. Studies of the four pull-push system demonstrated that the long push tubing provides powerful airflow in the face region with the DPM air mixture occupying more face region. Enhanced forward airflow momentum was associated with the short push tubing to confine DPM plume in the face region. On the other hand, short pull tubing could not exhaust DPM effectively because of the distant location of its influence region from the high DPM regions. Long or curved pull tubing had a much better DPM removal capacity and the contaminant air in the working area was sucked. The short push and curved pull tubing system stood out as the best design among all the four designs.

Simulation of DPM distribution in a long single entry with buoyancy effect was researched by Zheng et al. (2015a). Two types of the vehicles with six different DPM emission rates were designed to represent three LHDs and three trucks used in the DPM distribution based on an experiment conducted by the Diesel Emissions Evaluation Program (DEEP). ANSYS Fluent was used to carry out the DPM distribution analysis.

Twenty-four cases were simulated and the emissions from both truck and load-haul-dumps examined. The different designs were done in the CAD program and meshing was accomplished using GAMBIT module in the CFD program. Species transport model was used for modeling the DPM emission distribution. DPM was treated as gas and n-octane vapor (C_8H_{18}) was used to represent DPM. The standard K-Epsilon turbulence was used to model turbulence and the steady-state Navier–Stokes Equation, Energy Equation, and Continuity Equation were all solved. Acceleration due to gravity of (9.81 m/s^2) in the vertical downwards was set to account for the buoyancy effect. The critical boundary condition was the mass fraction of DPM at the diesel exhaust outlet and other boundary conditions used were entry inlet, entry outlet, diesel exhaust outlet, and wall. The face type, ventilation, diesel emission rate, buoyancy effect, and exhaust flow direction influenced DPM distribution pattern. It was concluded that miners working downwind of the engine need to wear respiratory protection equipment and engine operator has to take cover inside an environmental cab. Miners constantly working behind the tailpipe would be out of compliance under low DPM emission rate. The high temperature diesel exhaust tends to flow toward the roof and floats to the top of the ventilating air current due to buoyancy effect. Upstream miners far away from the diesel engine can be affected by high DPM diesel exhaust caused by a continuously pushed exhaust gas flow. Horizontally orientated tailpipes compared to inclined can provide constant pushing momentum and affect larger regions upstream with high DPM levels.

Effect of auxiliary ventilations on diesel particulate matter dispersion inside a dead-end entry was studied by Zheng et al. (2015b). The effect of four auxiliary ventilation systems on DPM distribution in a dead-end entry with loading operation was investigated

using computational fluid dynamics (CFD). The auxiliary ventilation systems used comprised: exhaust fan and tubing, push–pull system, blower fan and tubing, and jet fan. DPM dispersion pattern with unsteady state effect was examined using the species transport model with buoyancy effect. Results indicated high DPM levels in the face and dead-end entry regions during loading. Results from the study can aid in the selection of DPM control strategies and DPM annual training for underground miners. Design and setup of local ventilation are guided by the outcome of the study.

Thiruvengadam et al. (2016) carried out DPM simulations in an underground entry to strike a comparison between particle and species models. Two different solution models available in ANSYS Fluent were used to study 3-D simulations of DPM emission from the exhaust tail pipe of a load-haul-dump vehicle and DPM distribution inside an isolated zone in a typified underground mine. DPM was treated either as a continuous phase or as a secondary discrete phase while the incoming fresh air into the isolated zone was considered a continuous phase. Species transport model was used when DPM was treated as gas and discrete phase model was used when DPM was considered to be a particle. Comparison of DPM concentrations inside the isolated zone resulted in an accurate and economical solution technique for DPM evaluation.

Zheng et al. (2017) conducted a 3-D simulation of diesel particulate matter (DPM) distribution in a single straight entry for the Load-Haul-Dump loader (LHD)-truck loading and truck hauling operations using computational fluid dynamics approach. ANSYS Fluent software was used to carry out the simulations. The impact of truck motion on DPM distribution was captured using the dynamic mesh in FLUENT. The resultant DPM distributions were put under two scenarios, when the trucks were driving upstream and

downstream of the loading face. The air was considered as dry air and the humidity variations in the model was not accounted for simulation purposes. The incompressible ideal gas model calculated the density variation in the fluid arising from temperature gradient between the air and diesel exhaust. The species transport model was employed in determining DPM concentrations inside the single dead end entry. Air and DPM are allowed by the species transport model to diffuse to form a mixture and the mixture properties were derived using the mixing law for specific heat, thermal conductivity and viscosity, and the incompressible ideal gas law for density. The study did not consider the chemical reaction between the species. The standard $k-\varepsilon$ turbulence model with standard wall functions was used to model the turbulence in the flow. Results from the simulation can be used as a guide to determine whether DPM concentrations in a straight entry exceed the current U.S. regulatory requirement for DPM concentration (>160 µg/m3). Miners working close to the upstream region are exposed to high DPM concentrations due to the backflow of DPM plume toward the roof region of the upstream area resulting from buoyancy effect and low main airflow speed. The truck driver will not be affected by the high DPM plume when driving upstream after loading. The ventilation airflow, buoyancy effect and piston effect acting together flattened the diesel exhaust flow downstream from the truck engine. The exhaust flow from the truck cannot be clearly observed due to the high DPM fumes produced during loading when driving downstream after loading.

2.6.5. Methane Simulation. The release of large volumes of methane in coal mines is a constant source of worry due to potential threats. Most explosions in underground coal mines are as a result of methane-air mixtures, thus the need for an effective mine ventilation to ensure a safe and productive environment. Ren et al. (1997) studied methane flow around

longwall coal faces using CFD technique. The study constructed a model that has a methane-bearing seam 80 m above the working seam. The permeability values of the roof strata and the mining induced fractures were derived from laboratory studies. The methane emission and migration were successfully depicted by the pressure and velocity contours. Field data is necessary to validate CFD models.

Balusu et al. (2006) optimized gob methane drainage system. Several techniques were used during on-site monitoring, tracer gas tests, CFD simulations and field trials were among the methods employed in the exercise. The gas flow and buoyancy effect in the gob was analyzed using CFD. The CFD models were validated using field data. The study also examined the effect of face flow rate, drainage hole position, and spacing on methane drainage. Optimum gob gas control was achieved following results from CFD simulations and field investigations. The results demonstrated improved gas drainage compared to traditional gob gas methods.

Toraño et al. (2009) modeled ventilation and methane behavior of the roadway using computational fluid dynamics (CFD) in software ANSYS CFX. CFD modeling and field experiments were conducted to study the dead zone, airflow recirculation, and methane distribution. Field measurements were taken in an operating coal mine to validate CFD models. The study also compared four different turbulence models, which are SA, k–ω, k–ε and SST model, with the k–ε model chosen for downstream analysis because it agreed strongly with the field measurement. As demonstrated by study, there may be high methane concentration zones along roadway due to the limited supply of fresh airflow. The study proved that the auxiliary ventilation system is key in identifying potentially dangerous zones and inform the design of auxiliary ventilation.

Oraee and Goodarzi (2010) modeled Coal Seam Methane Drainage in Longwall Mining. Gas occurs in coalbed in an absorbed and free gas state. Absorbed gas is stored in the micro-pore structure and its transport is governed by diffusion theory. The free gas occurs in the fracture system and flows according to the seepage theory. The methane flow from seam is dependent upon the effective permeability of coal and the diffusion characteristics of coal. Coal has an extremely low permeability despite its porous nature. A mathematical model is derived for the diffusion theory of the in-situ coal degasification process. The main purpose of the theory is to provide a quantitative understanding of in-situ coal degasification. A two-dimensional, one-phase gas flow numerical model was developed to simulate the diffusion of gas through the coal seam. The finite elements method was used to solve the governing system of fully coupled non-linear partial differential equations. The model simulates a methane drainage system where the resultant risk is connected to the coefficient of diffusion, coal permeability, holes pattern and the duration for which the seam is subject to drainage. Studies show that vent holes are effective in decreasing emissions. This type of methane drainage can result in increased production in coal seams. It is also vital to continue methane drainage during the panel extraction to maximize reductions in longwall face emissions given shorter pre-mining methane drainage time. The model developed has the capability of computing the gas content of every space of coal panel at every time of the drainage process.

Kurnia et al. (2014) used CFD to simulate methane dispersion and innovative methane management in underground mining faces. Possible conditions which may prevail in a mine tunnel are investigated. A 3-D model is developed for a typical mine tunnel model mostly used in underground coal mining studies. The dimensions of the mine tunnel is 36

m long, 3.6 m wide and 2.9 m high. A ventilation duct with a diameter of 0.6 m is hung at 1.9 m height from the floor and 0.6 m from the tunnel wall on the access road. Methane is released from discrete sources in the mining face and dispersed by the airflow. Mass, momentum, energy, and species transport equations subject to appropriate boundary conditions are solved. The interaction between the species is included in the mixture density which is in line with the incompressible ideal gas law. The computational domains were created and meshed using Gambit software. Fluent was used to solve governing equations with the constitutive relations, turbulence model and boundary conditions. Simulation results indicate that the number and location of the methane sources and the amount of methane released from each source greatly affects methane dispersion inside mine tunnel. Methane monitoring is very crucial for establishing an effective control of methane concentration which is necessary for designing an effective mine ventilation system. Channeling the ventilation flow at a point is more effective compared to dispersing. New ideas provided by this research would facilitate the design of an “intelligent” cost-effective underground mine ventilation system.

2.7. BLAST FUMES AND RE-ENTRY TIMES

Post-blast re-entry times have safety, productivity and cost implication, hence choosing appropriate re-entry time is of paramount importance. A few techniques are available to estimate concentration and clearance times pertaining to underground blasting. In most cases the estimations are based on a variation of a mathematical logarithmic decay series which strongly relies on data monitoring and sampling methodology. De Souza (1990), studied the prediction of blast fumes and dilution ventilation requirements. An

explosive-testing technique was developed and the experimental results were combined with theoretical thermohydrodynamic calculations in order to design an accurate predictive model. A number of explosive compositions prepared at established compositions were tested under controlled conditions as part of the experimental procedure. The effect of several parameters including oxygen balance, particle size, and primer weight on fume production was studied. A sealed 1 m^3 blasting chamber was used for explosive detonation and gas collection. Gas compositions and concentrations were determined using a Carlo Erba® gas chromatograph Mega Model HRGC 5300, and a Spectra-Physics® SP4400 computer integrator was used for data reduction, storage and graphic display of test results. Tiger, a computer program was used for testing the thermohydrodynamic predictions of the explosive compositions. A series of relationships between fume production and oxygen balance, the velocity of detonation, particle size, and primer weight were developed. Thus, trends in fume production for typical commercial explosives used in underground mines can be determined. The study developed a mathematical model capable of determining dilution ventilation requirements and dilution times to minimize post-blast fume concentrations in the blasting area. Winn (2002), conducted a study into blast fumes and re-entry times in underground metalliferous mines. The study attempted to establish whether various underground metalliferous mines around Australia have in place appropriate re-entry times. It examined how mines reduce the exposure of blast fumes with their ventilation systems. Test data was examined to establish how well theoretical models of gas dilution represent the actual dilution of blast fumes. Further data analysis was performed to determine safe re-entry times to blasted areas based on measured blast fume concentrations. Outcome of the study show that for development headings ventilated with

ducting, there is no correlation between the decay constant fitted to test data and the decay constant calculated from quantity and volume measurements of the blast area, assuming the void exists beyond end of the ducting but there exists a correlation for stopes ventilated with primary ventilation. More test data would be required to confirm this hypothesis. Most development headings will have cleared in under 45 minutes in a well ventilated mining environment. For ventilated stopes, it may take up to 2 hours to get concentrations below the TWA. An Assessment Tool to minimize safe after blast re-entry time to improve the mining cycle has been developed by Gillies et al. (2004). A series of measurements of after blast fumes in various development heading arrangements has been carried out. The study was undertaken in an underground metal mine in Australia. Site tests were conducted to monitor and record the blast fumes generated from level development headings in the test mine and detailed testing procedures established. Analysis of the test results demonstrates that carbon monoxide is the critical gas in terms of defining minimum re-entry times. Also, test results for auxiliary ventilated headings highlight the fact that the power relationship best describes fume dilution as opposed to the classic exponential relationship for flow-through ventilation systems such as through the regulator doors and for naturally ventilated working areas, and this requires further testing to be confirmed. Two empirical equations have been developed to conservatively calculate re-entry times for development headings.

The available traditional methods for estimating blast re-entry times as discussed above, are unable to account for the variabilities in the ventilation and blasting process. In order to address the above weakness, researchers have used computational fluid dynamics (CFD) to study underground mine blast fume propagation. Lu (2011) performed a simulation study on blast fume diffusion characteristics of a driving face. Blast fume

diffusion characteristics of a driving face under 8 conditions and under different drift lengths and different outlet positions was studied. The paper concluded that the fume discharge time has a linear relationship with drift length and windpipe outlet position. When the drift length is longer than 10 m, the ventilation time for fume concentration lowering to the prescribed safety standards will increase 2 min or more. Conventional and numerical models of blasting gas behavior in auxiliary ventilation of mining headings has been studied by Torno (2013). The study was executed in a deep underground mine located in Northern Spain. Blasting gases, CO and NO_2, were measured in three cross-sections of the heading located at 20, 30 and 40 m from the heading face. Mathematical models of gas dilution have been developed based on the dilution time after blasting. 4D models have been developed using computational fluid dynamics (CFD) through software ANSYS CFX 12.0. The CFD model results were validated and compared to experimental models obtained in the measurement programmes. Based on the CFD models developed, other dilution mathematical models of blasting gases can be developed for other cross-sectional areas, the mass of explosives and other ventilation parameters. The experimental mathematical models and CFD models obtained allows the analysis of how the blasting gases behave and to be able to determine conditions safe for miners to return to a blasted area. From the above reviews, it can be clearly deduced that much work still needs to be done in the area of CFD application to blast fume concentrations and clearance.

2.8. SUMMARY

Literature on underground mine blasting and explosives; post-blast re-entry times and CFD applications to underground mine ventilation have been reviewed. Most

underground mines in the U.S. rely on experience and observation in setting re-entry times. Few underground mines use theoretical methods for estimating post-blast re-entry time despite the importance of the post-blast re-entry time. A few empirical relations are available in literature to assist in re-entry time estimation. The empirical relationships are however unable to account for the variations in the ventilation and blasting conditions. Computational fluid dynamics (CFD) has been used on limited bases to try to overcome the weaknesses presented by empirical formulas. CFD is yet to be used comprehensively to study the influence of duct discharge location on fume clearance. There is no means of calculating safe blast distance (i.e., blast exclusion zone). No comprehensive relationship exists for estimating post-blast re-entry time and optimal air quantity. Section 3 presents the theoretical formulation and governing equations used in solving the research problem.

3. THEORETICAL FORMULATION AND GOVERNING EQUATIONS

Analytical solutions to fundamental equations of fluid mechanics in the mining industry and other engineering communities can be very limited. The nonlinear partial differential equations contained in the governing equations are challenging to solve using analytical means and numerical methods such as computational fluid dynamics (CFD) is often necessary to solve complex geometry problems. Approximate solutions are derived using numerical methods and algorithms with the aid of a computer. A CFD program, ANSYS Fluent, was used to solve the governing equations in this research.

Analysis of airflow and blast fume propagation in the underground mine development heading was successfully executed by first of all developing physical models for different working arrangements and conditions. The different working conditions were achieved by varying heading dimensions, changing the explosive mass, applying different airflow quantities and varying face to duct distances among others. The geometries of the different models were designed using SOLIDWORKS®. The geometries were simplified to analyze the problem with reasonable effort. Computational meshes were created and then applied to the problem domain. After generating the mesh, boundary conditions and initial conditions were specified. This was followed by defining fluid parameters, physical properties, and solving techniques. Discretized equations were solved iteratively until convergence was achieved. The results of the simulations are then analyzed using various plots. The CFD models are then validated and improved using real field data as well as published mine data.

3.1. MATHEMATICAL MODELING

Blast fume and air flow in underground workings is simplified as Newtonian. Blast fume flow within the immediate blasting area mixes with air and is reduced to incompressible, turbulent, and non-reacting. The gases of immediate concern in the blast fume considered for this study are carbon monoxide (CO) and nitrogen dioxide (NO_2). The incompressible flow was assumed due to the following (Hartman, 1992):

(i) Pressure drop in long ventilation pipes did not exceed 5.0kPa; and (ii) Elevation differences did not exceed 427m.

To determine whether an underground mine ventilation flow is laminar or turbulent, the Reynolds number needs to be calculated. The Reynolds number is calculated using Equation 6 as follows:

$$\mathrm{Re} = \frac{\mathrm{v}D_{\mathrm{H}}}{v} \tag{6}$$

Where the v is the velocity, D_H is the equivalent diameter, and v is the kinematic viscosity. Turbulent flows occur at Re>> 4000, with a kinetic viscosity of air = 1.45 x 10^-5 m^2/s, the critical velocity of flow, $\mathrm{v} = \frac{0.06}{D_{\mathrm{H}}}$. Mine openings rarely have equivalent diameters less than 1 m (i.e. 0.06 m/s), therefore velocities exceeding 0.06 m/s will cause turbulent flow in mine openings.

3.1.1. Governing Equations. The continuity and momentum equations for describing flow in the underground mine are derived as follows:

Conservation of mass:

Applying the mass conservation law to an Infinitesimal fluid particle:

Rate of change of mass, $\frac{dm}{dt}$ = mass inflow (m_{in}) – mass outflow (m_{out}):

$$\frac{dm}{dt} = m_{in} - m_{out} \tag{17}$$

Mass (m) = Density (ρ) x Velocity (v) x Area of face (a)

$$m_{in} = \rho|_x u|_x dydz + \rho|_y v|_y dxdz + \rho|_z w|_z dxdy$$

$$m_{out} = \rho|_{x+dx} u|_{x+dx} dydz + \rho|_{y+dy} v|_{y+dy} dxdz + \rho|_{z+dz} w|_{z+dz} dxdy$$

Simplifying and rewriting:

$$m_{in} = \rho u|_x dydz + \rho v|_y dxdz + \rho w|_z dxdy \tag{18}$$

$$m_{out} = \rho u|_{x+dx} dydz + \rho v|_{y+dy} dxdz + \rho w|_{z+dz} dxdy \tag{19}$$

Mass (m) = Density (ρ) x volume (V):

$$m = \rho dxdydz$$

$$\frac{\mathrm{dm}}{\mathrm{dt}} = \frac{d\rho}{d\mathrm{t}}\mathrm{dxdydz} \tag{20}$$

Substituting Equations 18 to 20 into Equation 17:

$$(\rho u|_x dydz + \rho v|_y dxdz + \rho w|_z dxdy) - (\rho u|_{x+dx} dydz + \rho v|_{y+dy} dxdz + \rho w|_{z+dz} dxdy) = \frac{d\rho}{d\mathrm{t}}\mathrm{dxdydz}$$

Dividing both sides of the equation by dxdydz and simplifying:

$$\frac{-d(\rho u)}{d\mathrm{x}} - \frac{d(\rho v)}{d\mathrm{y}} - \frac{d(\rho w)}{d\mathrm{z}} = \frac{d\rho}{d\mathrm{t}}$$

$$\frac{d\rho}{d\mathrm{t}} + \frac{d(\rho u)}{d\mathrm{x}} + \frac{d(\rho v)}{d\mathrm{y}} + \frac{d(\rho w)}{d\mathrm{z}} = 0$$

Incompressible flow, Density (ρ) = constant:

$$\frac{d\mathrm{u}}{d\mathrm{x}} + \frac{d\mathrm{v}}{d\mathrm{y}} + \frac{d\mathrm{w}}{d\mathrm{z}} = 0 \tag{21}$$

Equation 21 is the final expression for conservation of mass for an incompressible, Newtonian flow.

Conservation of momentum:

Applying Newton's second law of motion to an Infinitesimal fluid particle:

(Rate of change of momentum in control volume) = (Rate of momentum inflow, M_{in}) – (Rate of momentum outflow, M_{out}) + (Sum of forces acting on control volume)

Momentum, M = mass (m) x velocity (v) = $\rho\underset{\sim}{u}(v.n)$:

X-component:

$$M_{in} = [\rho\underset{\sim}{u}u+\frac{d(\rho\underset{\sim}{u}u)}{dx}\frac{-\Delta x}{2}]\Delta y\ \Delta z$$

$$M_{out} = [\rho\underset{\sim}{u}u+\frac{d(\rho\underset{\sim}{u}u)}{dx}\frac{\Delta x}{2}]\Delta y\ \Delta z$$

Y-component:

$$M_{in} = [\rho\underset{\sim}{u}v+\frac{d(\rho\underset{\sim}{u}v)}{dy}\frac{-\Delta y}{2}]\Delta x\ \Delta z$$

$$M_{out} = [\rho\underset{\sim}{u}v+\frac{d(\rho\underset{\sim}{u}v)}{dy}\frac{\Delta y}{2}]\Delta x\ \Delta z$$

Z-component:

$$M_{in} = [\rho\underset{\sim}{u}w+\frac{d(\rho\underset{\sim}{u}w)}{dz}\frac{-\Delta z}{2}]\Delta x\ \Delta y$$

$$M_{out} = [\rho\underset{\sim}{u}w+\frac{d(\rho\underset{\sim}{u}w)}{dz}\frac{\Delta z}{2}]\Delta x\ \Delta y$$

$$M_{in}\text{-}M_{out} = \left[\frac{-d(\rho \underset{\sim}{u} u)}{dx} - \frac{d(\rho \underset{\sim}{u} v)}{dy} - \frac{d(\rho \underset{\sim}{u} w)}{dz}\right] \Delta x\ \Delta y\ \Delta z \quad (22)$$

Incompressible flow, ρ=constant and applying the chain rule to Equation 22:

$$M_{in}\text{-}M_{out} = -\rho\left[u\frac{d\underset{\sim}{u}}{dx} + v\frac{d\underset{\sim}{u}}{dy} + w\frac{d\underset{\sim}{u}}{dz}\right] + \underset{\sim}{u}\left(\frac{du}{dx} + \frac{dv}{dy} + \frac{dw}{dz}\right) \Delta x\ \Delta y\ \Delta z$$

$$\frac{du}{dx} + \frac{dv}{dy} + \frac{dw}{dz} = 0, \text{ Incompressible flow}$$

$$M_{in}\text{-}M_{out} = -\rho\left[u\frac{d\underset{\sim}{u}}{dx} + v\frac{d\underset{\sim}{u}}{dy} + w\frac{d\underset{\sim}{u}}{dz}\right]\Delta x\ \Delta y\ \Delta z$$

Converting from the vector form to the different directional form:

X-component:

$$-\rho\left[u\frac{du}{dx} + v\frac{du}{dy} + w\frac{du}{dz}\right]\Delta x\ \Delta y\ \Delta z \quad (23)$$

Y-component:

$$-\rho\left[u\frac{dv}{dx} + v\frac{dv}{dy} + w\frac{dv}{dz}\right]\Delta x\ \Delta y\ \Delta z \quad (24)$$

Z-component:

$$-\rho[u\frac{dw}{dx} + v\frac{dw}{dy} + w\frac{dw}{dz}]\Delta x\ \Delta y\ \Delta z \quad (25)$$

Body forces acting on a fluid particle:

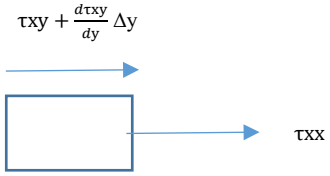

Gravitational force along x-direction:

$$\rho g_x\ \Delta x\ \Delta y\ \Delta z$$

Net viscous force along x-direction:

$$(\frac{d\tau xx}{dx} + \frac{d\tau xy}{dy} + \frac{d\tau xz}{dz})\Delta x\ \Delta y\ \Delta z$$

Summation of forces along X-direction:

$$\rho g_x\ \Delta x\ \Delta y\ \Delta z + (\frac{d\tau xx}{dx} + \frac{d\tau xy}{dy} + \frac{d\tau xz}{dz})\Delta x\ \Delta y\ \Delta z$$

$$(\rho g_x + \frac{d\tau xx}{dx} + \frac{d\tau xy}{dy} + \frac{d\tau xz}{dz})\Delta x\ \Delta y\ \Delta z \quad (26)$$

Similar expressions are repeated for the Y and Z components:

$$(\rho g_y + \frac{d\tau xy}{dx} + \frac{d\tau yy}{dy} + \frac{d\tau yz}{dz})\Delta x\, \Delta y\, \Delta z \quad \text{along Y} \tag{27}$$

$$(\rho g_y + \frac{d\tau xz}{dx} + \frac{d\tau yz}{dy} + \frac{d\tau zz}{dz})\Delta x\, \Delta y\, \Delta z \quad \text{along Z} \tag{28}$$

Substituting Equations (23-28) into Newton's second law of motion:

X-component:

$$\rho\frac{du}{dt}(\Delta x\, \Delta y\, \Delta z) = -\rho(u\frac{du}{dx} + v\frac{du}{dy} + w\frac{du}{dz})\Delta x\, \Delta y\, \Delta z + \rho g_x\, \Delta x\, \Delta y\, \Delta z +$$

$$(\frac{d\tau xx}{dx} + \frac{d\tau yx}{dy} + \frac{d\tau zx}{dz})\, \Delta x \Delta y \Delta z$$

Similar expressions are repeated for the Y and Z components and both sides of the equation divided by $\Delta x\, \Delta y\, \Delta z$:

$$\rho(\frac{du}{dt} + u\frac{du}{dx} + v\frac{du}{dy} + w\frac{du}{dz}) = \rho g_x + \frac{d\tau xx}{dx} + \frac{d\tau yx}{dy} + \frac{d\tau zx}{dz} \tag{29}$$

$$\rho(\frac{dv}{dt} + u\frac{dv}{dx} + v\frac{dv}{dy} + w\frac{dv}{dz}) = \rho g_y + \frac{d\tau xy}{dx} + \frac{d\tau yy}{dy} + \frac{d\tau zy}{dz} \tag{30}$$

$$\rho(\frac{dw}{dt} + u\frac{dw}{dx} + v\frac{dw}{dy} + w\frac{dw}{dz}) = \rho g_z + \frac{d\tau xz}{dx} + \frac{d\tau yz}{dy} + \frac{d\tau zz}{dz} \tag{31}$$

Equations 29 to 31 are referred to as Cauchy Momentum Equations.

For an Incompressible, Newtonian, Isotropic Fluid, the shear stresses are simplified as follows:

$$\tau yx = \tau xy = \mu \left(\frac{du}{dy} + \frac{dv}{dx}\right)$$

$$\tau yz = \tau zy = \mu \left(\frac{dv}{dz} + \frac{dw}{dy}\right)$$

$$\tau xz = \tau zx = \mu \left(\frac{du}{dz} + \frac{dw}{dx}\right)$$

$$\tau xx = -p+2\mu\frac{du}{dx} \; ; \; \tau yy = -p+2\mu\frac{dv}{dy} \; ; \; \tau zz = -p+2\mu\frac{dw}{dz}$$

Substitution:

$$\rho\frac{Du}{Dt} = \rho g_x - \frac{dp}{dx} + \mu \left(\frac{d^2 u}{dx^2} + \frac{d^2 u}{dy^2} + \frac{d^2 u}{dz^2}\right) \quad (32)$$

$$\rho\frac{Dv}{Dt} = \rho g_y - \frac{dp}{dy} + \mu \left(\frac{d^2 v}{dx^2} + \frac{d^2 v}{dy^2} + \frac{d^2 v}{dz^2}\right) \quad (33)$$

$$\rho\frac{Dw}{Dt} = \rho g_z - \frac{dp}{dz} + \mu \left(\frac{d^2 w}{dx^2} + \frac{d^2 w}{dy^2} + \frac{d^2 w}{dz^2}\right) \quad (34)$$

Equations 32 to 34 represent conservation of momentum for a Newtonian, incompressible fluid.

3.1.1.1. Turbulence modeling. Turbulent flows are defined by fluctuating velocity fields. This results in the fluctuation of transported quantities such as momentum, energy, and species concentration. The exact equations (Navier-stokes) describing the turbulence in a flow can be solved numerically. The exact solution to the Navier-stokes equations (N-S) is too accurate demanding huge computational time and cost. An averaged solution is okay for most engineering problems. The Navier Stokes equations generated after averaging operation is known as, Reynolds Averaged Navier Stokes equations (RANS). The time-averaged Navier-Stokes equation is solved in such a way that small-scale turbulent fluctuations do not have to be simulated. RANS is not a closed system since it contains unknown terms for the transport of mean momentum, mass, and heat of the turbulent motion and requires empirical input for closure (Zheng, 2011).

Any variable in a turbulent flow can be characterized as the sum of mean value and fluctuating value:

$$b = b_{av} + b'$$

$$b_{av} = \frac{1}{\Delta t}\int_{t}^{t+\Delta t} b\,dt$$

Where b = variable in turbulence flow, b_{av} represents the mean value, and b’ is the fluctuating value.

Time interval of integration should be big enough to smoothen out fluctuations and should also be small enough to capture any unsteadiness in the flow.

Substituting the various transport variables into the mass conservation and momentum equations yields the RANS:

$$\frac{d(\rho u_j)}{dx_j} = 0 \tag{35}$$

$$\frac{d(\rho u_i u_j)}{dx_j} = -\frac{dp}{dx_i} + \frac{d}{dx_i}\mu\left(\frac{du_i}{dx_j}+\frac{du_j}{dx_i}\right)+ \frac{d}{dx_i}(-\rho(u'_i u'_j) \tag{36}$$

An additional term, $-\rho (u'_i u'_j)$, known as the Reynolds stress is introduced to capture the effect of turbulence in the flow. There are various turbulence models available to help represent the turbulence in a flow and the selection of the turbulence model is crucial in CFD analysis. Numerical methods such as the finite volume method (FVM), finite element method (FEM), and the finite difference method (FDM) are available to solve RANS.

The widely recognized standard k-ε model is used to model the turbulence in the flow. It is the simplest and complete turbulence model because it allows the turbulent velocity and length scale to be determined independently. The standard k-ε model is a semi-empirical model established on model transport equations for the turbulence kinetic energy (k) and its dispersion rate (ε). The model transport equation for k is derived from the exact equation, while the model transport equation for ε is attained using physical reasoning. The governing equations for the standard k-ε model for incompressible viscous turbulent flow are derived as shown below:

Turbulent kinetic energy (k):

$$\text{The rate of change of k: } \frac{d(\rho k)}{dt} \tag{37}$$

$$\text{Transport of k by convection: } \frac{d}{dx_i}(\rho k u_i) \tag{38}$$

$$\text{Diffusive transport: } \frac{d}{dx_j}\left[(\mu+\frac{\mu_t}{\sigma_k})\frac{dk}{dx_j}\right] \tag{39}$$

Generation of turbulent kinetic energy due to mean velocity, G_k:

$$-\rho\,(u'_i u'_j)\frac{d(u_j)}{dx_i} \tag{40}$$

Generation of turbulence kinetic energy due to buoyancy, Gb:

$$\beta g_i \frac{\mu_t}{pr_t}\frac{dT}{dx_i} \tag{41}$$

$$\text{Rate of destruction: } \rho\varepsilon \tag{42}$$

Putting Equations 37-42 together:

$$\frac{d(\rho k)}{dt} + \frac{d}{dx_i}(\rho k u_i) = \frac{d}{dx_j}\left[\left(\mu + \frac{\mu_t}{\sigma_k}\right)\frac{dk}{dx_j}\right] - \rho\left(u'_i u'_j\right)\frac{d(u_j)}{dx_i} + \beta g_i \frac{\mu_t}{pr_t}\frac{dT}{dx_i} - \rho\varepsilon \quad (43)$$

Turbulent dissipation (ε):

$$\text{The rate of change of } \varepsilon: \frac{d(\rho\varepsilon)}{dt} \quad (44)$$

$$\text{Transport of } \varepsilon \text{ by convection: } \frac{d}{dx_i}(\rho\varepsilon u_i) \quad (45)$$

$$\text{Diffusive transport: } \frac{d}{dx_j}\left[\left(\mu + \frac{\mu_t}{\sigma_\varepsilon}\right)\frac{d\varepsilon}{dx_j}\right] \quad (46)$$

$$\text{Turbulent viscosity, } \mu_t\text{: } c_\mu \frac{k^2}{\varepsilon}\text{; } c_{\mu=0.09}$$

$$\text{Rate of production: } c_{1\varepsilon}\frac{\varepsilon}{k}G_k \quad (47)$$

$$\text{Rate of destruction: } c_{2\varepsilon}\frac{\varepsilon^2}{k}\rho \quad (48)$$

Putting Equations 44-48 together:

$$\frac{d(\rho\varepsilon)}{dt} + \frac{d}{dx_i}(\rho\varepsilon u_i) = \frac{d}{dx_j}\left[\left(\mu + \frac{\mu_t}{\sigma_\varepsilon}\right)\frac{d\varepsilon}{dx_j}\right] + c_{1\varepsilon}\frac{\varepsilon}{k}G_k - c_{2\varepsilon}\frac{\varepsilon^2}{k}\rho \quad (49)$$

Where σ_k and σ_ε are the turbulent Prandtl numbers for k and ε, respectively; g_i is the gravitational vector in the ith direction; and C_1 and C_2 are constants.

Turbulent viscosity, μ_t is related to turbulent kinetic energy (k) and turbulent dissipation (ε) by Equation 50 as shown below:

$$\mu_t = c_\mu \frac{k^2}{\varepsilon} \tag{50}$$

Where, constant $c_{\mu=0.09}$

The Reynolds stress is related to the turbulent viscosity, μ_t by Equation 51 as follows:

$$-\rho\,(u'_i u'_j) = \mu_t \left(\frac{dU_i}{dx_j} + \frac{dU_j}{dx_i}\right) \tag{51}$$

Once the turbulent kinetic energy (k) and turbulent dissipation (ε) are obtained from the model transport equations, the turbulent viscosity can be calculated. The Reynolds stress is then calculated using Equation 51. Modeling the Reynolds stress keeps the RANS equation closed.

3.1.1.2. Species transport. The movement of gases and liquids in our environment affects our lives profoundly. Transport of pollutants in air, water or soil and temperature fluctuations are caused by convection and diffusion, hence the ability to understand, predict, and control transport phenomena is vital for many industrial applications (Dmitri, 2010). Convection-diffusion conservation equation for a mixture of different species in a solution are presented below:

Concentration of species per unit time (C_t) + Convective term (F_c) + Diffusive term (F_D) = 0

$$C_t + F_c + F_D = 0 \tag{52}$$

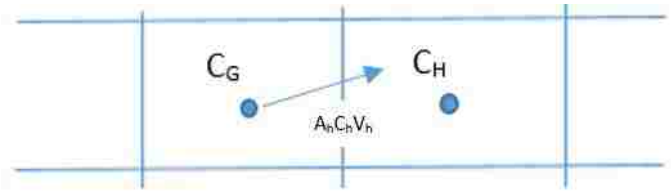

Moving from G to H:

$$C_t = \frac{dC_h}{dt} \tag{53}$$

Convective term (F_C) = Area (A_h) X Velocity (V_h) X Concentration (C_h):

$$F_C = A_hV_hC_h = \frac{d}{dx_i}(c_h\, v_i) \tag{54}$$

Diffusive term (F_D) = Area (A_h) X Concentration gradient (C_g) X Diffusion coefficient (D_c):

$$F_D = D_CA_h \frac{dc}{dx}\Big|_h = \frac{d}{dx_i}\left(D_c\frac{d}{dx_i}\right) \tag{55}$$

Substituting Equations 53-55 into Equation 52:

$$\frac{dC_h}{dt} + \frac{d}{dx_i}(c_h v_i) + \frac{d}{dx_i}(D_c \frac{d}{dx_i}) = 0 \quad (56)$$

Mixture concentration = Mixture density, ρ = summation of concentrations = $\sum_i c_i$

$$\text{Mass fraction, } Y_i = \frac{C_i}{\rho}, \; c_i = \rho Y_i$$

Substituting $C_h = \rho Y_i$; $v_i = \vec{u}$ into Equation 56:

$$\frac{d(\rho Y_i)}{dt} + \frac{d}{dx_i}(\rho Y_i \vec{u}) + \frac{d}{dx_i}(D_c \frac{d}{dx_i}) = 0$$

Rewriting and rearranging:

$$\frac{d(\rho Y_i)}{dt} + \Delta.(\rho Y_i \vec{u}) = -\Delta.\vec{J_i} \quad (57)$$

Where $\vec{J_i}$ is the mass diffusion in turbulent flows.

For mass diffusion in turbulent flows, the turbulent diffusion coefficient is calculated from the turbulent Viscosity, μ_t:

$$D_c = \frac{\mu_t}{\rho S c_t} \quad (58)$$

Where the turbulent Schmidt number, Sct= 0.7 modal constant.

The Reynolds averaged Navier Stokes (RANS) equations, the standard k-ε equations, the transport species equations, and the boundary conditions need to be solved. These, however, cannot be solved analytically since these equations are complex and non-linear coupled partial differential equations. Hence, the finite volume method in ANSYS Fluent software is used to solve these equations.

3.1.2. Finite Volume Method (FVM). The finite volume method is a numerical means of solving partial differential equations in the form of algebraic equations. How this works is to take a fluid domain and divide it into multiple cells called control volumes. A control volume balance is performed for the mass, momentum, and species transport at the cell faces. The resulting integral forms of the governing equations and boundary conditions are converted to algebraic equations relating the cell-center values. The algebraic equations relating the various cell-center values are then solved to determine the velocities, pressure and mass fractions of gases at the cell centers.

The finite volume method was used for this study because conservation is built into the method. This means that mass and momentum at the faces surrounding a control volume are conserved. The finite volume method is also good for complex and irregular geometries and domains.

3.2. COMPUTATIONAL FLUID DYNAMICS (CFD) SIMULATION OF BLAST FUMES IN UNDERGROUND MINES

3.2.1. Physical Model and Meshing. The heading geometries were built using SOLIDWORKS®. Different geometries were designed for most commonly used cross-sectional areas 9 m^2, 16 m^2, 20 $m^{2,}$ and 25 m^2. Forcing auxiliary fan with ducting of

1000mm in diameter was used. The geometries were exported to ANSYS Fluent for meshing. The mesh elements were generally tetrahedral in shape. The boundary layers were made finer by inserting inclusion zones as well as sizing the edges of the geometries. The next step after geometry and meshing is computational fluid dynamics (CFD) modeling and simulation.

3.2.2. Boundary and Initial Conditions. The boundary conditions used for the simulation were inlet velocity at the main drive entry and at the fan duct face, pressure outlet at the main drive exit and wall conditions. The main drive inlet velocity was 1 m/s. The air used for the simulation was considered dry and the humidity variations in the model was not considered. The properties of air used in the simulation are as follows: Density= 1.225 kg/m^3; Specific heat (Cp) =1006 j/kg-K; Thermal conductivity=0.0242 w/m-K; Viscosity 1.789e-05 kg/m-s; and Temperature= 300 K. Initial concentration of carbon monoxide (CO) and nitrogen dioxide (NO_2) gases in the blast fume were 0.015 and 0.002 respectively based on a total explosive gas yield of 1.08 m^3/kg (Stewart, 2014). The boundary and initial conditions used for the blast fume simulation are summarized in Table 3.1.

3.2.3. Model Setup and Numerical Solution. The density variation in the fluid due to the temperature gradient between the blast fume and air was calculated using the incompressible ideal gas model. The species transport model in Fluent was used to model the species CO, NO_2, and air. The three species were allowed to diffuse and form a mixture using the incompressible ideal gas law for density, the mixing law for specific heat, thermal conductivity, and viscosity. The chemical reaction between the species was not considered in this study. Reynolds averaged Navier-Stokes, continuity, momentum, and energy

equations were used to solve airflow in the computational domain. Mass fractions for CO and NO_2 were determined using the species transport equation. The standard k-ε model was used to model turbulence in the flow. The residuals required for convergence were set as follows: momentum, continuity, mass fraction of CO, the mass fraction of NO_2, k, and ε be smaller than 10^{-4}; and the energy equation smaller than 10^{-7}. A time step size of 1 s was used for the transient flow calculation for durations required for fume concentrations to be reduced to acceptable limits.

The differential form of governing equations and boundary conditions are converted to integral forms. The Integral forms of the governing equations and boundary conditions are further converted to algebraic equations relating cell-center values in a process known as discretization. The highly non-linear algebraic equations are then converted to linearized algebraic equations. These linearized algebraic equations are solved iteratively by first initializing guess values and updating these guess values. The solution is converged when the imbalances are reduced below the set threshold.

Table 3.1. Boundary and initial conditions used for simulation

Boundaries	Boundary conditions
Main airflow inlet	Velocity (normal to boundary)=1m/s Temperature of air, T=300 k
Main airflow outlet	Pressure outlet
Initial CO concentration	Mass fraction, M_f = 0.015
Initial NO_2 concentration	Mass fraction, M_f = 0.002
Walls	No slip boundary conditions Adiabatic walls (heat flux=0)

3.3. SUMMARY

The mass, momentum, and species transport equations necessary to model the blast fume problem have been developed. Analytical methods cannot be used to solve these governing equations because of the complexity and highly nonlinear nature of these governing equations. The governing equations and the boundary conditions are solved using the finite volume method in ANSYS Fluent. The finite volume method involves dividing the computational domain into smaller bits and quantities conserved for each cell. The integral forms of the governing equations are converted to algebraic forms relating the cell-center values. These algebraic equations are solved iteratively until the solution converges.

Geometries of the various heading arrangements are designed in SOLIDWORKS® and after exported to ANSYS Fluent. Computational meshes are created and the boundary conditions and initial conditions assigned. The fluid parameters and the solving techniques are defined. Discretized equations are solved iteratively until the imbalances fall below a threshold. The simulation results and discussions are presented in Section 4.

4. CFD SIMULATION RESULTS AND DISCUSSIONS

The computational fluid dynamic (CFD) simulations of the blast fume were successfully conducted for this research. These CFD simulations were categorized into the following: (i) mesh independence study, (ii) blowing and exhausting ventilation system, (iii) selection of appropriate gas for downstream analysis, (iv) analysis of the effect of duct discharge location on fume clearance, (v) development of safe blast exclusion zones, and (vi) development of a relationship between optimal air quantity and post-blast re-entry time.

4.1. MESH INDEPENDENCE STUDY

The mesh independency is needed to determine whether the numerical solution depends on the mesh size. The mesh independent solution does not change significantly even when you refine your mesh further. Fine mesh provides a more accurate solution but with relatively longer computational time. It is generally advantageous to choose a mesh size that lies in between coarse and fine so long as no appreciable difference in solution is obtained. The accuracy of the CFD simulations is significantly improved by the mesh independency study.

Test of mesh-independency was carried out using three different mesh types: coarse mesh (121,212 nodes), medium mesh (243,305 nodes) and fine mesh (487,458 nodes). A mesh with very large elements (i.e. coarse mesh) that converged was used as an initial case. The number of nodes of the coarse mesh was doubled to get a mesh with intermediate sized elements (i.e. medium mesh). The medium mesh was further refined by doubling the number of nodes to generate a mesh with small element sizes (i.e. fine mesh).

The initial simulation was conducted on the coarse mesh setup until convergence was attained. The mesh size was then refined globally by doubling the number of nodes and the simulation was carried out again until convergence. The results were compared with the results of the initial simulation. The difference between results of the two simulations was significant. This means the solution is still changing and not yet independent of the mesh size, so a third simulation was necessary. The mesh size is then further refined by doubling the number of nodes and the whole process of simulation was repeated for this mesh size setup. The results of the second and the third simulations were comparable. This means a solution that is independent of the mesh has been obtained. The medium size mesh was therefore used for downstream analysis in order to reduce computational time while maintaining a reasonable numerical solution accuracy.

The simulation was conducted using the following parameters: mass of explosive 200 kg; cross-sectional area of 16 m^2; heading length of 40 m; airflow of 3 m^3/s; and 121,212 nodes (coarse mesh), 243,305 nodes (medium mesh) and 487,458 nodes (fine mesh). The Velocity contours of carbon monoxide (CO) concentrations at approximately 2 m above the floor are shown by Figures 4.1 to 4.6.

Figures 4.1 and 4.2 illustrate contours representing CO concentration for a coarse mesh at a simulation time of 1 hr and 30 min respectively. Figures 4.3 and 4.4 show contours representing CO concentration for a medium mesh at a simulation time of 1 hr and 30 min respectively. Contours representing CO concentration for a fine mesh at a simulation time of 1 hr and 30 min are shown in Figures 4.5 and 4.6 respectively.

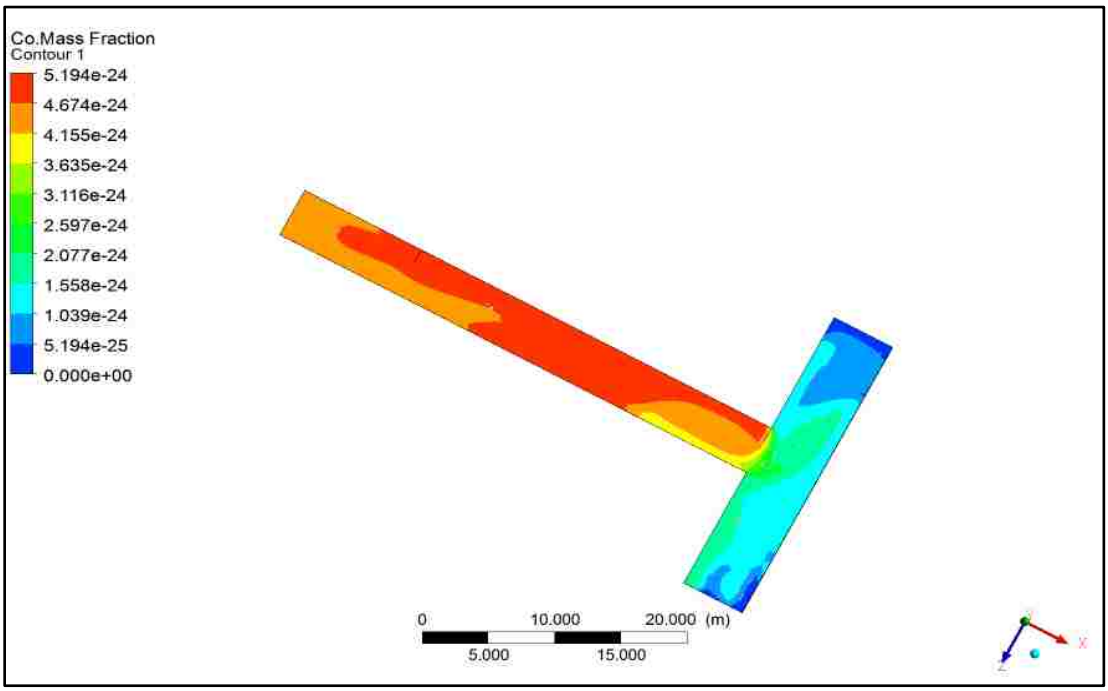

Figure 4.1. CO concentration at 1 hr for coarse mesh

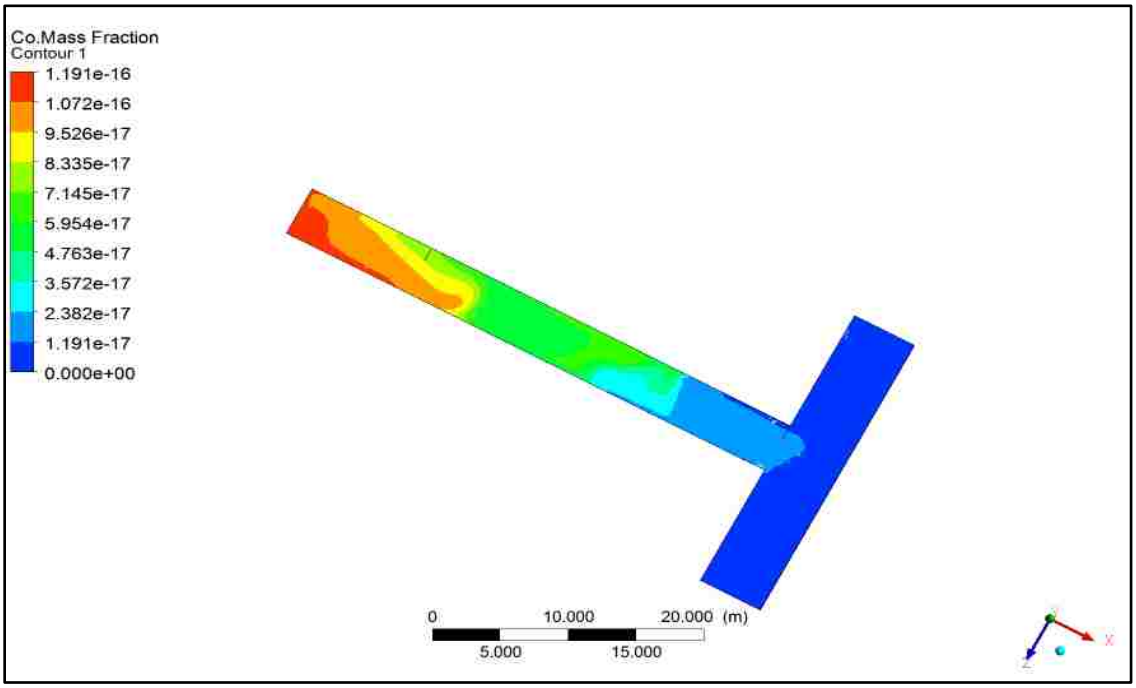

Figure 4.2. CO concentration at 30 min for coarse mesh

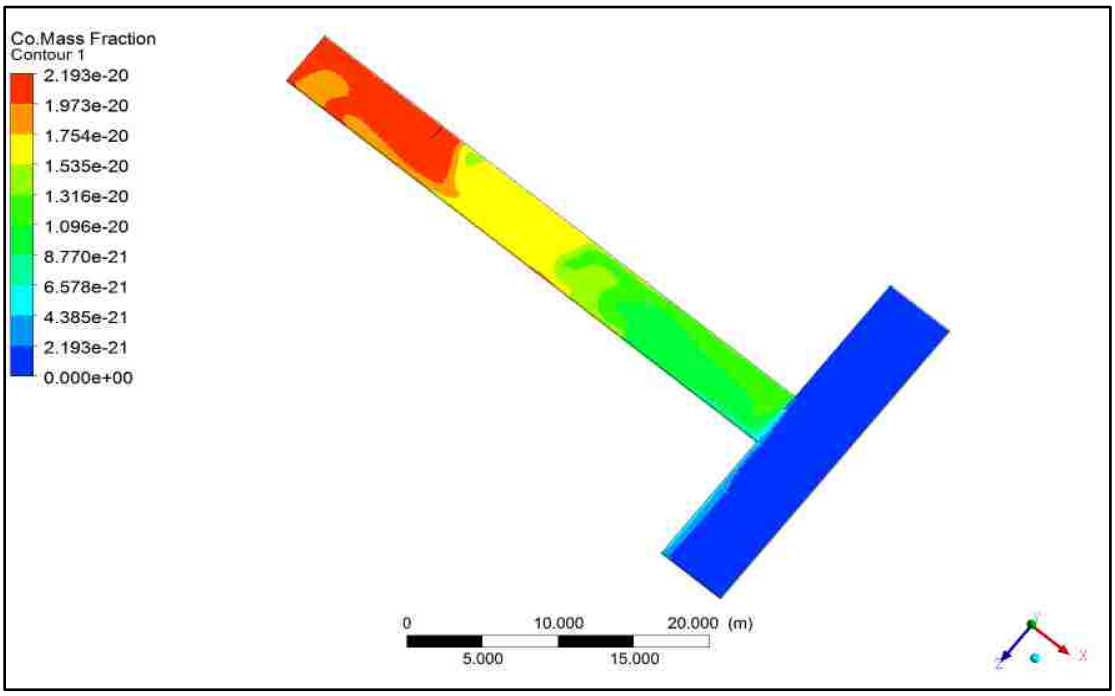

Figure 4.3. CO concentration at 1 hr for medium mesh

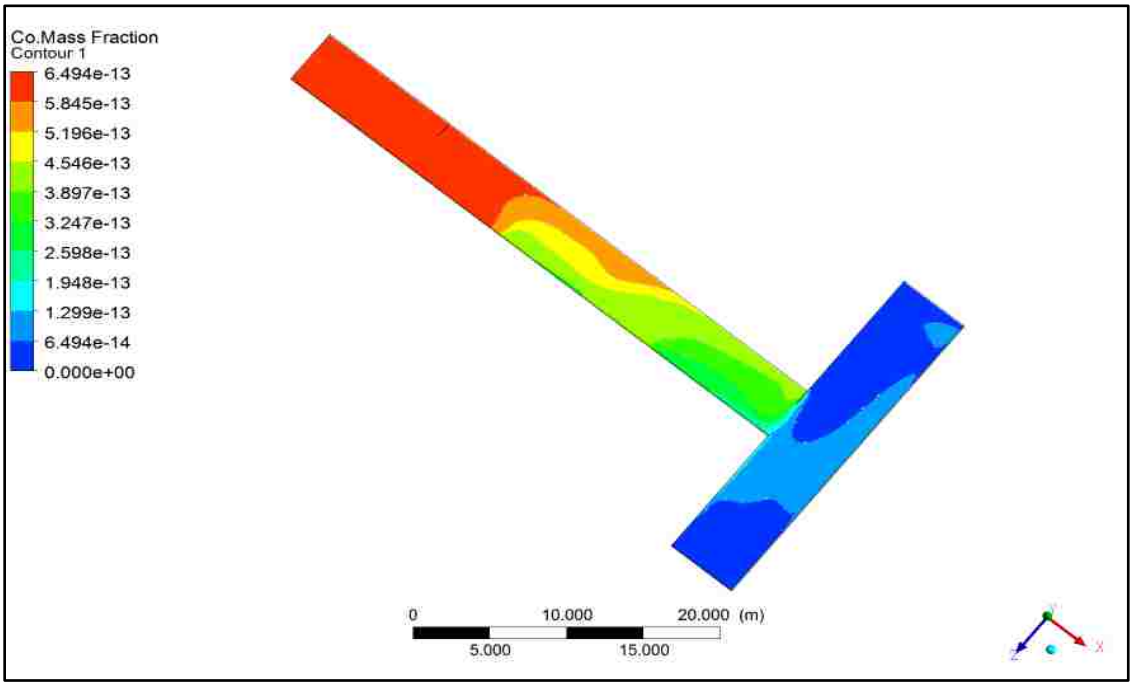

Figure 4.4. CO concentration at 30 min for medium mesh

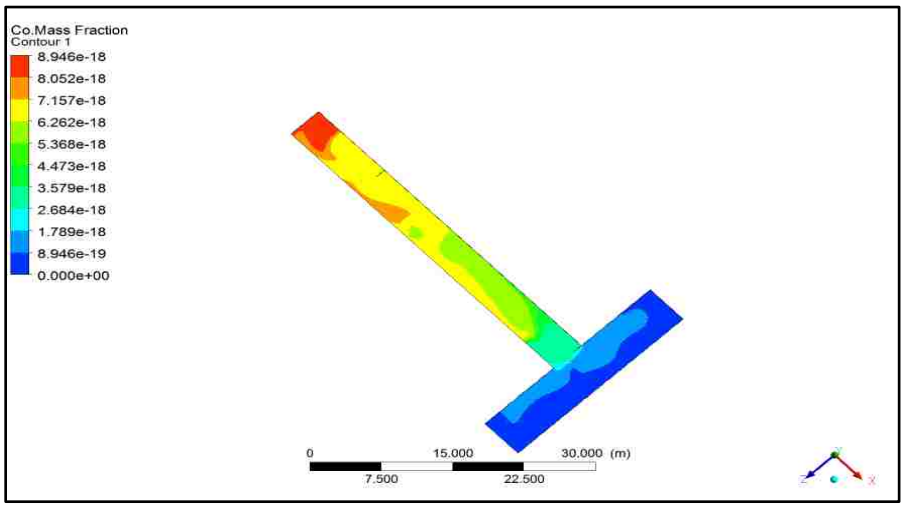

Figure 4.5. CO concentration at 1 hr for fine mesh

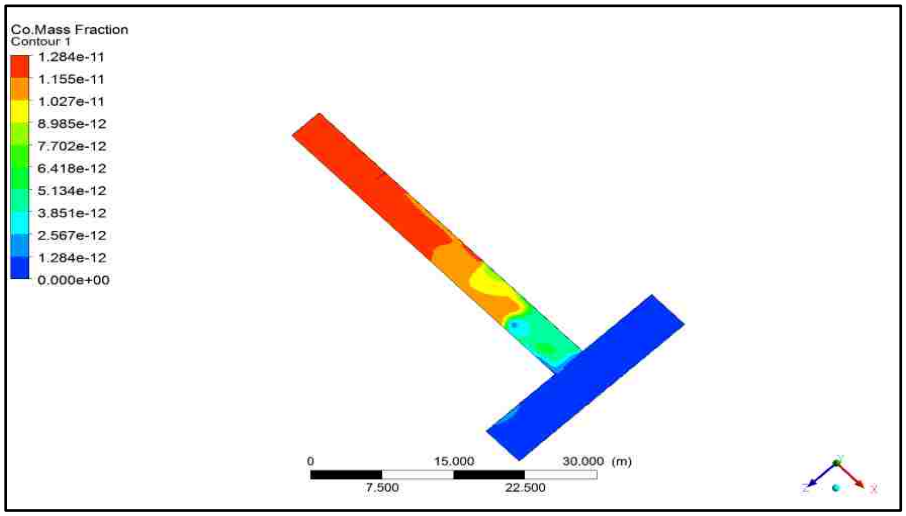

Figure 4.6. CO concentration at 30 min for fine mesh

As illustrated by Figures 4.1 to 4.6 above, the maximum CO concentrations along the heading for the coarse, medium, and fine meshes were close. Additionally, the CO concentrations were below the threshold simulating for 30 min and 1 hr. The nodes and

computational time for the various mesh sizes is summarized in Table 4.1. Figure 4.7 highlights CO concentrations at various simulation times for the different mesh sizes.

Table 4.1. Nodes and computational time for the mesh sizes

Mesh Type	Number of Nodes	Computational Time (hr)
Coarse	121,212.00	3.2
Medium	243,305.00	5.9
Fine	487,458.00	7.5

As observed from Table 4.1 above, the computational time needed for convergence increases with increasing number of nodes.

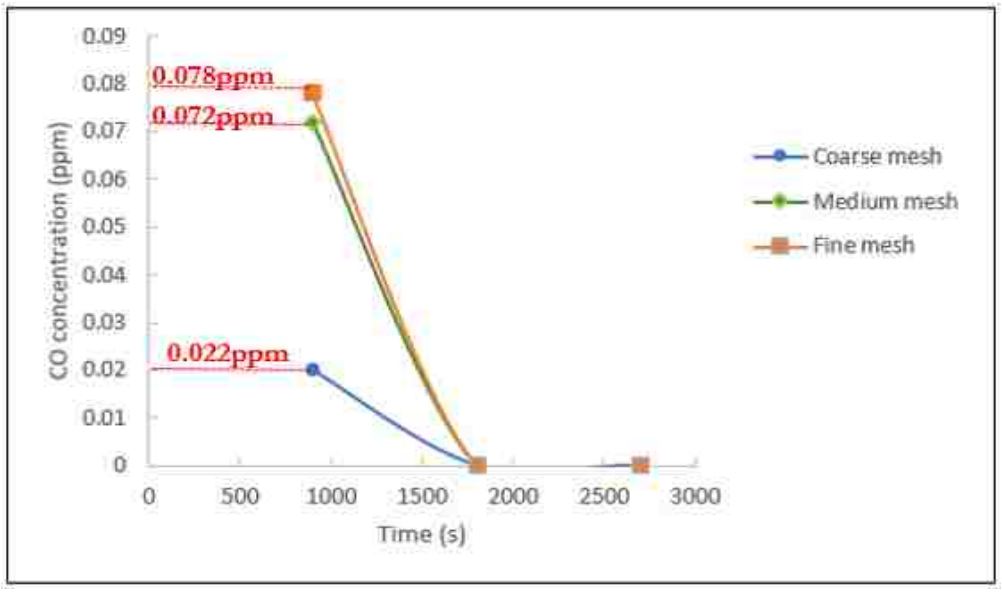

Figure 4.7. CO concentrations at different times for different mesh sizes

As observed from Figure 4.7, carbon monoxide concentration for the coarse mesh digresses significantly compared with the medium and fine meshes at the 900 s mark. However, the concentrations of the medium and the fine mesh closely match at various times. Doubling the number of nodes for the coarse mesh yields a concentration of 0.072 ppm (i.e. 72 % change) at a simulation time of 900 s for the medium sized mesh. At a simulation time of 900 s, the CO concentration recorded for the fine mesh after doubling the number of nodes for the medium mesh is 0.078 (i.e. 7 % change). This implies that there is no significant variation in simulation results for the medium and fine mesh sizes. The medium mesh size is used for downstream analysis since it gave acceptable simulation results at a reasonable computational time.

4.2. BLOWING AND EXHAUSTING VENTILATION SYSTEM

The blowing and exhausting ventilation systems are the commonly used ventilation systems in the underground mining ventilation setup. The blowing ventilation system ensures that fresh air reaches the heading face. The high velocity air released from the fan breaks into the cloud of blast fumes and clears the noxious gases from the heading face. The exhaust ventilation system involves the fan sucking the blast fumes from the heading face.

A detailed CFD study was conducted to determine which of the ventilation setup is suitable for controlling blast fumes in a typical leveled underground development heading. An explosive mass of 200 kg; a cross-sectional area of 16 m^2; air flow of 10 m^3/s; and heading length of 40 m were the parameters used for the simulation.

Figures 4.8 and 4.9 show contours representing CO concentration at the development heading for the blowing and the exhausting ventilation systems respectively.

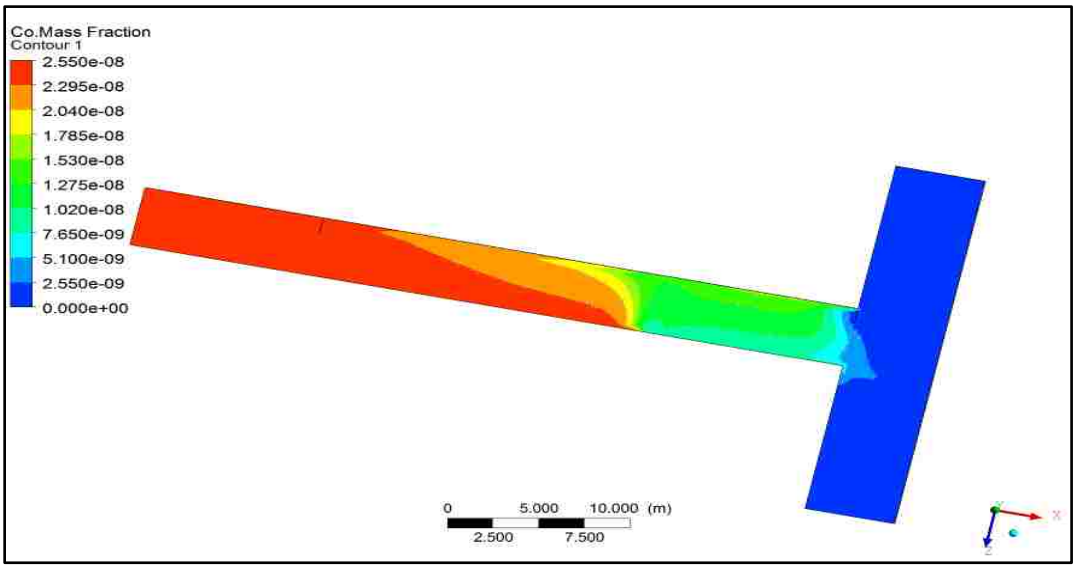

Figure 4.8. Blowing ventilation system

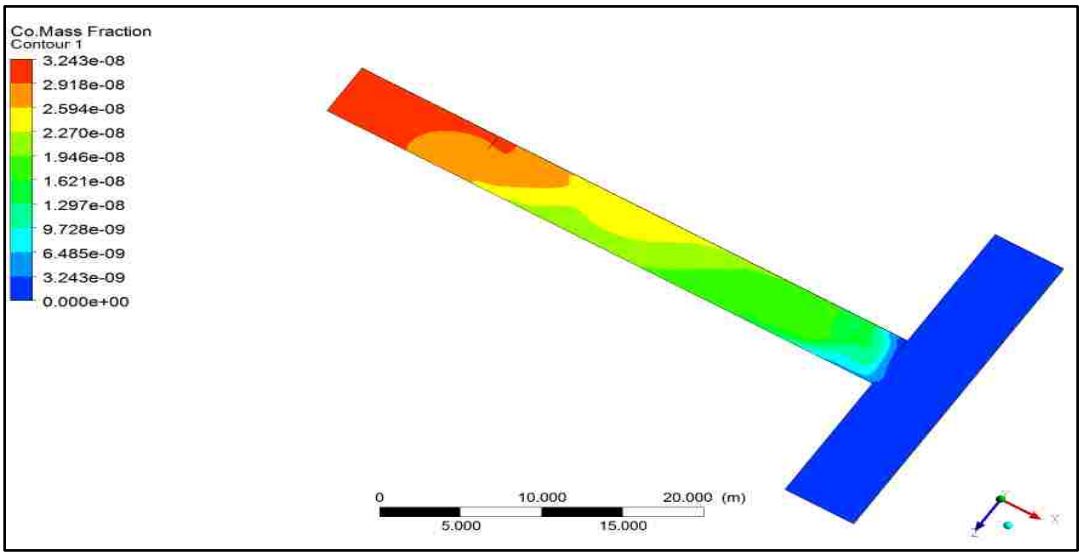

Figure 4.9. Exhausting ventilation system

As observed in Figures 4.8 and 4.9, the maximum CO concentration for the blowing and the exhausting ventilation systems is 0.025 ppm and 0.032 ppm respectively. Since the results for both ventilation systems were very close, either method could be used for simulation purposes. However, the blowing ventilation system was adopted for downstream analysis.

4.3. SELECTION OF APPROPRIATE GAS FOR DOWNSTREAM ANALYSIS

This part of the research focused on selecting a single gas for downstream analysis. The main drivers for this selection are available computational capacities and the high cost of gas monitors. Therefore, one of the two most critical noxious gases, CO and NO_2 needs to be chosen for this research project. To decide which noxious gas to use for the research, a simulation was conducted under the following conditions: mass of explosive =200 kg; area of face = 25 m^2; length of heading = 50 m; and fan airflow=10 m^3/s.

Figures 4.10 and 4.11 show contours of gas concentrations at section 2 m high above floor after blast for CO and NO_2 respectively. From Figure 4.10, the maximum concentration of CO in the immediate work area is 18.6 ppm, which is below the threshold of 25 ppm (defined by NIOSH). The maximum concentration of NO_2 in Figure 4.11 is 1.99 ppm, which is below the threshold of 3 ppm (defined by NIOSH). It can be clearly observed from Figures 4.10 and 4.11 that when CO content reaches the standard level, NO_2 content is far below the concentration standard. Hence, CO is used for downstream analysis in this research.

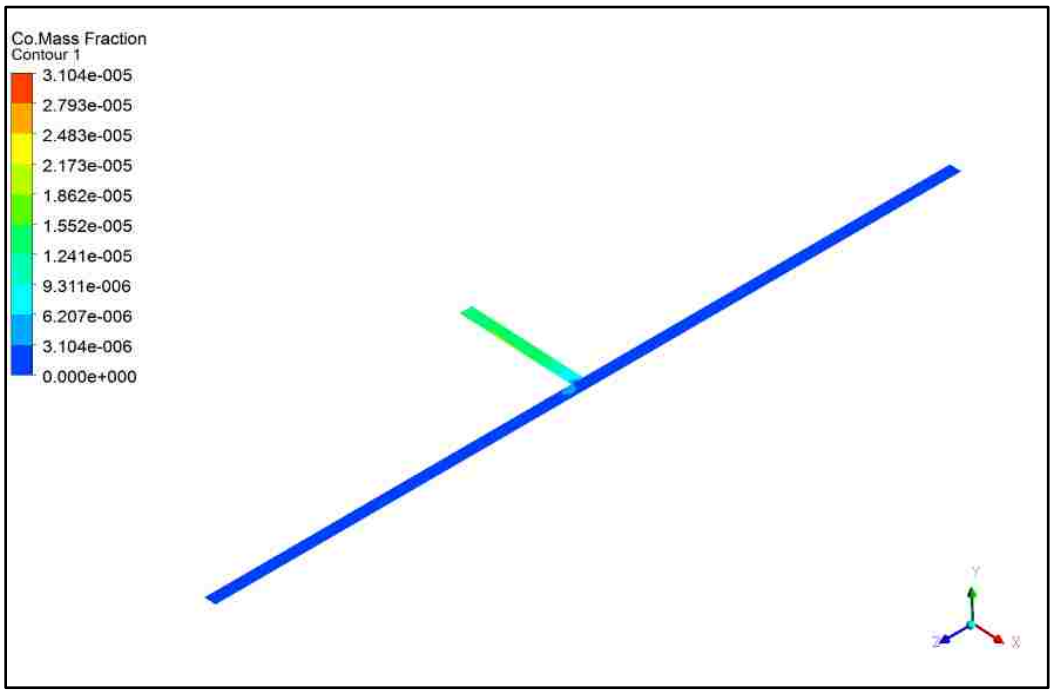

Figure 4.10. Carbon monoxide concentration after simulation

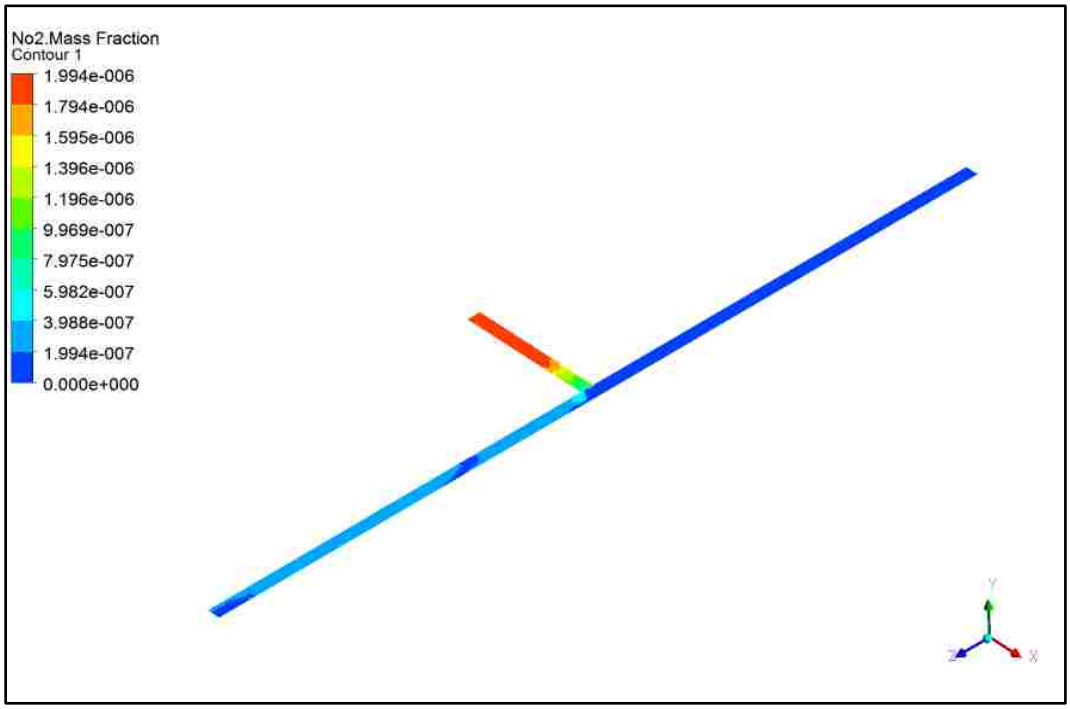

Figure 4.11. Nitrogen dioxide concentration after simulation

4.4. INVESTIGATING THE EFFECT OF DISCHARGE LOCATION ON BLAST FUME CLEARANCE

Deciding where to locate the fan duct for optimal results as the heading length increases is critical. The fan duct discharge should be located at a distance safe from fly rocks and where the fresh air is able to penetrate the cloud of blast fume and remove the noxious gases from the heading face. To determine an optimal duct discharge location for effective fume clearance, a relationship between duct discharge location and post-blast re-entry time needs to be established.

4.4.1. Case 1. This scenario was designed to examine the effect of varying duct discharge location on fume clearance. Conditions employed for the simulation are as follows: cross-sectional area of 25 m^2; 300 kg of explosive; 10 m^3/s of fresh air; and discharge location of 7 m, 10 m, 13 m, and 20 m from the heading face. The unsteady flow was calculated using a time step of 1 s for the total time duration of 3600 s. Variation of CO concentration with time for the various discharge locations is captured by Figure 4.12.

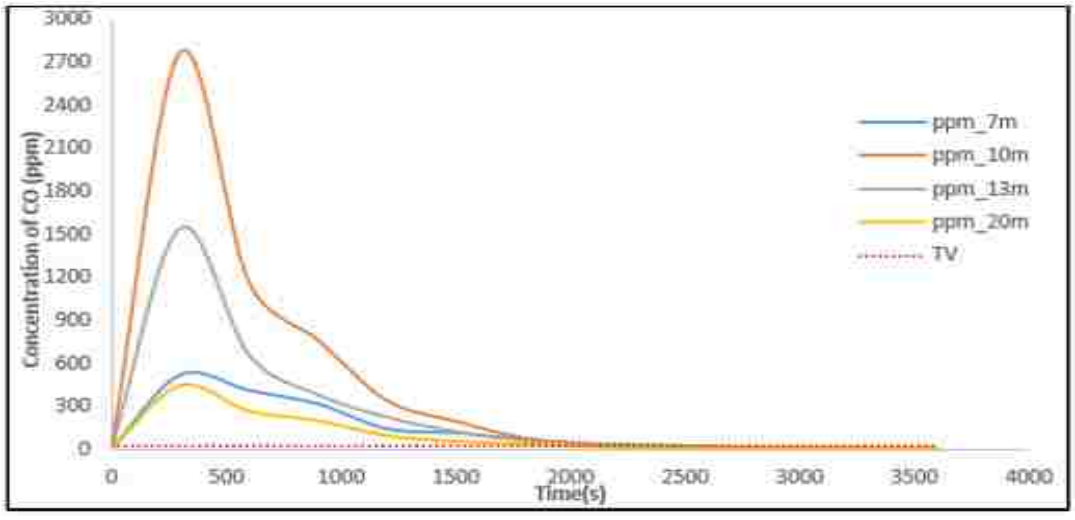

Figure 4.12. Carbon monoxide concentration with time

As observed from Figure 4.12, discharge location 10 m recorded the highest CO concentration at 5 min after blast followed by 13 m, 7 m and finally 20 m. There is no significant difference in the clearance times to draw any conclusion. This may be due to the relatively shorter discharge locations used for the simulations. Further studies is therefore required at this point to clearly establish the relationship between duct discharge location and fume clearance time, hence post-blast re-entry time.

4.4.2. Case 2. Case 2 was designed with much longer duct discharge locations and relatively longer mining development headings. The relationship between the cross-sectional area, the duct discharge location and post-blast re-entry time was also examined by introducing cross-sectional areas 16 m^2 and 20 m^2. Settings used for the simulation are as follows: cross-sectional area of 16 m^2 and 20 m^2; 200 kg of explosive; 10 m^3/s of fresh air; duct discharge locations 10 m, 30 m, 60 m, and 70 m; and drive lengths of 70 m, 90 m, and 100 m. Diagrams of the computational domains used for the simulation are detailed in Figures 4.13 to 4.16.

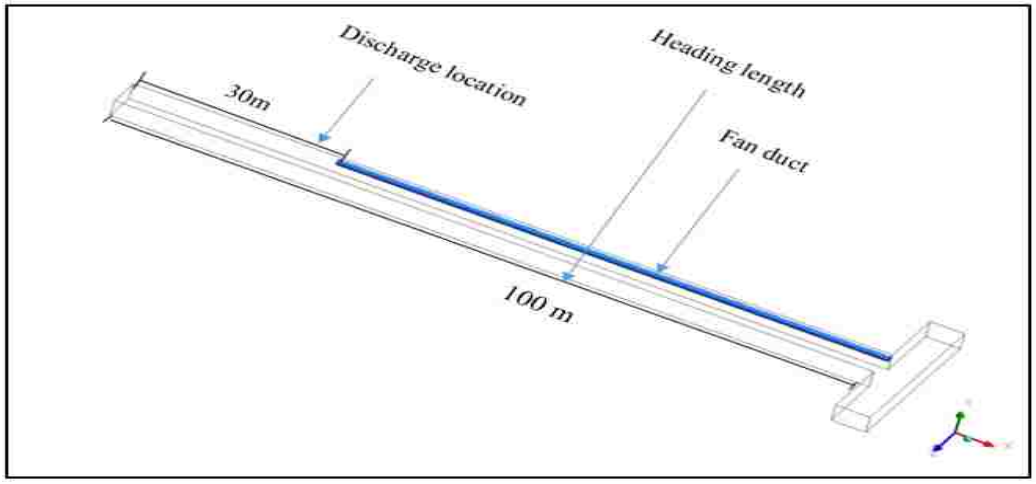

Figure 4.13. Discharge location of 30 m and heading length 100 m

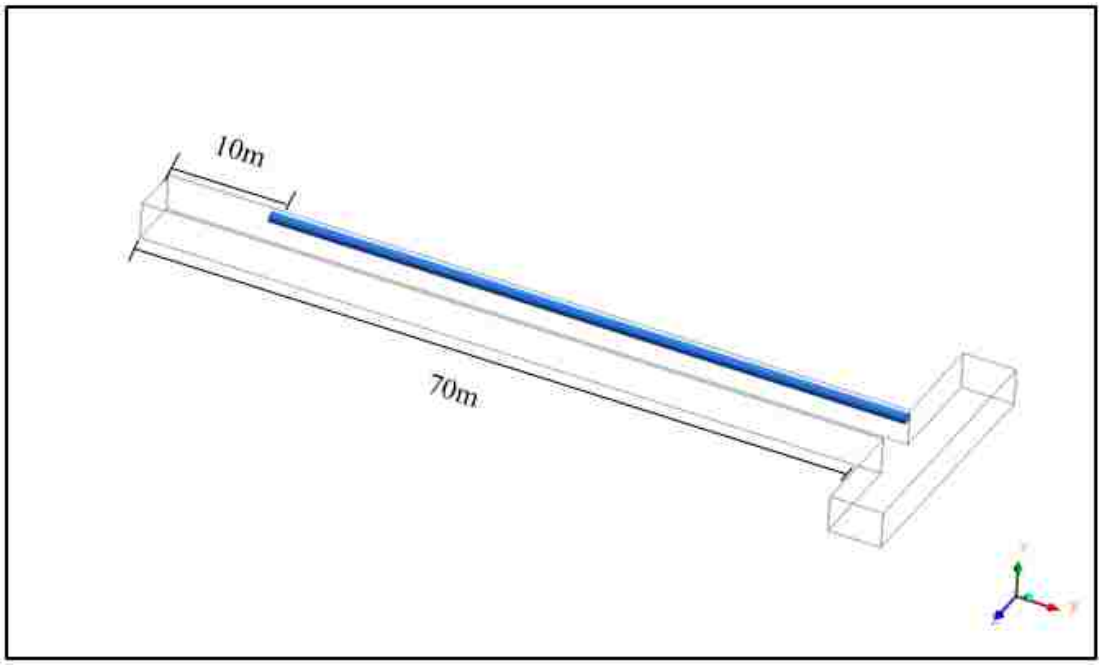

Figure 4.14. Discharge location of 10 m and length 70 m

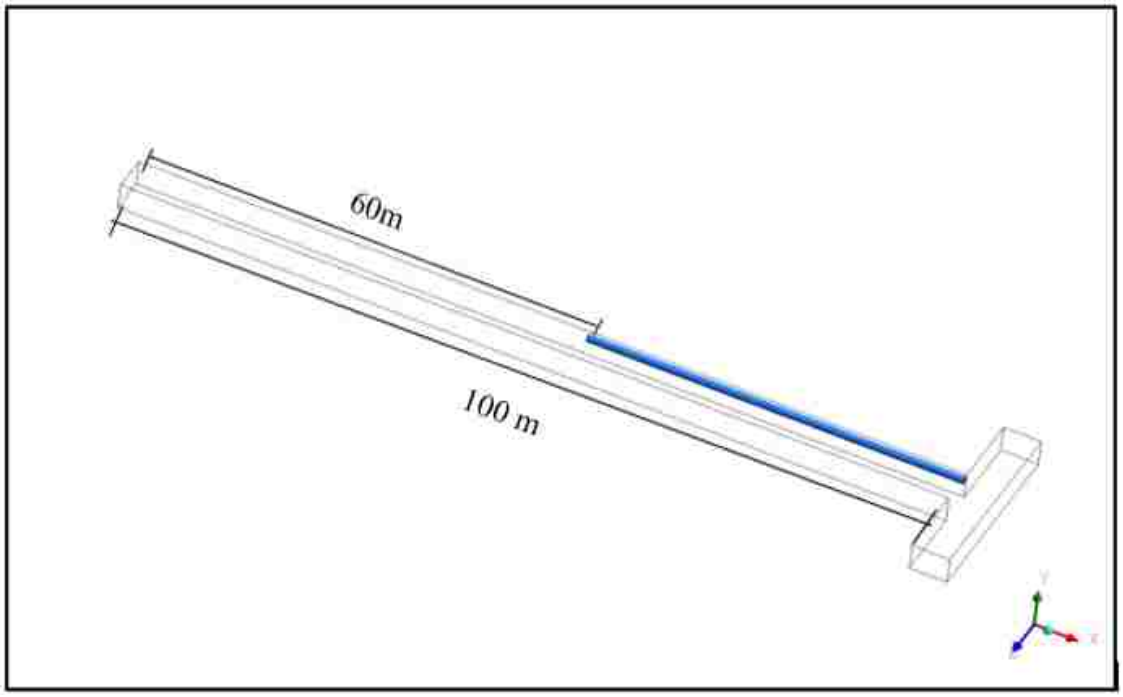

Figure 4.15. Discharge location of 60 m and length 100 m

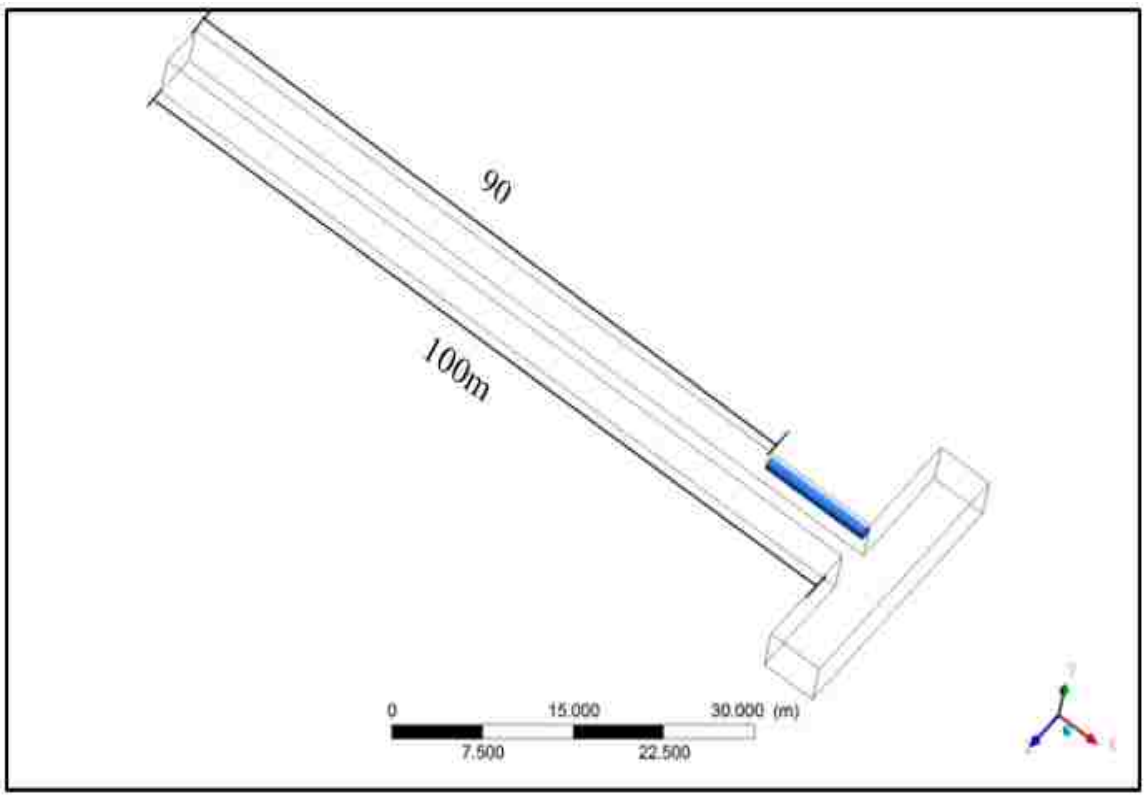

Figure 4.16. Discharge location of 90 m and length 100 m

Simulations were conducted for durations required to bring CO concentrations below the threshold. Contours representing CO concentrations for a cross-sectional area of 20 m^2 with various duct discharge locations and heading lengths are presented in Figures 4.17 to 4.22.

Figures 4.17 and 4.18 represent CO distribution along a heading length of 70 m, 10 m duct location, and 200 kg of explosive with maximum CO concentration of 1.7e-07 ppm closer to the heading face.

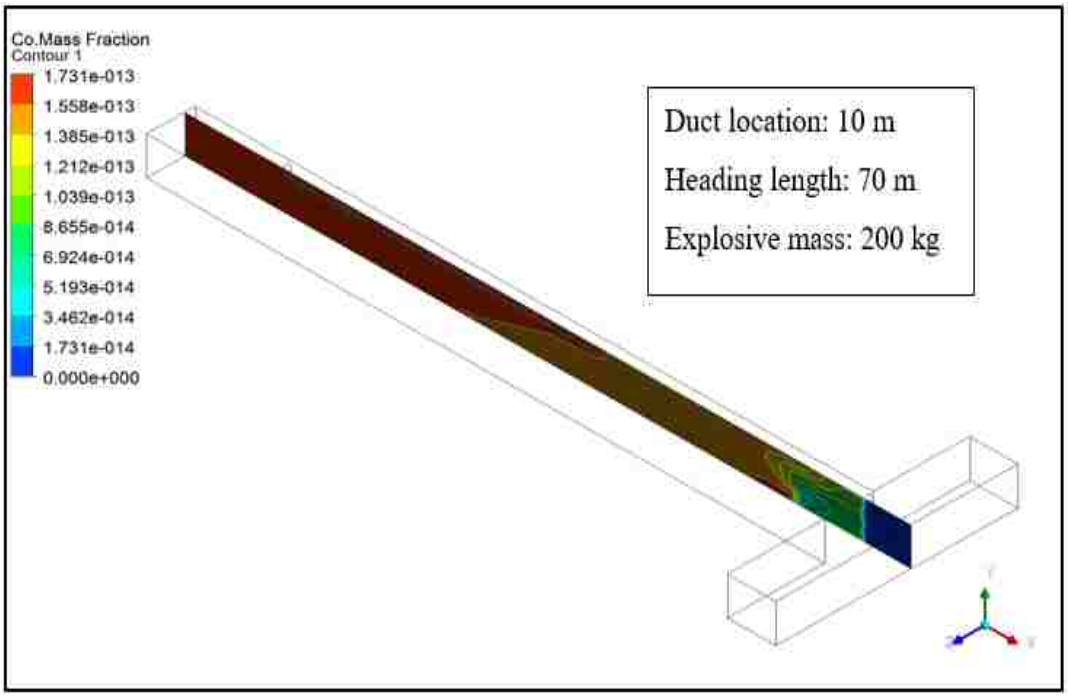

Figure 4.17. Contours representing CO concentration

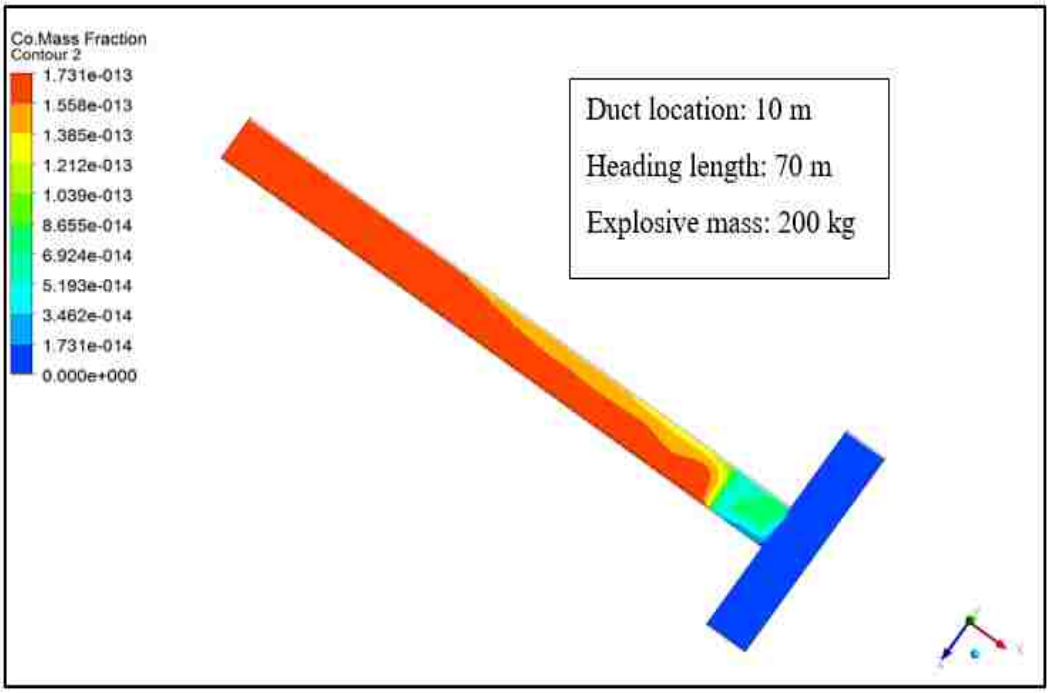

Figure 4.18. Contours showing CO content

Figures 4.19 and 4.20 show CO distribution along the heading length with maximum CO concentration of 3.38 ppm close to the face for a duct location of 30 m, heading length of 100 m, and 200 kg of explosive mass.

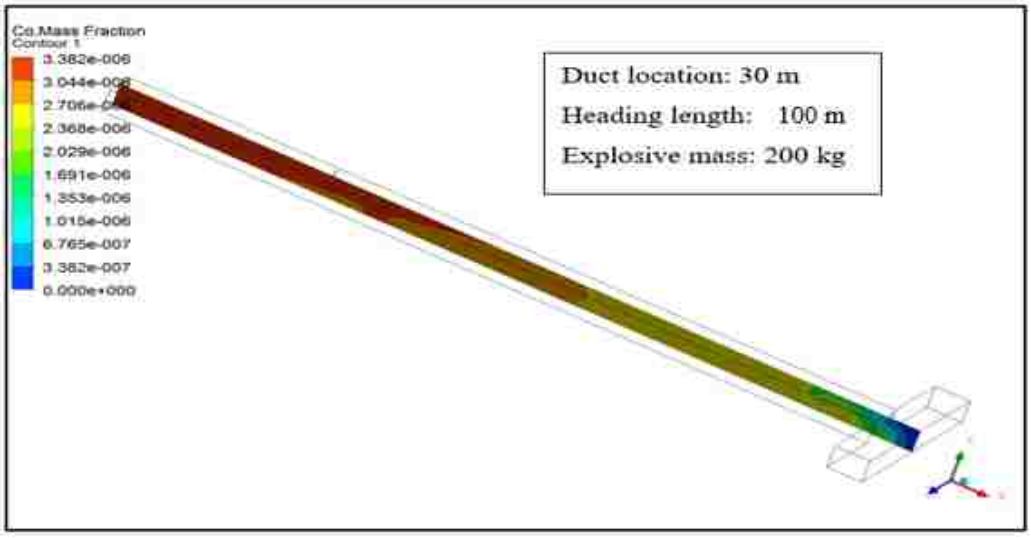

Figure 4.19. CO distribution along heading length

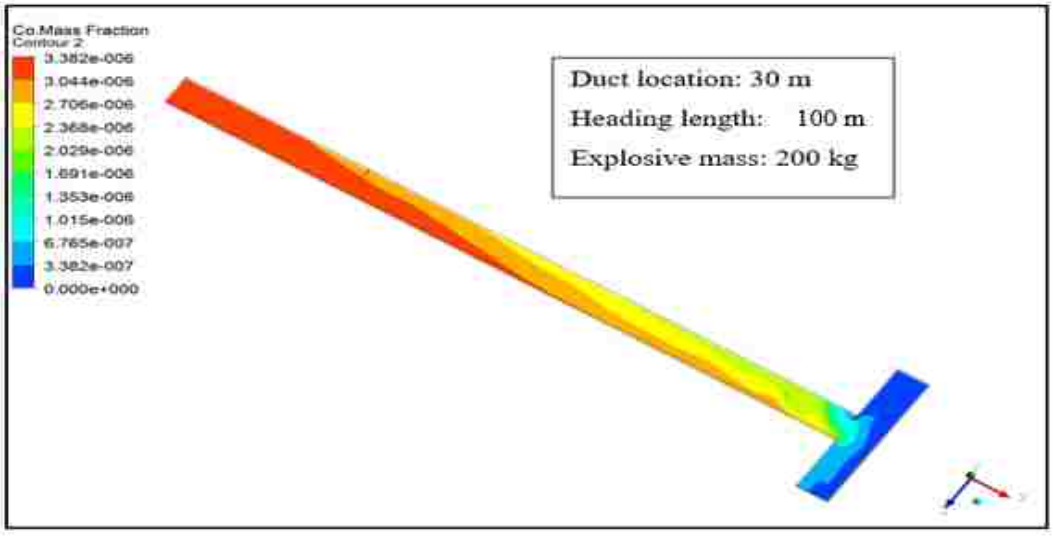

Figure 4.20. CO dispersion along heading length

Figures 4.21 and 4.22 show CO concentration along the heading length of 100 m, 60 m of duct location, and 200 kg of explosive mass with maximum CO concentration of 14 ppm around the heading face.

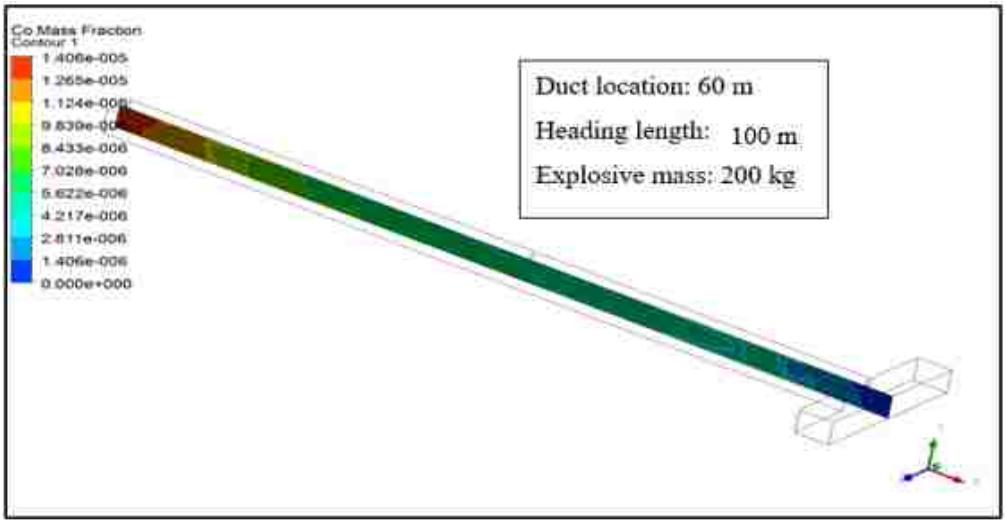

Figure 4.21. Contours showing CO concentration

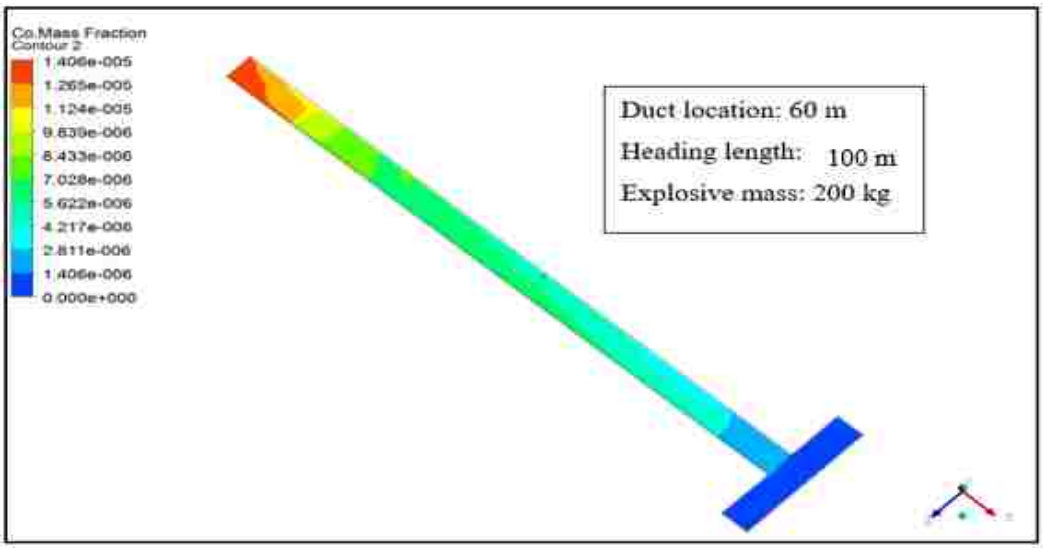

Figure 4.22. CO concentration along heading length

Figure 4.23 shows the relationship between clearance time and discharge location for the various heading lengths 70 m, 90 m, and 100 m.

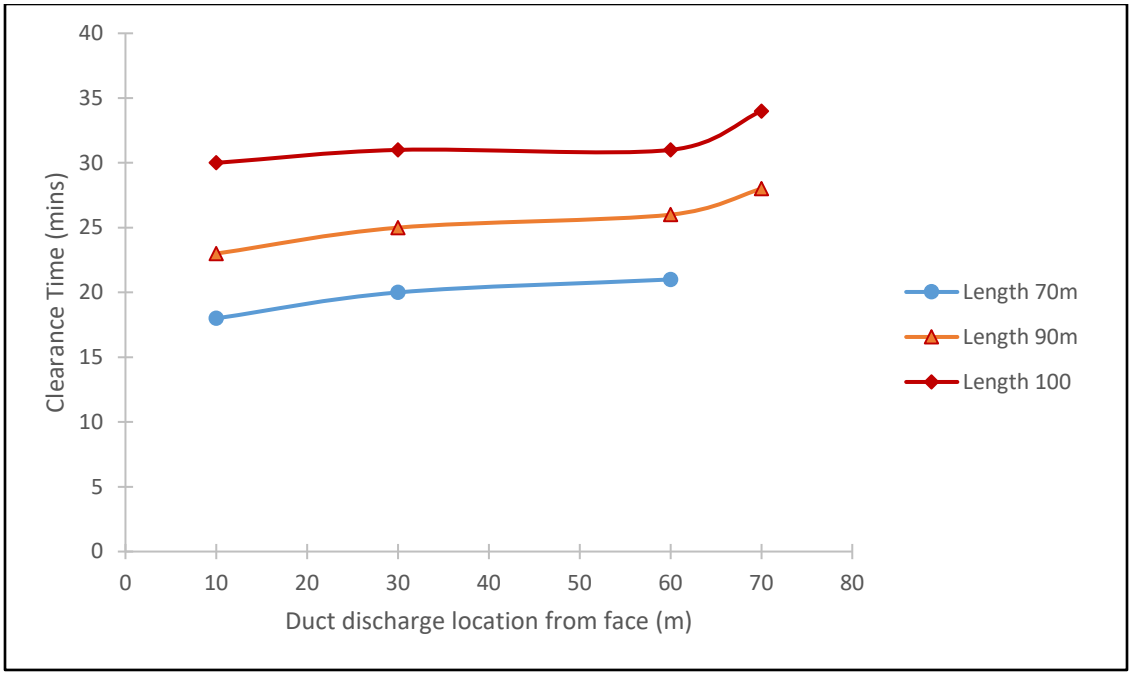

Figure 4.23. Variation of fume clearance with distance from heading face

The efficiency of CO clearance decreases with increasing heading length as observed from Figures 4.17 to 4.22. Additionally, the concentration of CO decreases gradually with time as the heading length increases with the maximum CO concentrations occurring closer to the heading face. This is because fresh air is well directed and penetrates the cloud of blast fume better clearing the noxious gases when the fan duct is of closer proximity to heading face.

As seen from Figure 4.23, the heading lengths of 70 m, 90 m, and 100 m had blast fumes reduced below the threshold after 20, 26 and 32 min, respectively. The clearance

time increases with increasing heading length because the extra length introduced increases the working space volume. This implies that more time is needed to clear the blast fumes within the extra working space volume created. Thus, it is always best practice to place duct discharges closer to the driving face.

Simulations were carried out for durations required to reduce CO concentrations to acceptable limits. Contours illustrating CO concentrations for a cross-sectional area of 16 m^2 with various duct discharge locations and heading lengths are presented in Figures 4.24 to 4.33.

Figures 4.24 and 4.25 represent CO distribution along the heading length of 70 m, duct location of 10 m, and explosive mass of 200 kg with maximum CO concentration of 2e-05 ppm.

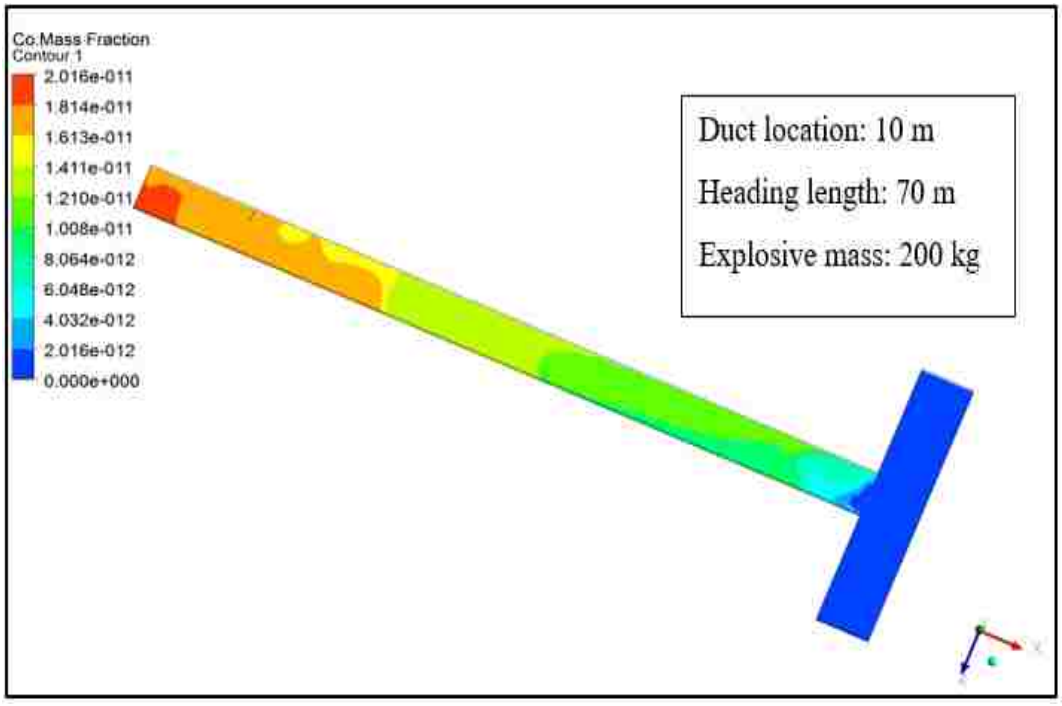

Figure 4.24. Contours highlighting CO distribution

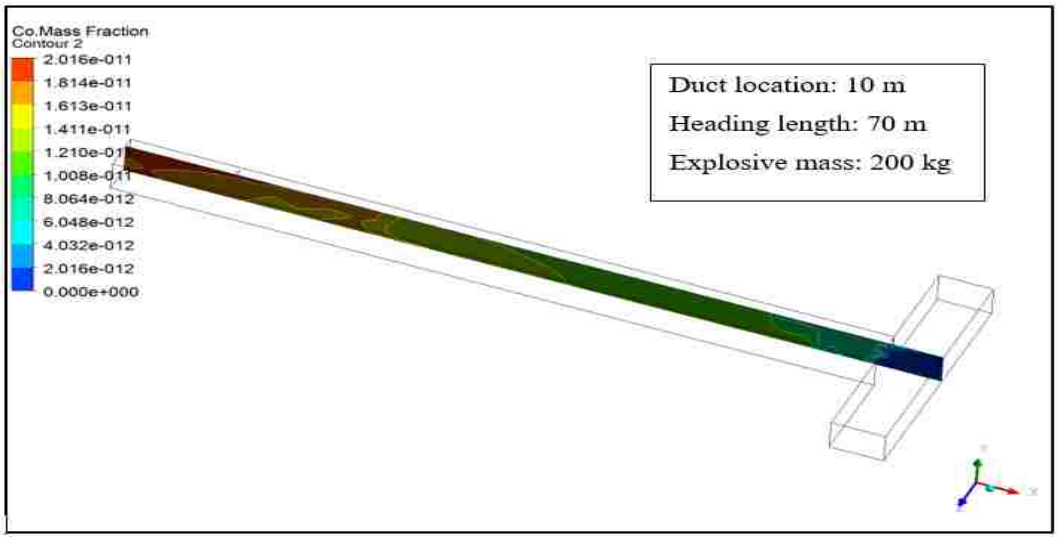

Figure 4.25. Contours representing CO concentration

Figures 4.26 and 4.27 show CO concentration along the heading length with maximum CO concentration of 12 ppm for an explosive mass of 200 kg, heading length of 100 m, and duct location of 10 m.

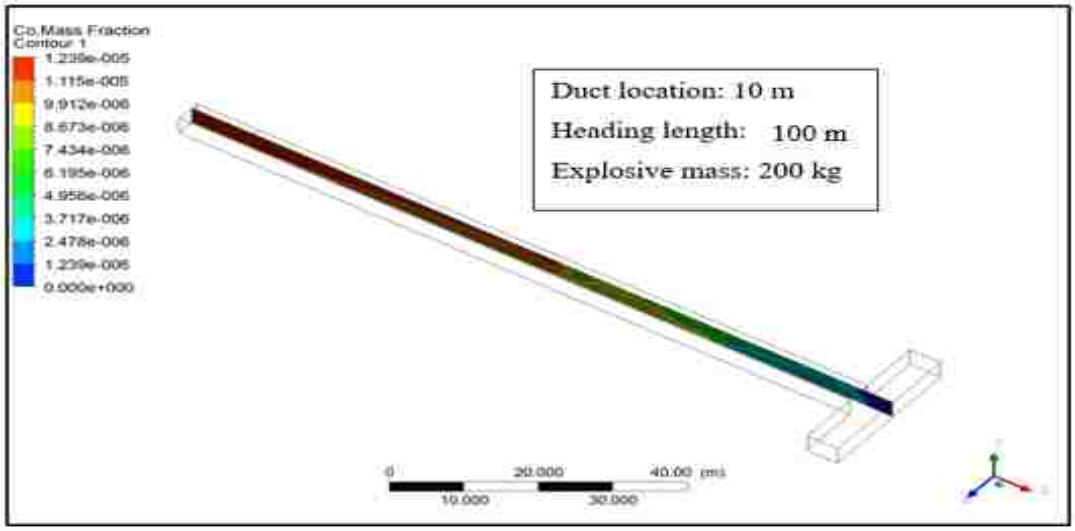

Figure 4.26. Contours showing CO distribution

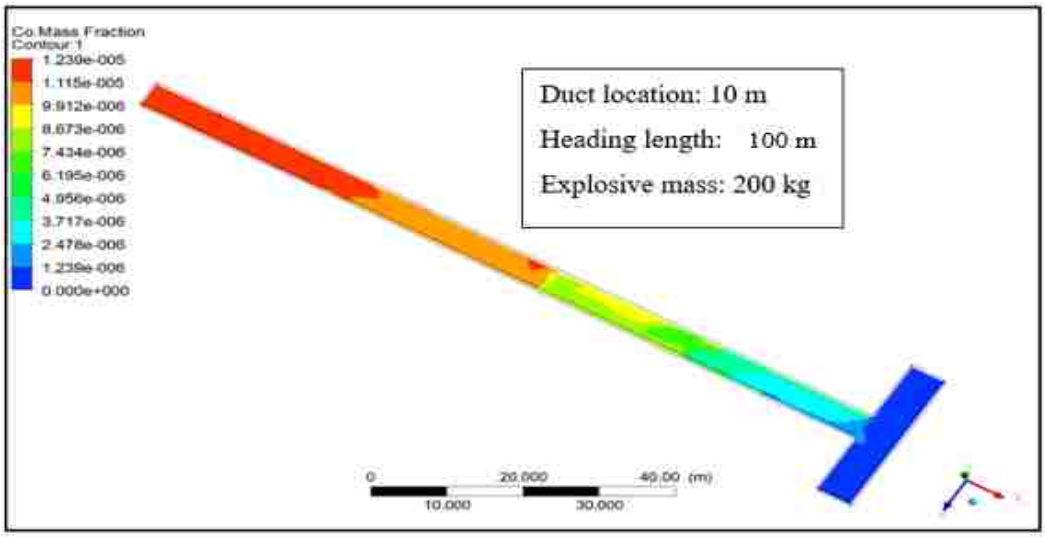

Figure 4.27. Contours representing CO content

Figures 4.28 and 4.29 highlight CO concentration along the heading length with maximum CO concentration of 21 ppm for an explosive mass of 200 kg, heading length of 100 m, and duct location of 30 m.

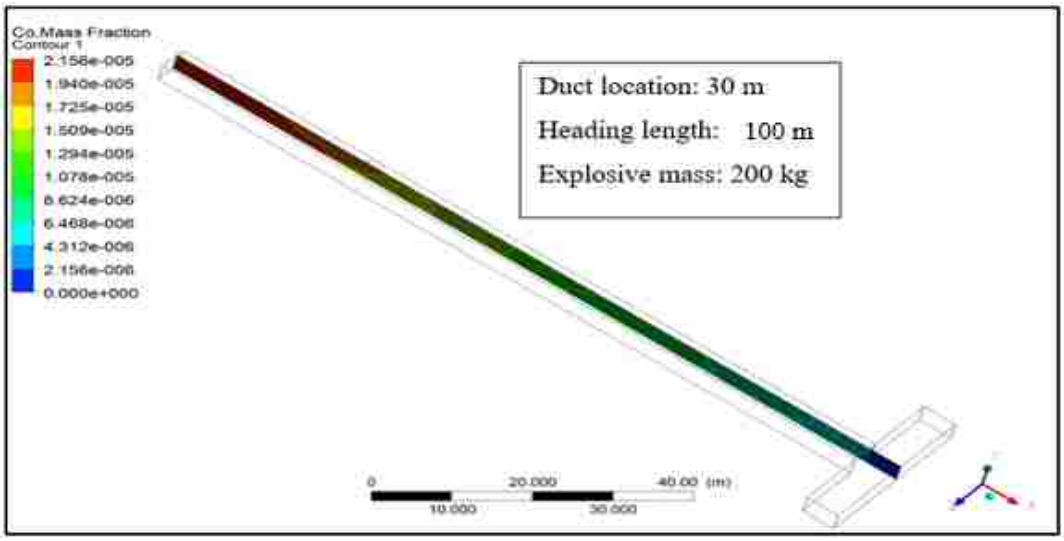

Figure 4.28. Contours representing CO concentration

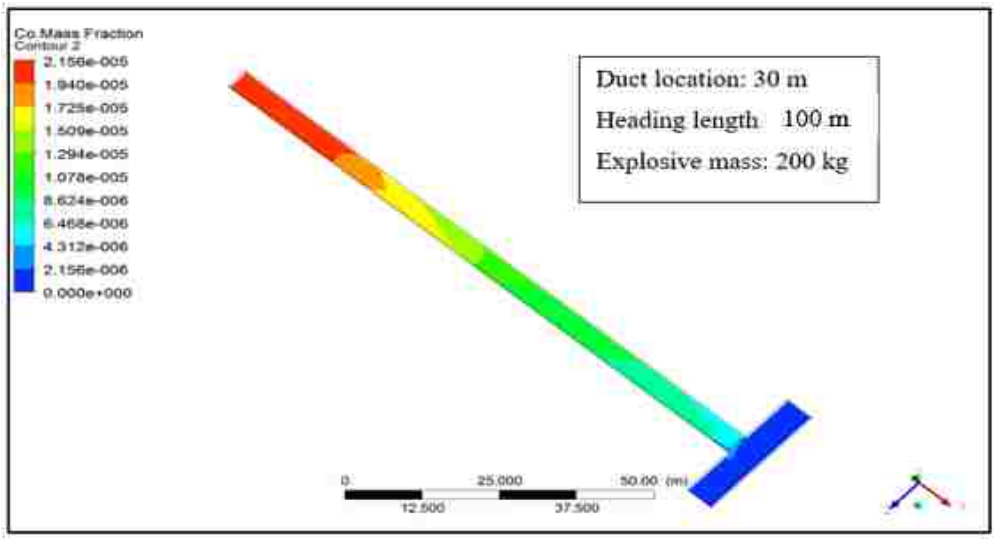

Figure 4.29. Contours representing CO content along heading length

Figures 4.30 and 4.31 illustrate CO concentration along the heading length with maximum CO concentration of 0.91 ppm for an explosive mass of 200 kg, heading length of 70 m, and duct location of 60 m.

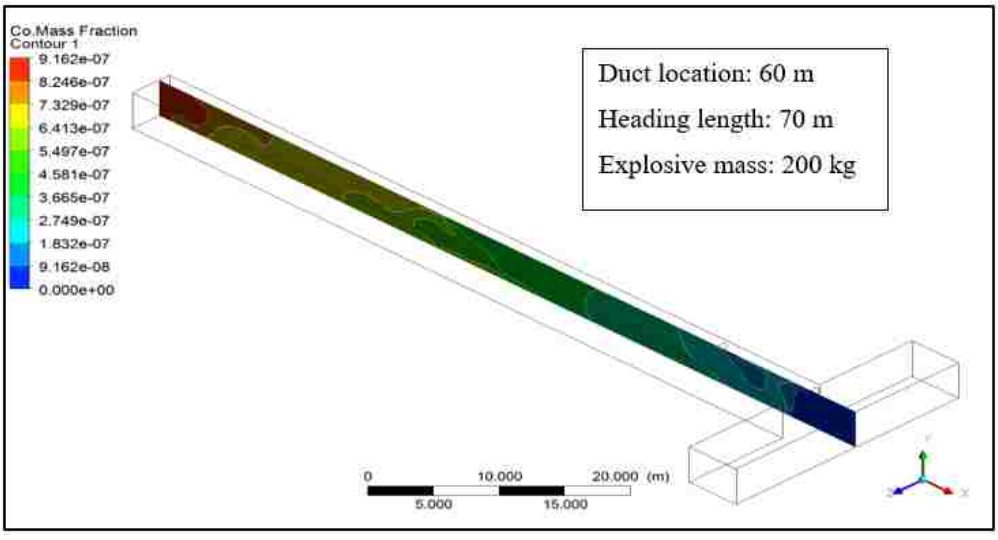

Figure 4.30. CO content along heading length

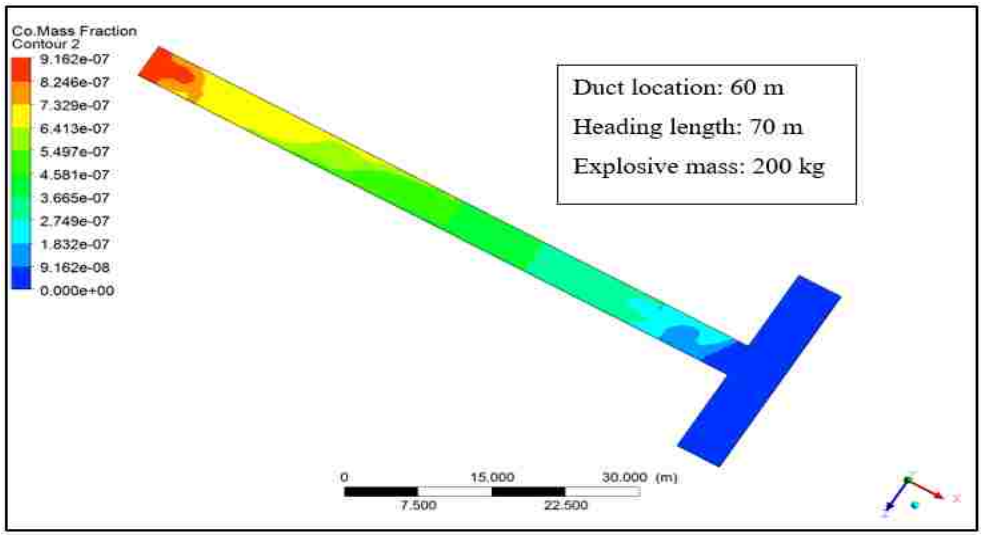

Figure 4.31. CO dispersion along heading length

Figures 4.32 and 4.33 present CO concentration along the heading length with maximum CO concentration of 23 ppm for an explosive mass of 200 kg, heading length of 90 m, and duct location of 60 m.

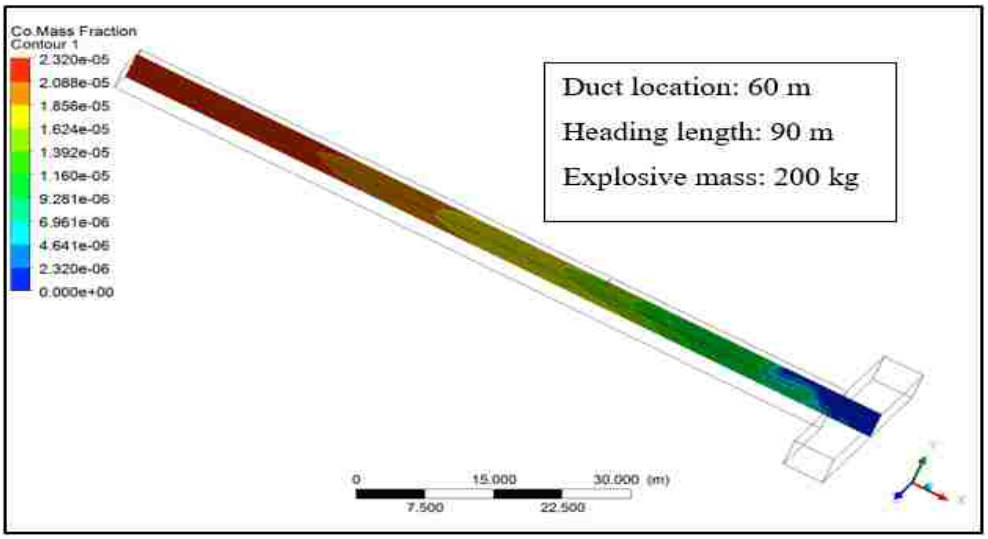

Figure 4.32. Contours demonstrating CO dispersion

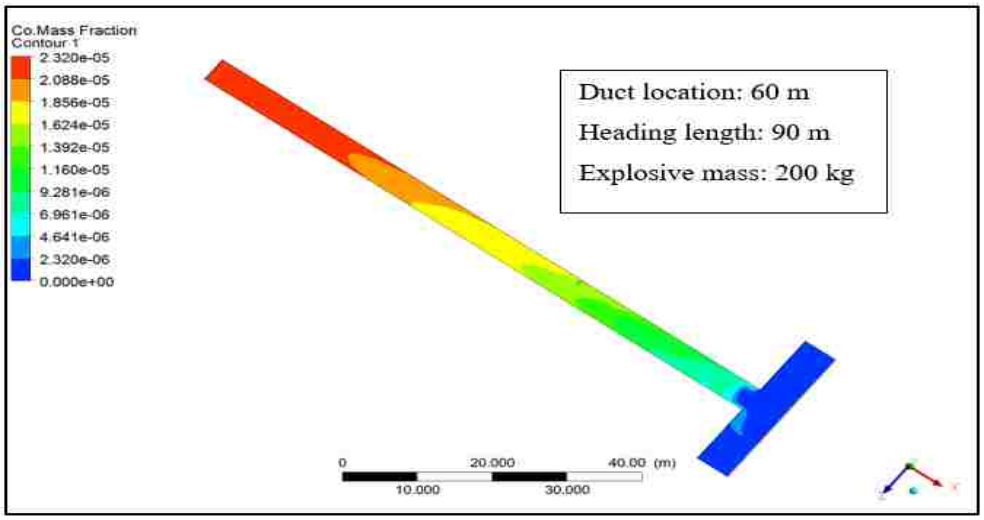

Figure 4.33. Contours demonstrating CO concentration

Figure 4.34 demonstrates the relationship between clearance time and discharge location for the various heading lengths. A detailed list of results from the simulations can be found in Appendix A.

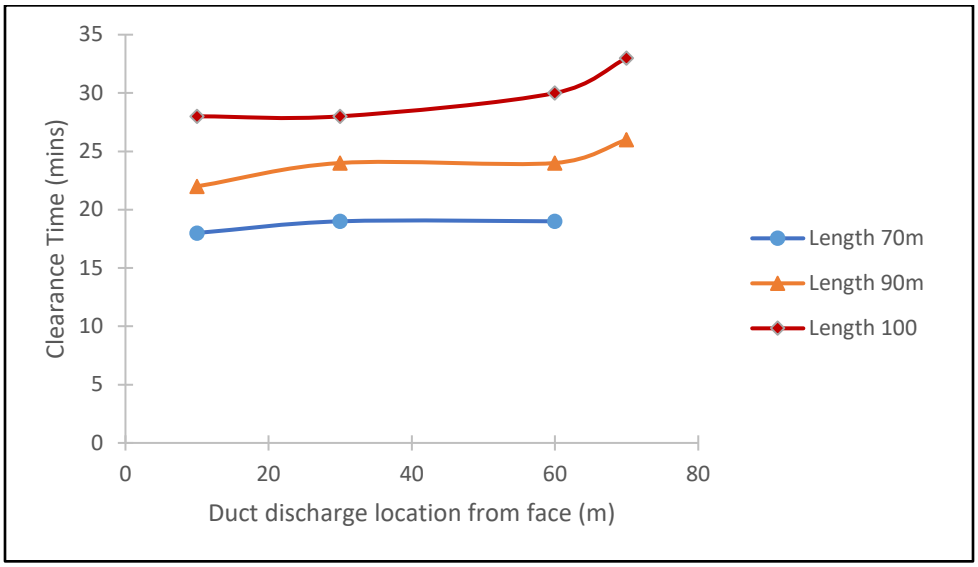

Figure 4.34. Variation of fume clearance with distance from heading face

As highlighted in Figures 4.24 to 4.34, fume clearance is more effective with relatively shorter heading lengths and closer duct discharge location from heading face. This is because the fresh air is able to penetrate and dilute the blast fume better with relatively shorter discharge locations carrying the noxious gases away from the working zone. The heading length of 70 m recorded the least clearance time while the heading length of 100 m had the highest clearance time as observed in Figure 4.34. There is a gradual increase in post-blast re-entry time from 10 m to 60 m, then a sharp rise beyond 60 m discharge location for the 70 m heading length. However, there were significant changes in clearance time for length 90 m and 100 m at the various discharge locations. Additionally, fume clearance time is more sensitive to heading length than it is to duct discharge location. Based on the simulation results, an optimal duct discharge location of 10 m to 60 m is suggested for a maximum working space volume of 2,500 m^3.

4.5. ESTABLISH SAFE BLAST EXCLUSION ZONES

Immediately after blasting, noxious gas concentration rises to its peak and quickly spreads out to farther distances. Mine workers are supposed to stay a certain distance away from the blast location. This stay-off distance should be safe enough to prevent workers from coming into contact with the highly concentrated blast fumes, hence protecting the workers from blast fume poisoning. To develop the safe distances, a relationship between safe blast distance and input parameters needs to be established. Various ventilation and blasting conditions were modeled and simulated to determine this relationship. A total of 45 test simulations were conducted at a time step size of 1 s and CO concentrations along the heading were recorded.

Table 4.2 shows a summary of the various conditions used for the CFD simulation with mass of explosives, cross-sectional area, and air quantity as input parameters. The relationship between the mass of explosive and the safe distance from blast location is expressed in Figure 4.35.

Table 4.2. Input variables for CFD modeling and simulation

Mass of Explosive (kg)	Cross-sectional Area (m^2)	Airflow quantity (m^3/s)
200	16	2.5, 5, 10, 20, 30
	20	2.5, 5, 10, 20, 30
	25	2.5, 5, 10, 20, 30
300	16	2.5, 5, 10, 20, 30
	20	2.5, 5, 10, 20, 30
	25	2.5, 5, 10, 20, 30
400	16	2.5, 5, 10, 20, 30
	20	2.5, 5, 10, 20, 30
	25	2.5, 5, 10, 20, 30

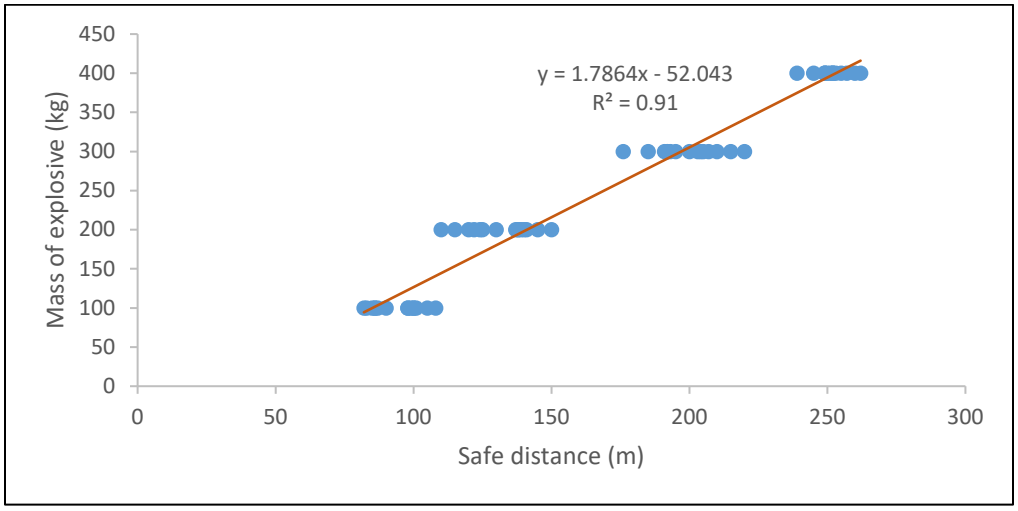

Figure 4.35. Variation of fume clearance with distance from heading face

Figure 4.35 demonstrates a linear relationship between the explosive mass and the safe distance from heading face. The mass of explosive was used for the plot because it was the most sensitive input parameter based on the simulation results. Appendix B captures all other simulation results from the tests conducted. Blast exclusion zones for specific cases would have to be calculated using a comprehensive relationship. A multivariate regression analysis was used to establish a relationship between the safe blast distance and the input parameters. The developed equation gives satisfactory results with a coefficient of determination (R^2) of 0.90. Equation 59 is the established relationship for estimating safe blast distance based on the simulation results:

$$D = 0.30M - 1.83A - 1.46Q + 222.22 \quad (59)$$

Where, D is the safe distance (m) from the face, M represents the mass of the explosive (kg); A is the cross-sectional area of heading face (m^2), and Q is the quantity of fresh air from fan (m^3/s).

4.6. ESTABLISHING A RELATIONSHIP BETWEEN OPTIMAL AIR QUANTITY AND POST-BLAST RE-ENTRY TIME

Mine Safety and Health Administration (MSHA) has set a post-blast re-entry time of one hour for underground mines. However, it is well-known that it sometimes takes several hours after blasting for gas concentrations to reduce to acceptable limits rendering the one-hour post-blast re-entry time noneffective. To overcome the above setback, most underground mines have resorted to blasting at the end of the working shift, allowing ample time for blast fume to clear. However, several of these underground mines have relatively

longer time lapse in between shifts and simply set fans at high speeds. Little or no attention at all is given to the cost incurred in running large volumes of air over the period, often resulting in high ventilation cost.

Most underground mines rely on observations and experiences in setting post-blast re-entry time. A few of the mines use the available empirical methods for estimating post-blast re-entry time, often resulting in the selection of inappropriate post-blast re-entry times. Since overestimation of post-blast re-entry time can delay production and underestimation can result in blast fume poisoning, it is imperative to derive appropriate post-blast re-entry times. To derive optimal post-blast re-entry times, a relationship between air quantity and post-blast re-entry time is required.

This part of the research uses CFD simulations to establish a relationship between airflow quantity and post-blast re-entry time. Based on the established relationship, optimal air quantity would be supplied to blasted areas based on the desired re-entry time, hence reducing ventilation cost. The established relation can also be used to determine optimal post-blast re-entry times.

The CFD simulations were conducted based on a fixed duct discharge location of 10 m and three main input parameters: the mass of explosive, the cross-sectional area, and airflow quantity. Details of these input parameters are summarized in Table 4.3. The computational domains for the various heading arrangements with varying explosive mass, cross-sectional area, and air quantity are highlighted by Figures 4.36 to 4.39. Simulations were performed at a time step size of 1 s and for durations required for carbon monoxide (CO) concentrations to fall below the 25ppm/$2.5x10^{-5}$ threshold.

Table 4.3. Input variables for CFD modeling and simulation

Mass of Explosive (kg)	Cross-sectional Area (m^2)	Airflow quantity (m^3/s)
100	16	2.5, 5, 10, 20, 30
	20	2.5, 5, 10, 20, 30
	25	2.5, 5, 10, 20, 30
200	16	2.5, 5, 10, 20, 30
	20	2.5, 5, 10, 20, 30
	25	2.5, 5, 10, 20, 30
300	16	2.5, 5, 10, 20, 30
	20	2.5, 5, 10, 20, 30
	25	2.5, 5, 10, 20, 30
400	16	2.5, 5, 10, 20, 30
	20	2.5, 5, 10, 20, 30
	25	2.5, 5, 10, 20, 30

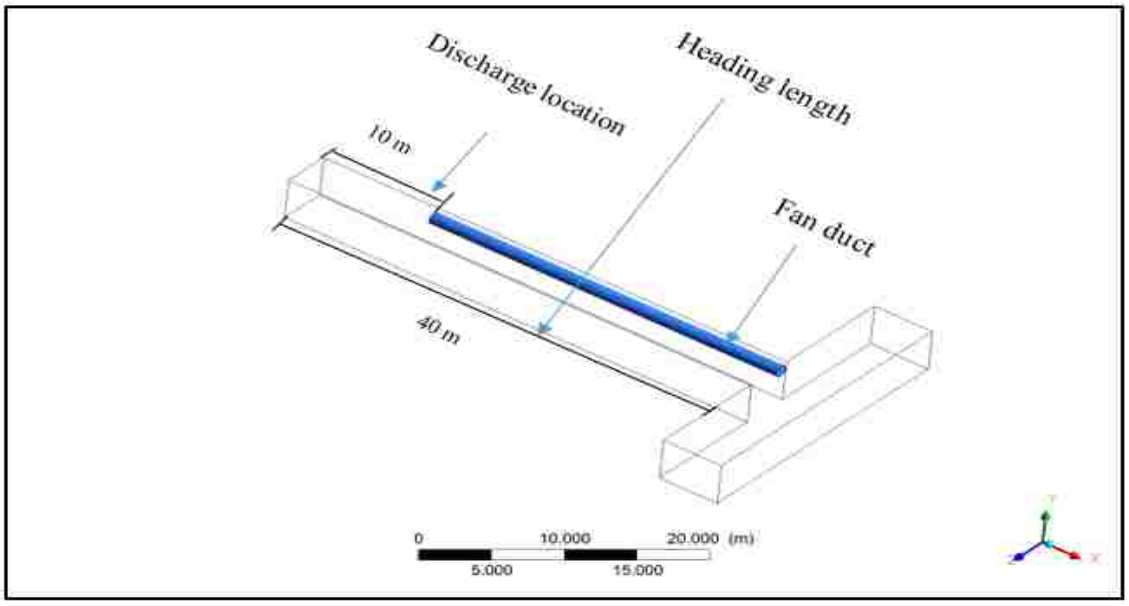

Figure 4.36. Cross-sectional area of 16 m^2 and heading length 40 m

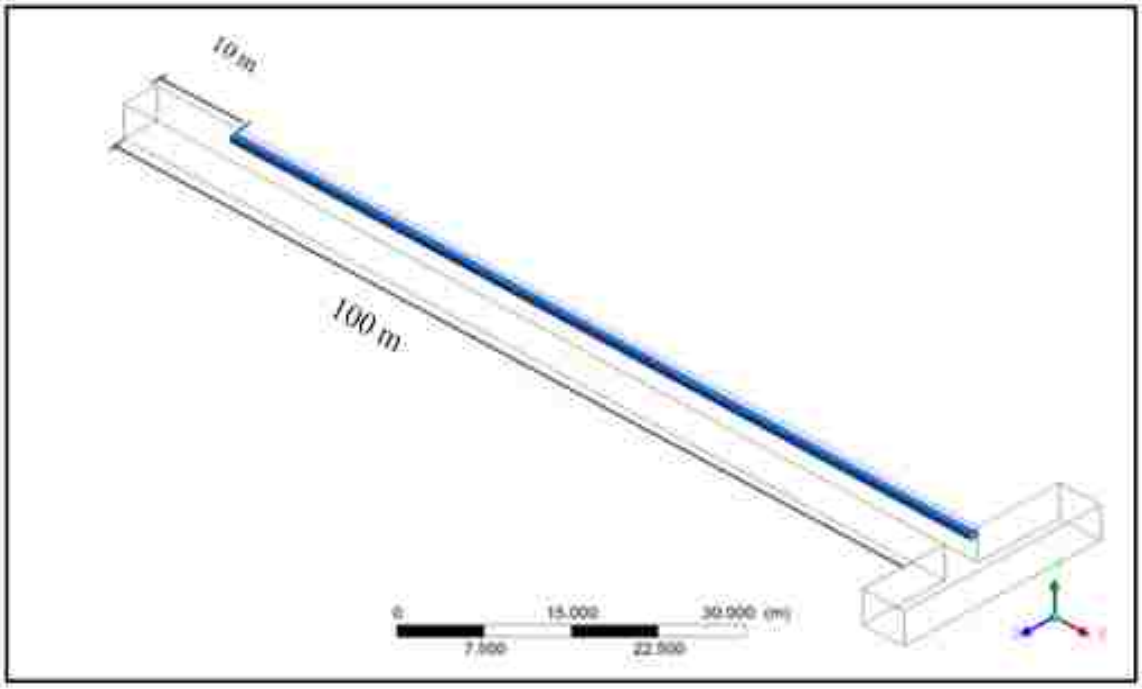

Figure 4.37. Cross-sectional area of 16 m^2 and heading length 100 m

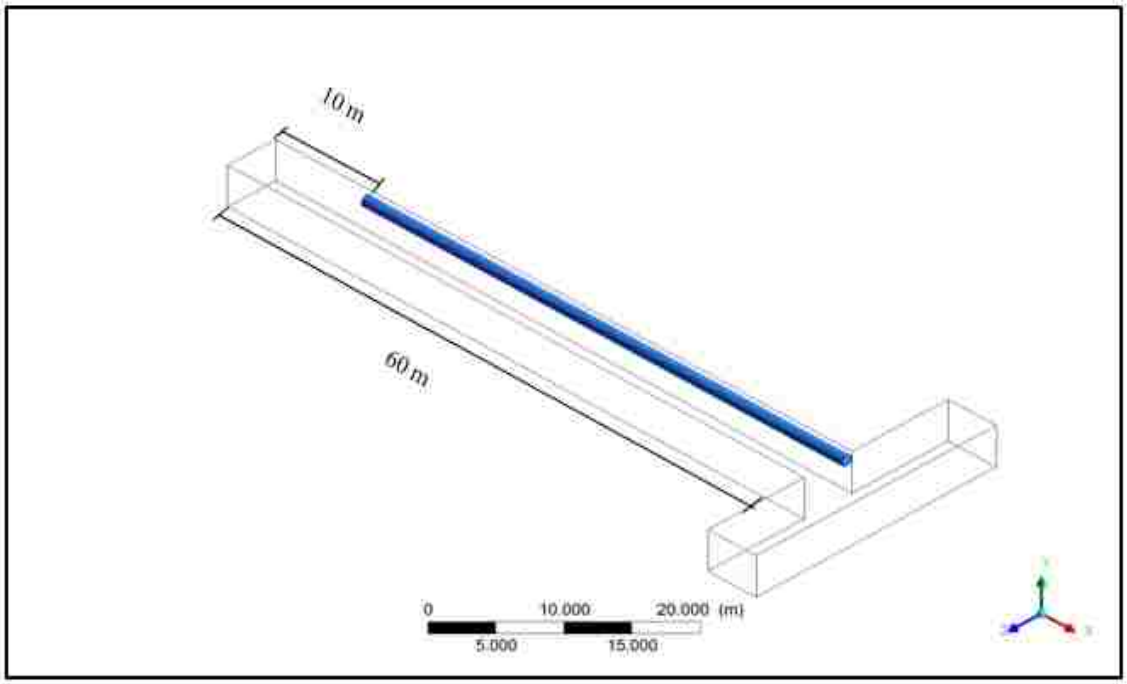

Figure 4.38. Cross-sectional area of 20 m^2 and heading length 60 m

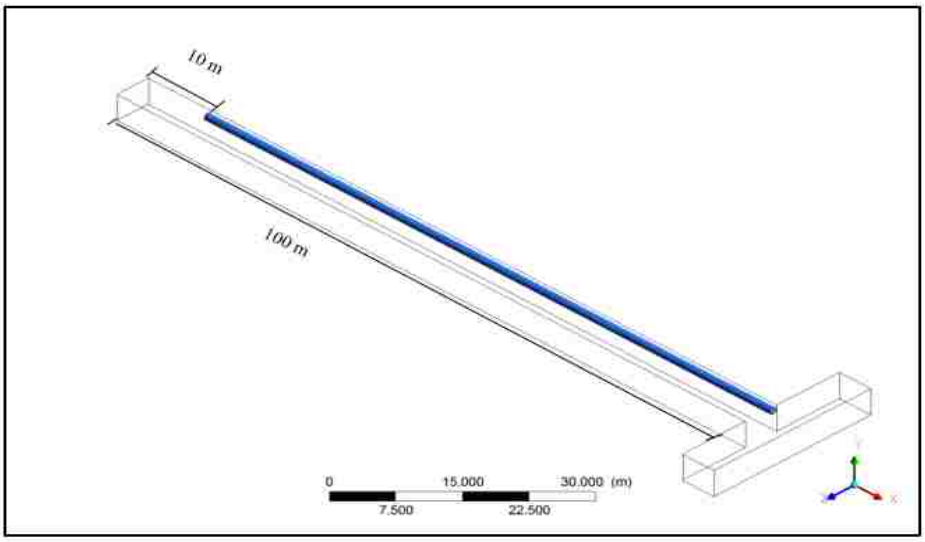

Figure 4.39. Cross-sectional area of 25 m^2 and heading length 100 m

Results showing contours of CO concentration for the explosive mass of 100 kg, 200 kg, 300 kg and 400 kg are represented by Figures 4.40 to 4.44.

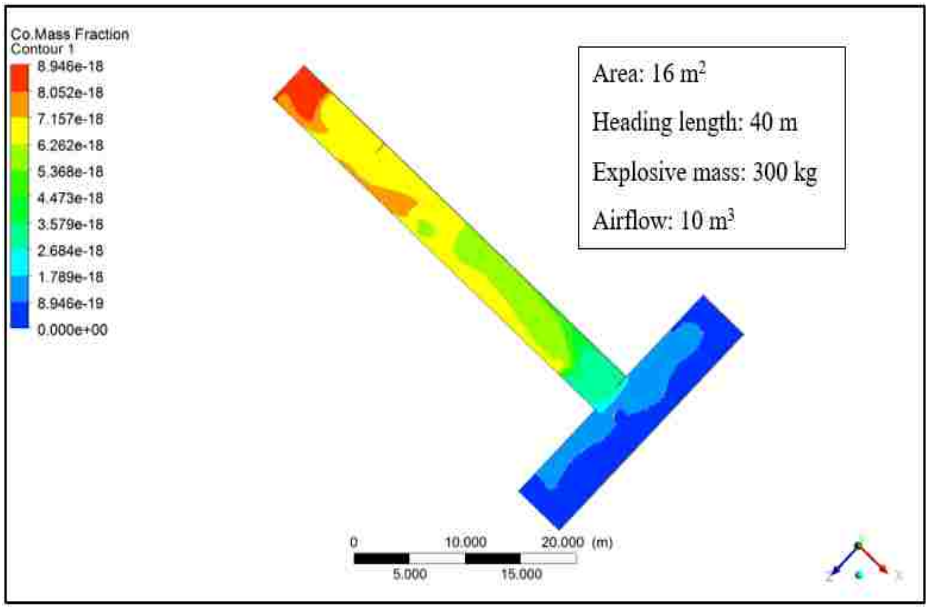

Figure 4.40. Contours representing CO content

Figure 4.40 represents contours of CO concentration for a cross-sectional area of 16 m^2, heading length of 40 m, explosive mass of 300 kg and an airflow of 10 m^3. Figure 4.41 shows contours of CO concentration for a cross-sectional area of 20 m^2, heading length of 60 m, explosive mass of 200 kg, and an airflow of 10 m^3. The CO content decreases with increasing distance from the heading face.

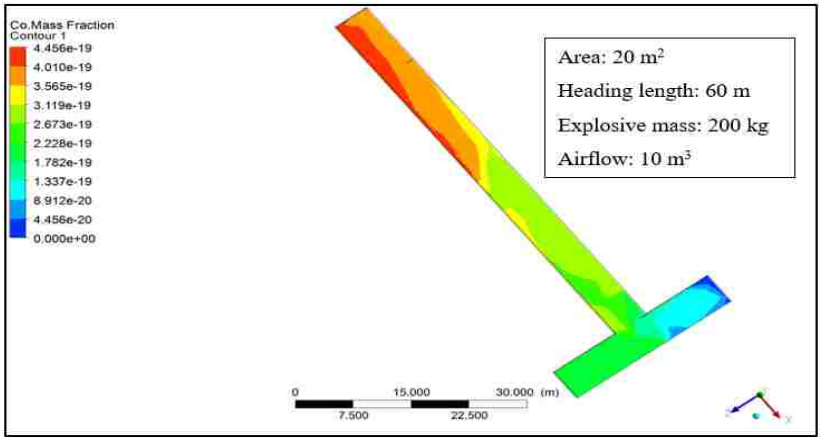

Figure 4.41. CO concentration along heading length 60 m and mass of 200 kg

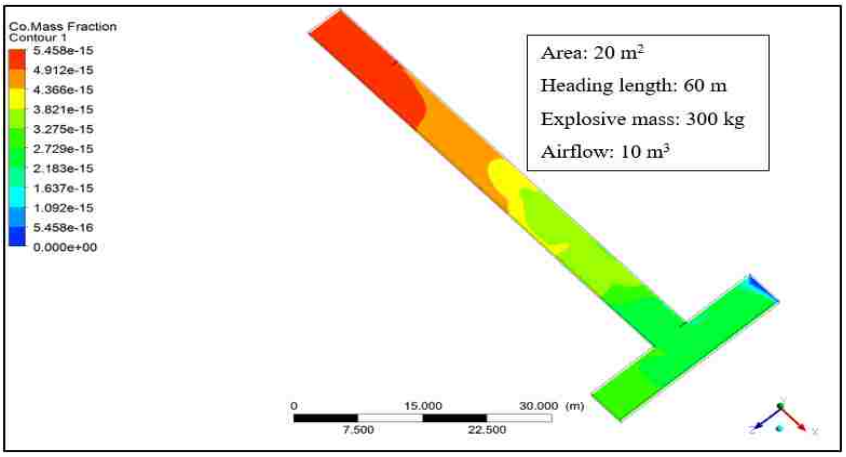

Figure 4.42. Contours showing CO concentration along a heading length of 60 m and mass of 300 kg

Figure 4.42 highlights contours of CO concentration for a cross-sectional area of 20 m^2, heading length of 60 m, explosive mass of 300 kg, and an airflow of 10 m^3. As observed from Figure 4.42, there is a uniform spread of CO content along the entire length of the heading length. A CO concentration of 5.4e-15 is dispersed over a length of 20 m from the face, then gradually decreases to a concentration of 2.7e-15 approximately, 50 m from the heading face.

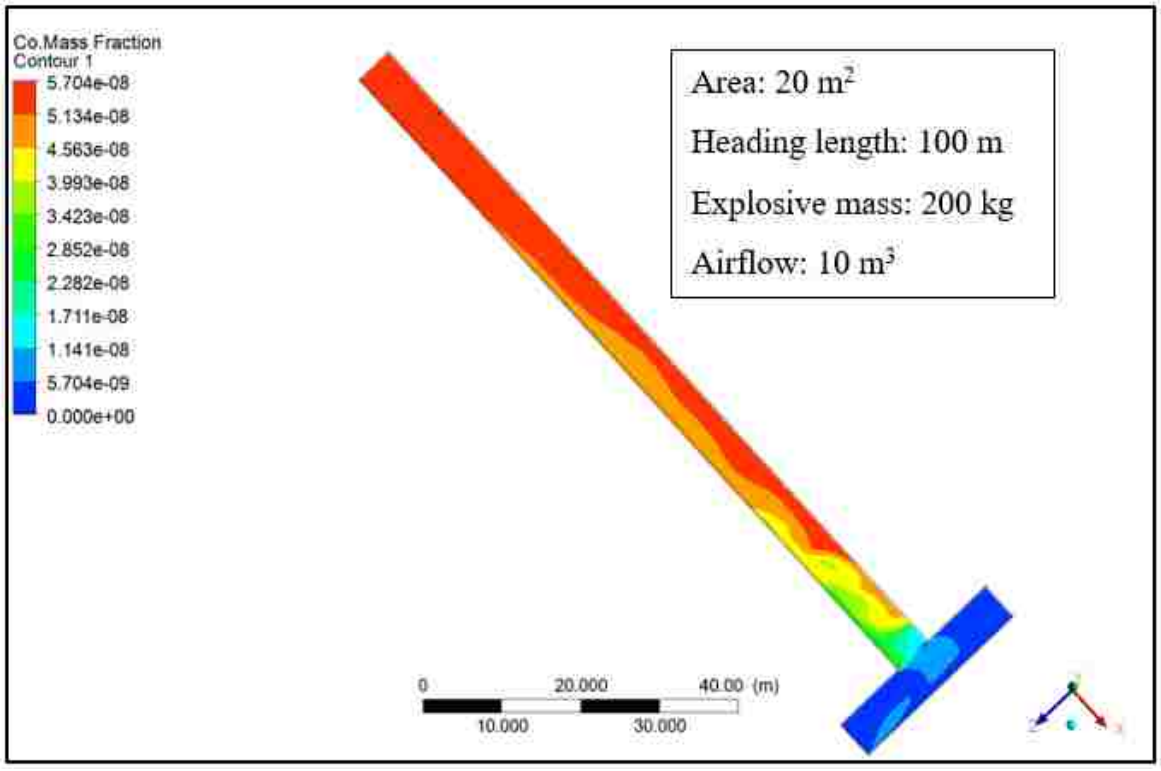

Figure 4.43. CO dispersion along a heading length of 100 m and mass of 200 kg

Figure 4.43 represents contours of CO concentration for a cross-sectional area of 20 m^2, heading length of 100 m, explosive mass of 200 kg, and an airflow of 10 m^3. There

is a non-uniform distribution of CO content over the development heading length with a maximum CO concentration of 5.7e-08 and a minimum concentration of 1.14e-08. Figure 4.44 shows contours of CO concentration for a cross-sectional area of 20 m^2, heading length of 100 m, explosive mass of 200 kg, and an airflow of 20 m^3.

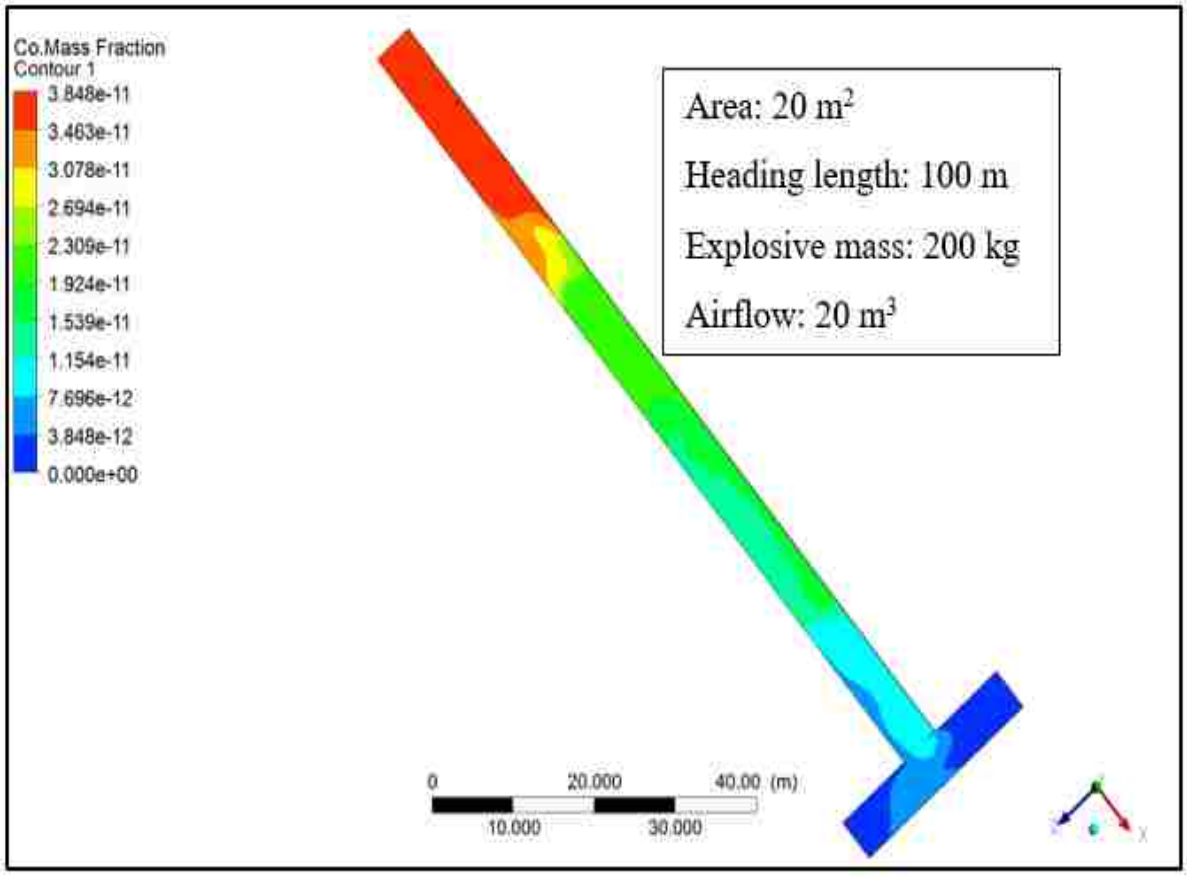

Figure 4.44. CO concentration with a mass of 200 kg and airflow of 20 m^3

Re-entry time as illustrated by Figures 4.40 to 4.44, is sensitive to the mass of explosive, airflow, length of heading and cross-sectional area of heading. As the mass of the explosive increases, the blast fume yield increases under the same operating conditions,

thus increase in the post-blast re-entry time. It is also noticed from simulation results that blast fume clearance time is reduced with increasing airflow. Moreover, the effectiveness of fume clearance reduces with increasing heading length.

A sensitivity analysis conducted on the blast input parameters revealed that the mass of explosive is the most sensitive input parameter to post-blast re-entry time. Thus, the relationship between airflow and post-blast re-entry time for explosive mass 100 kg, 200 kg, 300 kg and 400 kg have been established and captured by Figures 4.45 to 4.48 respectively.

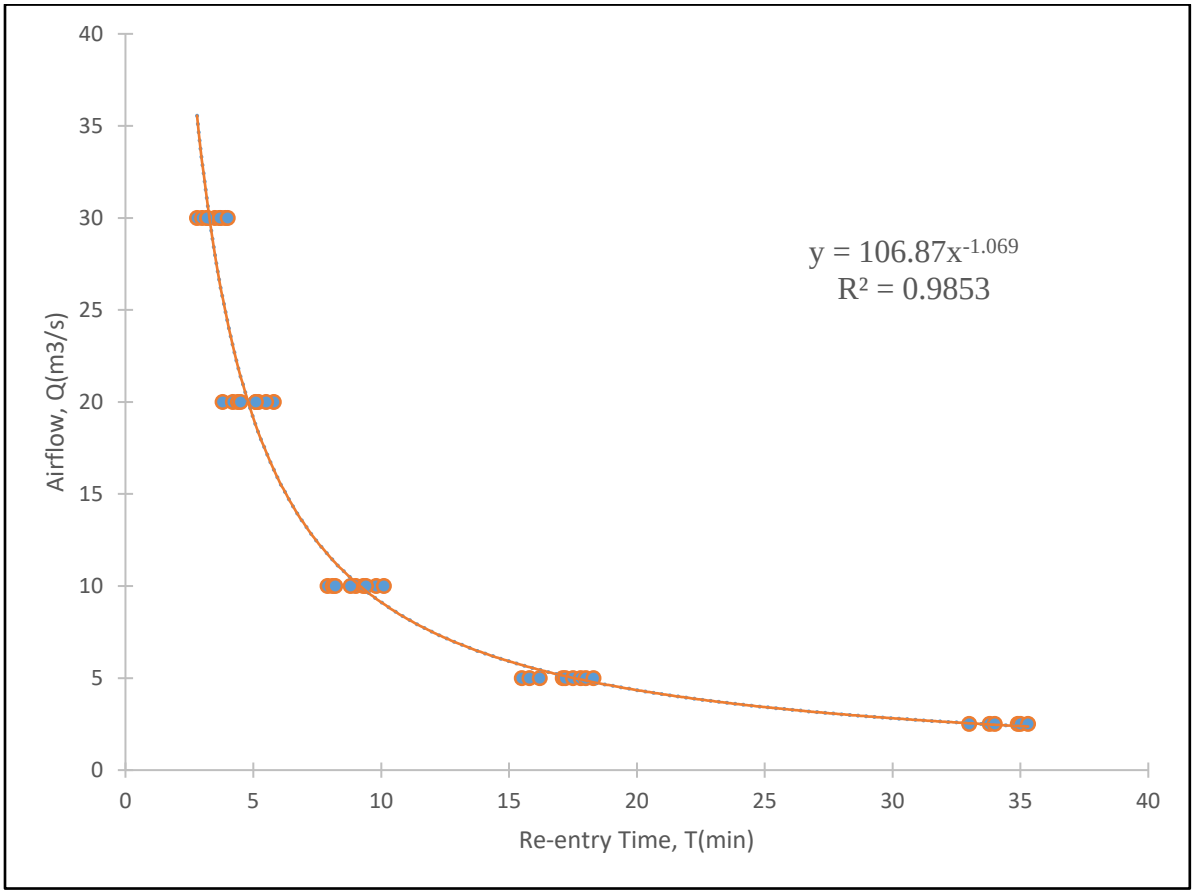

Figure 4.45. Relationship between airflow and re-entry time for a mass of 100 kg

Using an explosive mass of 100 kg and holding all the other parameters specified in Table 4.3 constant, generates results represented by Figure 4.45. A power relationship best correlates the airflow (Q) and re-entry time (T) with a coefficient of determination (R^2) of 0.985. The simplified relationship between Q and T is expressed in Equation 60 as follows:

$$Q = 106.87T^{-1.069} \quad (m^3/s) \tag{60}$$

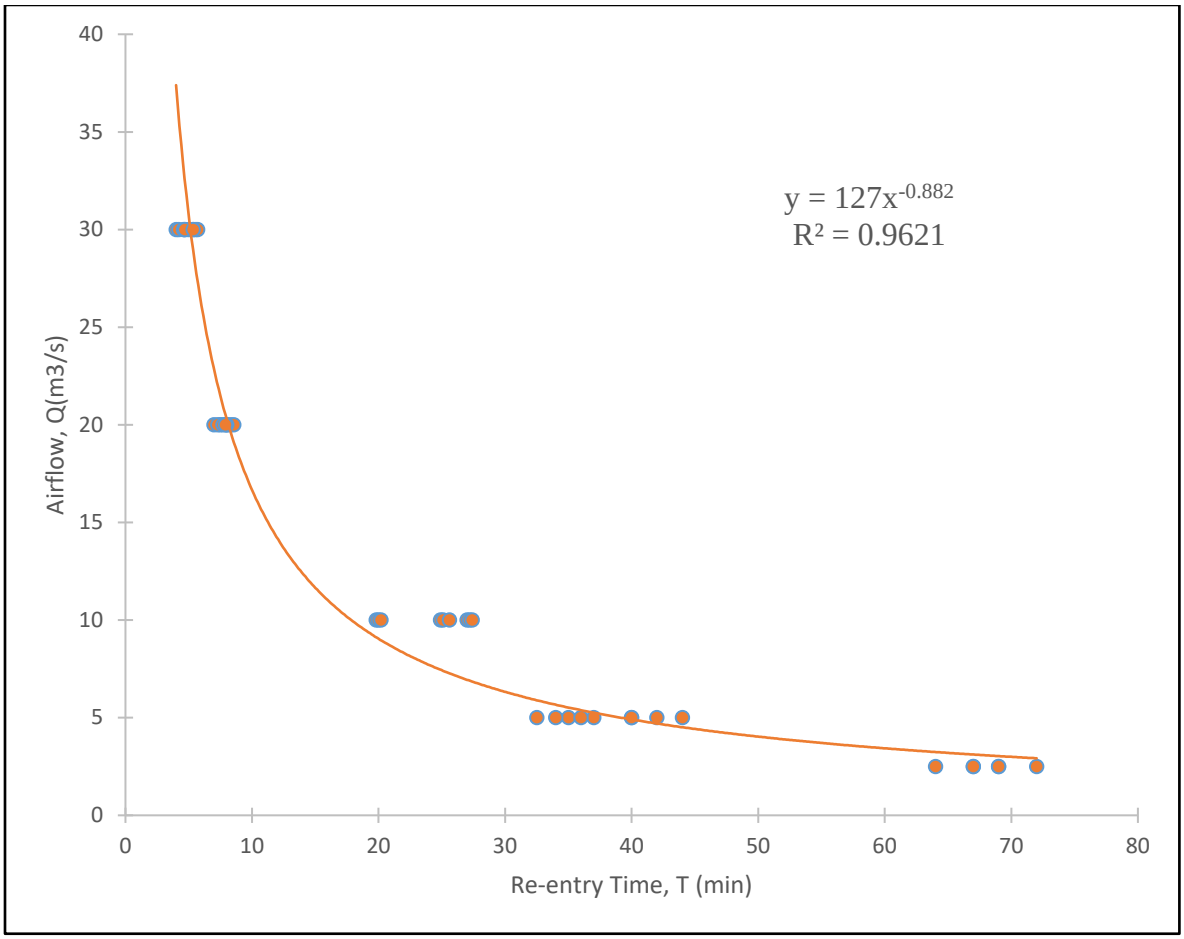

Figure 4.46. Relationship between airflow and re-entry time for a mass of 200 kg

Based on an explosive mass of 200 kg and maintaining all the other parameters specified in Table 4.3 constant generates results represented by Figure 4.46. A power relationship best correlates the airflow (Q) and re-entry time (T) yielding a coefficient of determination (R^2) of 0.962. The simplified relationship between Q and T is expressed in Equation 61 as follows:

$$Q = 127T^{-0.882} \quad (m^3/s) \tag{61}$$

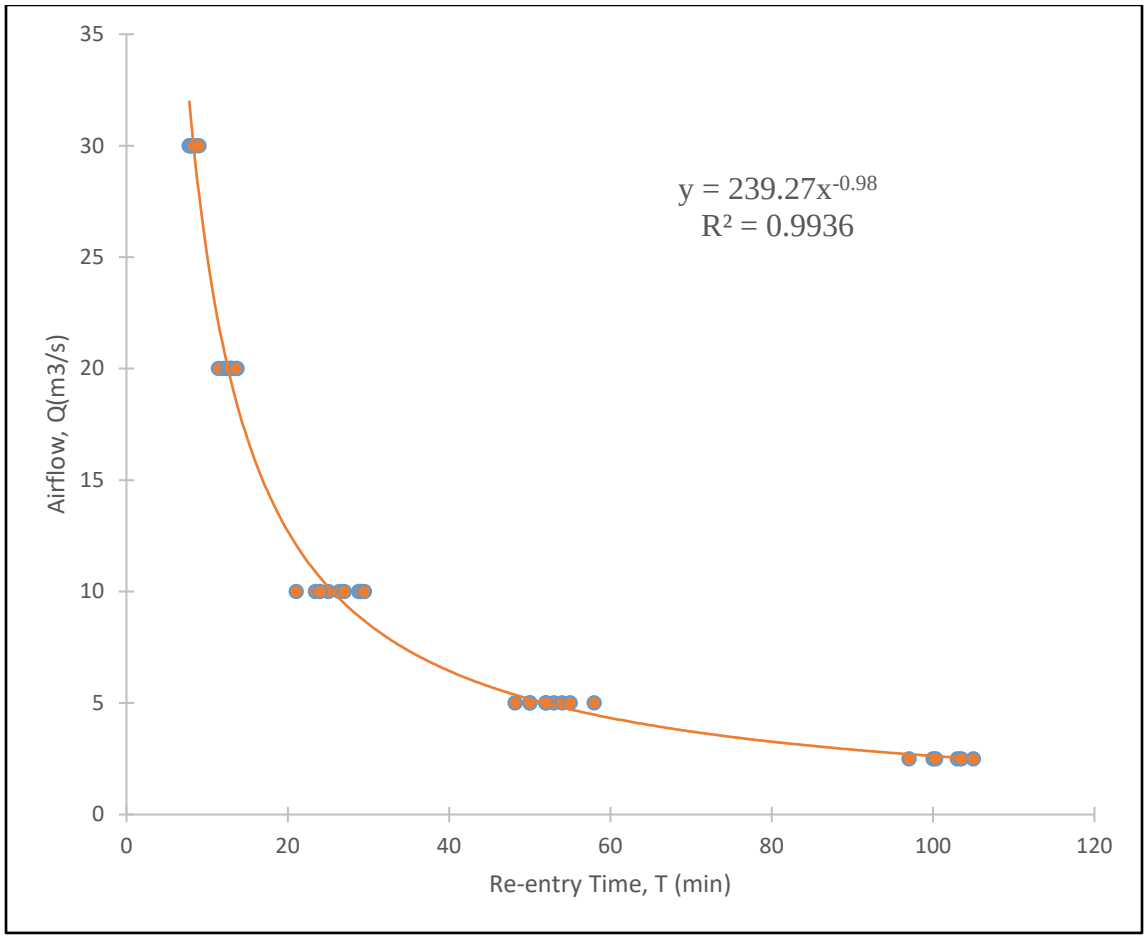

Figure 4.47. Relationship between airflow and re-entry time for a mass of 300 kg

Based on the explosive mass of 300 kg and keeping all the other parameters specified in Table 4.3 constant produces results captured by Figure 4.47. A power relationship best relates the airflow (Q) and re-entry time (T) resulting in a coefficient of determination (R^2) of 0.993. The simplified equation between Q and T is given in Equation 62 as expressed below:

$$Q = 239.27T^{-0.98} \quad (m^3/s) \tag{62}$$

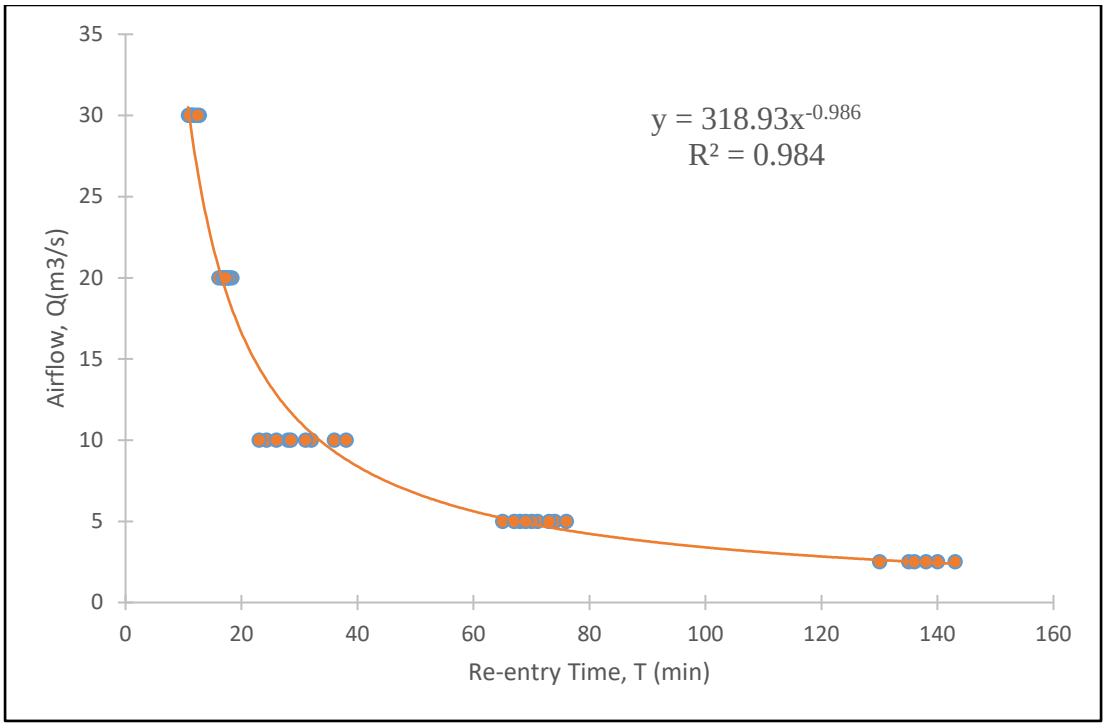

Figure 4.48. Relationship between airflow and re-entry time for a mass of 400 kg

Using explosive mass of 400 kg and holding all the other parameters specified under Table 4.3 constant yields results captured by Figure 4.48. A power relationship best

correlates the airflow (Q) and re-entry time (T) with a coefficient of determination (R^2) of 0.984. The simplified relationship between Q and T is given in Equation 63 as shown below:

$$Q = 318.93T^{-0.984} \quad (m^3/s) \tag{63}$$

Graph depicting the relationship between airflow and re-entry time for the various explosive masses is captured in Figure 4.49. More of the simulation results are presented in Appendix B.

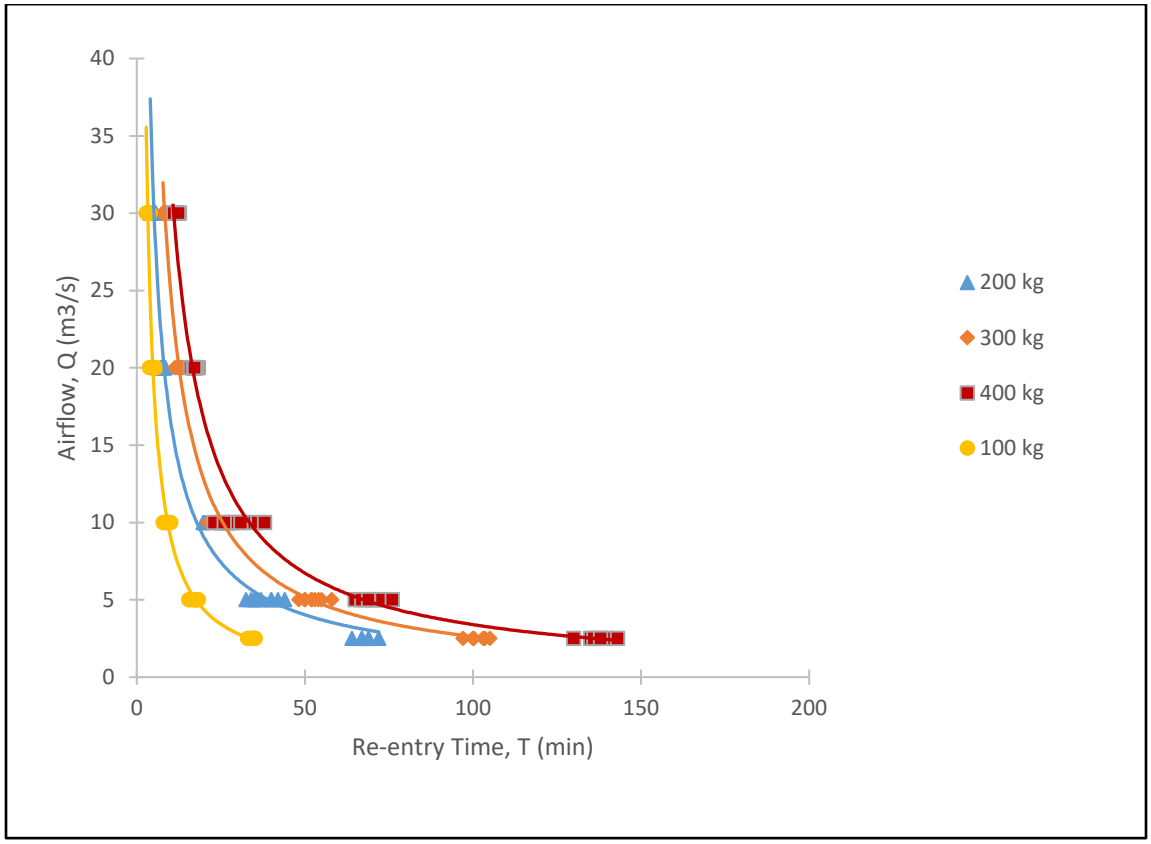

Figure 4.49. Relationship between airflow and re-entry time for various masses

Combining results illustrated in Figures 4.45 to 4.48 produces Figure 4.49. Figure 4.49 suggests that re-entry time increases with increasing explosive mass for a constant airflow. This is because relatively high explosive mass results in large blast fume generation which takes more time to be reduced to safe levels. Thus, for a given explosive mass, an optimal airflow can be chosen based on the desired re-entry time and vice versa using Figure 4.49.

4.7. SUMMARY

This chapter covers the simulation results and discussions. A grid independency study was conducted to obtain the optimum mesh size for downstream simulations. The medium size mesh was selected based on simulation results. Carbon monoxide (CO) gas was selected for downstream analysis because at defined thresholds, NO_2 concentration is insignificant. The forcing ventilation system was chosen for fume clearance given the fact that there was no significant difference comparing the results of the forcing and exhausting systems. Results demonstrate that the efficiency of the forcing ventilation system decreases with increasing fan duct discharge location from heading face. Fume clearance time increases with increasing development heading length. An equation (i.e. Equation 59) has been established for calculating safe blast distances. Based on the established relation, miners would have an understanding of blast fume dispersion and would strategically avoid sensitive areas. Four equations have been derived to conservatively estimate optimal air quantity and post-blast re-entry time. Experimentation and validations are captured in Section 5.

5. EXPERIMENTATION AND VALIDATION

5.1. MISSOURI S&T EXPERIMENTAL MINE

A blast was conducted at the Missouri Experimental Mine to monitor carbon monoxide (CO) concentrations for validating the proposed CFD model. The blast is part of a plan to extend the face of a drift at the Experimental Mine. The cross-sectional area of the drift is 3 m x 3 m and 2 m of face advance. Other parameters for the blast were: mass of explosive of 64 kg; fan exhaust flow rate is 3 m^3/s and is located 20 m from the face; 34 holes are blasted with 0.6 m burden and 0.6 m spacing; the blast hole diameter is 0.05 m. Figures 5.1 to 5.3 are diagrams representing drilled face, loaded holes, and ventilation fan.

Figure 5.1. Representation of the 34 holes schematic drill pattern

Figure 5.2. Representation of explosives and detonators loaded into holes

Figure 5.3. Illustration of exhaust fan at the surface

5.1.1. Calibration and Monitoring. Two Gasbadge pro CO monitors from Industrial scientific were used for detecting CO from the blast fume. The monitors were calibrated using standard 100 ppm CO gas. The calibration was carried out using 34 L CO gas cylinder, 3 ft. Tygon gas tubing, and a 0.5 Lpm gas regulator. The sensing range of the CO sensor is 0 to 1,500 ppm with a resolution of 1 ppm.

Sensor 1(position 1) was hanged from the roof at a distance of 17 m from the heading face. Sensor 2 (position 2) was attached to the heading wall at a distance of 23 m from the heading face. The monitor location was chosen based on proximity to the face, adequate covering against fly rocks and zones of little or no interference from human activity. Notably, there was no background CO concentration since this experiment was the only blast. The exhaust fan located 20 m from the heading face was turned on 3 min after the blast to clear the blast fumes. Monitor located 17 m from the drift face is shown by Figures 5.4.

Figure 5.4. Sensor 1 location

Once the experiment was completed, the sensors were collected from their various positions at the mine 5 hr after the blast. The CO concentrations and alarm events were downloaded onto a PC via the Gasbadge pro datalink.

Sensor readings showing a variation of CO concentrations with time is represented by Figure 5.5.

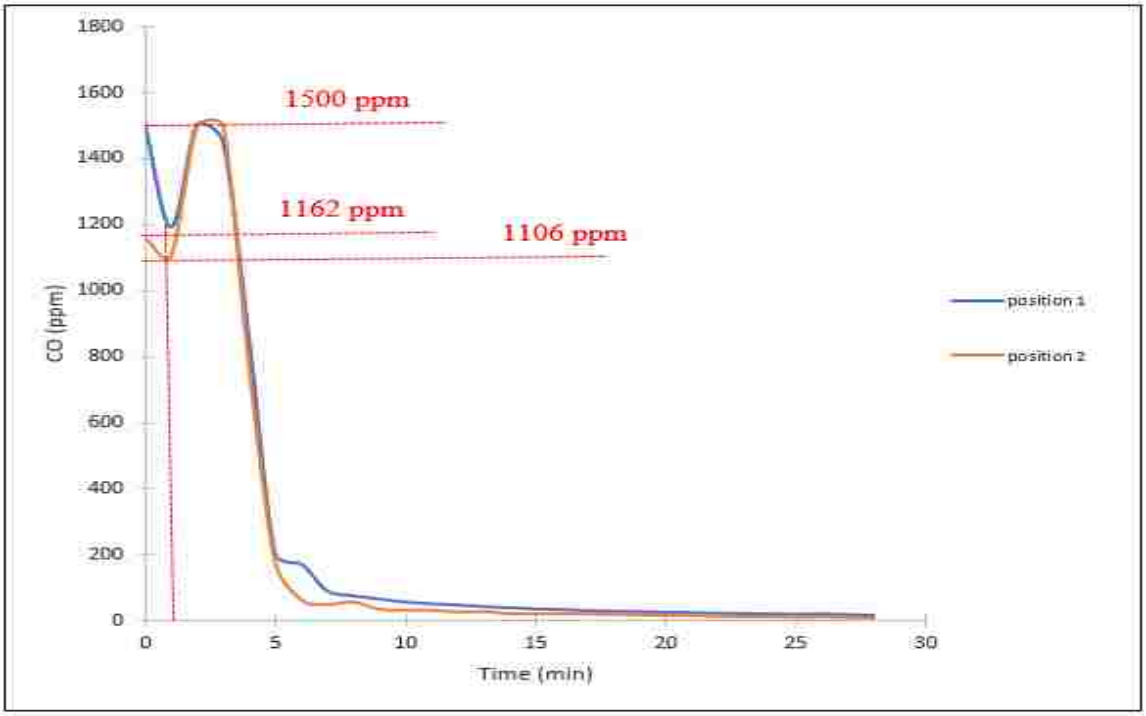

Figure 5.5. Sensor readings showing variation of CO concentration with time

As seen in Figure 5.5, sensors 1 and 2 recorded 1,500 ppm and 1,162 ppm of CO respectively at time zero. The concentrations notably reduced to 1,200 ppm and 1,106 ppm for sensor 1 and 2 respectively at time 1 min. Then a rise to a peak concentration of 1,500 ppm for both monitors 3 min after blasting. This is followed by a decrease in carbon

monoxide concentrations to 172 ppm and 66 ppm for 17 m and 23 m from face respectively after 7 min. Then a gradual decrease in CO content with time.

The drop in CO concentration at 1 min is due to the suction effect of the blast pressure. The high blast pressure creates a vacuum behind the cloud of blast fumes which sucks the fumes in a backward direction reducing the amount of CO read by the sensors, which explains the observed drop in CO sensor readings at 1 min. CO concentrations are slightly higher for sensor 1 (at 17 m from the face) compared to sensor 2 (at 23 m from the face). This is because CO concentration decreases with increasing distance from the heading face.

Figure 5.6 is an expansion of Figure 5.5 to show details of CO clearance time around the threshold (i.e., 25 ppm) in an attempt to define a safe time interval

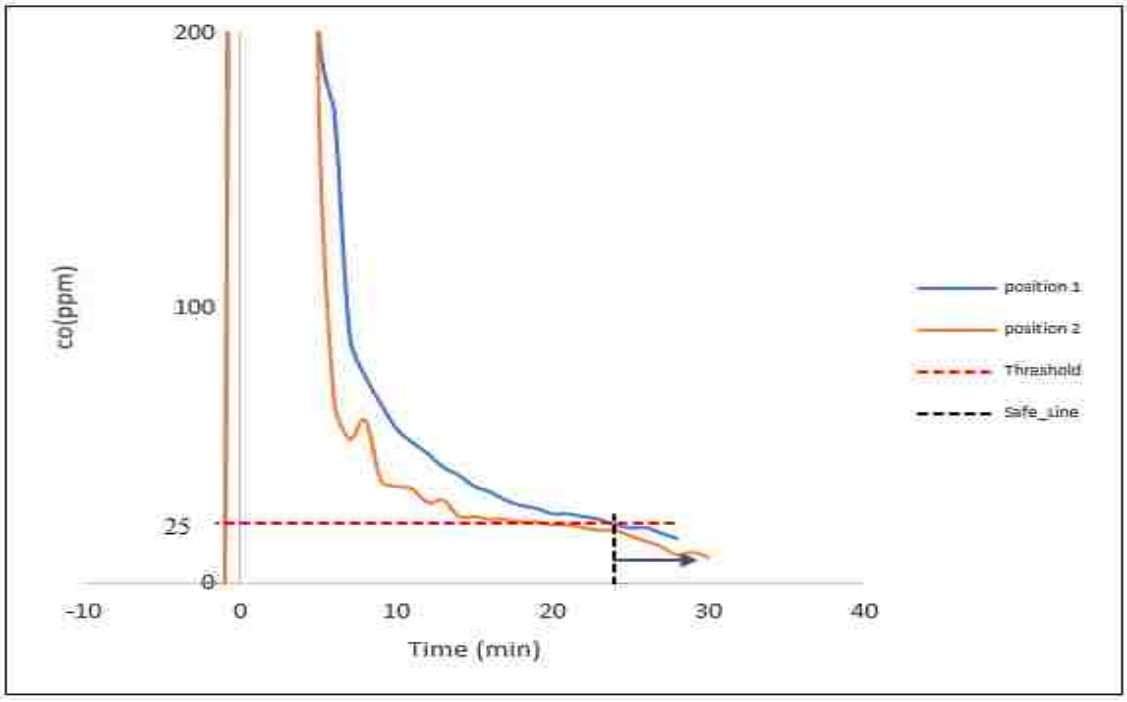

Figure 5.6. Sensor readings showing the safe time zone

As observed from Figure 5.6, CO concentrations were reduced below the 25 ppm limit 25 min after blasting. Hence, 25 min after the blast defines the safe time zone. This means that given the blast input parameters, miners can return to the working zone any time after 25 min.

5.1.2. Development of CFD Model. The experiment was reconstructed in a virtual environment using CFD in ANSYS Fluent. The settings and boundary conditions used for the CFD model and simulation are the same as used in Section 4. Figure 5.7 shows the geometry of the model containing an exhaust fan with flow rate 3 m^3/s located 20 m from the heading face.

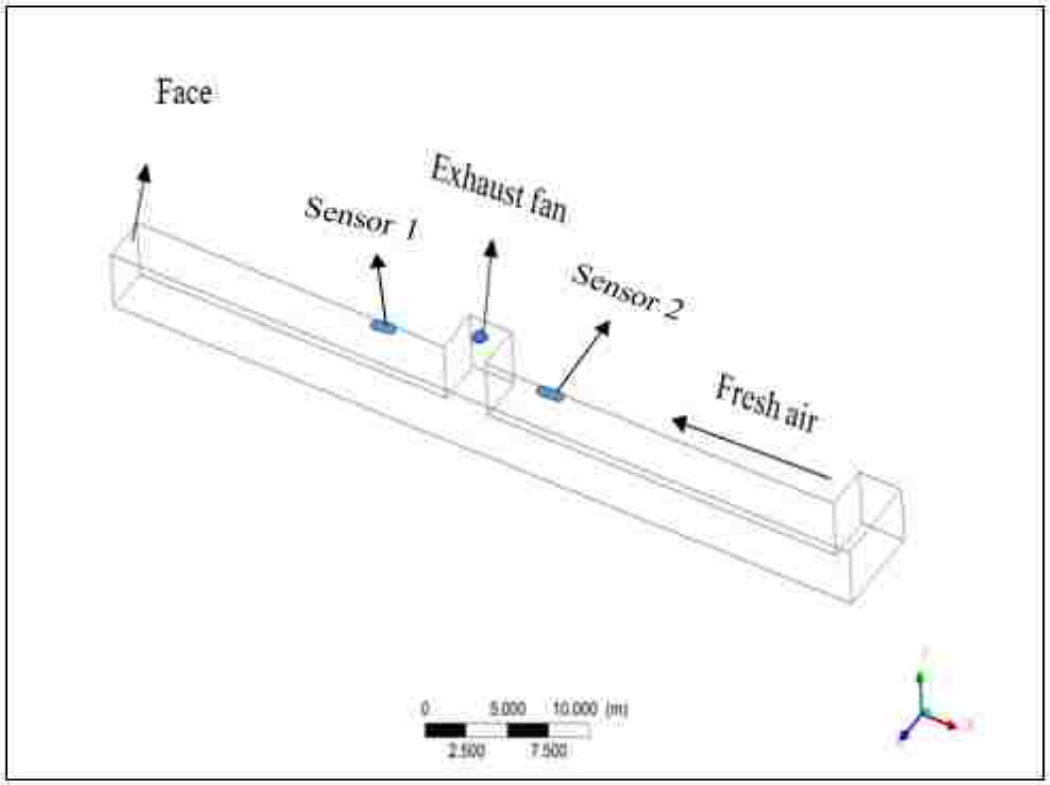

Figure 5.7. Model geometry

The results from the CFD simulation is compared with the experimental results. Figures 5.8 and 5.9 compares CO concentrations for both CFD simulation and experimental results at positions 1 and 2 respectively.

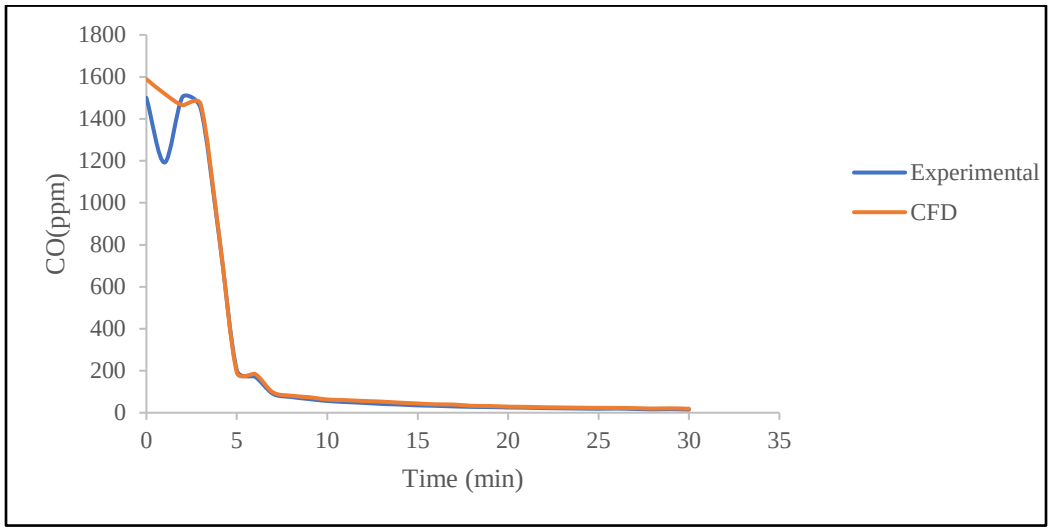

Figure 5.8. CFD and experiment results at position 1

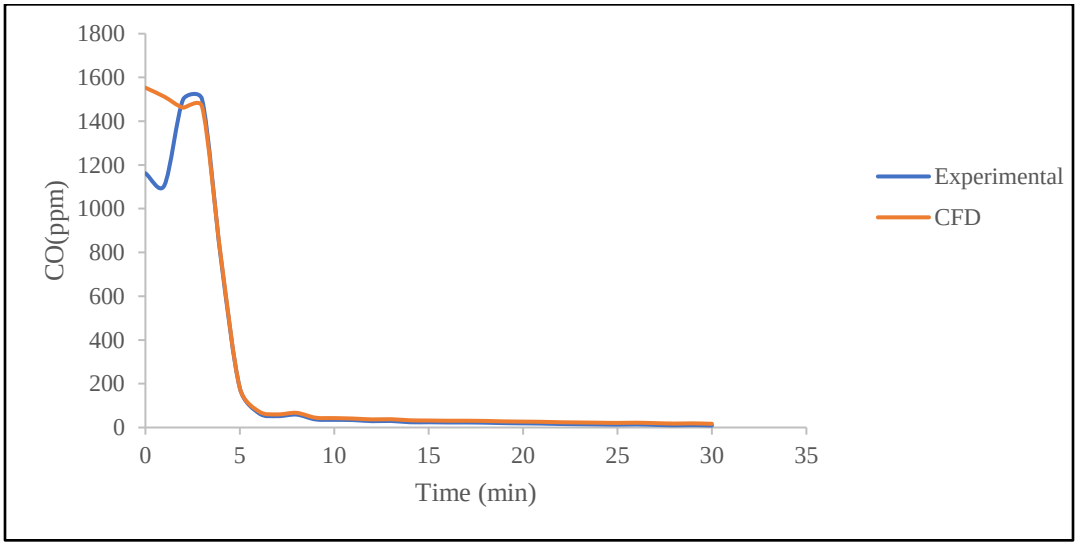

Figure 5.9. CFD and experiment results at position 2

Although there is a strong match between the CFD and experimental results as observed in Figures 5.8 and 5.9, the CFD model CO concentrations are slightly higher than the experimental values (difference of 7 %). The difference is attributed to the quantity of gases trapped in the muck pile and released over time (Torno, 2013) in the experimental case. Additionally, there is a drop of 93 % at 25 min for the experimental results since CO concentration reduces rapidly with time. The percentage difference is used for the comparison instead of the root mean square error (RMSE) since the comparison involves a single experiment and a CFD model.

The relationship between the experimental and CFD results for sensors 1 and 2 are expressed by Figures 5.10 and 5.11 respectively.

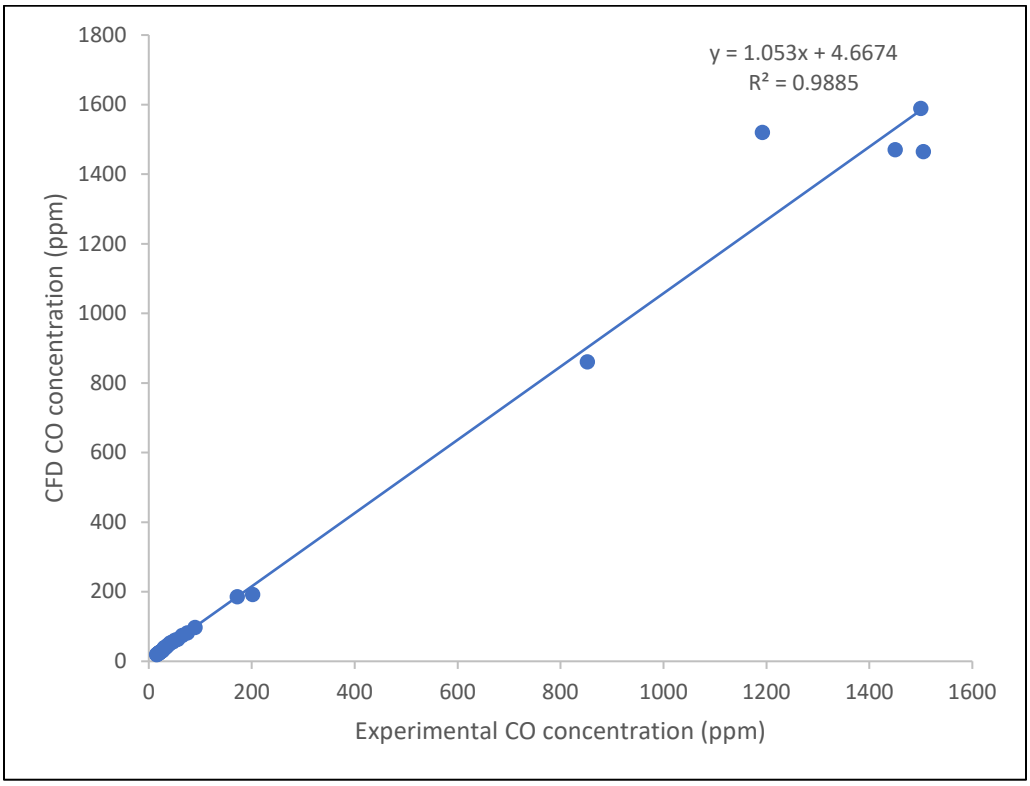

Figure 5.10. Relationship between CFD and experimental values at position 1

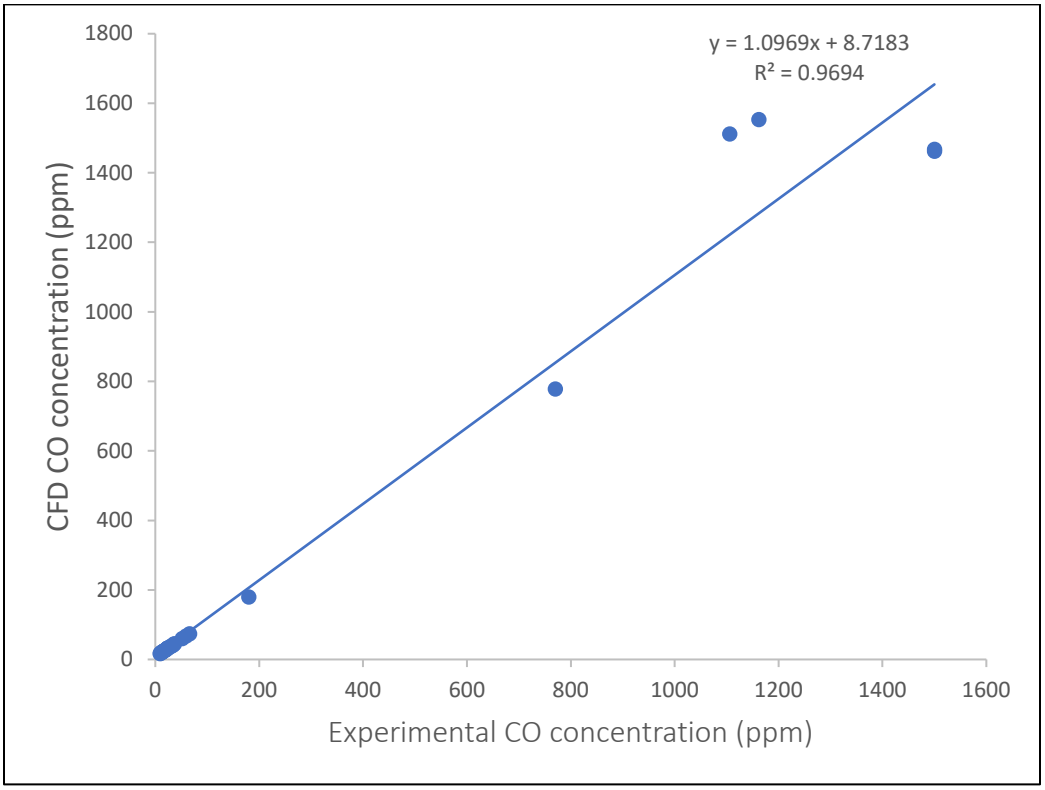

Figure 5.11. Relationship between CFD and experimental values at position 2

As shown in Figures 5.10 and 5.11, there exist a strong correlation between CFD and experimental values for both monitor locations with a coefficient of determination, R^2 of 0.988 and 0.969 respectively. The R^2 value decreases with increasing distance from the face. As the experimental results compare favorably with CFD model results, the CFD model can be used for predictions.

5.2. VALIDATION

5.2.1. Re-entry Time. Since there exists a strong agreement between the experimental and CFD values, CFD simulations were conducted for various explosive

quantities and airflows. The simulation values were compared with the results from the predictive equations generated in Section 4 (i.e., Equations 60 to 63).

Simulations were conducted with the following parameters: cross-sectional area 9 m^2; explosive mass 100 kg, 200 kg, 300 kg, and 400 kg; and air flow 2.5 m^3, 5 m^3, and 10 m^3 and the re-entry times recorded. Validated CFD model re-entry times were compared with the re-entry times estimated using Equations 60 to 63.

Table 5.1 captures the post-blast re-entry times for the various explosive masses and airflows. The remainder of the results is detailed in Appendix C.

Table 5.1. Post-blast re-entry time based on validated CFD model and the equations

Mass (kg)	**Airflow(m^3/s)**	**Re-entry Time_Simulations (min)**	**Re-entry Time_Equation (min)**	**Difference (%)**
100	2.5	30	32	6%
	5	15	17	12%
	10	7	9	22%
200	2.5	60	77	22%
	5	31	36	14%
	10	15	17	12%
300	2.5	91	102	11%
	5	45	50	10%
	10	23	25	8%
400	2.5	119	131	9%
	5	60	66	9%
	10	30	33	9%

Figure 5.12 shows a post-blast re-entry time comparison between results from the validated CFD models and results based on developed equations.

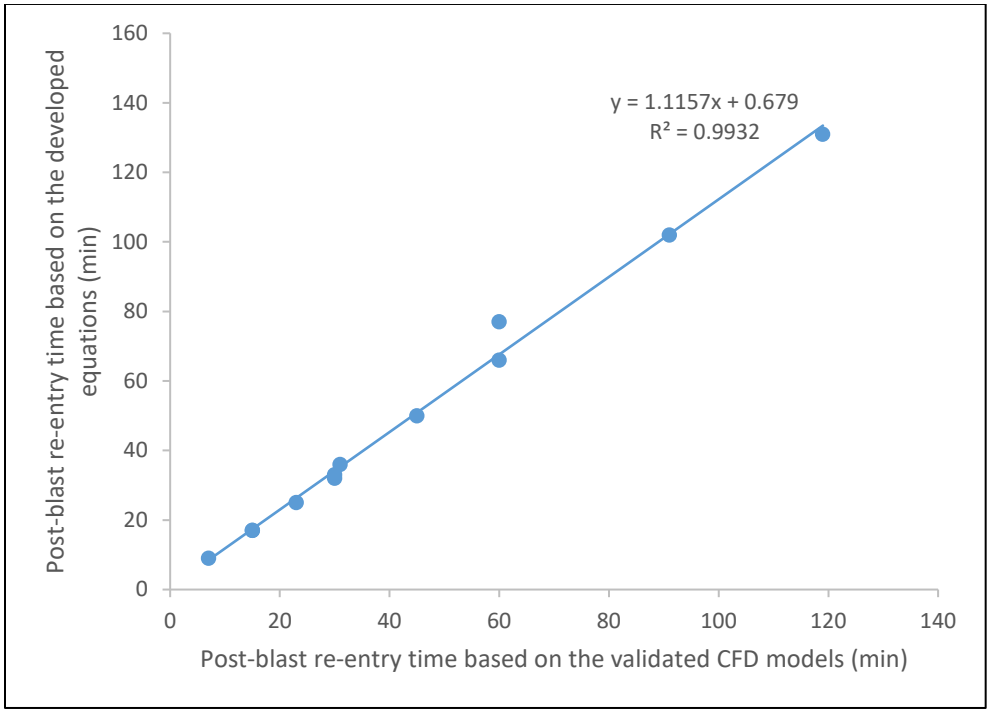

Figure 5.12. Relationship between developed relations and CFD model values

There is a strong agreement between the results from the validated CFD models and the equations with a root mean square error (RMSE) of 7.5. The coefficient of determination (R^2) between the CFD model and the theoretical analysis was 0.993 as illustrated in Figure 5.12. This implies that Equations 60 to 63 can be used with confidence to predict post-blast re-entry time for a maximum working space volume of 2,500 m^3.

5.2.2. Safe Blast Distance. Simulations using the proposed CFD model were carried out using the following parameters: cross-sectional area 9 m^2; explosive mass

100 kg, 200 kg, 300 kg, and 400 kg; and air flow 2.5 m^3, 5 m^3, and 10 m^3 and the safe distances recorded. The safe distances from the verified CFD models are compared with those from the developed equations.

Table 5.2 summarizes safe distances for the various explosive masses and airflows based on the validated CFD models and equations.

Table 5.2. Safe blast distances derived using validated CFD model and the equations

Mass (kg)	Airflow(m^3/s)	Distance _Validated CFD model (m)	Distance_Equation (m)	Difference (%)
100	2.5	222	231	4%
	5	221	228	3%
	10	221	221	0%
200	2.5	277	262	6%
	5	275	258	7%
	10	261	251	4%
300	2.5	285	292	2%
	5	284	288	1%
	10	283	280	1%
400	2.5	305	321	5%
	5	303	318	5%
	10	300	310	3%

Figure 5.13 highlights the relationship between the safe distances estimated from the validated CFD models and those from Equation 59. Appendix C contains the results from the complete set of CFD simulations.

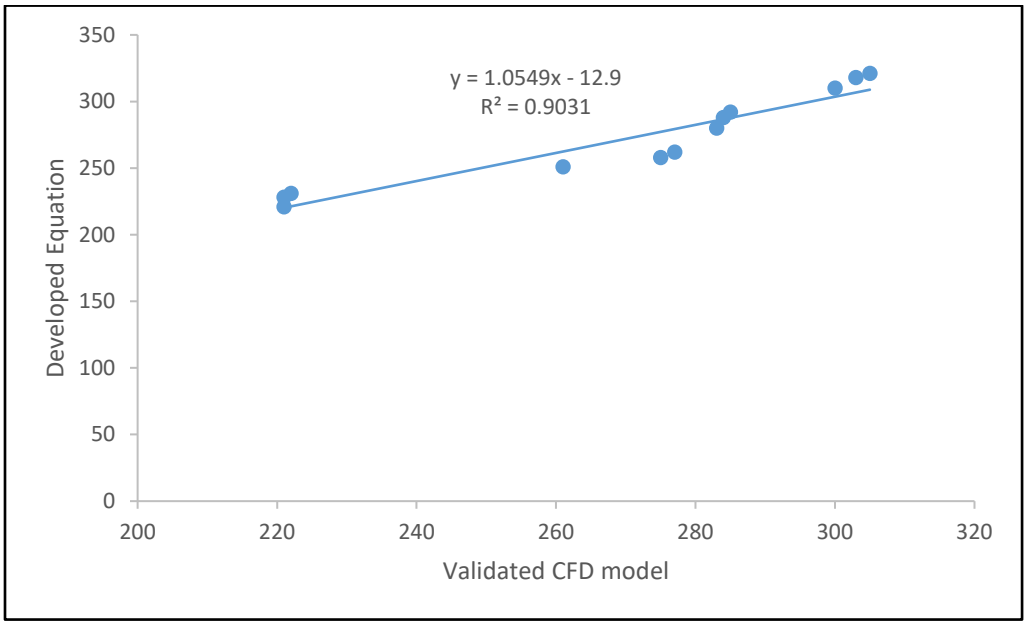

Figure 5.13. Relationship between predictors and CFD values

There is a strong agreement between the results from the validated CFD models and the predictors with a root mean square error (RMSE) of 10.7. The coefficient of determination (R^2) between the CFD model and the theoretical analysis was 0.903 as shown in Figure 5.13. This means that Equation 59 can be used to conservatively estimate safe blast distances.

5.3. SUMMARY

The CFD model was successfully validated with data from Missouri S&T Experimental Mine. The validated CFD model was then used for simulating various underground development heading arrangements. The simulation results were compared with those from the developed equations in Section 4. The developed equations and the validated CFD models compare favorably with a root mean square error (RMSE) of 7.5 and 10.7 for post-blast re-entry time and safe blast distance respectively. Hence, the equations can be confidently used for predicting post-blast re-entry time and safe blast distance. Section 6 covers the conclusions and recommendations for future work.

6. CONCLUSIONS, PHD CONTRIBUTIONS AND RECOMMENDATIONS FOR FUTURE WORK

6.1. SUMMARY AND CONCLUSIONS

Blasting operations using standard industry explosives in the underground mine development heading result in the release of noxious fumes such as carbon monoxide (CO), nitrogen dioxide (NO_2) and ammonia (NH_3). These noxious gases need to be cleared within a reasonable time frame before re-entry of miners to the working area. Poor procedures for determining optimal post-blast re-entry times has resulted in several injuries, fatalities and production losses. The injuries and fatalities are attributable to workers returning to work zones too soon after blasting and/or workers located within blast exclusion zones immediately after blasting. Determining the optimal post-blast re-entry time is vital since overestimation of re-entry time results in production losses, while underestimation introduces health and safety concerns. Moreover, providing a means of estimating safe blast distance would prevent miners from blast fuming as a result of location in blast exclusion zones.

Underground mine operations schedule blasts at the end of a working shift to allow enough time for blast fumes to clear. The disadvantages of doing this are: (i) concentrations of noxious gases might not be reduced below thresholds before the next shift resumes work, and (ii) ventilation fans run at unregulated speeds resulting in relatively high ventilation cost. Thus, it is imperative to provide optimal air quantity based on the desired post-blast re-entry time to eliminate the outlined disadvantages above.

Dilution with fresh air is one of the best means of controlling blast fumes in underground mines. This involves the removal of contaminated air within a reasonable

time before re-entry of workers to the work zone. An important factor associated with blast fume dilution and clearance which has been neglected is the optimal duct discharge location. The effect of duct discharge location on fume clearance, hence post-blast re-entry time was investigated in this study.

The research was geared towards establishing a safe, productive and cost-effective underground mine operations using computational fluid dynamics (CFD) approach. This was accomplished by determining: (i) safe blast exclusion zones; (ii) optimal discharge locations; and (iii) suitable post-blast re-entry time and optimal air quantity based on commonly used ventilation and blasting conditions. The literature review has showcased vital aspects of previous research, namely: (i) blast fume and constituent gases; (ii) mathematical modeling of blast fume dispersion; (iii) post-blast re-entry time determination and (iv) studying blast fume propagation in underground mines using CFD. The Literature review revealed that: (i) a complex 4-dimensional flow dynamics analysis of underground mine fume concentrations and clearance is needed; (ii) a detailed study is needed to understand the influence of fresh air duct discharge location on fume dilution and clearance; (iii) there are currently no means of estimating safe blast distances i.e. blast exclusion zones, and (iv) there is a lack of a comprehensive relationship for estimating post-blast re-entry time in underground mines.

To accomplish the research objectives, mathematical models describing blast fume dispersion in the underground mine development heading were successfully developed. The corresponding governing equations and boundary conditions derived were complex and coupled nonlinear partial differential equations, thus could not be solved analytically. The finite volume method (FVM) in ANSYS Fluent was used for the modeling and

simulations. The finite volume method involves solving partial differential equations in the form of algebraic equations. The finite volume method was chosen because the mass, momentum, and energy at the faces surrounding a control volume are conserved.

Geometries of the various heading arrangements were designed using SOLIDWORKS®. Computational fluid dynamic modeling and simulations of various development heading arrangements have been successfully carried out using ANSYS Fluent for the various research objectives. An experiment was also successfully conducted at the Missouri S&T Experimental Mine to acquire blast data to validate the CFD models. The drift arrangement was reconstructed using ANSYS Fluent and the results compared with that of the experimental. Computational fluid dynamics simulation results compare favorably with blast data from Missouri S&T Experimental Mine with a coefficient of determination (R^2) of 0.97. As a result, an equation has been developed to predict safe blast distances prior to blasting. This creates safe blast exclusions zones that keep miners away from blast fume poisoning. Four equations have been developed to conservatively estimate optimal post-blast re-entry time and optimal air quantity in the underground mine development heading. This would improve the safety and production needs of the underground mine as well as reduce the ventilation cost associated with an unregulated fan airflow. The theories developed from this research and their associated findings will serve as a basis for future research in related areas. Results obtained from the study and its validation are summarized below:

1. An analysis of the results shows that carbon monoxide (CO) is the critical gas in terms of re-entry time, and thus is used for downstream analysis carried out by this research. This is because, at threshold, NO_2 concentrations were immaterial.

2. Effect of fan duct discharge location on blast fume clearance: Results indicate that as the duct discharge location increases from the heading face, the forcing ventilation effectiveness decreases, hence increasing post-blast re-entry time. This is due to the low velocity air reaching the heading face because of advancing duct discharge location from the heading face. Research results also show that fume clearance time increases with increasing heading length. This is because more time is needed to clear the blast fumes occupying the extra working space volume created. A range of optimal duct discharge location from 10 m to 60 m is recommended for underground development headings with a maximum working space volume of 2,500 m^3.

3. Safe blast exclusion zone: Results show a linear relationship between safe blast distance from heading face and the explosive mass. A recommended minimum safe distance from blast location is 310 m based on an explosive mass range of 100 kg to 400 kg, with a cross-sectional area 16 m^2 to 25 m^2, and an airflow rate of 2.5 m^3/s to 30 m^3/s. Equation 59 has been established and validated for estimating specific safe blast distances. Equation 59 is valid under the blasting conditions specified above.

4. Estimating optimal air quantity and post-blast re-entry time: Results of this study indicate that the power relationship best depicts the relationship between air quantity and post-blast re-entry time. Four equations (i.e., Equations 60 to 63) have been developed and validated to conservatively estimate optimal air quantity and

optimal post-blast re-entry time based on explosive quantities of 100 kg, 200 kg, 300 kg and 400 kg with a maximum underground mine development working space volume of 2,500 m^3. Providing optimal air quantity based on the desired re-entry time minimizes the cost of ventilation significantly.

6.2. PHD RESEARCH CONTRIBUTIONS

The research is an effort towards developing a safe, productive and cost-effective underground mine operations by resolving the problems associated with blast fume concentration, dilution, and clearance. The key contributions from this research are outlined below:

1. This is the first attempt at deriving an equation for estimating safe blast distances in the underground mine development heading. There were no scientific means of determining blast exclusion zones. However, this does not preclude the use of sensors in detecting noxious gases emanating from blast fumes.

2. Prior to this research, there was no detailed and well validated CFD model for estimating optimal post-blast re-entry time and optimal airflow in the underground mine development heading. This research has pioneered in proposing comprehensive relationships for estimating optimal air quantity and optimal post-blast re-entry time in the underground mine development heading.

3. A complex 4-dimensional flow dynamics analysis of underground mine blast fume dispersion and clearance has been developed. This was achieved using

Computational fluid dynamics in ANSYS Fluent. Prior to this study, computational fluid dynamics had been used on limited bases to attempt resolving the problems associated with underground mine blast fumes.

4. A detailed study into the influence of fan duct discharge location on post-blast re-entry time has been investigated. There was a lack of detailed study into how duct discharge location affected blast fume clearance.

6.3. RECOMMENDATIONS FOR FUTURE WORK

This research has made significant strides towards improving safety and production in the underground mine development heading. Several important discoveries and equations have emanated from this research but more work is still necessary. There is the need for more experimentation to confirm the results from this research. Potential areas and ideas relating to post-blast underground mine environment that are worth looking into are discussed below:

1. More experiments need to be conducted at underground mine development headings to confirm and validate the findings and relationships developed in this research, thus improving the level of predictability of the models. Because of the cost associated with the blasting activity, a single blast was conducted. Moreover, there was no detailed blast fume data published in literature for validation purposes.

2. Rigorous studies need to be conducted into the long-term effects of the gases emanating from blast fumes in underground mines. Only the short term exposures

have been given considerable attention but there could be long term effects as a result of continuous exposures. Results of the study into the long term effects of noxious gas exposures might trigger the examination of the effectiveness of the standards for regulating blast fume exposures.

3. Multi-gas analysis could be conducted by including other noxious gases such as nitrogen dioxide gas (NO_2) in the simulation. The results can be compared with the outcome using only carbon monoxide (CO). This study can be made possible using a powerful computer processor with a fast solver. Acquisition of a multi-gas detector is also necessary for monitoring the gases involved in the study.

4. CFD simulations could be conducted for blasting conditions that were excluded in this study. Equations 59 to 63 could be improved by considering explosive masses in excess of 400 kg and working space volumes beyond 2,500 m^3. Future studies can consider varying the ammonium nitrate fuel oil (ANFO) fuel/oxidizer ratio to compare with the results from this research.

5. The effect of fan start time on post-blast re-entry time can be studied. Fans are generally turned on immediately after blasting in the underground mine setup. Knowledge of when to turn on ventilation fans for effective blast fume clearance is vital.

6. A CFD study of combined rock dust and blast fume propagation and clearance could be investigated. This will present understanding on how the rock dust and blast fume interact as well as the influence of this interaction on post-blast re-entry time. A study could also be conducted to ascertain how changes in the geology (i.e., rock type) of the mine affect blast fume clearance, hence post-blast re-entry time.

7. The knowledge and expertise from this study could be broadly employed in: studying methane flow and explosions, gob gas flow, diesel particulate matter (DPM) propagation and control, and dust dispersion. A CFD study of blast fume propagation and clearance in underground mine stopes and room and pillar mining system could also be investigated.

APPENDIX A

EFFECT OF DISCHARGE LOCATION ON FUME CLEARANCE

Cross-sectional area 20 m^2 & Mass 200 kg

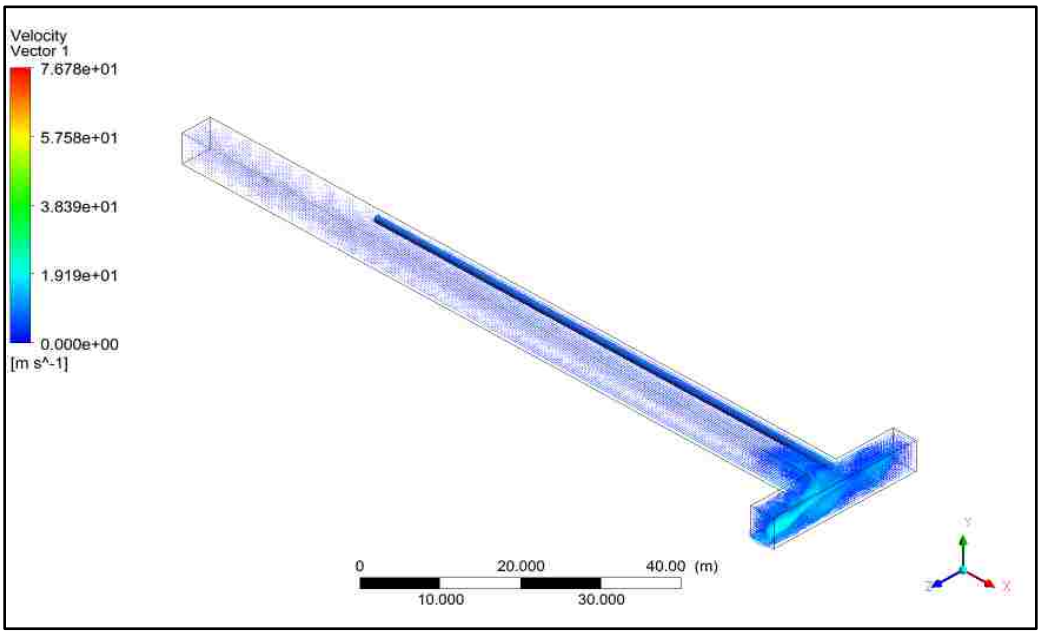

Velocity vector_30m from face_100 m length

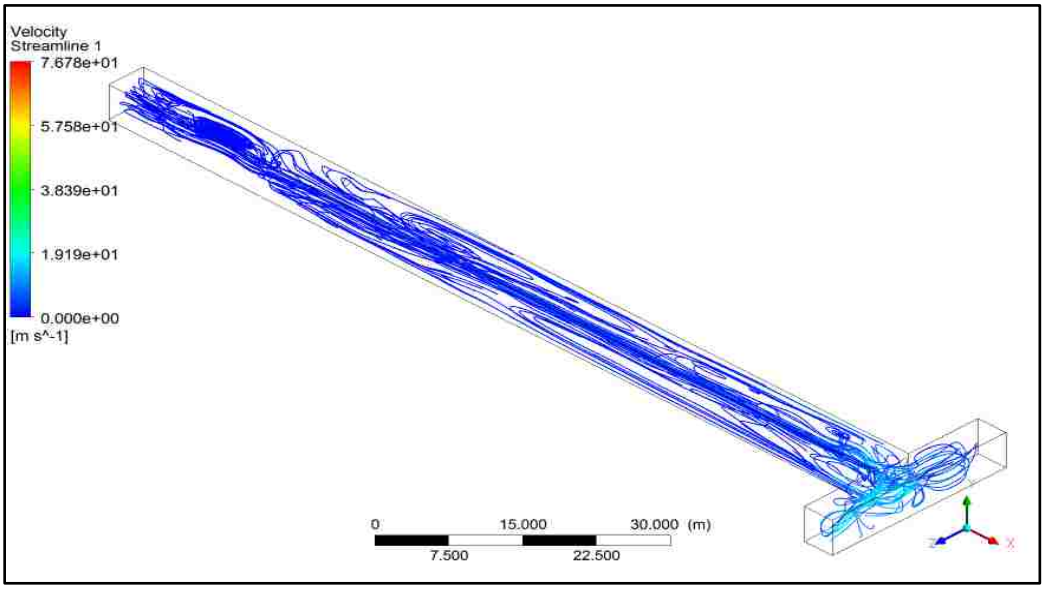

Velocity streamline_30m from face_100 m length

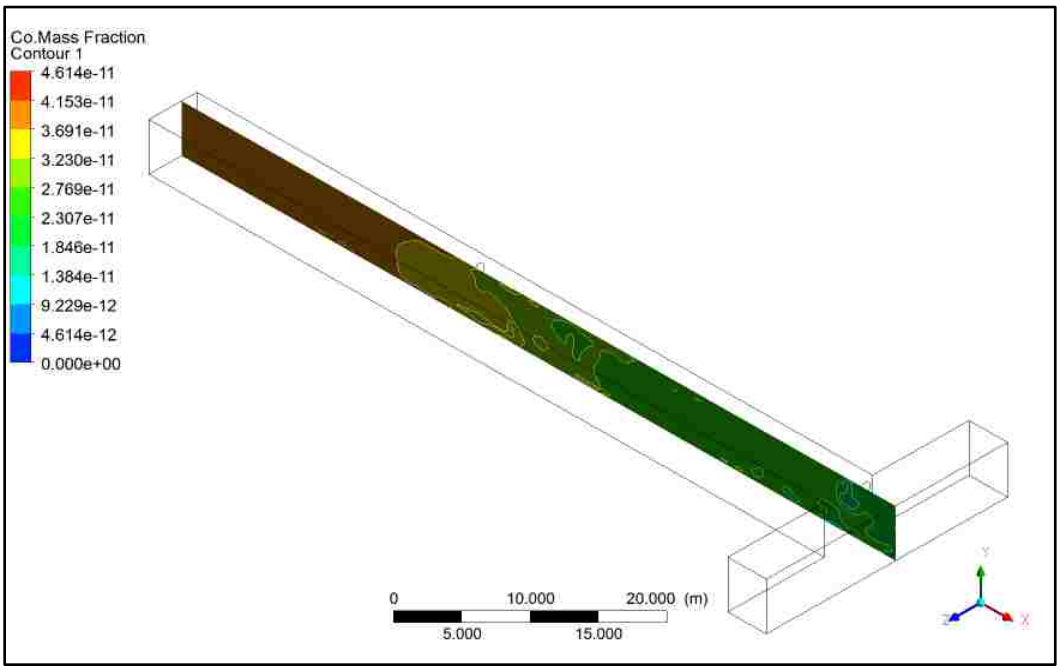

CO concentration_30m from face_70 m length

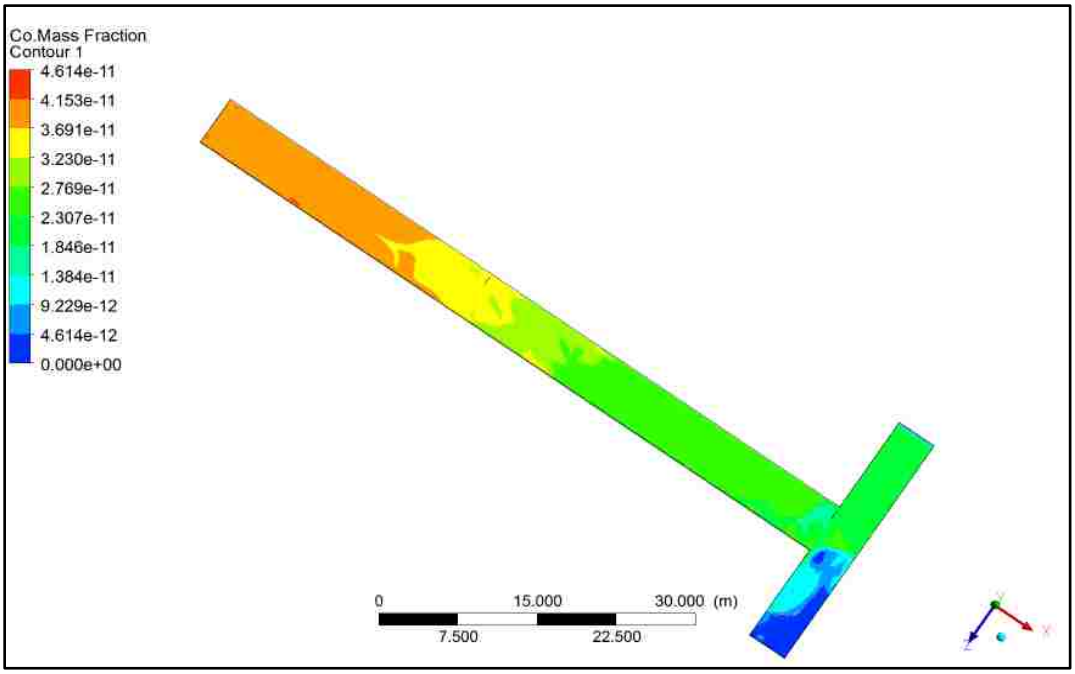

CO concentration_30m from face_70 m length

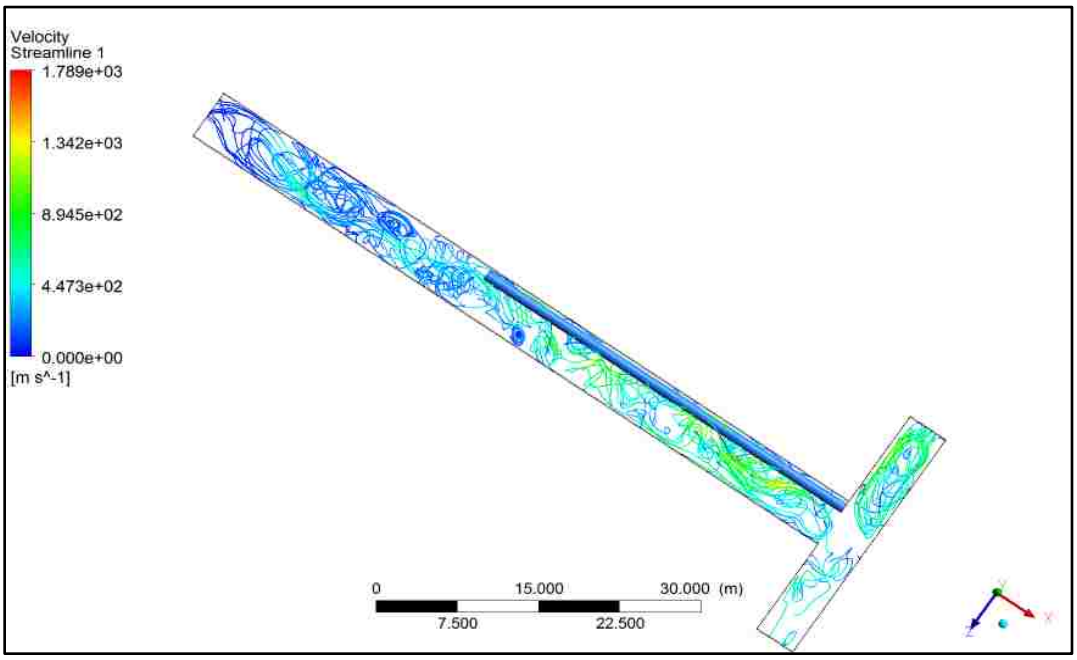

Velocity streamline_30m from face_70 m length

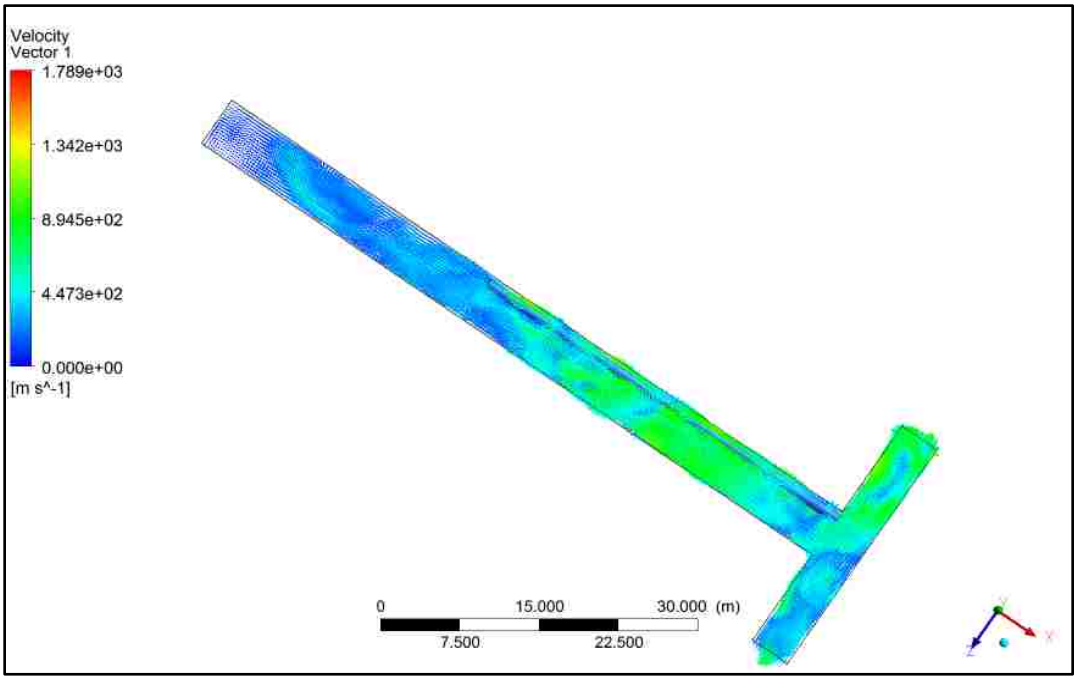

Velocity vector_30m from face_70 m length

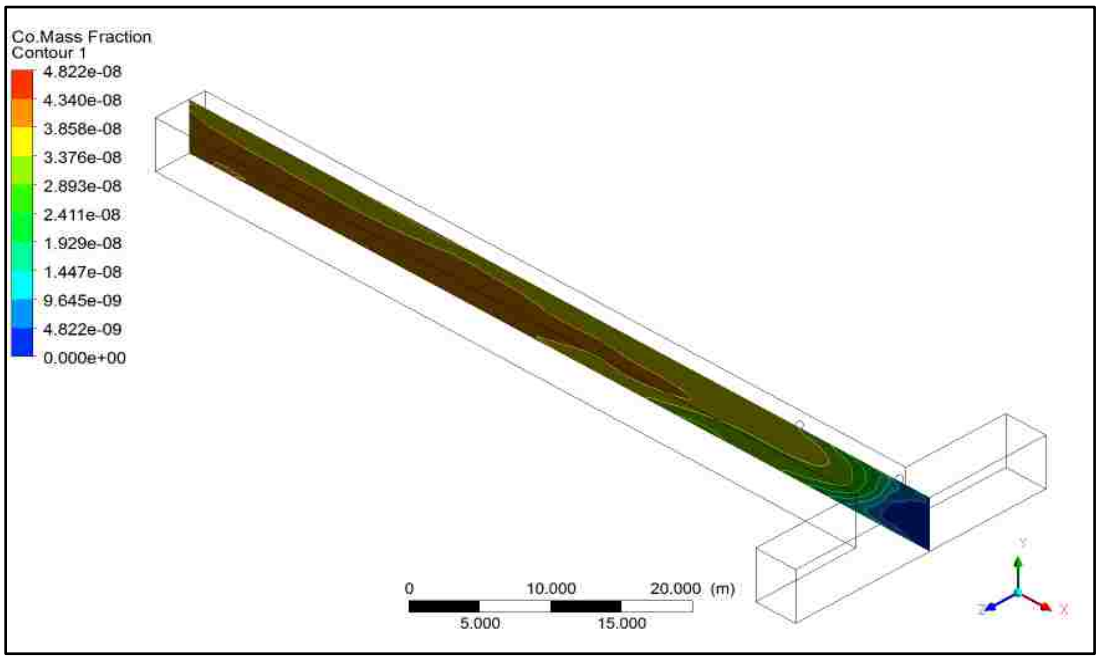

CO concentration_60m from face_70 m length

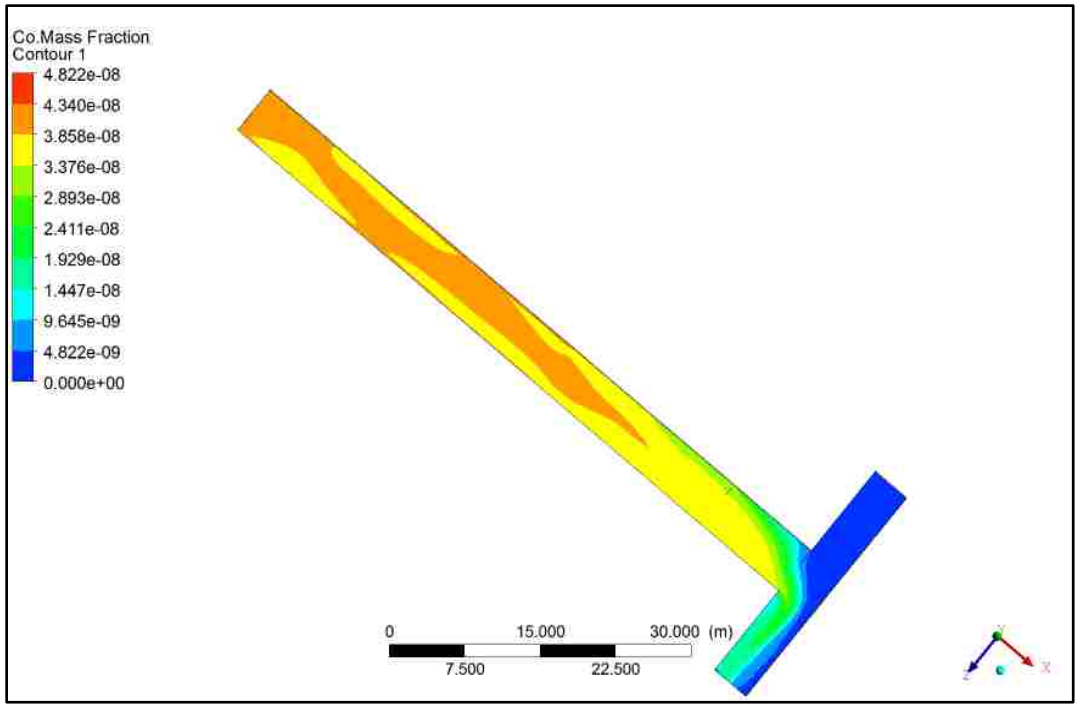

CO concentration_60m from face_70 m length

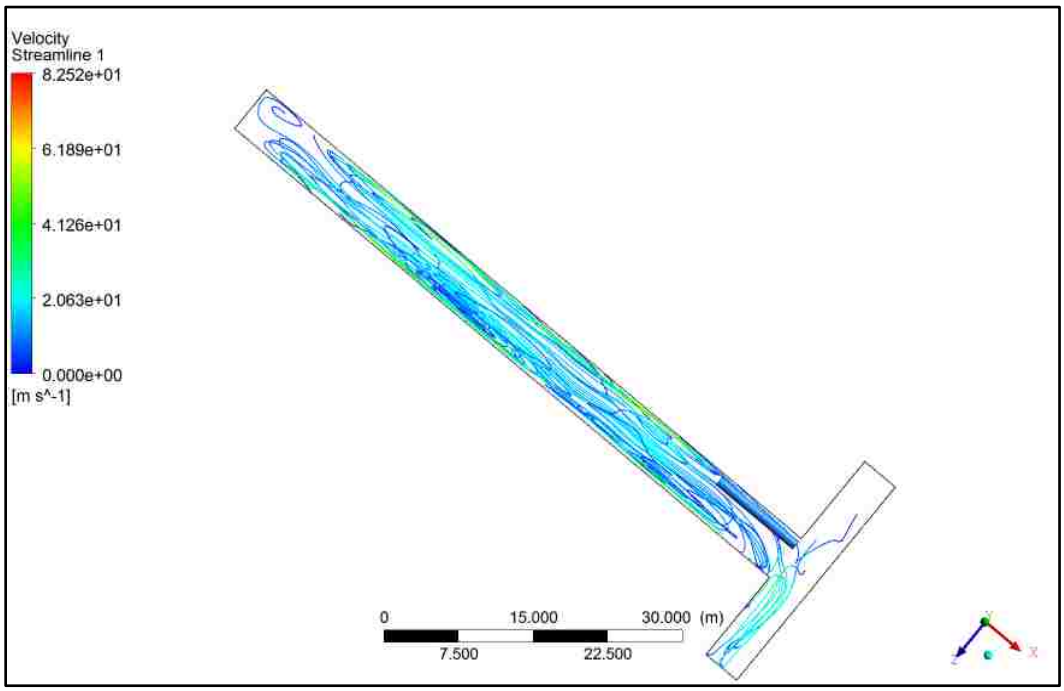

Velocity steamline_30m from face_70 m length

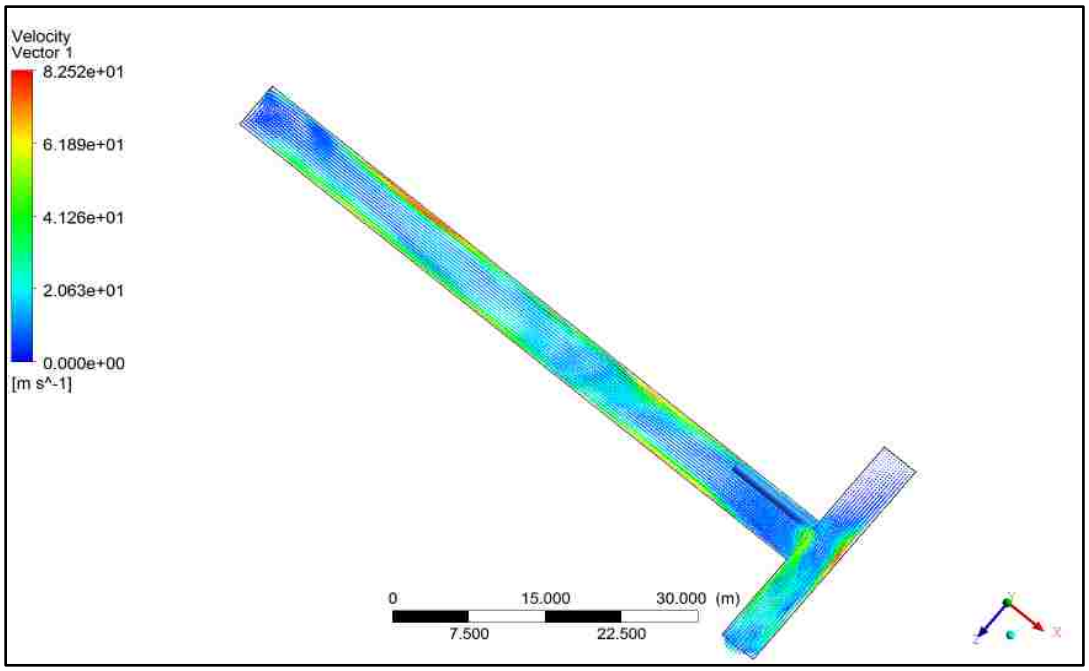

Velocity streamline_60m from face_70 m length

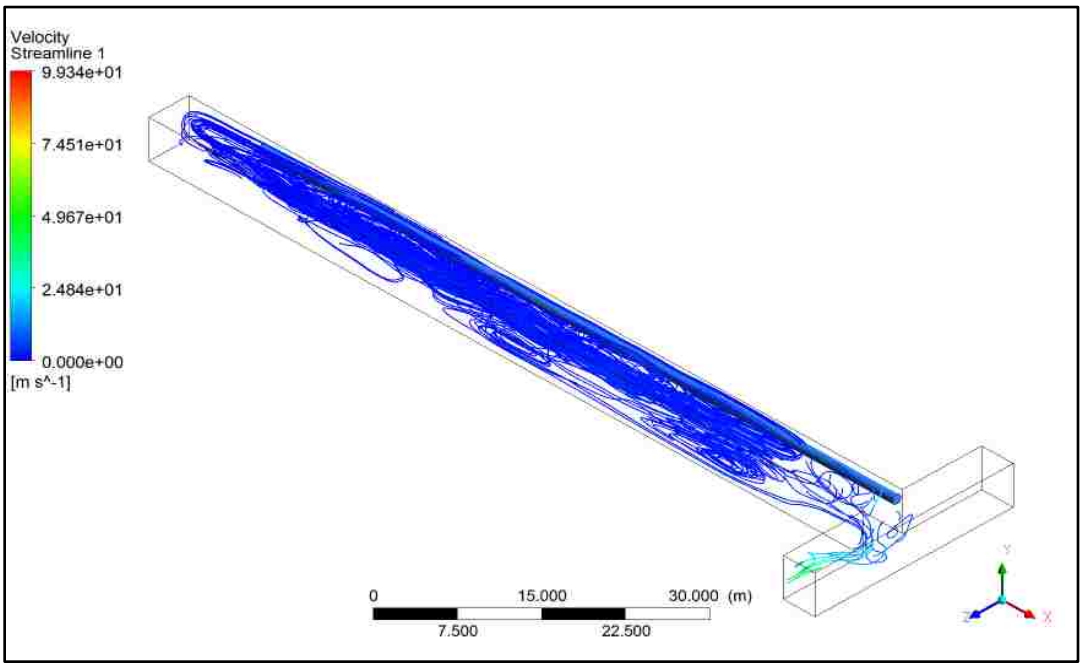

Velocity streamline_10m from face_90 m length

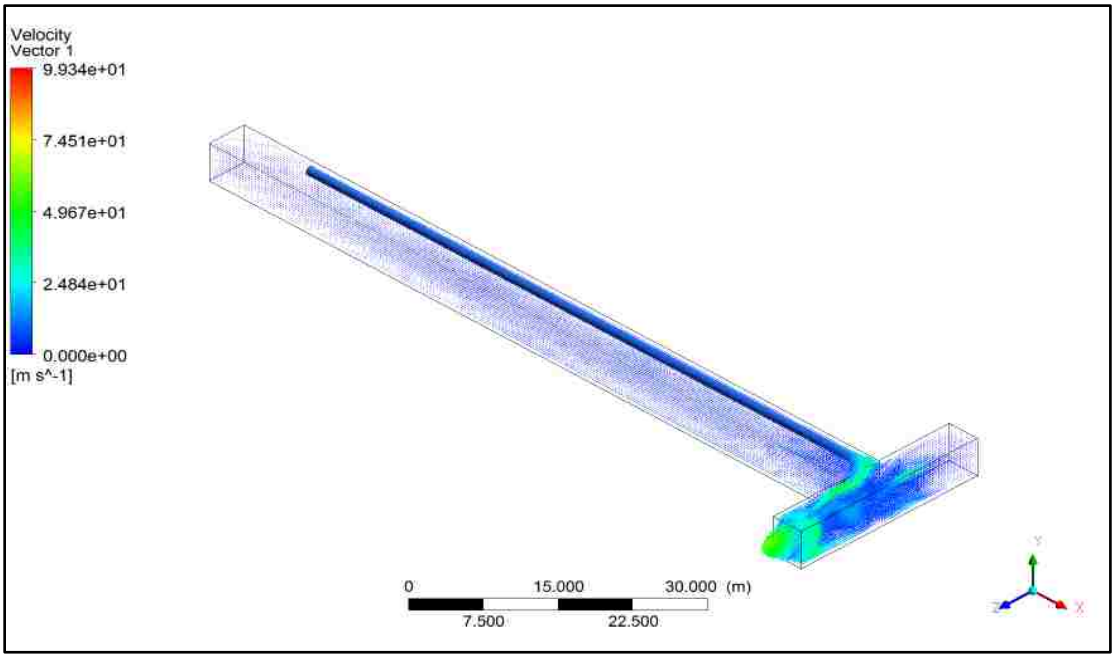

Velocity streamline_10m from face_70 m length

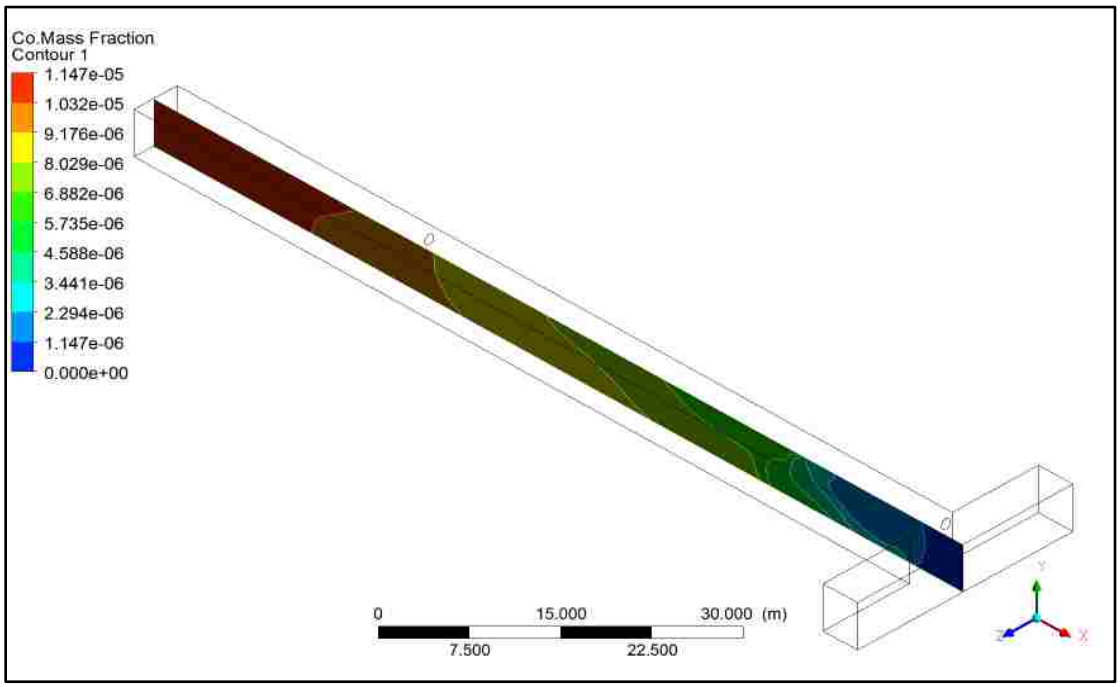

CO concentration_30m from face_90 m length

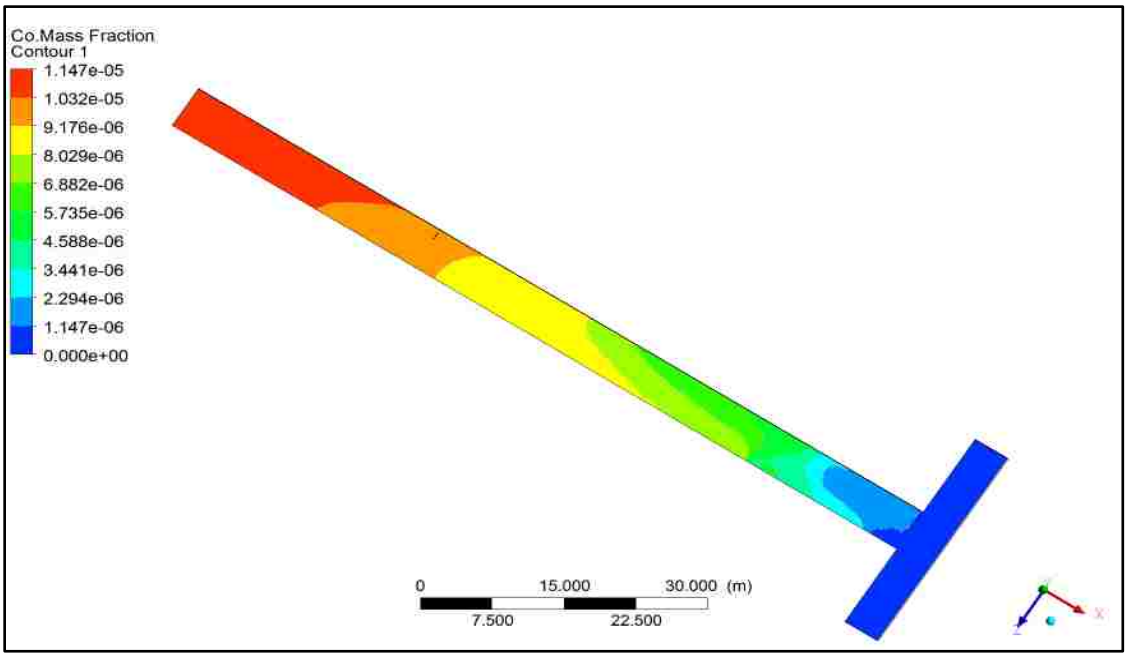

CO concentration_30m from face_90 m length

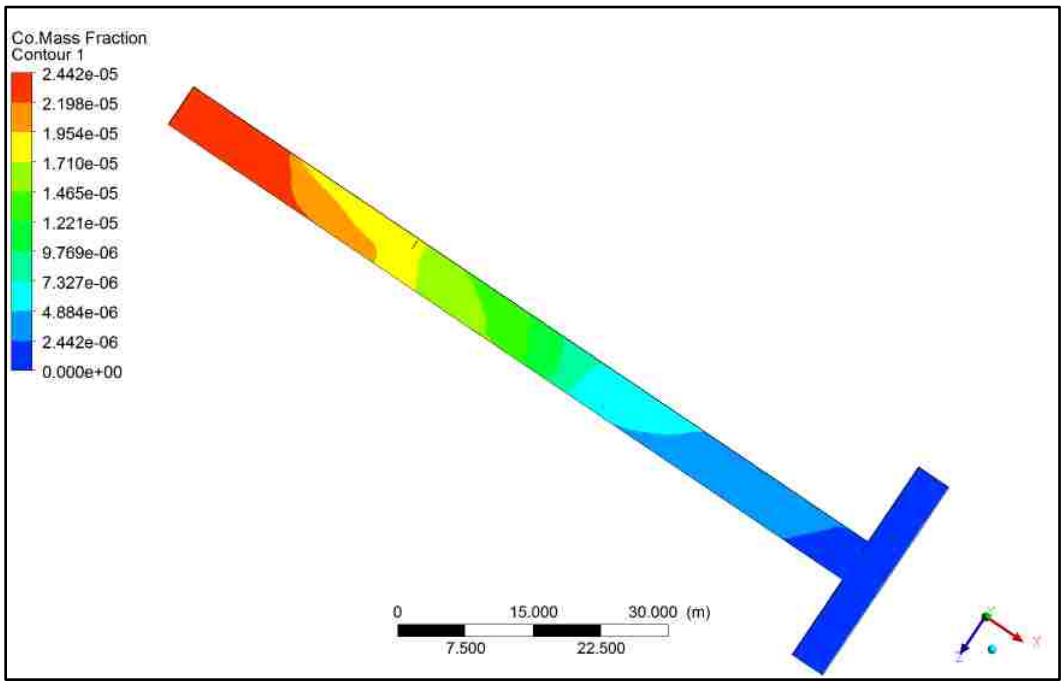

CO concentration_10m from face_90 m length

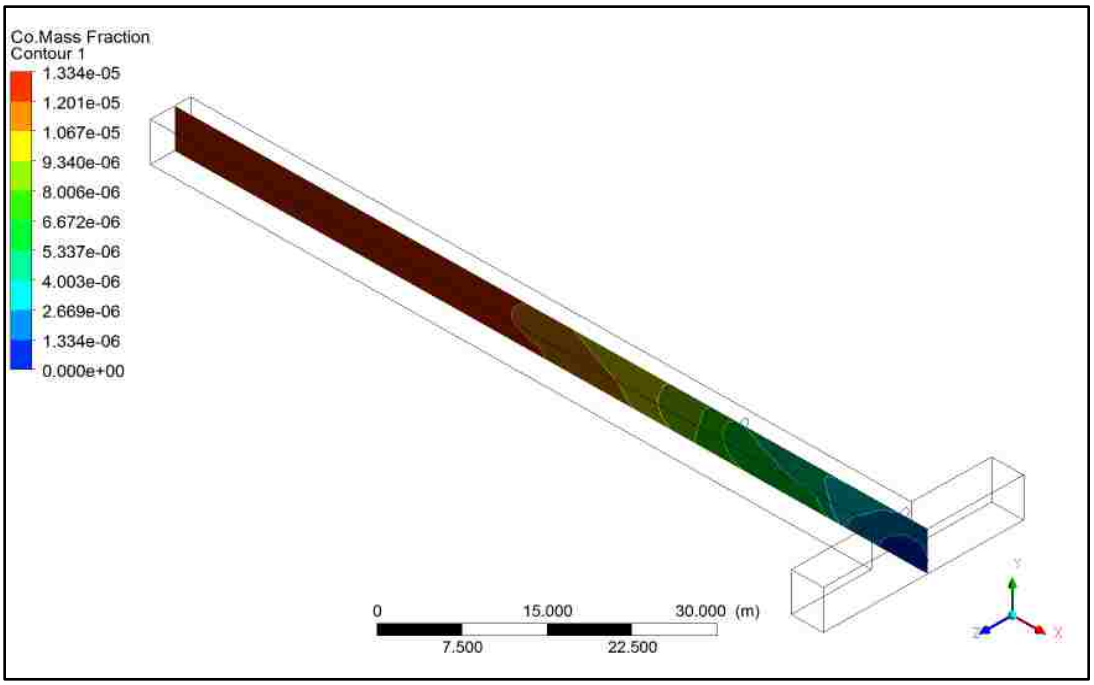

CO concentration_70m from face_90 m length

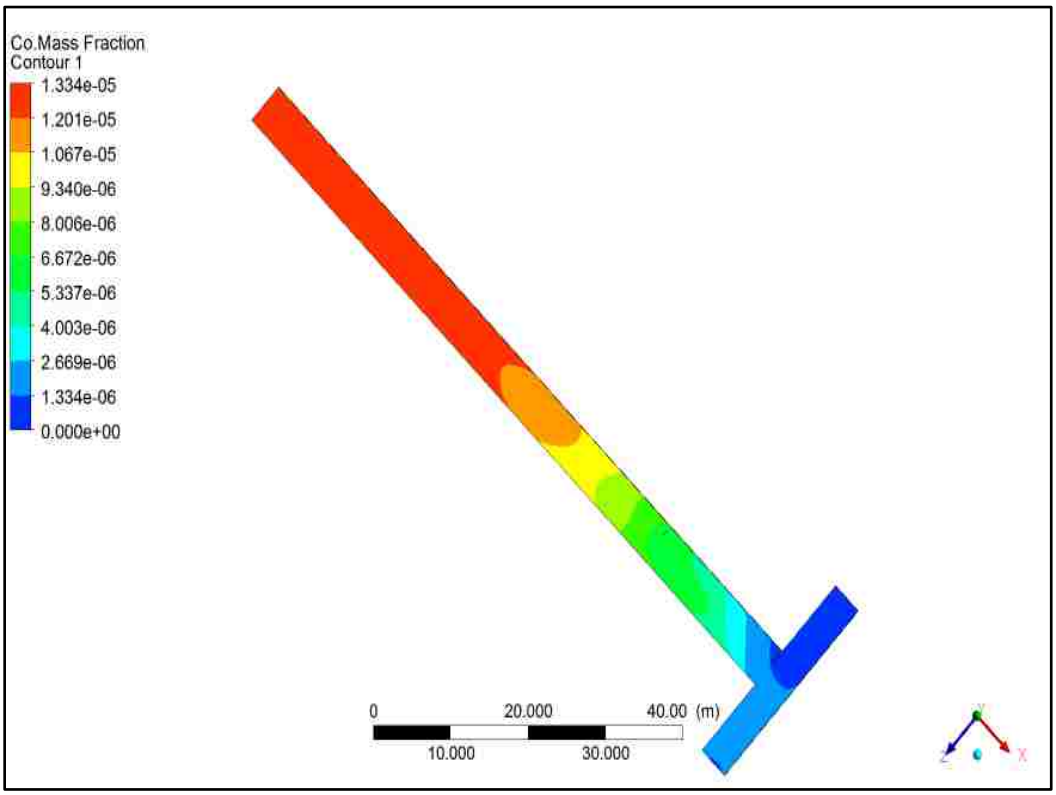

CO concentration_70m from face_90 m length

Cross-sectional area 16 m^2 & Mass 200 kg

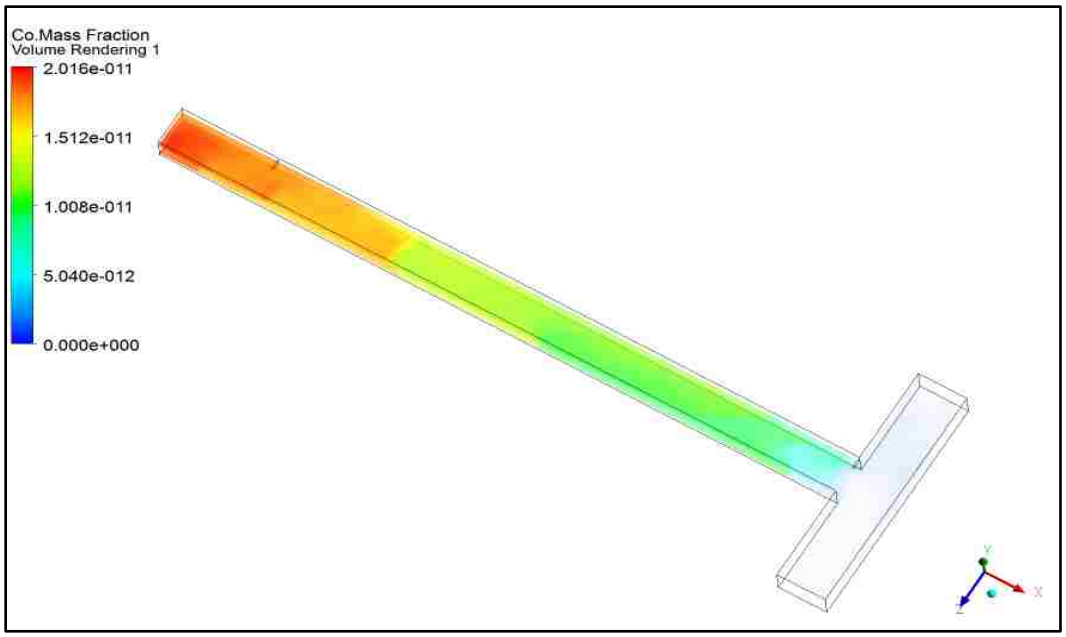

CO concentration_10m from face_70 m length

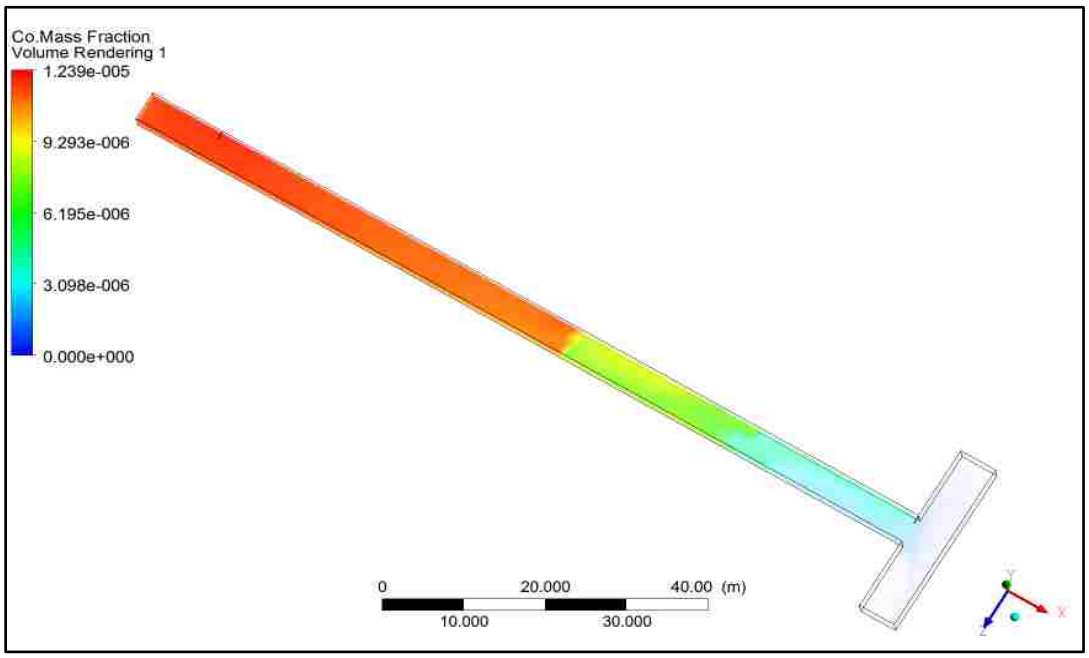

CO concentration_10m from face_100 m length

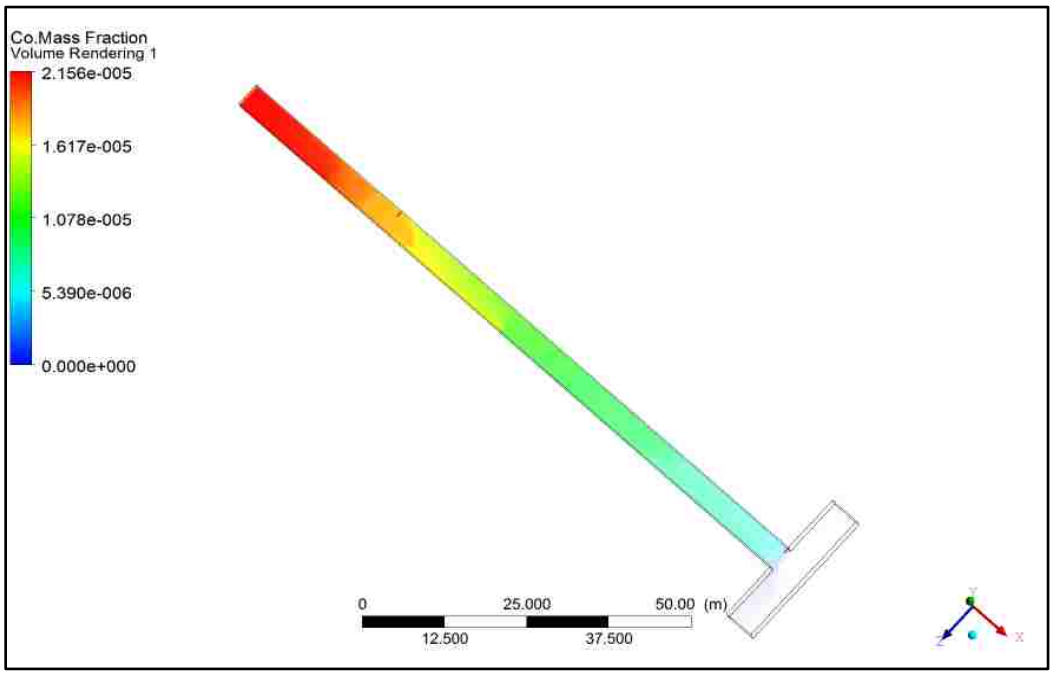

CO concentration_30m from face_100 m length

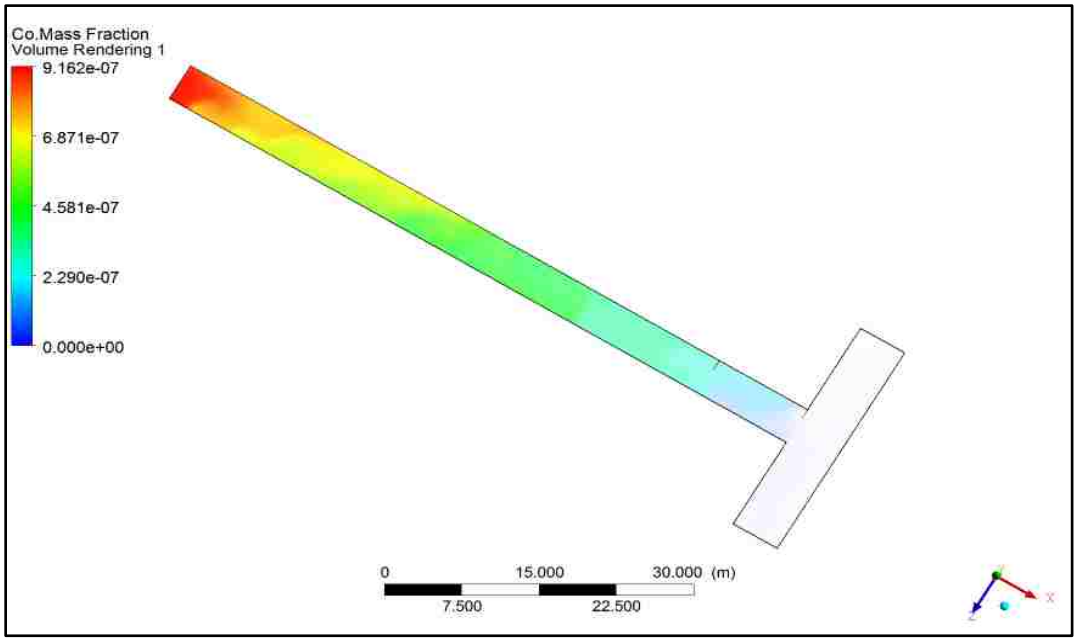

CO concentration_60m from face_70 m length

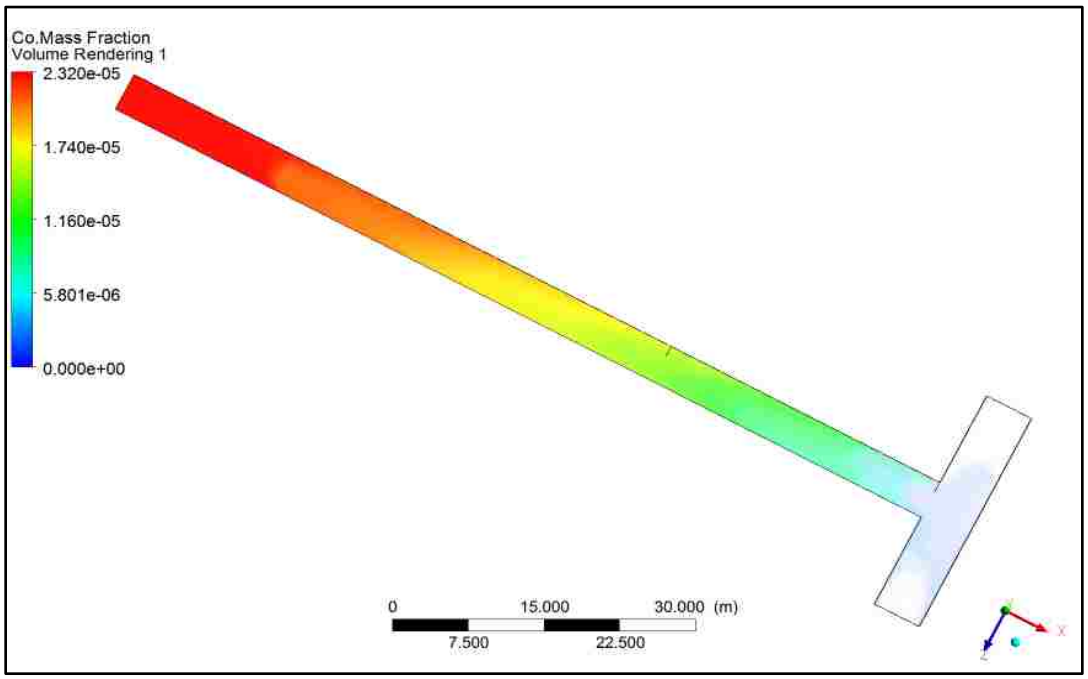

CO concentration_60m from face_90 m length

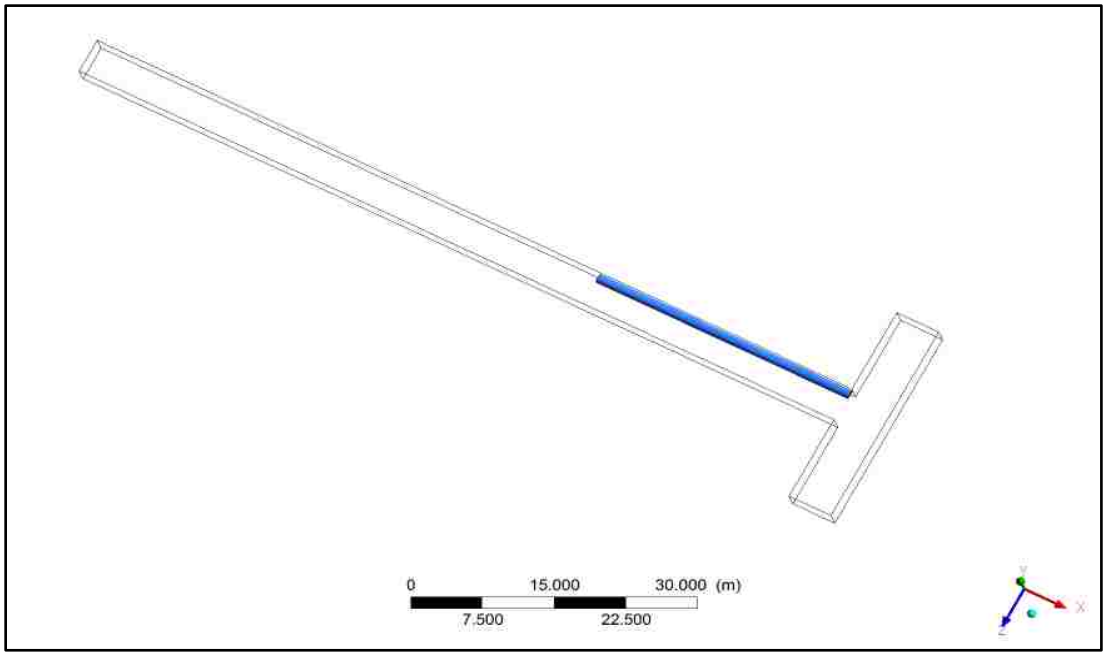

Computational domain _60 m from face_90 m length

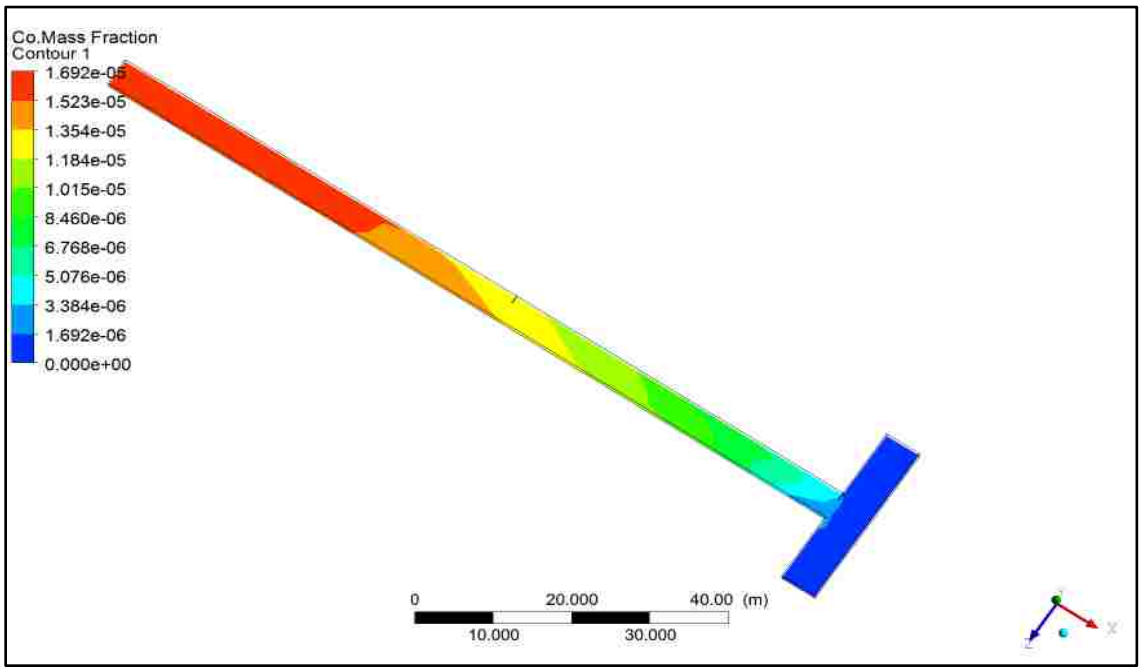

CO concentration_60m from face_100 m length

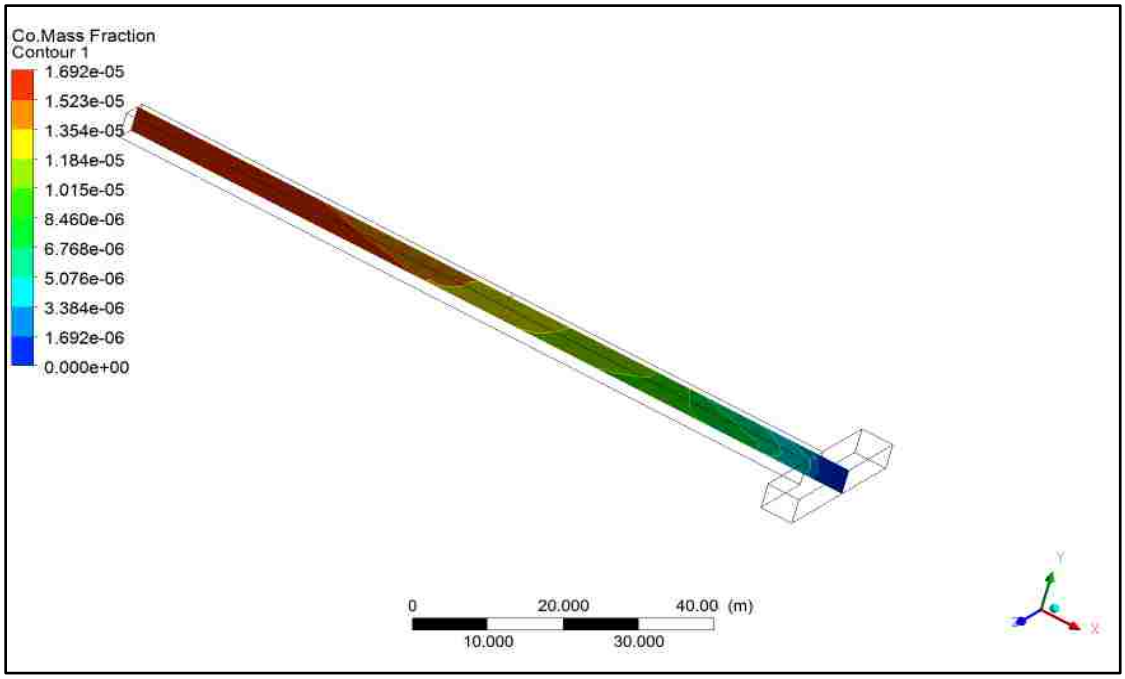

CO concentration_60m from face_100 m length

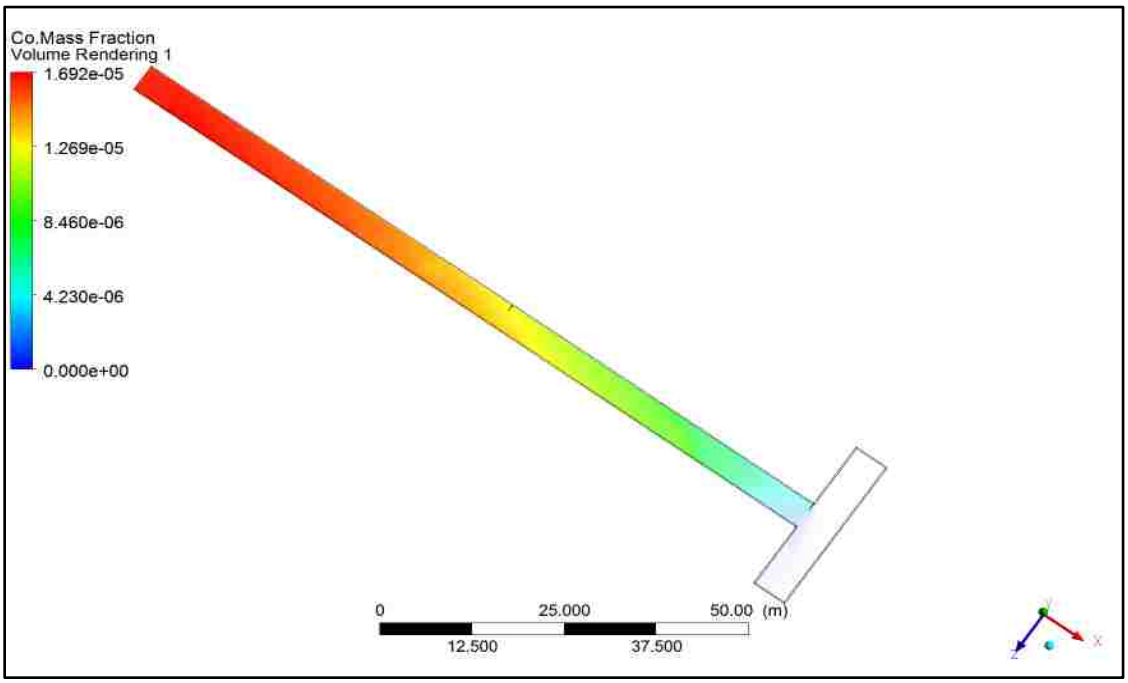

Co concentration_volume rendering_60 m from face_100 m length

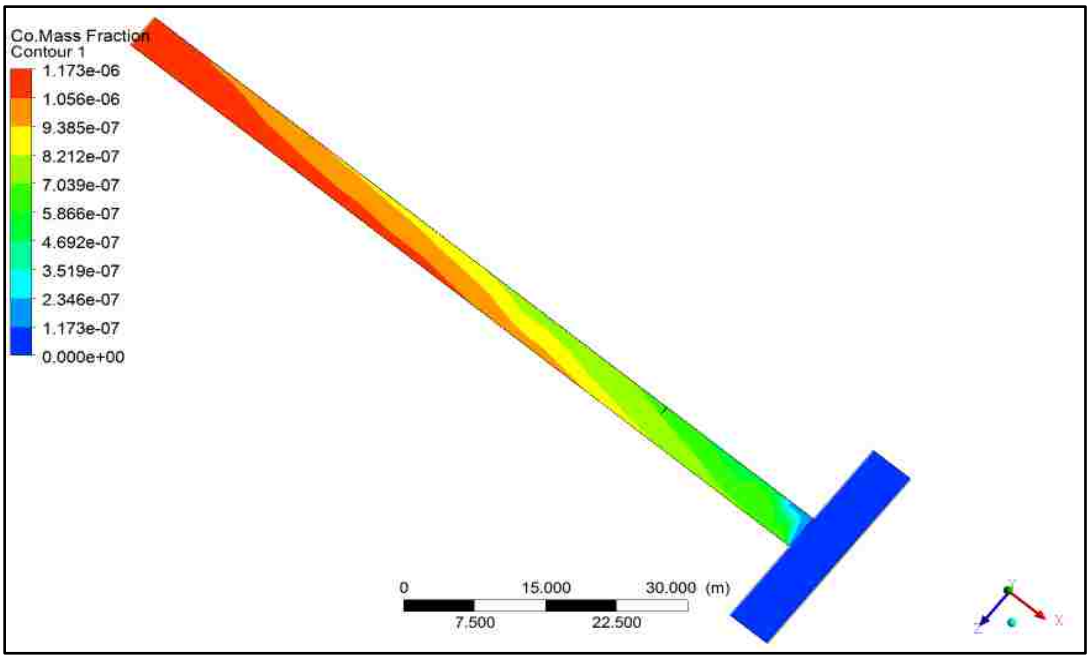

CO concentration_70m from face_90 m length

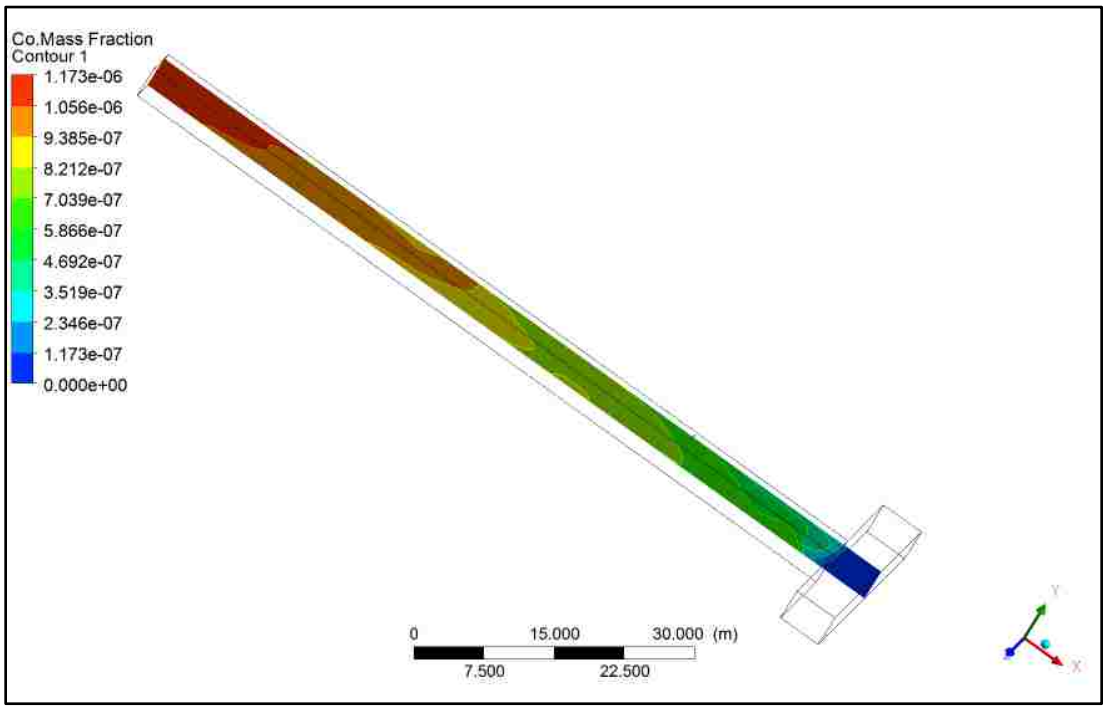

CO concentration_70 m from face_90 m length

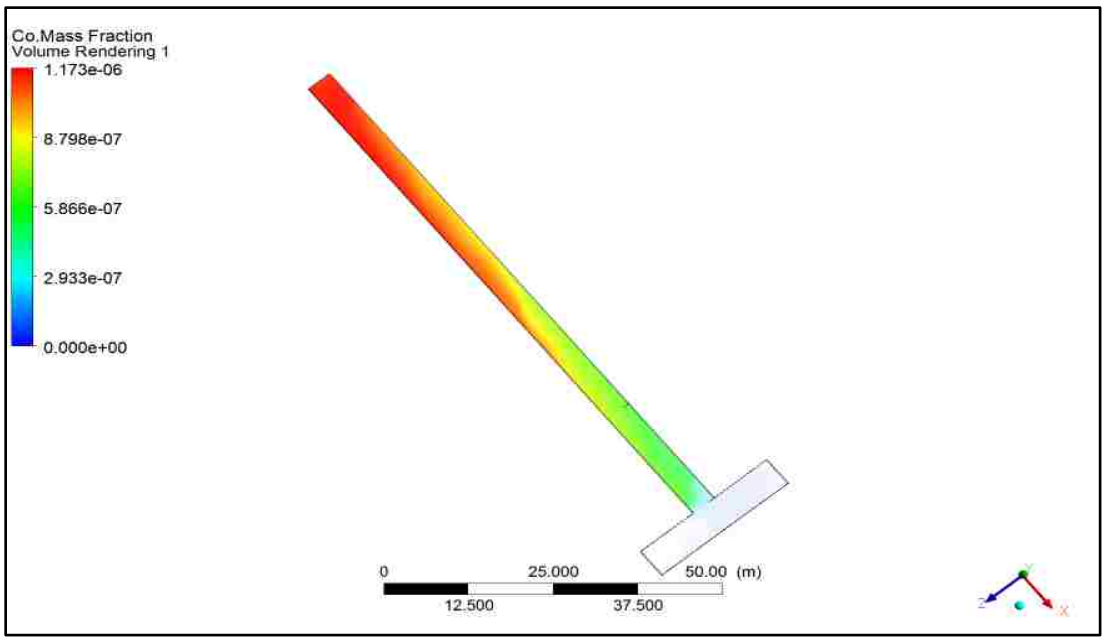

Co concentration_volume rendering_70 m from face_90 m length

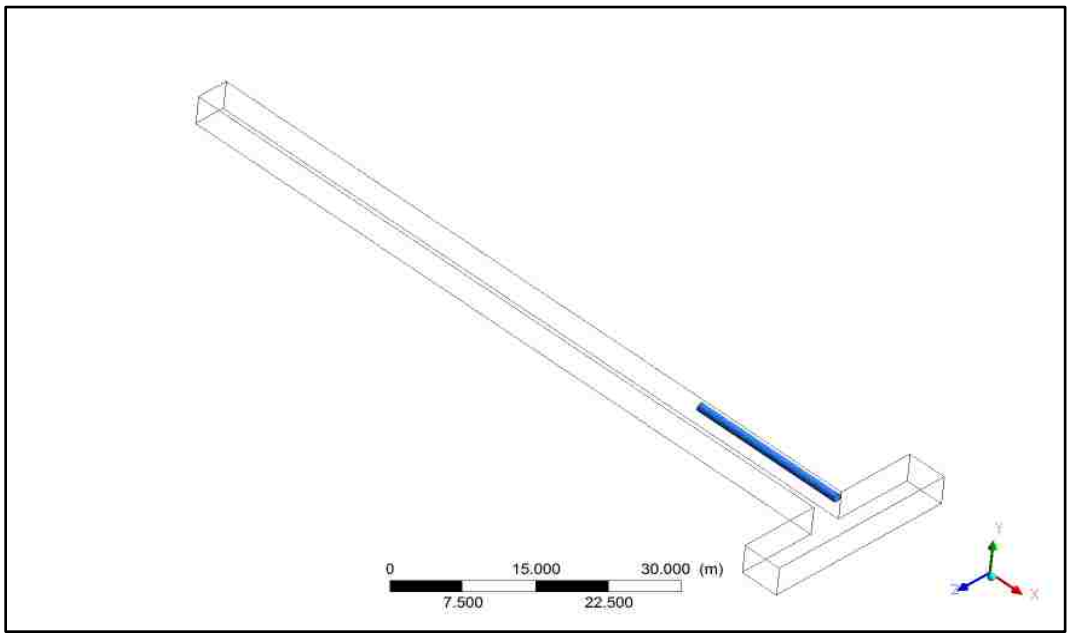

Computational domain_ 70m from face_90 m length

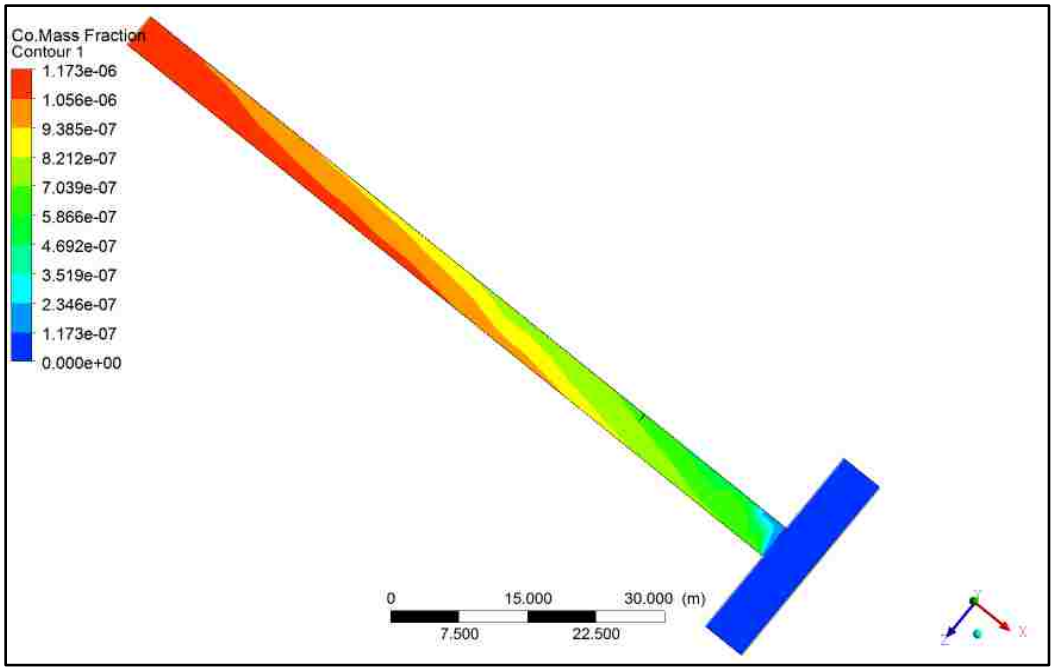

CO concentration_70m from face_100 m length

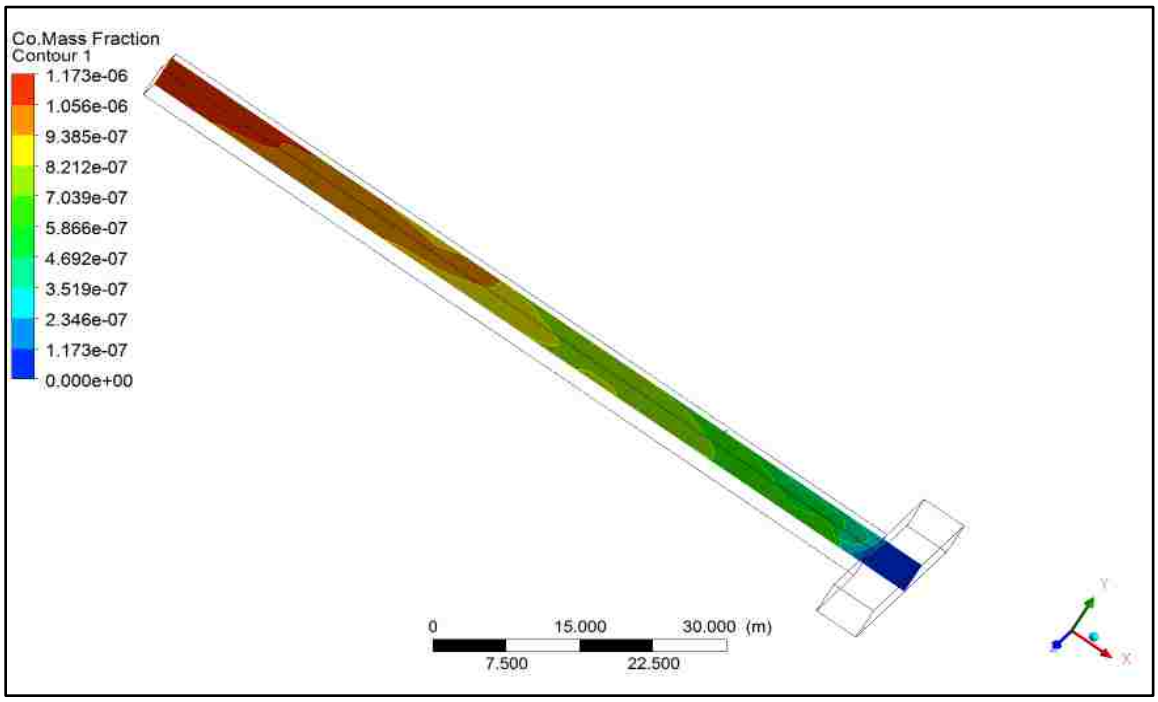

CO concentration_70m from face_100 m length

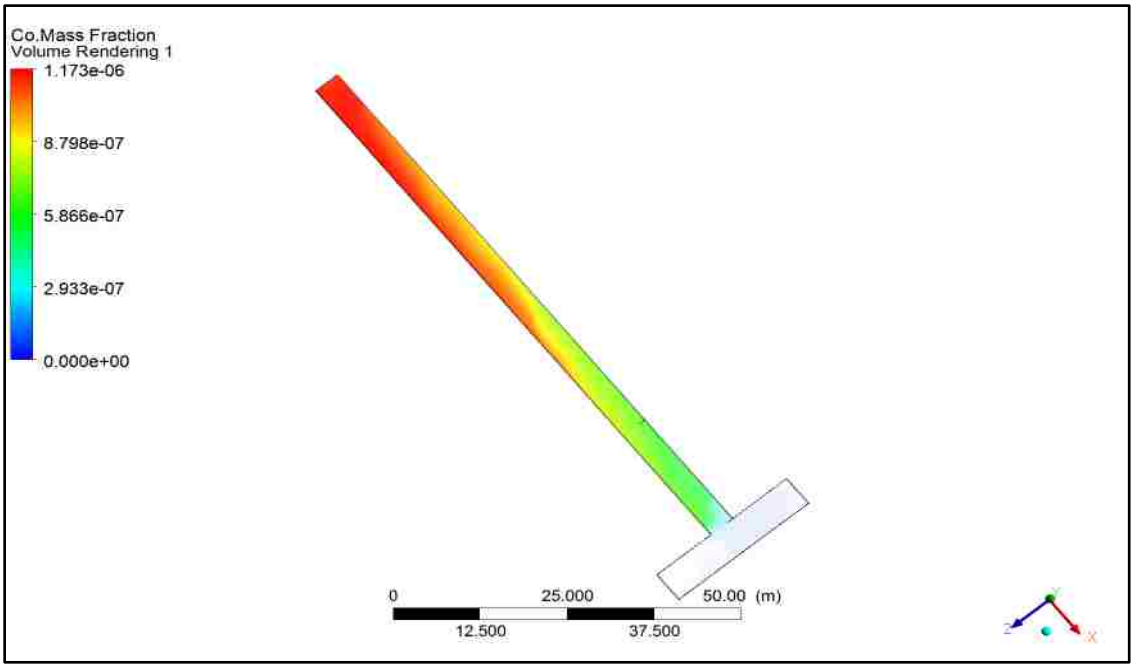

Co concentration_volume rendering_70m from face_100 m length

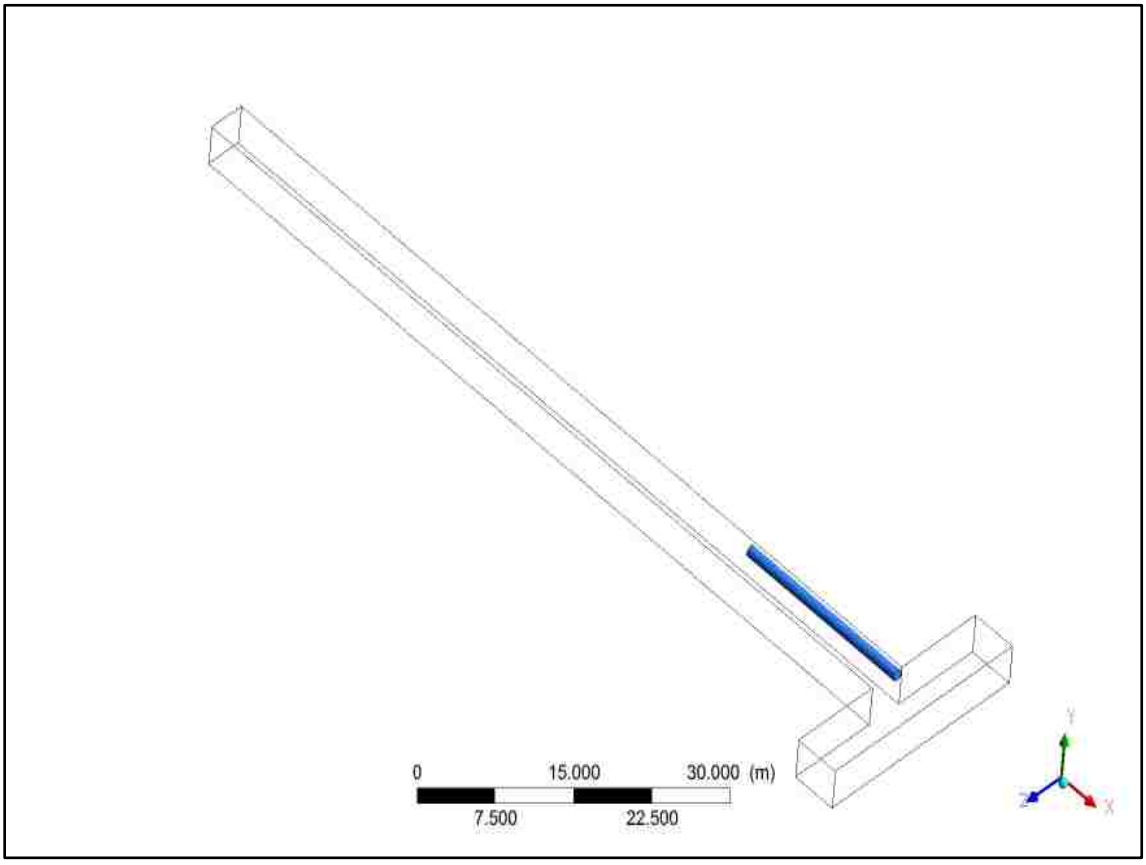

Computational domain_ 70m from face_110 m length

APPENDIX B

OPTIMAL AIR QUANTITIES

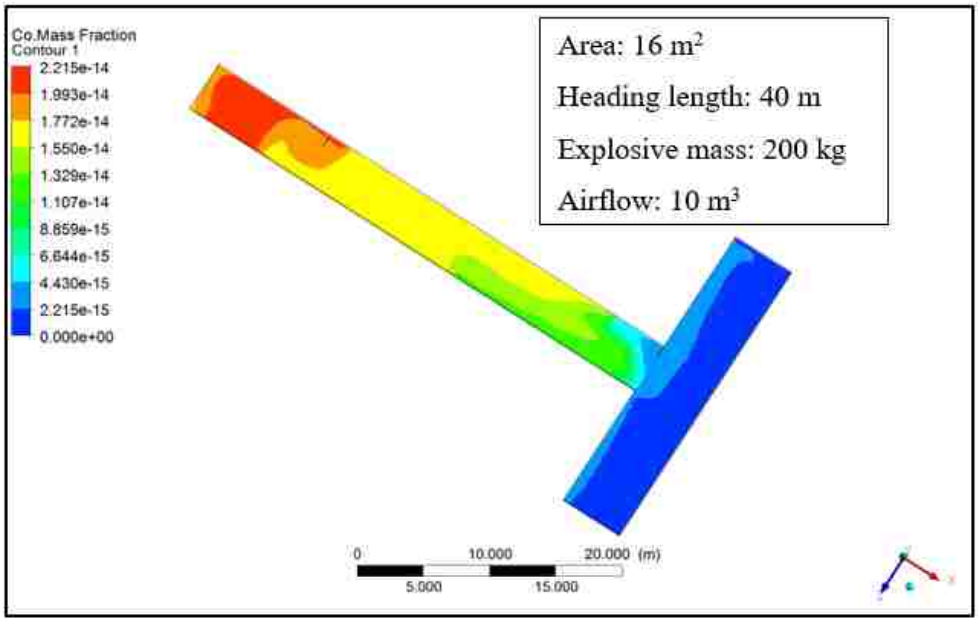

CO Concentration_ 16 m^2 _200 kg_10 m^3_40 m

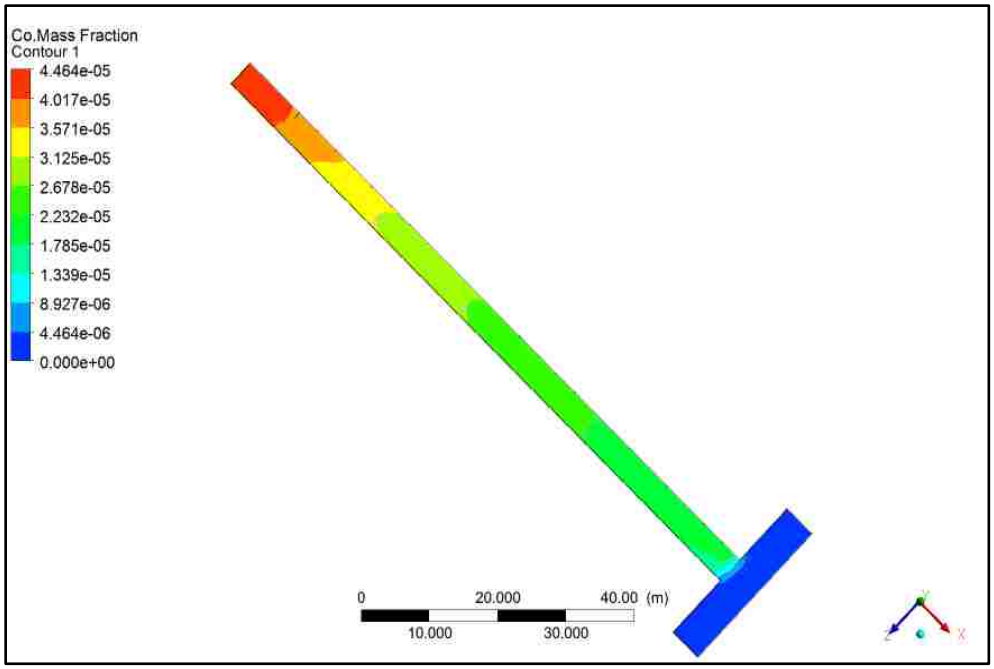

CO Concentration_ 16 m^2 _200 kg_10 m^3_100 m

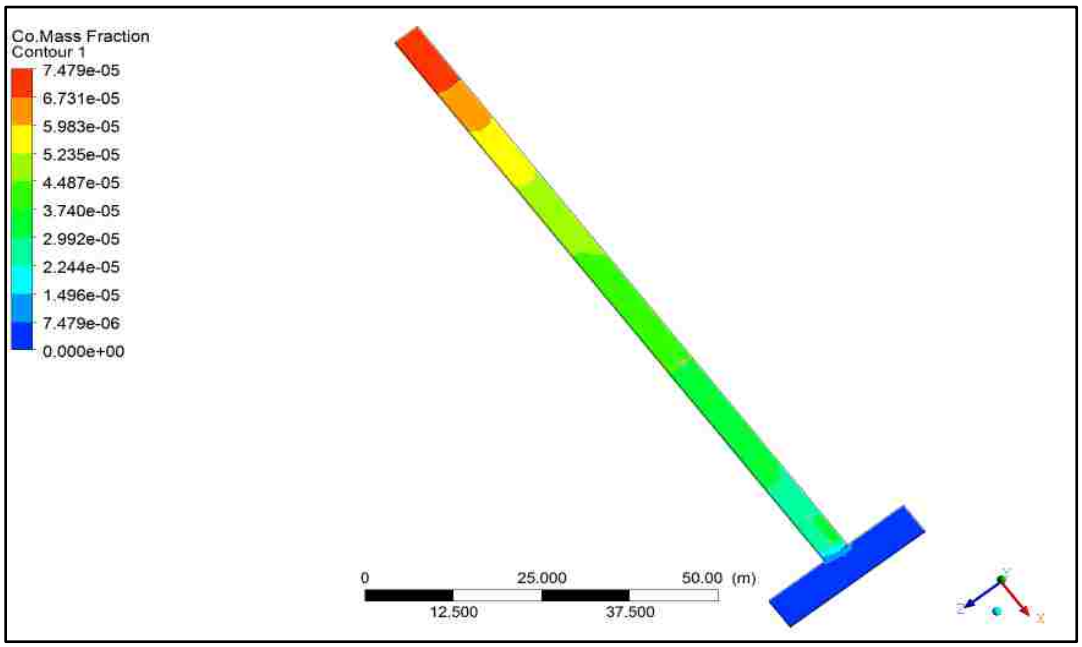

CO Concentration_ 16 m^2 _300 kg_10 m^3_100 m

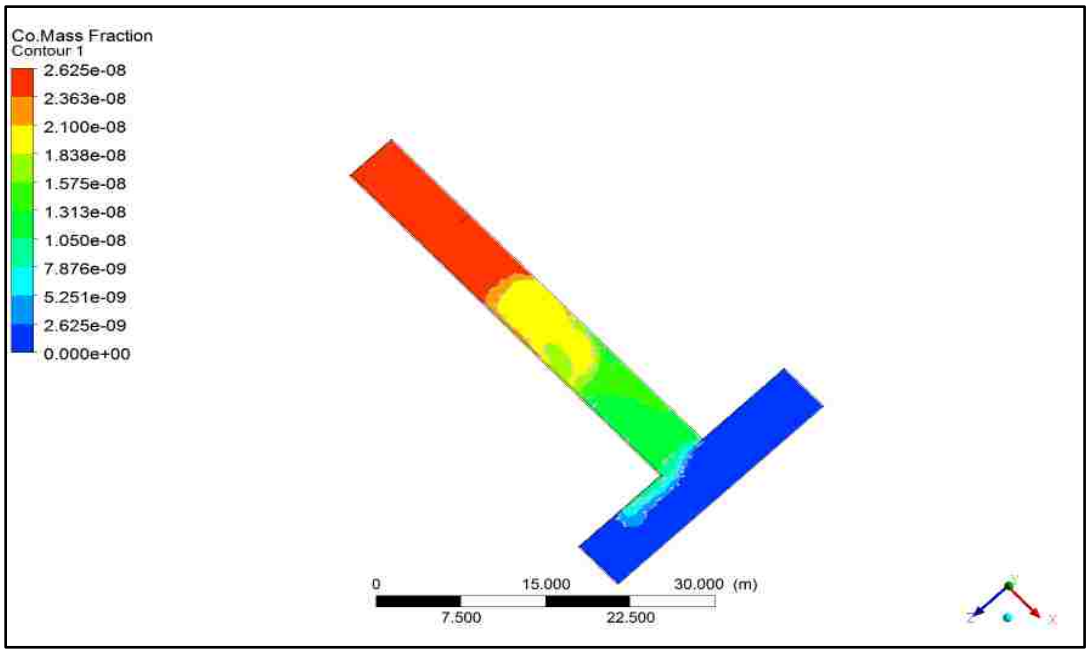

CO Concentration_ 25 m^2 _200 kg_10 m^3_40 m

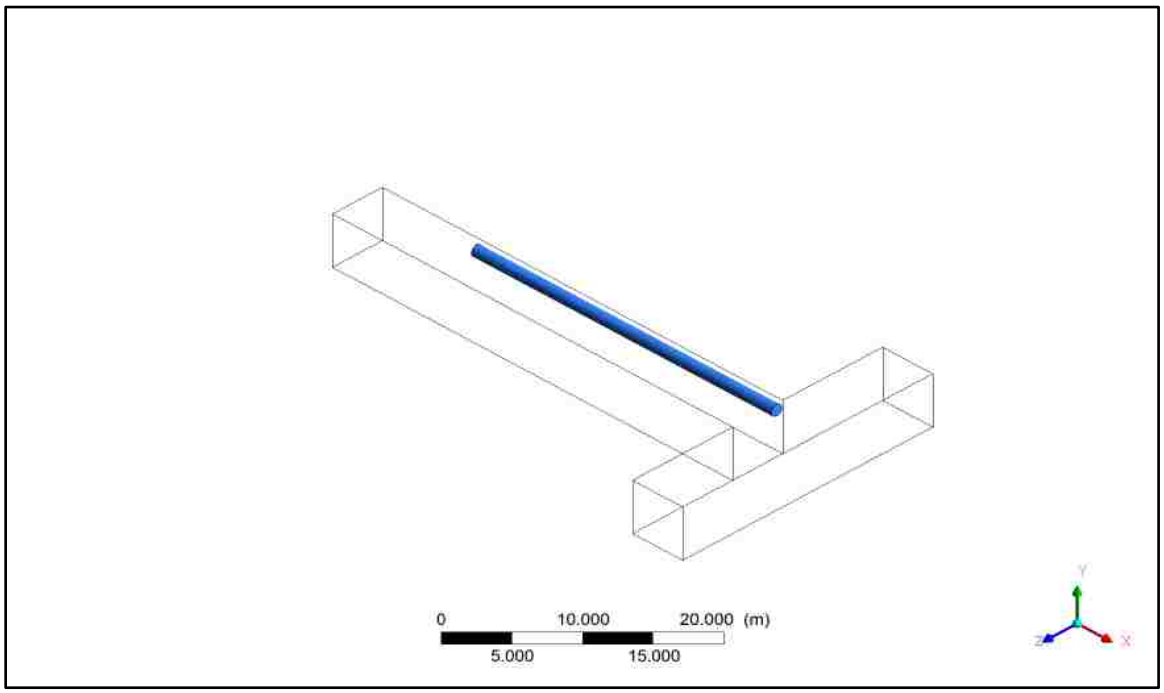

Computational domain_10 from face_40 m length

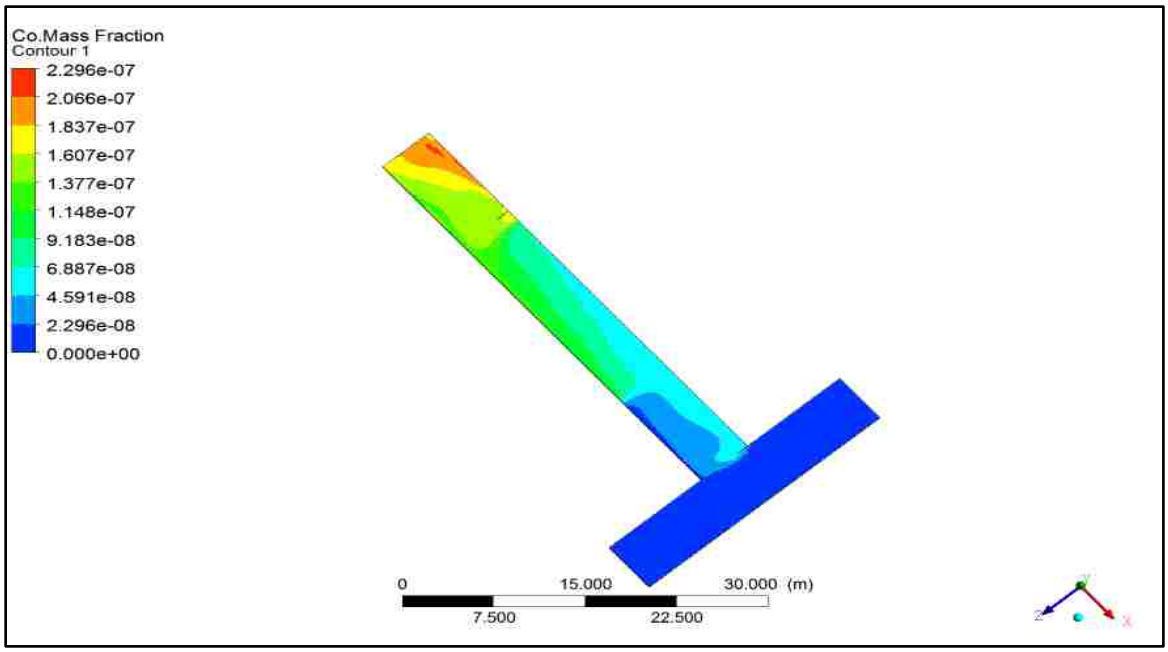

CO Concentration_ 25 m^2 _300 kg_10 m^3_40 m

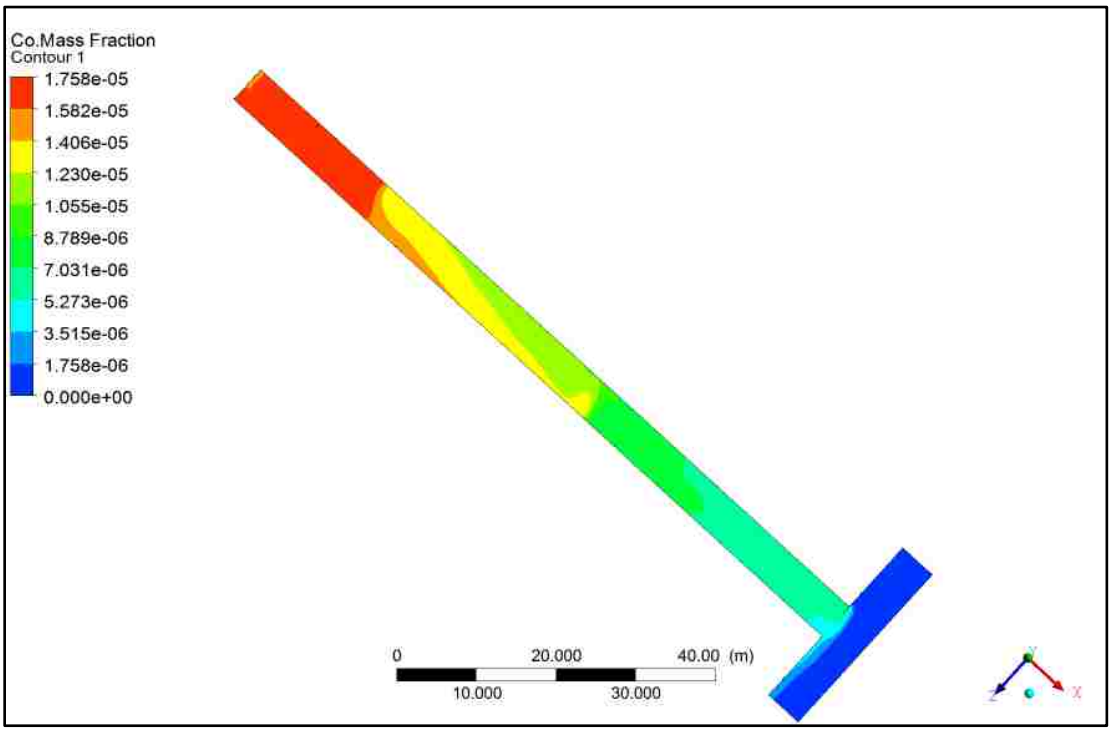

CO Concentration_ 25 m^2 _200 kg_10 m^3_100 m

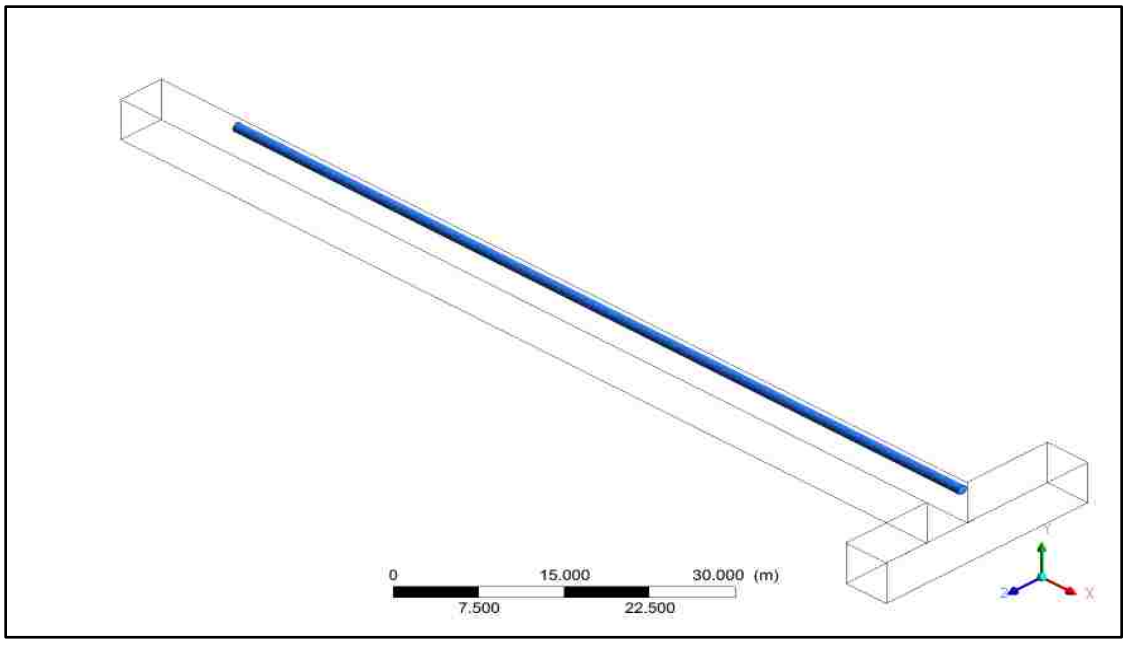

Computational domain _100 m length

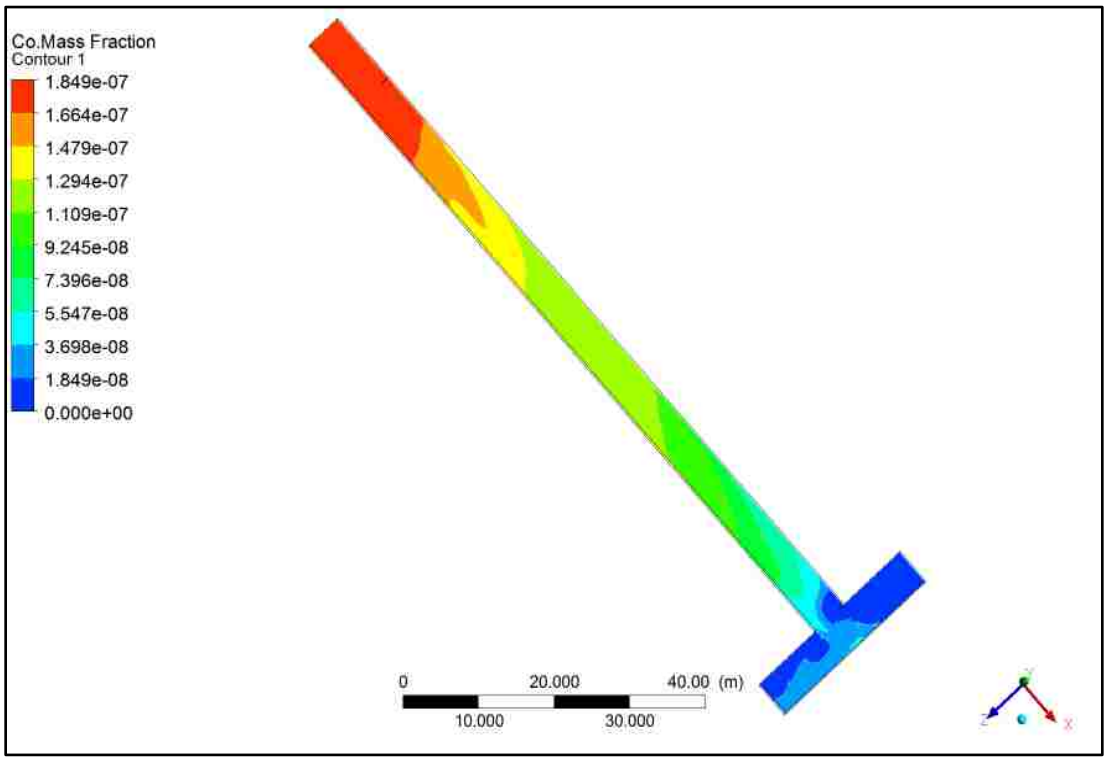

CO Concentration_ 25 m^2 _200 kg_20 m^3_100 m

APPENDIX C

EXPERIMENTATION AND VALIDATION

Technical Specs

Item	Certifed Pre-Owned Single Gas Detector	Battery Life	2600 hr.
Gas Type	CO	Display	Graphical LCD
Detects	Carbon Monoxide	Interchangeable Sensors	Yes
Sensor Range	0 to 1500 ppm	Height	3-45/64"
Resolution	1 ppm	Width	2"
Housing Color	Black	Depth	1-1/8"
Operating Temp. Range	-40 Degrees to 60 Degrees C (-40 Degrees to 140 Degrees F)	Standards	UL and cUL - Class I, Div 1, Groups A, B, C, D; T4-Class I, Zone 0, AEx ia IIC T4
Alarm Setting	Adjustable	Features	User-Adjustable TWA and STEL Alarms, Datalogging, DS2 Docking Station(TM) Compatible, Display Backlight, Four-Button Operation, Water Resistance, Event-Logging, Top Mounted Sensor
Alarm Type	Audible (95dB), Visual, Vibrating		
Battery Type	CR2 Lithium	Includes	Battery

Technical Specs

Item	Datalink Cable	Features	Instantly Download Alarm Events And Instrument Details, PC Via USB Interface
Power Source	120VAC	For Use With	PC Based Software Package And Monitors 6NE60 to 6NE65

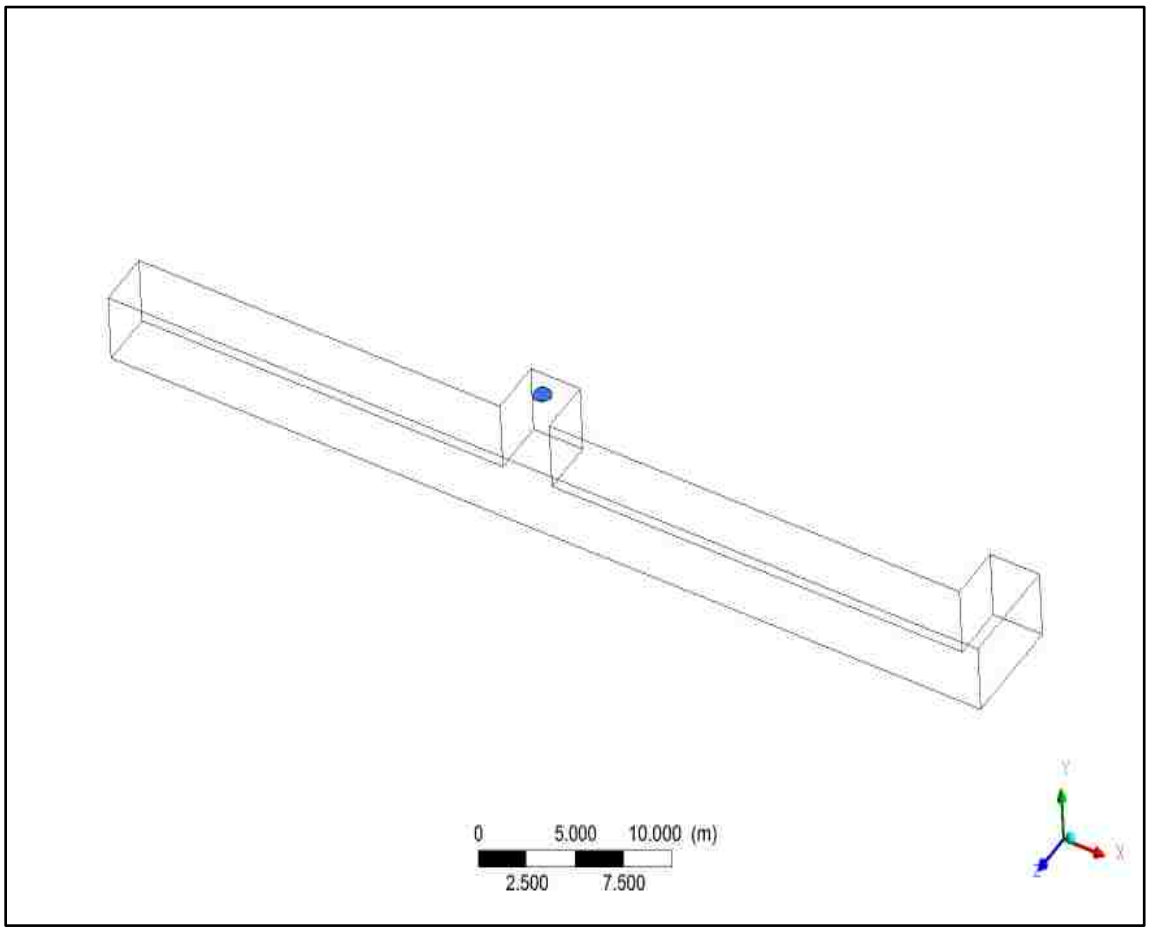

50 m length drive

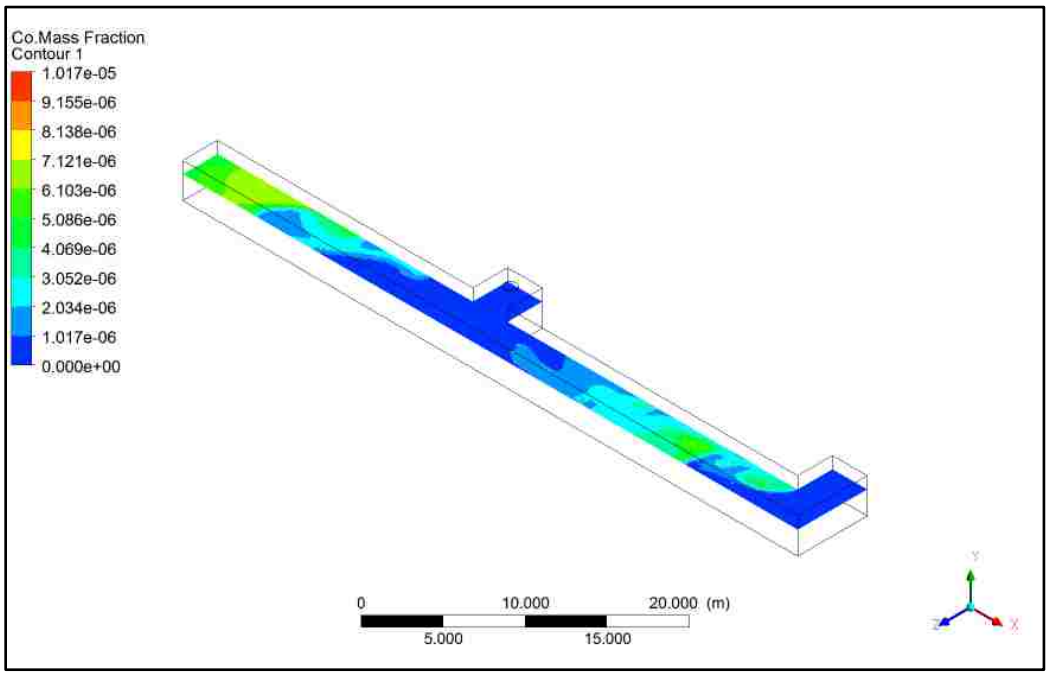
Co.Mass Fraction
Contour 1
1.017e-05
9.155e-06
8.138e-06
7.121e-06
6.103e-06
5.086e-06
4.069e-06
3.052e-06
2.034e-06
1.017e-06
0.000e+00
0
10.000
20.000 (m)
5.000
15.000
Y
Z
X

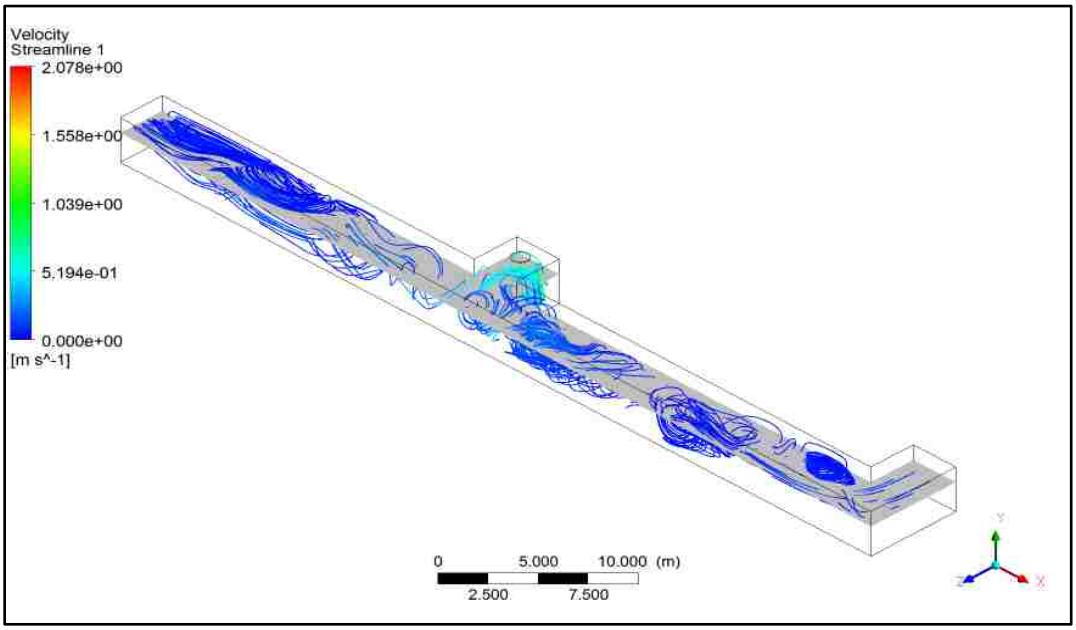
Velocity
Streamline 1
2.078e+00
1.558e+00
1.039e+00
5.194e-01
0.000e+00
[m s^-1]
0
5.000
10.000 (m)
2.500
7.500
Y
Z
X

100 kg_2.5 m^3/s

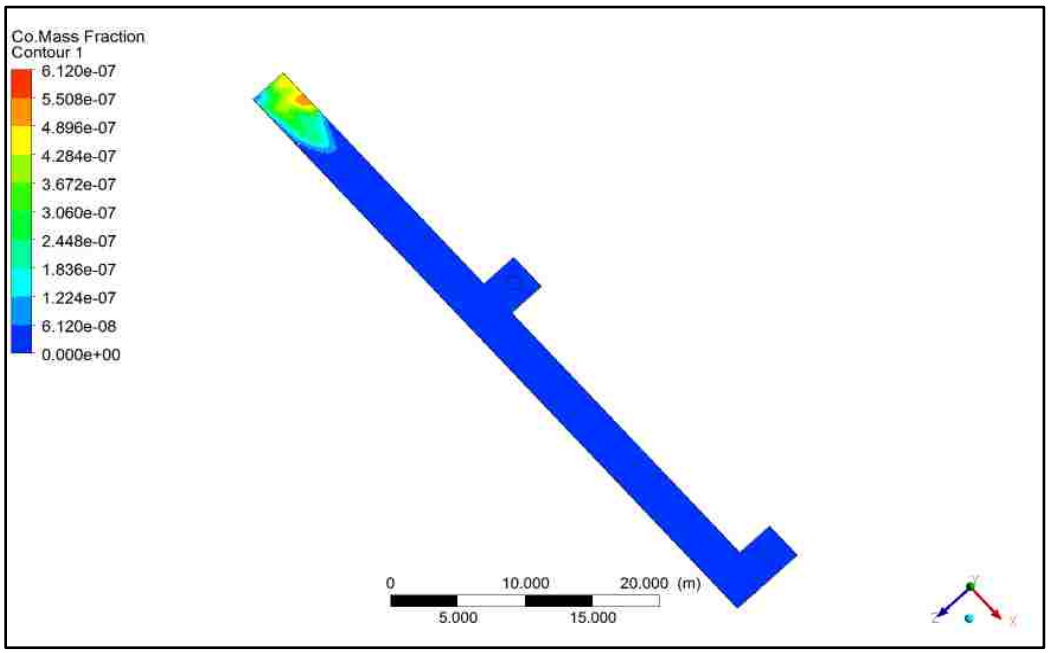
Co.Mass Fraction
Contour 1
6.120e-07
5.508e-07
4.896e-07
4.284e-07
3.672e-07
3.060e-07
2.448e-07
1.836e-07
1.224e-07
6.120e-08
0.000e+00
0
10.000
20.000 (m)
5.000
15.000

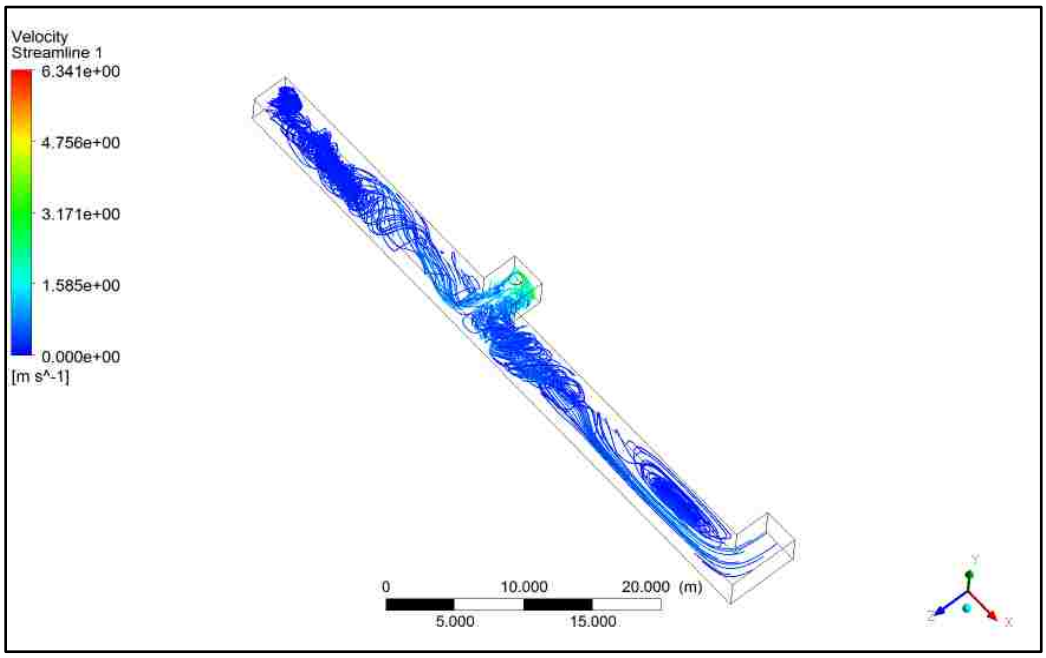
Velocity
Streamline 1
6.341e+00
4.756e+00
3.171e+00
1.585e+00
0.000e+00
[m s^-1]
0
10.000
20.000 (m)
5.000
15.000

100 kg_5 m^3/s

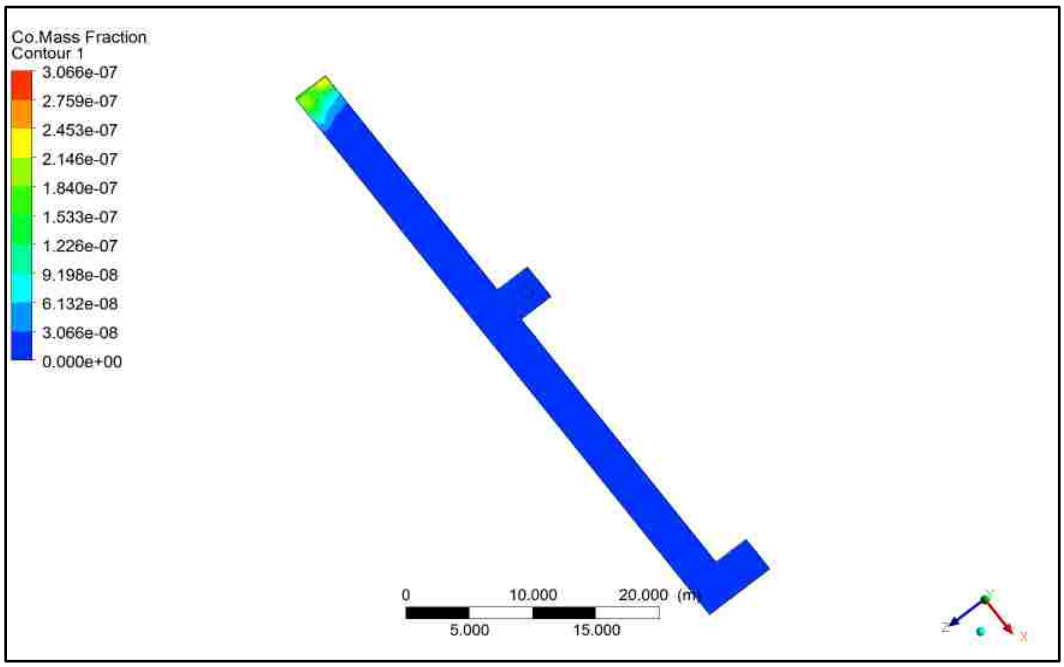
Co.Mass Fraction
Contour 1
3.066e-07
2.759e-07
2.453e-07
2.146e-07
1.840e-07
1.533e-07
1.226e-07
9.198e-08
6.132e-08
3.066e-08
0.000e+00
0
10.000
20.000 (m)
5.000
15.000

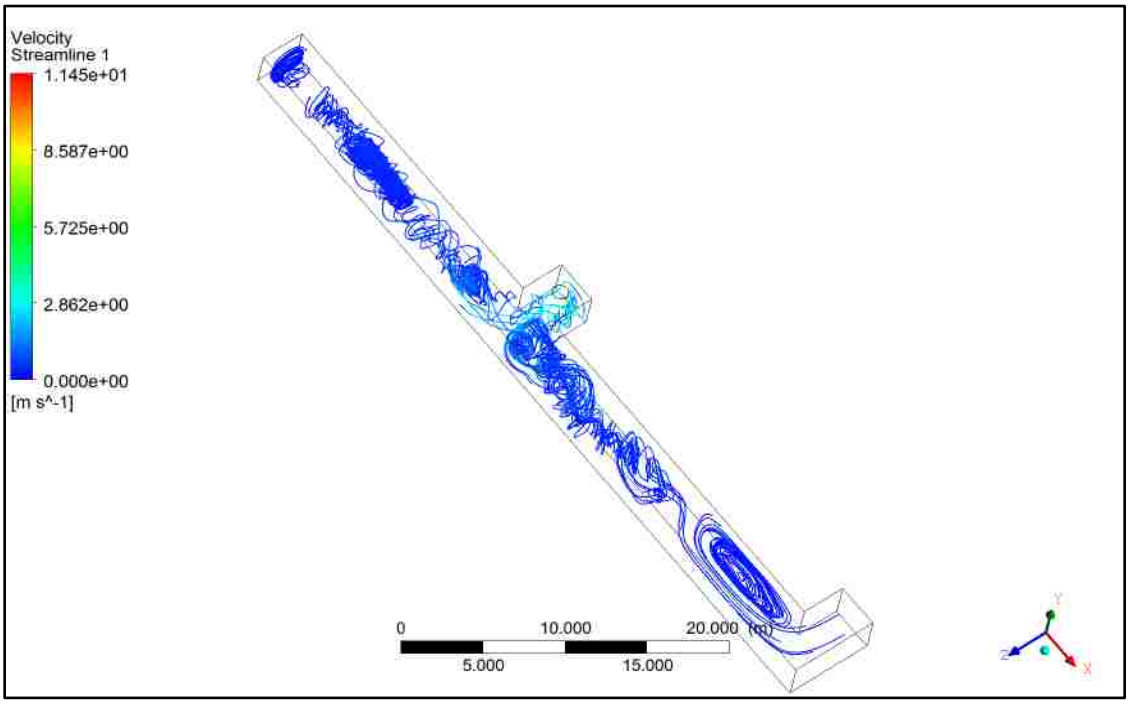
Velocity
Streamline 1
1.145e+01
8.587e+00
5.725e+00
2.862e+00
0.000e+00
[m s^-1]
0
10.000
20.000 (m)
5.000
15.000

100 kg_10 m^3/s

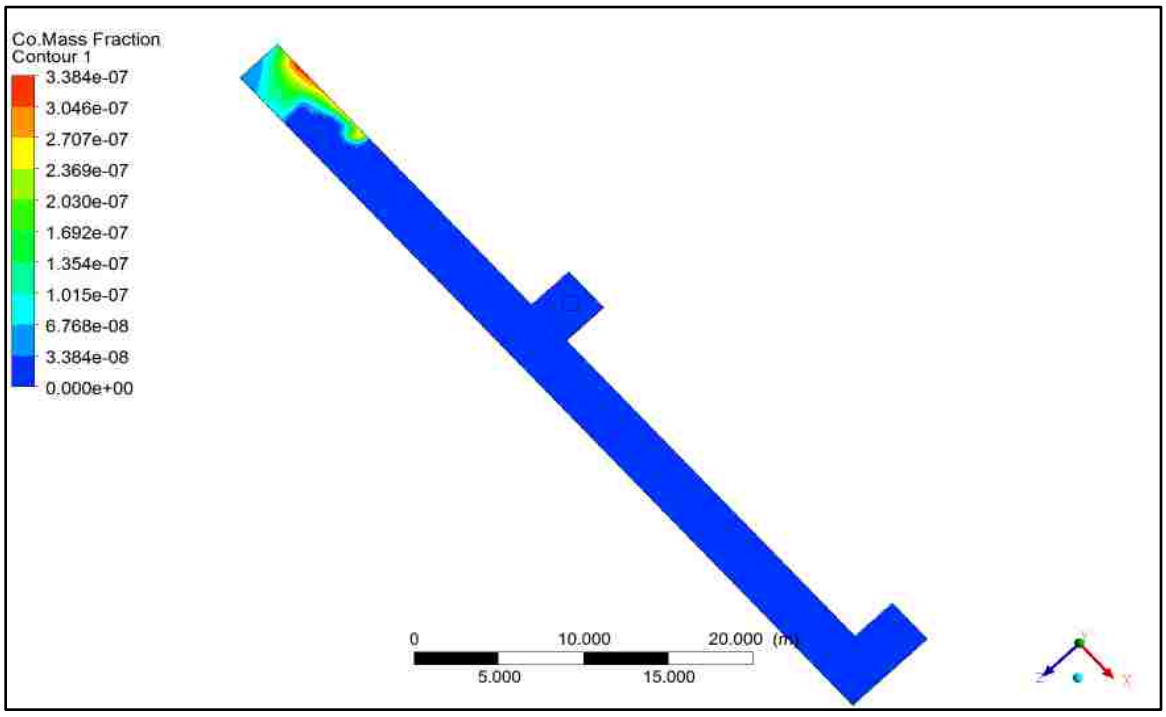
Co.Mass Fraction
Contour 1
3.384e-07
3.046e-07
2.707e-07
2.369e-07
2.030e-07
1.692e-07
1.354e-07
1.015e-07
6.768e-08
3.384e-08
0.000e+00
0
10.000
20.000 (m)
5.000
15.000

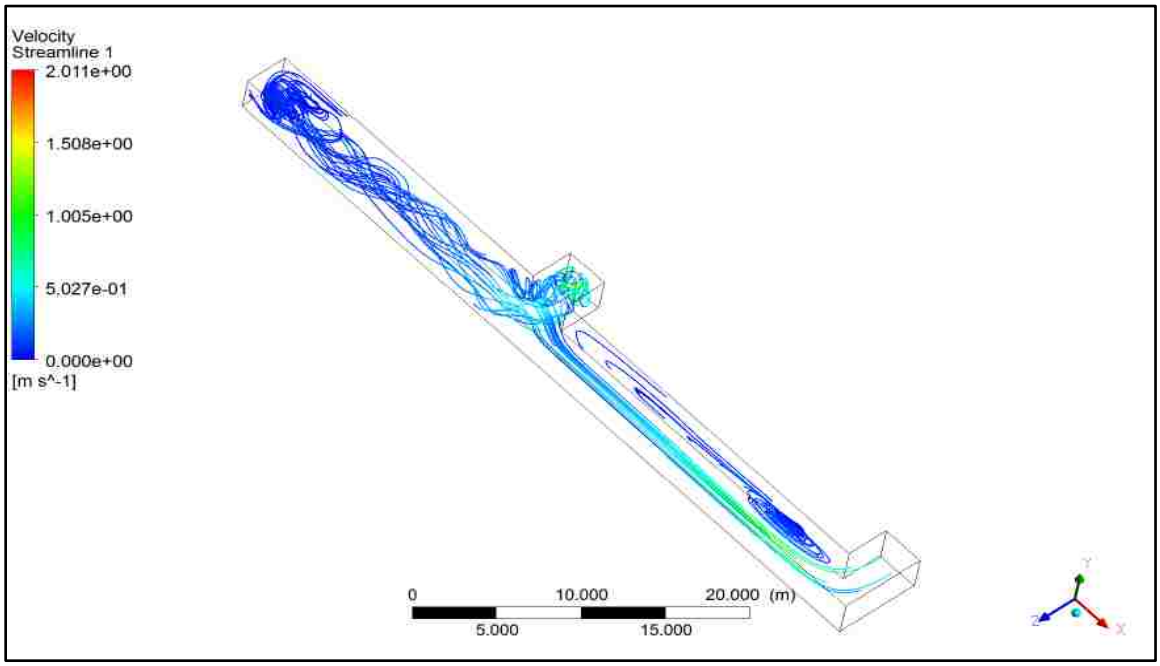
Velocity
Streamline 1
2.011e+00
1.508e+00
1.005e+00
5.027e-01
0.000e+00
[m s^-1]
0
10.000
20.000 (m)
5.000
15.000

200 kg_2.5 m^3/s

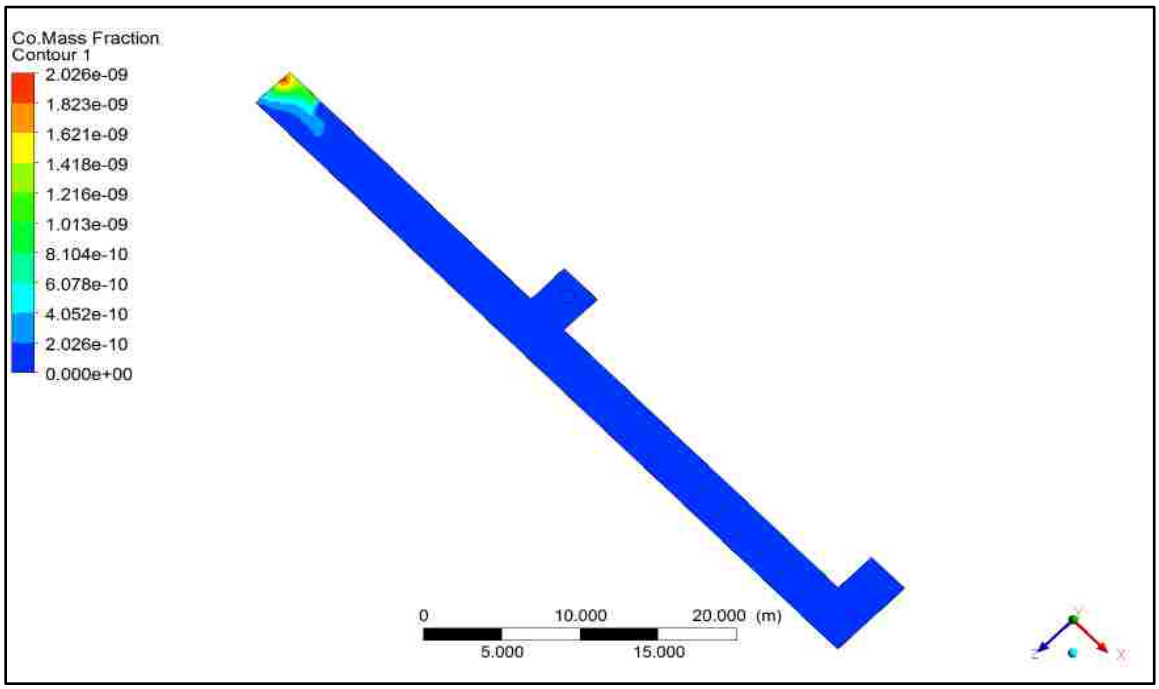
Co.Mass Fraction
Contour 1
2.026e-09
1.823e-09
1.621e-09
1.418e-09
1.216e-09
1.013e-09
8.104e-10
6.078e-10
4.052e-10
2.026e-10
0.000e+00
0
10.000
20.000 (m)
5.000
15.000

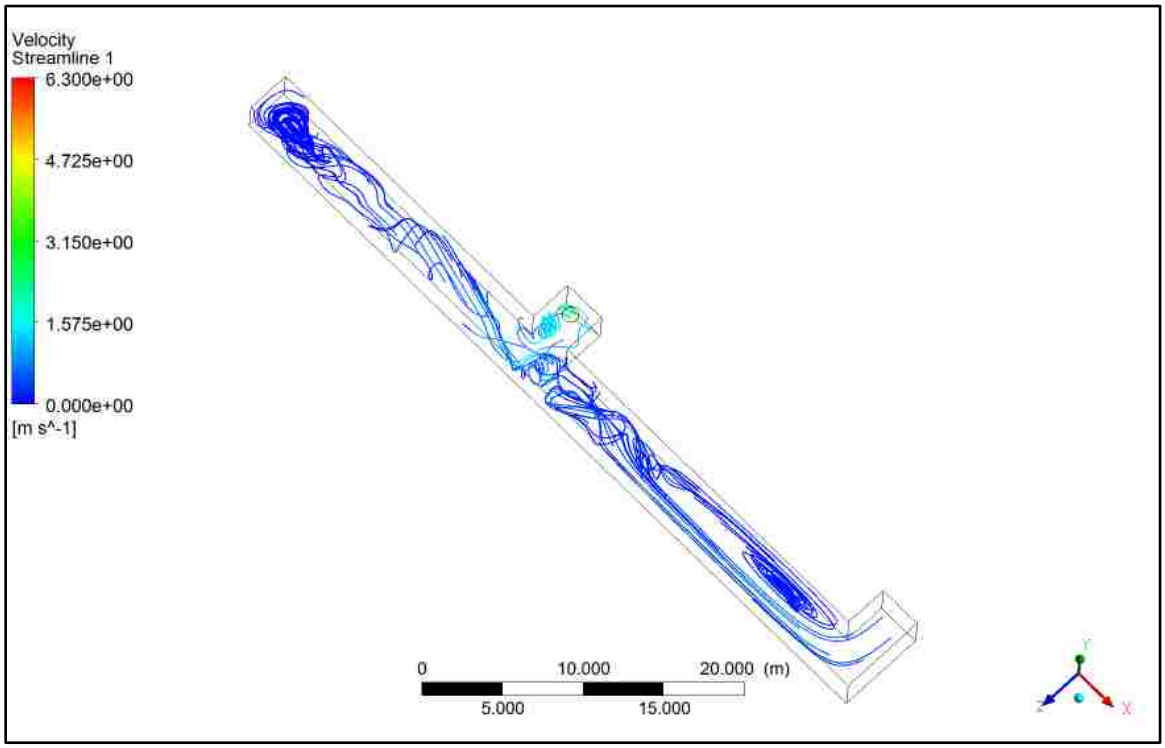
Velocity
Streamline 1
6.300e+00
4.725e+00
3.150e+00
1.575e+00
0.000e+00
[m s^-1]
0
10.000
20.000 (m)
5.000
15.000

200 kg_5 m^3/s

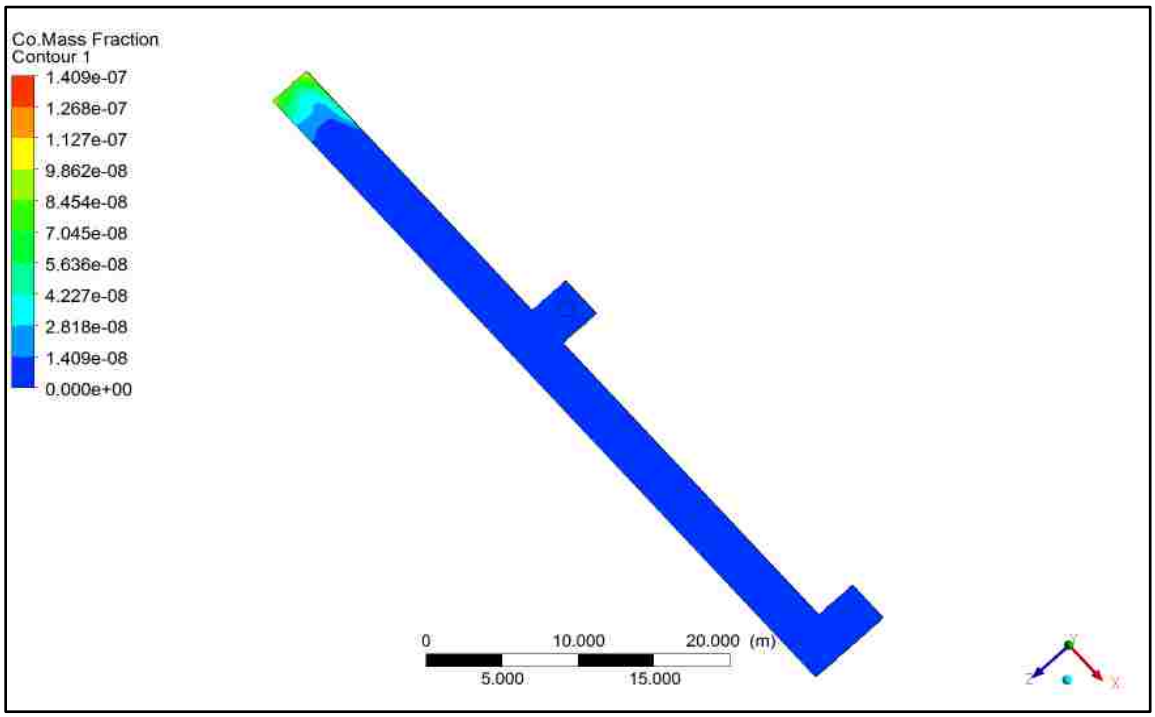
Co.Mass Fraction
Contour 1
1.409e-07
1.268e-07
1.127e-07
9.862e-08
8.454e-08
7.045e-08
5.636e-08
4.227e-08
2.818e-08
1.409e-08
0.000e+00
0
10.000
20.000 (m)
5.000
15.000

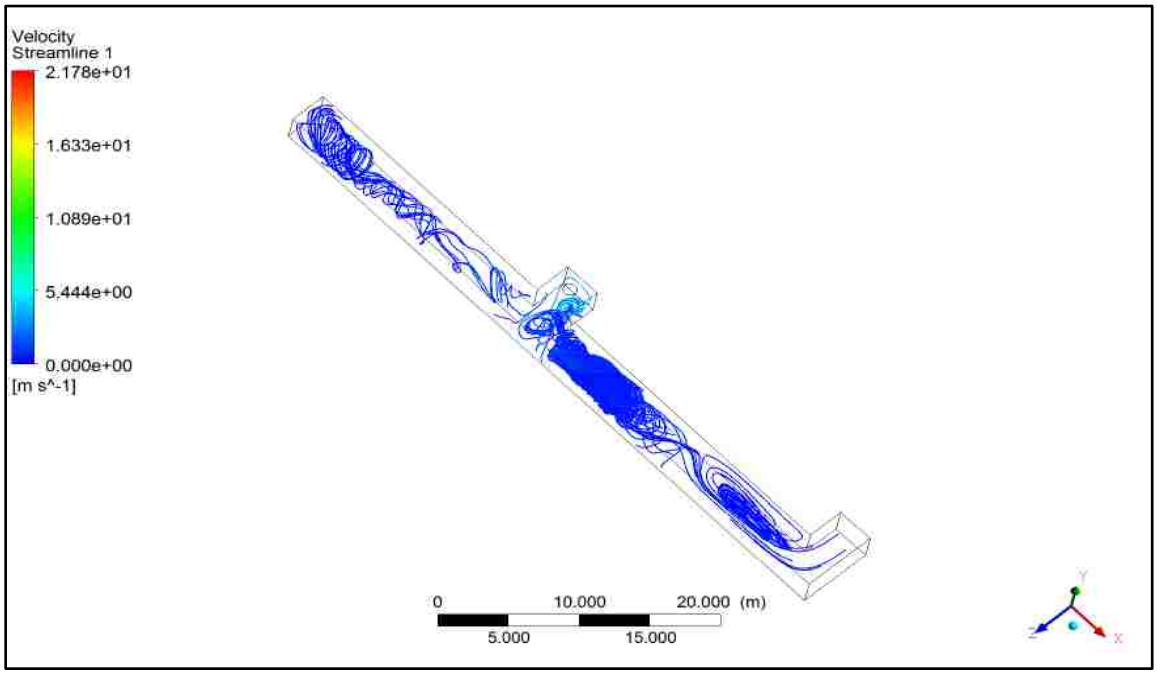
Velocity
Streamline 1
2.178e+01
1.633e+01
1.089e+01
5.444e+00
0.000e+00
[m s^-1]
0
10.000
20.000 (m)
5.000
15.000

200 kg_10 m^3/s

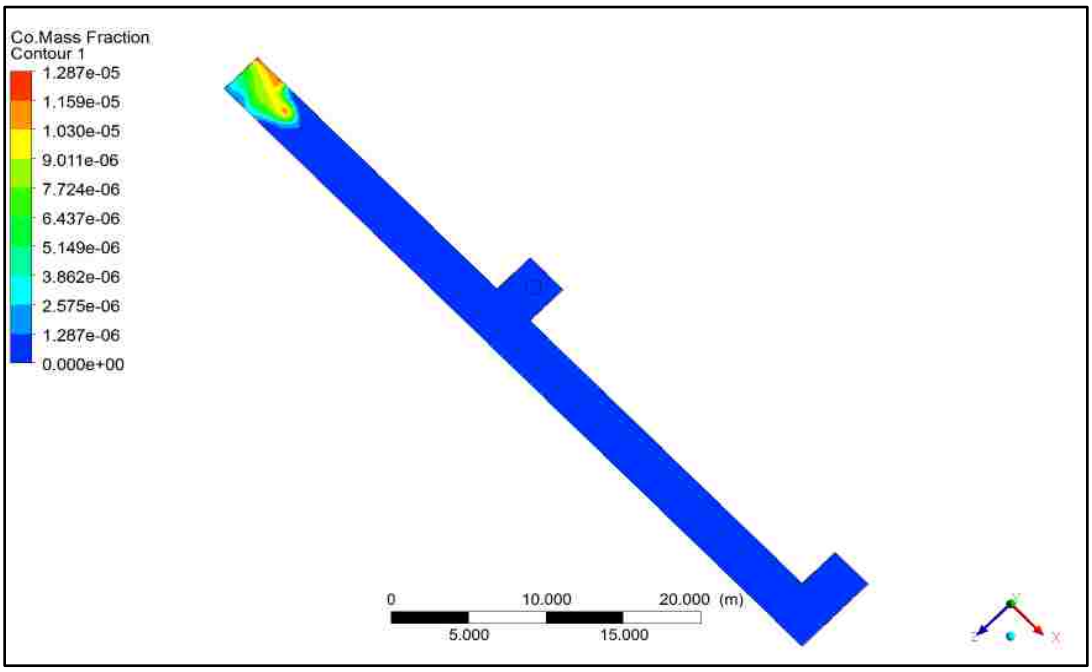
Co.Mass Fraction
Contour 1
1.287e-05
1.159e-05
1.030e-05
9.011e-06
7.724e-06
6.437e-06
5.149e-06
3.862e-06
2.575e-06
1.287e-06
0.000e+00
0
10.000
20.000 (m)
5.000
15.000

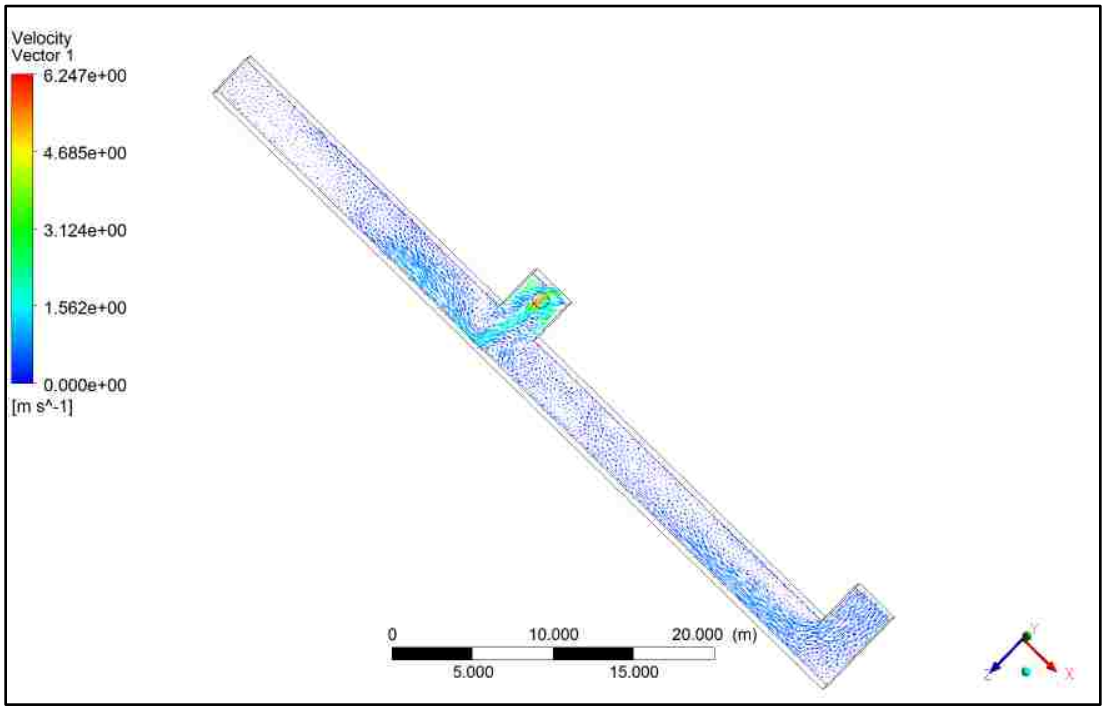
Velocity
Vector 1
6.247e+00
4.685e+00
3.124e+00
1.562e+00
0.000e+00
[m s^-1]
0
10.000
20.000 (m)
5.000
15.000

300 kg_2.5 m^3/s

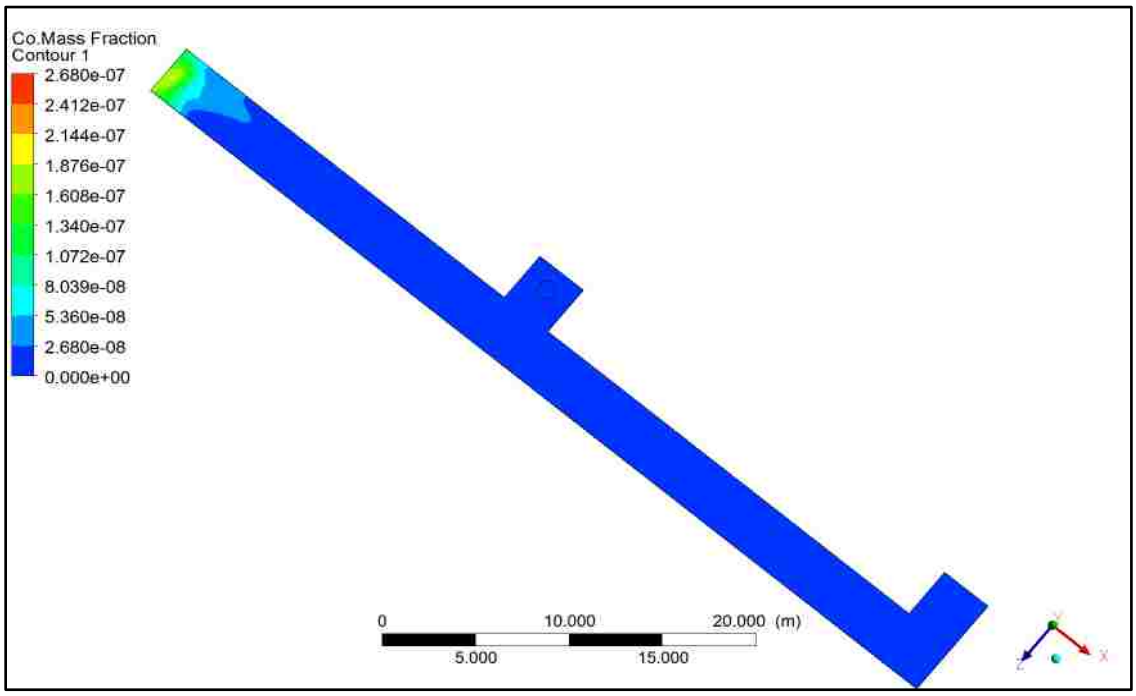
Co.Mass Fraction
Contour 1
2.680e-07
2.412e-07
2.144e-07
1.876e-07
1.608e-07
1.340e-07
1.072e-07
8.039e-08
5.360e-08
2.680e-08
0.000e+00
0
10.000
20.000 (m)
5.000
15.000

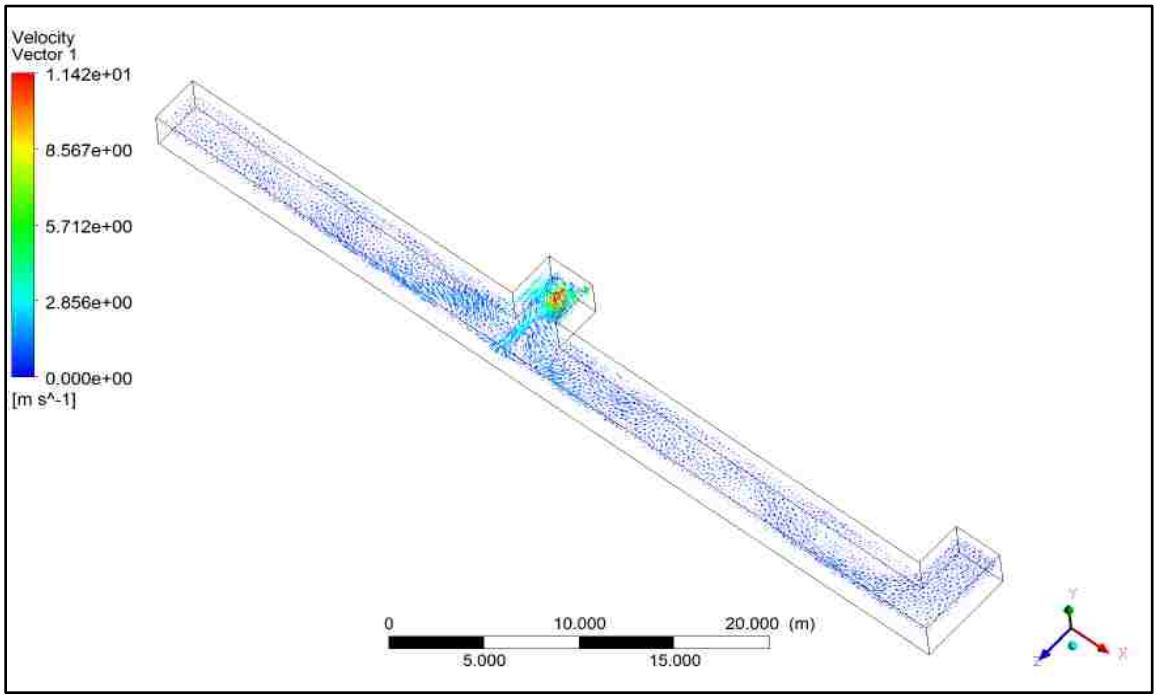
Velocity
Vector 1
1.142e+01
8.567e+00
5.712e+00
2.856e+00
0.000e+00
[m s^-1]
0
10.000
20.000 (m)
5.000
15.000

300 kg_5 m^3/s

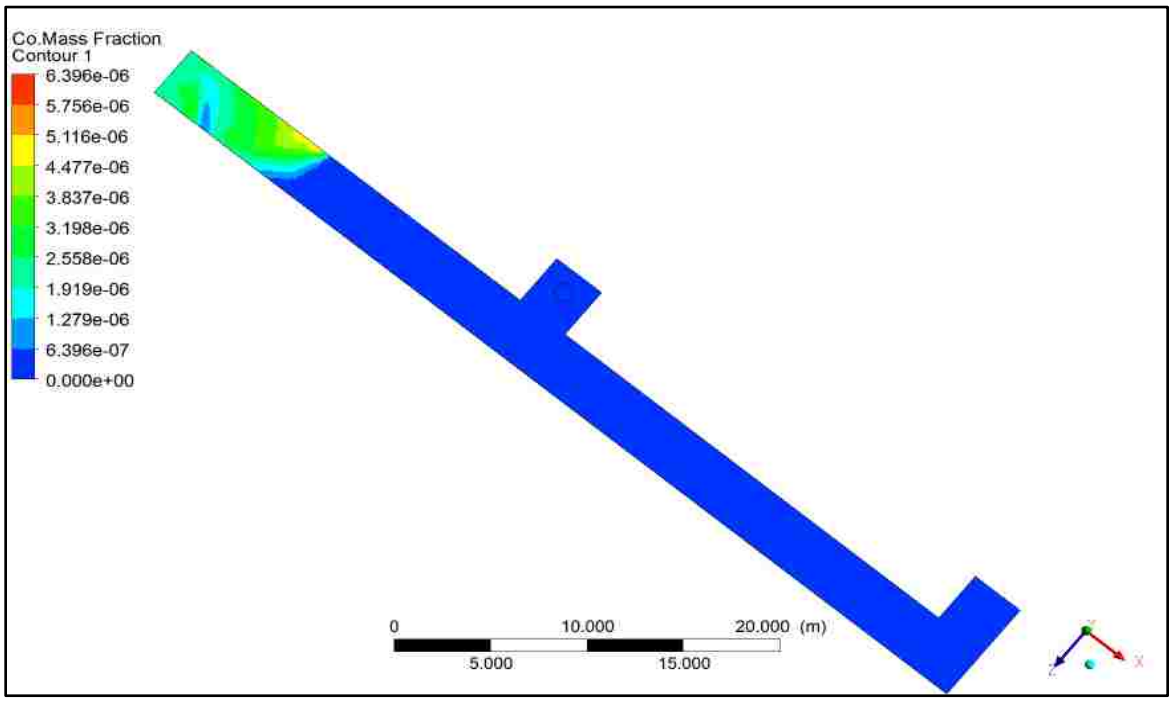
Co.Mass Fraction
Contour 1
6.396e-06
5.756e-06
5.116e-06
4.477e-06
3.837e-06
3.198e-06
2.558e-06
1.919e-06
1.279e-06
6.396e-07
0.000e+00
0
10.000
20.000 (m)
5.000
15.000

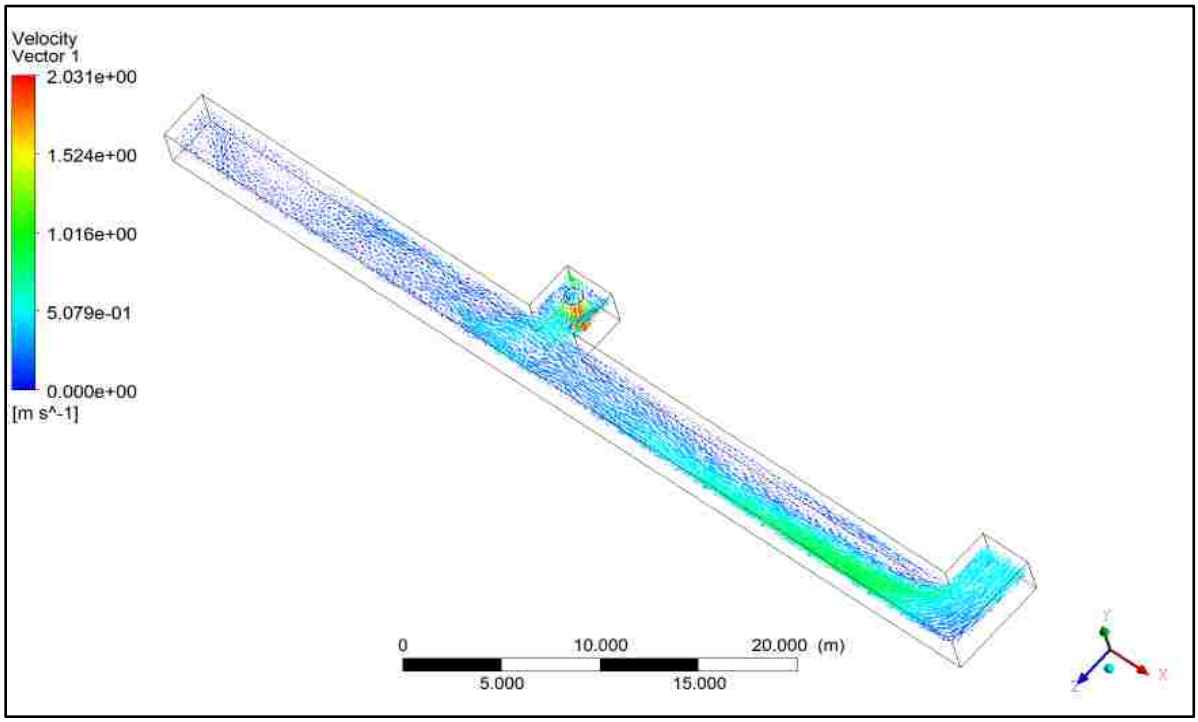
Velocity
Vector 1
2.031e+00
1.524e+00
1.016e+00
5.079e-01
0.000e+00
[m s^-1]
0
10.000
20.000 (m)
5.000
15.000

300 kg_10 m^3/s

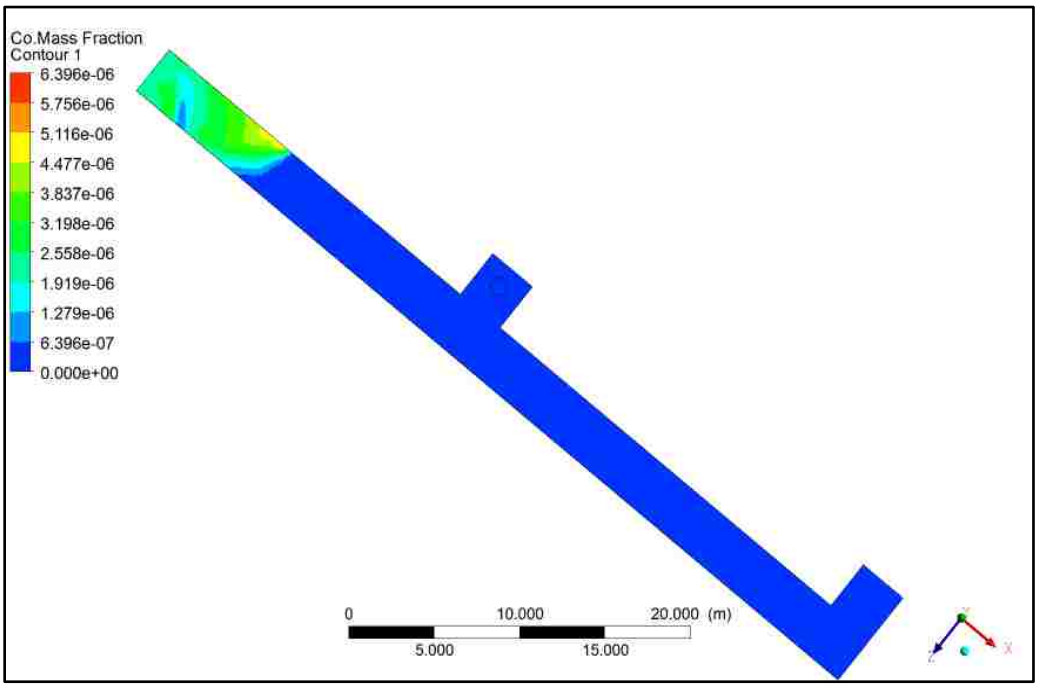
Co.Mass Fraction
Contour 1
6.396e-06
5.756e-06
5.116e-06
4.477e-06
3.837e-06
3.198e-06
2.558e-06
1.919e-06
1.279e-06
6.396e-07
0.000e+00
0
10.000
20.000 (m)
5.000
15.000

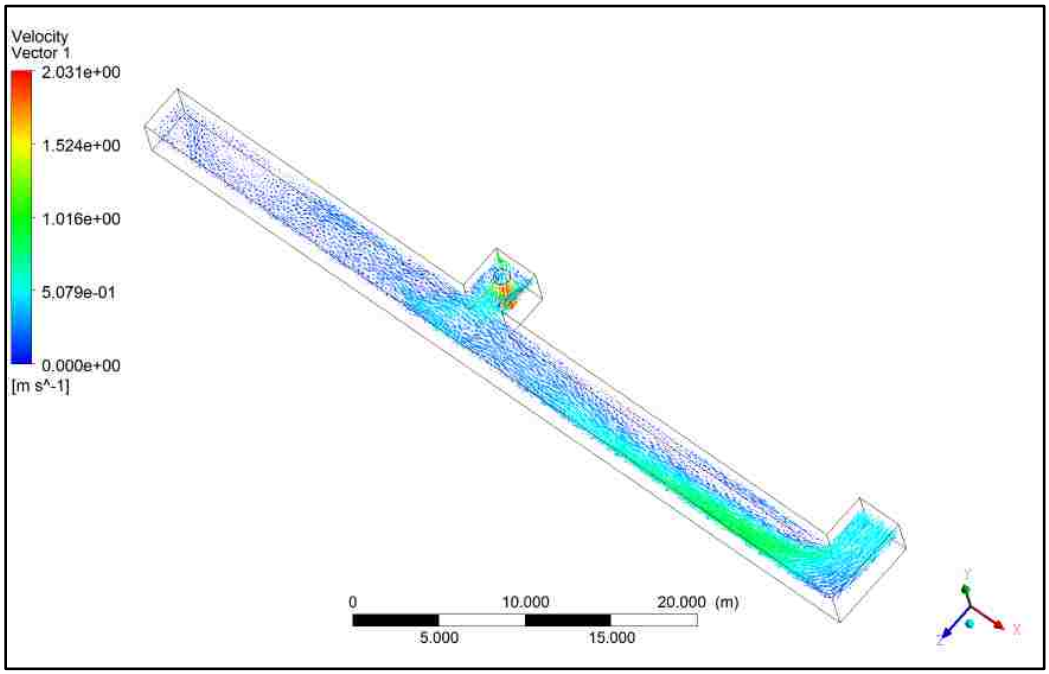
Velocity
Vector 1
2.031e+00
1.524e+00
1.016e+00
5.079e-01
0.000e+00
[m s^-1]
0
10.000
20.000 (m)
5.000
15.000

400 kg_5 m^3/s

Safe distance

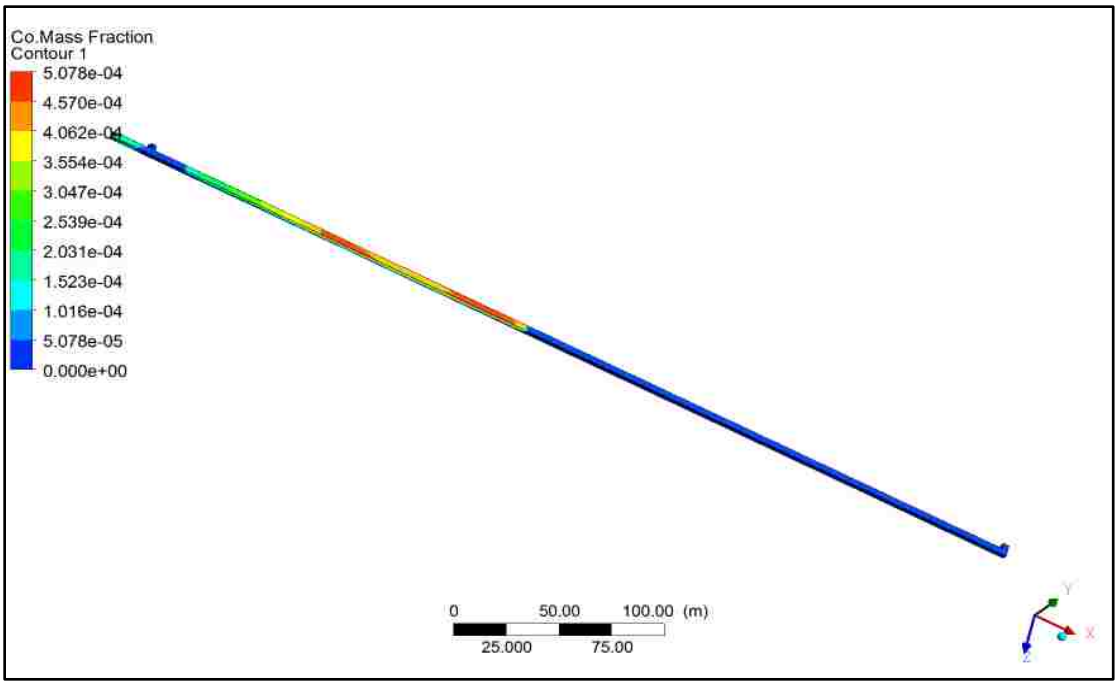

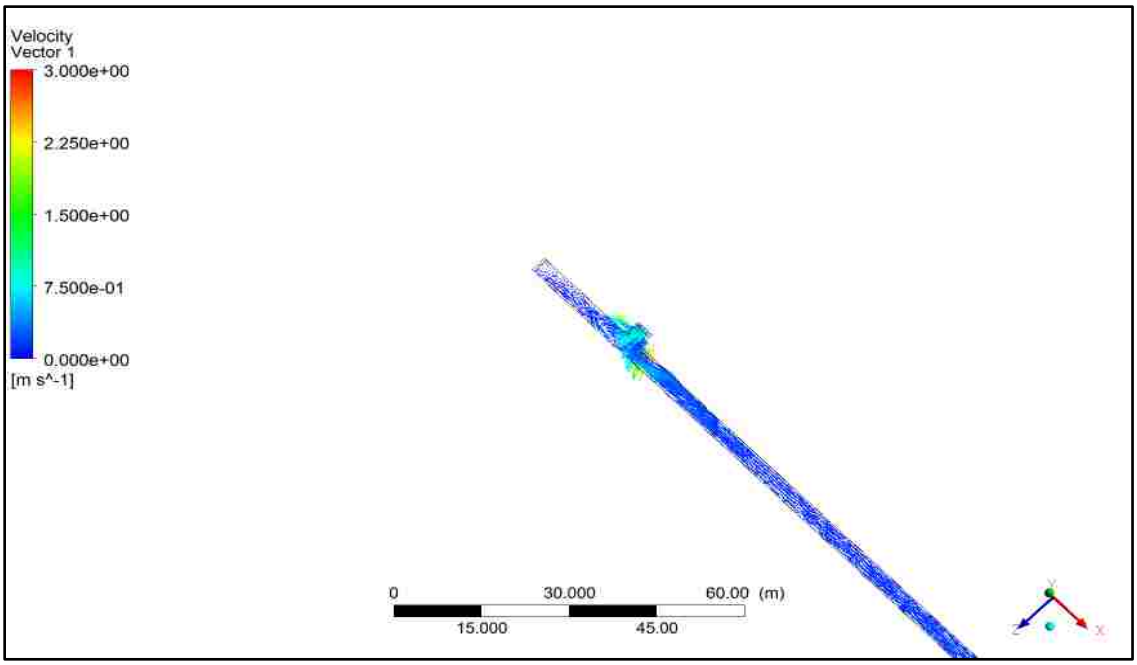

64 kg_2.5 m^3/s

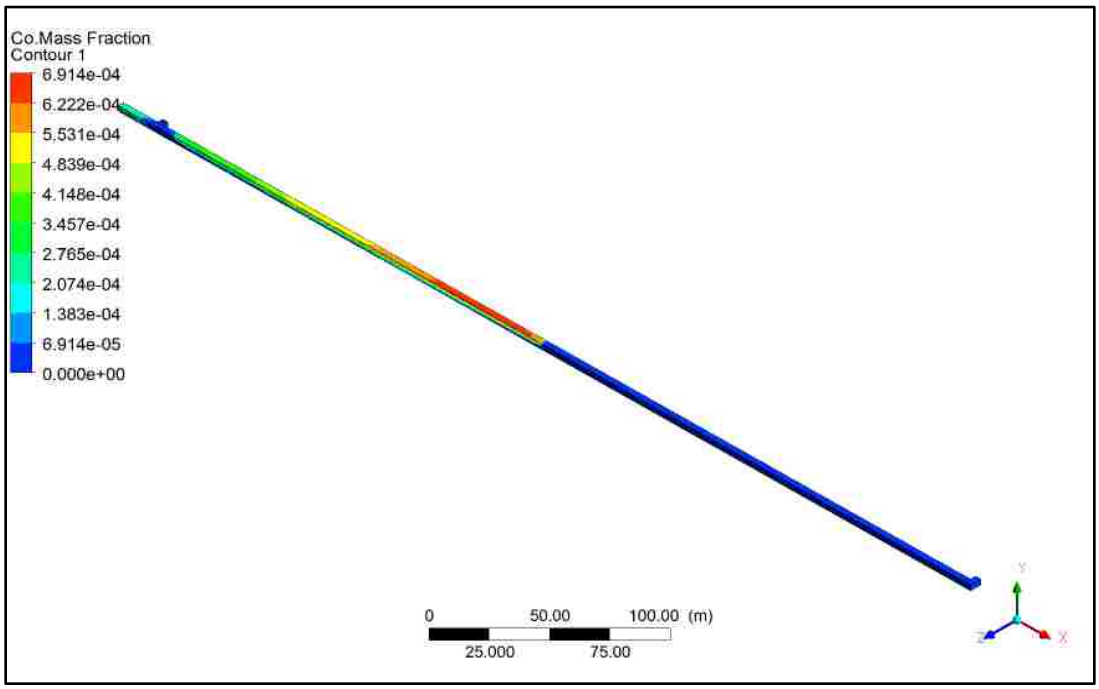
Co.Mass Fraction
Contour 1
6.914e-04
6.222e-04
5.531e-04
4.839e-04
4.148e-04
3.457e-04
2.765e-04
2.074e-04
1.383e-04
6.914e-05
0.000e+00
0
50.00
100.00 (m)
25.000
75.00

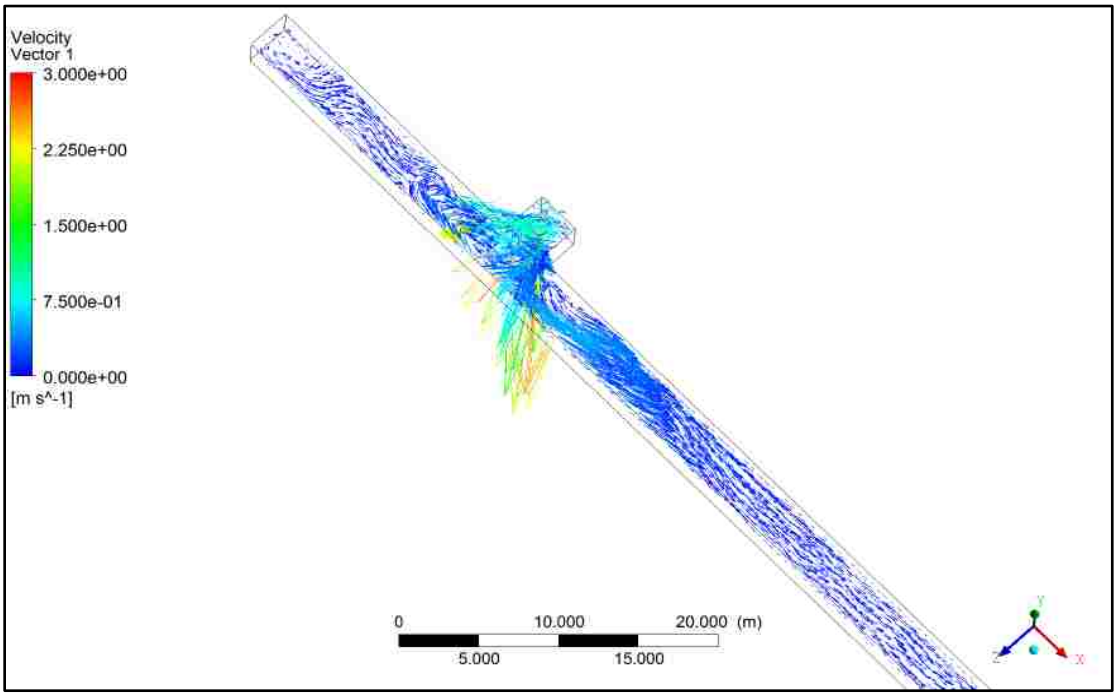
Velocity
Vector 1
3.000e+00
2.250e+00
1.500e+00
7.500e-01
0.000e+00
[m s^-1]
0
10.000
20.000 (m)
5.000
15.000

100 kg_2.5 m^3/s

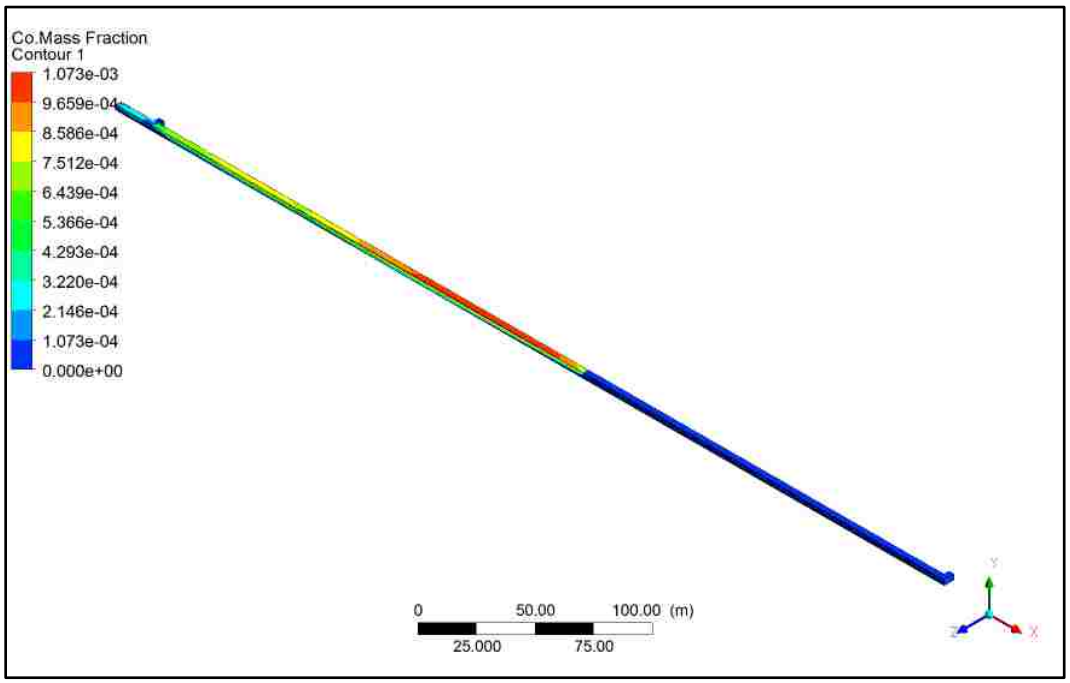
Co.Mass Fraction
Contour 1
1.073e-03
9.659e-04
8.586e-04
7.512e-04
6.439e-04
5.366e-04
4.293e-04
3.220e-04
2.146e-04
1.073e-04
0.000e+00
0
50.00
100.00 (m)
25.000
75.00
Y
Z
X

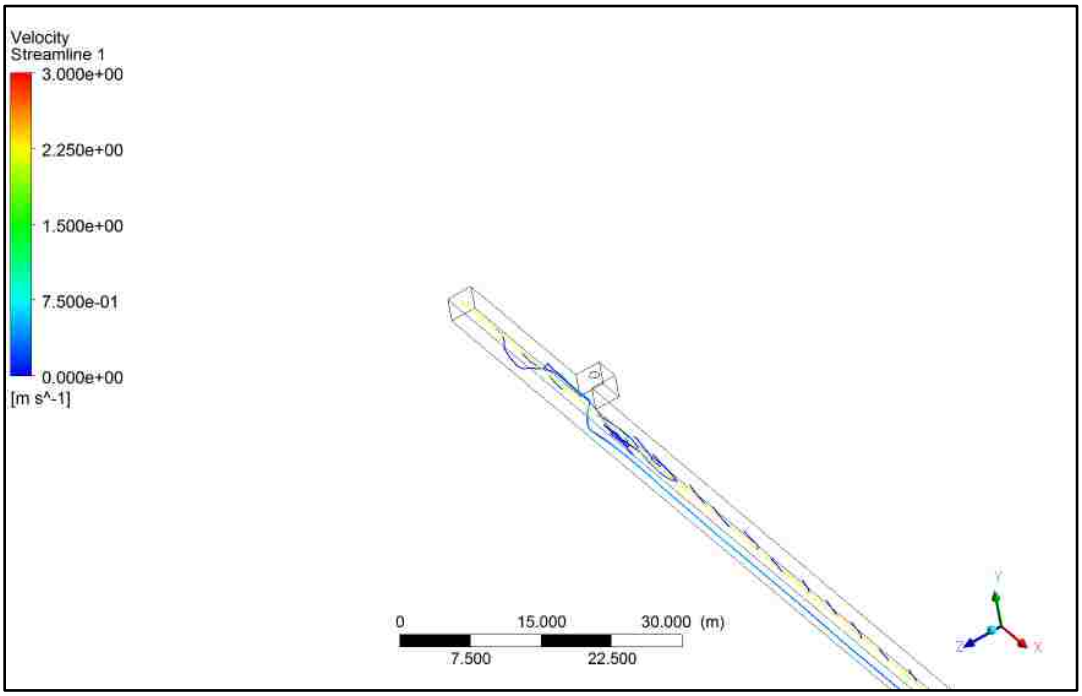
Velocity
Streamline 1
3.000e+00
2.250e+00
1.500e+00
7.500e-01
0.000e+00
[m s^-1]
0
15.000
30.000 (m)
7.500
22.500
Y
Z
X

200 kg_2.5 m^3/s

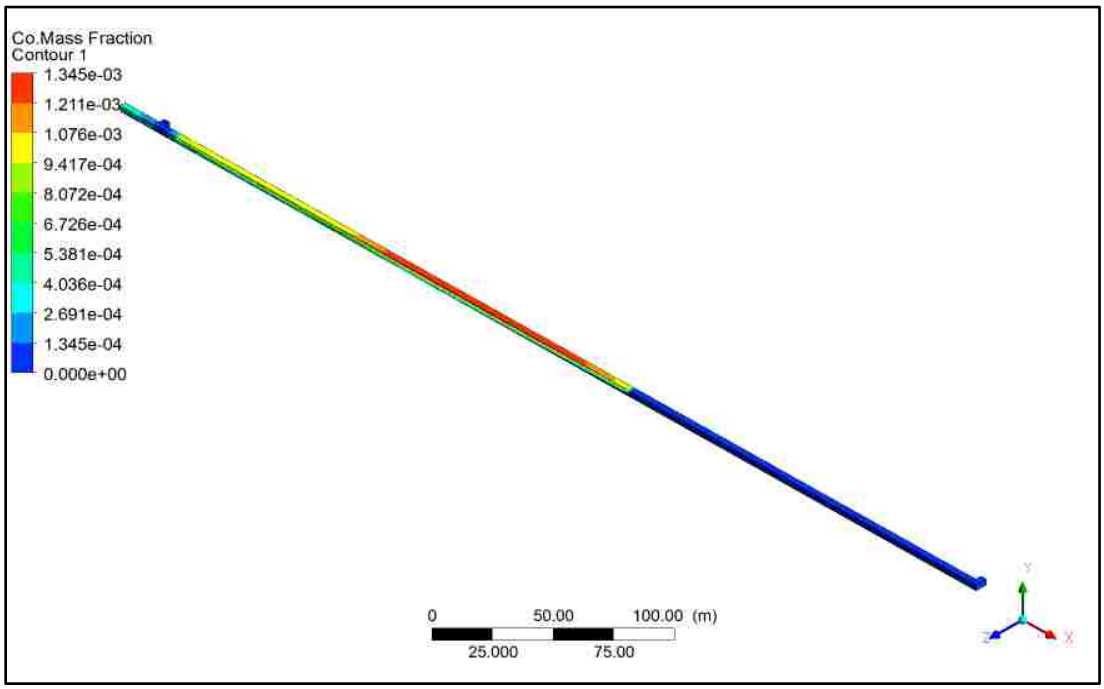
Co.Mass Fraction
Contour 1
1.345e-03
1.211e-03
1.076e-03
9.417e-04
8.072e-04
6.726e-04
5.381e-04
4.036e-04
2.691e-04
1.345e-04
0.000e+00
0
50.00
100.00 (m)
25.000
75.00

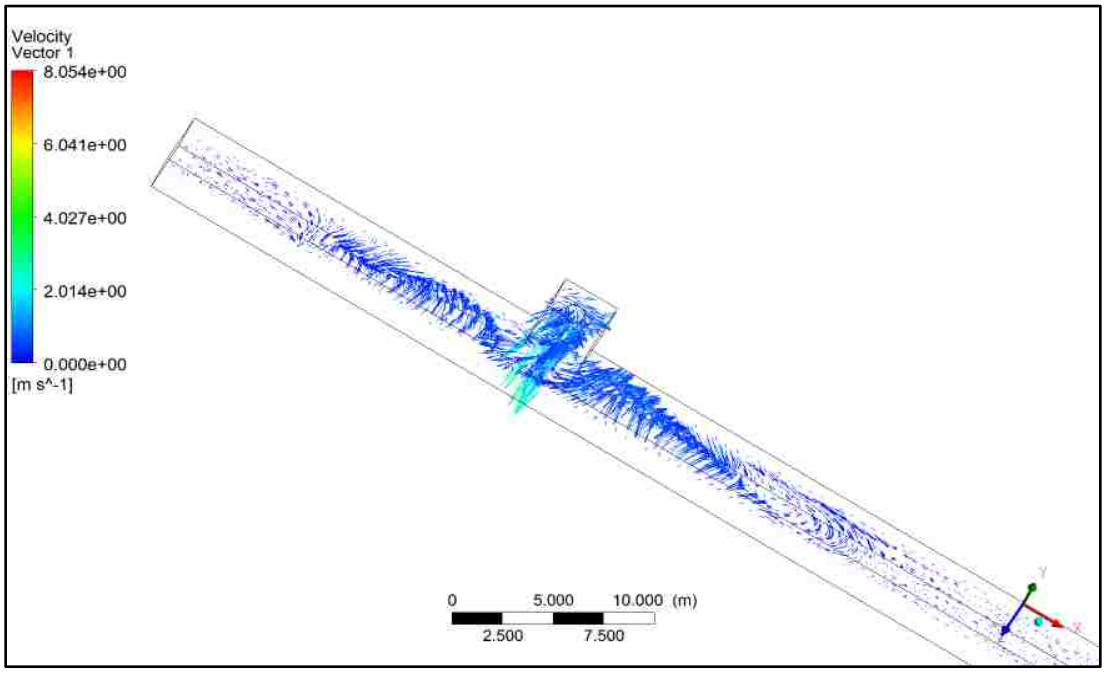
Velocity
Vector 1
8.054e+00
6.041e+00
4.027e+00
2.014e+00
0.000e+00
[m s^-1]
0
5.000
10.000 (m)
2.500
7.500

300 kg_2.5 m^3/s

BIBLIOGRAPHY

Adamus, A., Voráček, V., & Hanák, Z. (2003). Evaluation of inertisation of the longwall district 138202 in Lazy Coal Mine. Coal-Ores-Geological survey, 10(1), 12.

Bakker, A., & Marshall, E. M. (2006). Computational fluid dynamics. Lecture 4-Classification of Flows.

Balusu, R., Chaudari, S., Harvey, T., & Ren, T. (2005). An investigation of air and dust flow patterns around the longwall shearer. In Proceedings of the 8th International Mine Ventilation Congress, Brisbane Australia, The Australasian Institute of Mining and Metallurgy (pp. 135-142).

Balusu, R., Tuffs, N., & Harvey, T. (2006). Surface goaf gas drainage strategies for highly gassy longwall mines.

Banerjee, S. C. (2000). Prevention and combating mine fires. CRC Press.

Batchelor, G. (2000). Introduction to Fluid Mechanics.

Blazek, J. (2015). Computational fluid dynamics: principles and applications. Butterworth-Heinemann.

Borland, C. J. (1986). XTRAN3S-Transonic Steady and Unsteady Aerodynamics for Aeroelastic Applications. Air Force Wright Aeronautical Laboratories, AFWAL-TR-85-3124 Report.

Brooks, K., & Glasser, D. (1986). A simplified model of spontaneous combustion in coal stockpiles. Fuel, 65(8), 1035-1041.

Bugarski AD, Cauda EG, Janisko SJ (2010). Aerosols emitted in underground mine air by diesel engine fueled with biodiesel. J Air Waste Manag Assoc 60:237–244.

Bugarski AD, Janisko SJ, Cauda EG (2011). Diesel aerosols and gases in underground mines: guide to exposure assessment and control. Department of Health and Human Services, Centers for Disease Control and Prevention, National Institute for Occupational Safety and Health, Office of Mine Safety and Health Research, Pittsburgh, PA.

Carras, J. N., & Young, B. C. (1994). Self-heating of coal and related materials: models, application and test methods. Progress in Energy and Combustion Science, 20(1), 1-15.

Cecala AB, Organiscak JA, Zimmer JA (2005) Reducing enclosed cab drill operator's respirable dust exposure with effective filtration and pressurization techniques. J Occup Environ Hyg 2:54–63.

Cerny, V., Klan, J., & Lankova, S. (1971). Balance of oxygen consumption during coal oxidation. Acta Montana, 14, 52-68.

Chen, D., Nie, W., Cai, P., & Liu, Z. (2018). The diffusion of dust in a fully-mechanized mining face with a mining height of 7 m and the application of wet dust-collecting nets. Journal of Cleaner Production, 205, 463-476.

Colaizzi, G. J. (2004). Prevention, control and/or extinguishment of coal seam fires using cellular grout. International journal of coal geology, 59(1-2), 75-81.

Cook, M. A. (1974). The science of industrial explosives. Ireco Chemicals.

Davidson, R. M. (1990). Natural oxidation of coal (Vol. 29, p. 76). London: IEA Coal Research.

Davis, J.D. and Reynolds, D.A. (1928). Spontaneous heating of coal. TP 409. US Bureau of Mines. pp. 74.

De Souza, E. M., & Katsabanis, P. D. (1991). On the prediction of blasting toxic fumes and dilution ventilation. Mining Science and Technology, 13(2), 223-235.

Dmitri, Kuzmin (2010). A Guide to Numerical Methods for Transport Equations.

Drela, M. (1990). Newton solution of coupled viscous/inviscid multielement airfoil flows. In 21st Fluid Dynamics, Plasma Dynamics and Lasers Conference (p. 1470).

Eames, I., & Flor, J. B. (2011). New developments in understanding interfacial processes in turbulent flows.

Edward M. Green (2006). Explosives regulation in the USA. Industrial Materials (465): 78.

Edwards, J. C., & Hwang, C. C. (1999). CFD analysis of mine fire smoke spread and reverse flow conditions.

Edwards, J. C., Franks, R. A., Friel, G. F., & Yuan, L. (1900). Experimental and modeling investigation of the effect of ventilation on smoke rollback in a mine entry.

Edwards, J. S., Ren, T. X., & Jozefowicz, R. (1996). Using computational fluid dynamics (CFD) to solve mine safety and health problems. In International Journal of Rock Mechanics and Mining Sciences and Geomechanics. Abstracts (Vol. 5, No. 33, p. 234A).

Engineering ToolBox, (2003). Reynolds Number.

EPA (2002). Health assessment document for diesel engine exhaust. U.S. Environmental Protection Agency.

Feng, G., Zhang, A., Hu, S., Cheng, J., Miu, X., Hao, G., & Zhao, G. (2018). A methodology for determining the methane flow space in abandoned mine gobs and its application in methane drainage. Fuel, 227, 208-217.

Feroze, T., & Genc, B. (2017). Evaluation of line brattice length in an empty heading to improve air flow rate at the face using CFD. International Journal of Mining Science and Technology, 27(2), 253-259.

Fluent Inc. (2006). Instruction manual.

Fromm, J. E., & Harlow, F. H. (1963). Numerical solution of the problem of vortex street development. The Physics of Fluids, 6(7), 975-982.

Gallo, N., (1995). Leakage Performance of ACME ACFABTM Auxiliary Ventilation Ducting, Undergraduate Thesis (unpublished), University of Queensland, Brisbane.

Geankoplis, C. J. (2003). Solutions Manual to Accompany Transport Processes and Separation Process Principles: (includes Unit Operations). Prentice Hall Professional Technical Reference.

Geng, F., Luo, G., Wang, Y., Peng, Z., Hu, S., Zhang, T., & Chai, H. (2018). Dust dispersion in a coal roadway driven by a hybrid ventilation system: A numerical study. Process Safety and Environmental Protection, 113, 388-400.

Gillies, A. D. S., Wu, H. W., & Shires, D. (2004). Development of an assessment tool to minimize safe after blast re-entry time to improve the mining cycle. In

Gou, Y., Shi, X., Zhou, J., Qiu, X., & Chen, X. (2017). Characterization and Effects of the Shock Losses in a Parallel Fan Station in the Underground Mine. Energies, 10(6), 785.

Grewer, T. (1994). Thermal Hazards of Chemical Reactions (Industrial Safety Series).

Grychowski, T. (2014). Multi sensor fire hazard monitoring in underground coal mine based on fuzzy inference system. Journal of Intelligent & Fuzzy Systems, 26(1), 345-351.

Guo, H., Yuan, L., Shen, B., Qu, Q., & Xue, J. (2012). Mining-induced strata stress changes, fractures and gas flow dynamics in multi-seam longwall mining. International Journal of Rock Mechanics and Mining Sciences, 54, 129-139.

Guřanová, P. (2008). Spontaneous combustion of coal and its early detection on OKR mines.

Handa, T., Nishimoto, T., Morita, M., and Komada, J. (1985). Spontaneous combustion of coal. Fire Science and Technology, vol. 5. pp. 21-30.

Hansen, R. (2018). Modeling temperature distributions and flow conditions of fires in an underground mine drift. Geosystem Engineering, 1-16.

Hargreaves DM, Lowndes IS (2007). The computational modeling of the ventilation flows within a rapid development drivage. Tunn Undergr Space Technol 22:150–160.

Harlow, F. H. (2004). Fluid dynamics in group T-3 Los Alamos national laboratory: (LA-UR-03-3852). Journal of Computational Physics, 195(2), 414-433.

Harlow, F. H., & Welch, J. E. (1965). Numerical calculation of time-dependent viscous incompressible flow of fluid with free surface. The physics of fluids, 8(12), 2182-2189.

Hartman, H. L. (1992). SME mining engineering handbook (Vol. 2). S. G. Britton (Ed.). Denver: Society for Mining, Metallurgy, and Exploration.

Heerden, J., & Sullivan, P. (1993). The application of CFD for evaluation of dust suppression and auxiliary ventilating systems used with continuous miners. In Proceeding of the 6th US Mine Ventilation Symposium (pp. 293-297).

Hu, L. H., Fong, N. K., Yang, L. Z., Chow, W. K., Li, Y. Z., & Huo, R. (2007). Modeling fire-induced smoke spread and carbon monoxide transportation in a long channel: fire dynamics simulator comparisons with measured data. Journal of Hazardous Materials, 140(1-2), 293-298.

Hu, L. H., Tang, F., Yang, D., Liu, S., & Huo, R. (2010). Longitudinal distributions of CO concentration and difference with temperature field in a tunnel fire smoke flow. International Journal of Heat and Mass Transfer, 53(13-14), 2844-2855.

Hu, S. G., & Xue, S. (2011). Gel fire suppressants for controlling underground heating. Journal of Coal Science and Engineering (China), 17(3), 256.

Huang, J., Bruining, J., & Wolf, K. H. (2001). Modeling of gas flow and temperature fields in underground coal fires. Fire Safety Journal, 36(5), 477-489.

Ichinose, M., Nakayama, S., Uchino, K. I., & Inoue, M. (1998). In-situ measurement and simulation by CFD of methane gas distribution at a heading faces. JOURNAL-MINING AND MATERIALS PROCESSING INSTITUTE OF JAPAN, 114, 769-775.

Jahir, T., Zhao, J., Mohammed, M. H., & McCullough, J. D. D. (n.d.). Using Gas Monitoring and Personnel & Vehicle Tracking to Maximize the Benefits of Ventilation-on-Demand in Underground Mining Operations.

James, S. (2011). Black lung disease seen rising in US miners.

Jin, Y., Uth, M. F., Kuznetsov, A. V., & Herwig, H. (2015). Numerical investigation of the possibility of macroscopic turbulence in porous media: a direct numerical simulation study. Journal of Fluid Mechanics, 766, 76-103.

Jones, R.E. and Townend, D.T.A. (1949). Oxidation of coal. Journal of the Society of Chemical Industry, vol. 68. pp. 197.

Kaymakp, E. and Didari, V. (2000). Relations between coal properties and spontaneous combustion parameters. Turkish Journal of Engineering and Environmental Sciences, vol. 26. pp. 59-64.

Kissell, F. N., & Wallhagen, R. E. (1976). Some new approaches to improve ventilation of the working face. In Proceeding of the NCA/BCR Coal Conference (Louisville, KY (pp. 325-338).

Kollipara VK, Chugh YP, Relangi DD (2012). A CFD analysis of airflow patterns in face area for continuous miner making a right turn cut. In: 2012 SME annual meeting & exhibit, preprint 12–132.

Krishnaswamy, S., Agarwal, P. K., & Gunn, R. D. (1996). Low-temperature oxidation of coal. 3. Modeling spontaneous combustion in coal stockpiles. Fuel, 75(3), 353-362.

Kurnia JC, Sasmito AP, Wong WY, Mujumdar AS (2014) Prediction and innovative control strategies for oxygen and hazardous gases from diesel emission in underground mines. Sci Total Environ 481:317–334.

Kurnia, J. C., Sasmito, A. P., & Mujumdar, A. S. (2014). CFD simulation of methane dispersion and innovative methane management in underground mining faces. Applied Mathematical Modelling, 38(14), 3467-3484.

Kurnia, J. C., Sasmito, A. P., & Mujumdar, A. S. (2014). Dust dispersion and management in underground mining faces. International Journal of Mining Science and Technology, 24(1), 39-44.

Kurnia, J. C., Sasmito, A. P., Hassani, F. P., & Mujumdar, A. S. (2015). Introduction and evaluation of a novel hybrid brattice for improved dust control in underground mining faces: A computational study. International Journal of Mining Science and Technology, 25(4), 537-543.

Launder, B., & Spalding, D. (1974). The numerical computation of turbulent flows. Computer Methods in Applied Mechanics and Energy, 3, 269–289.

Lei Z, Yang J, Zhuang Z, Roberge R (2013). Simulation and evaluation of respirator faceseal leaks using computational fluid dynamics and infrared imaging. Ann Occup Hyg 57(5):493–506.

Li, L., Beamish, B.B., and Jiang D.Y. (2009). Self-activation theory of spontaneous combustion of coal. Journal of China Coal Society, vol. 34, no. 4. pp. 505-508.

Li, M., Wu, C., Zhou, Z. Y., Lian, W. C., & Chen, Z. X. (2018). Design and Optimum of Dust Collector with Corrugated Plate for Underground Mine. Advances in Civil Engineering, 2018.

Li, Z., Saydam, S., Mitra, R., & Chalmers, D. (2016). Potential use of thin spray-on liners for gas management in underground coal mines. Journal of the Southern African Institute of Mining and Metallurgy, 116(12), 1091-1100.

Litton, C. D., & Perera, I. E. (2015). Evaluation of sensors for mine fire detection using an atmospheric monitoring system. Mining Engineering, 67(6).

Lowndes, I. (2005). The improved ventilation and dust capture in underground crushing plants.

Lü, W. S., He, L., & Yang, P. (2011). Simulation study of blast fume diffusion characters of driving face. Journal of Coal Science and Engineering (China), 17(1), 47-51.

Marshak, A., & Davis, A. (Eds.). (2005). 3D radiative transfer in cloudy atmospheres. Springer Science & Business Media.

McGinn S, Ellington R, Penney J (2010). Diesel emissions: mechanics' maintenance manual. Diesel Emissions Evaluation Program (DEEP).

McGinn S, Grenier M, Gangal M, Rubeli B, Bugarski A, Schnakenberg G, Johnson R, Petrie D, Crowther G, Penney J (2004). Brunswick mine diesel particulate filter field study. Diesel emissions evaluation program (DEEP) final report of investigation.

McGrattan, K., Hostikka, S., Floyd, J., Baum, H., Rehm, R. G., Mell, W., & McDermott, R. (2010). Fire dynamics simulator (version 5), technical reference guide. NIST special publication, 1018(5).

McMurtry, P. A., Gansauge, T. C., Kerstein, A. R., & Krueger, S. K. (1993). Linear eddy simulations of mixing in a homogeneous turbulent flow. Physics of Fluids A: Fluid Dynamics, 5(4), 1023-1034.

Mishra, D. P., Kumar, P., & Panigrahi, D. C. (2016). Dispersion of methane in tailgate of a retreating longwall mine: a computational fluid dynamics study. Environmental Earth Sciences, 75(6), 475.

Mishra, D. P., Sahu, A., & Panigrahi, D. C. (2019). Design of Auxiliary Ventilation System for Effective Dust Dispersion in Underground Coal Mine Development Heading—A Computational Simulation Approach. In Proceedings of the 11th International Mine Ventilation Congress (pp. 146-158). Springer, Singapore.

Moloney, K. W., Lowndes, I. S., & Hargrave, G. K. (1999). Analysis of flow patterns in drivages with auxiliary ventilation. Transactions of the Institution of Mining and Metallurgy. Section A. Mining Industry, 108.

MSHA (2013) Practical ways to reduce exposure to diesel exhaust in mining—a toolbox. U.S. Department of Labor, Mine Safety and Helath Administration.

Nakayama, S. (1999). Simulation of methane gas distribution by computational fluid dynamics. In International symposium on mining science and tecnology'99 (pp. 259-262).

NIOSH (1988). Carcinogenic effects of exposure to diesel exhaust. National Institute for Occupational Safety and Health (NIOSH), Department of Health and Human Services.

Noakes, Cath; Sleigh, Andrew (2009). "Real Fluids". An Introduction to Fluid Mechanics. University of Leeds. Archived from the original on 21 October 2010. Retrieved 23 November 2010.

Noll JD, Patts L, Grau R (2008).The effects of ventilation controls and environmental cabs on diesel particulate matter concentrations in some limestone mine. In: Proceedings of the 12th US/North American mine ventilation symposium, Reno, NV, USA, June 9–12, pp 463–468.

Norman G.J. (2015). Explosive. Encyclopedia Britannica.

Oraee, K., & Goodarzi, A. (2010). Mathematical modeling of coal seam methane drainage in longwall mining. In SME Annual Meeting and Exhibit (pp. 548-552).

Oren, O. and Sensogut, C. (2010). Spontaneous combustion liability of Kutahya (Turkey) region lignites. Energy Sources, Part A, vol. 32. pp. 877-885.

Ozdogan, M. V., Turan, G., Karakus, D., Onur, A. H., Konak, G., & Yalcin, E. (2018). Prevention of spontaneous combustion in coal drifts using a lining material: a case study of the Tuncbilek Omerler underground mine, Turkey. Journal of the Southern African Institute of Mining and Metallurgy, 118(2), 149-156.

Papakonstantinou, K. A., Kiranoudis, C. T., & Markatos, N. C. (2002). Numerical simulation of CO2 dispersion in an auditorium. Energy and Buildings, 34(3), 245-250.

Papanikolaou, E. A., Venetsanos, A. G., Heitsch, M., Baraldi, D., Huser, A., Pujol, J., & Markatos, N. (2010). HySafe SBEP-V20: numerical studies of release experiments inside a naturally ventilated residential garage. International journal of hydrogen energy, 35(10), 4747-4757.

Papanikolaou, E., Venetsanos, A. G., Cerchiara, G. M., Carcassi, M., & Markatos, N. (2011). CFD simulations on small hydrogen releases inside a ventilated facility and assessment of ventilation efficiency. International journal of hydrogen energy, 36(3), 2597-2605.

Parra, M. T., Villafruela, J. M., Castro, F., & Mendez, C. (2006). Numerical and experimental analysis of different ventilation systems in deep mines. Building and Environment, 41(2), 87-93.

Patel, M. K., Cross, M., & Markatos, N. C. (1988). An assessment of flow oriented schemes for reducing 'false diffusion'. International Journal for numerical methods in engineering, 26(10), 2279-2304.

Philips, H., Uludac, S., and Chabedi, K. (2011). Prevention and control of spontaneous combustion. Coaltech Research Association, Johannesburg, South Africa.

Ren, T. X., & Balusu, R. (2008). Innovative CFD modeling to improve dust control in longwalls. University of Wollongong and the Australiasian Institute of Mining and Metallurgy, 137-142.

Ren, T. X., Edwards, J. S., & Jozefowicz, R. R. (1997). CFD modeling of methane flow around longwall coal faces. In Proceedings of the 6th International Mine Ventilation Congress (pp. 17-22). Pittsburgh.

Ren, T., & Balusu, R. (2010). The use of CFD modelling as a tool for solving mining health and safety problems.

Ren, T., Wang, Z., & Cooper, G. (2014). CFD modelling of ventilation and dust flow behaviour above an underground bin and the design of an innovative dust mitigation system. Tunnelling and Underground Space Technology, 41, 241-254.

Ren, T., Wang, Z., & Zhang, J. (2018). Improved dust management at a longwall top coal caving (LTCC) face–A CFD modelling approach. Advanced Powder Technology.

Reyes, G., Hurtado, J. P., Vargas, J. P., & Acuña, E. I. (2017). Computational fluid dynamics study of primary parallel fan stations.

Rundell B, Ledin M-C, Hammarstrom U, Stjernberg N, Lundback B, Sandstrom T (1996). Effects on symptoms and lung function in humans experimentally exposed to diesel exhaust. Occup Environ Med 53:658–662.

SaraÇ, S. and Soyturk, T. (1992). An investigation on the liability of Tuncbilek lignites to spontaneous combustion. Proceedings of the 8th Coal Congress of Turkey, Zonguldak, 6-8 June 2012. pp. 141-152.

Sasmito, A. P., Birgersson, E., Ly, H. C., & Mujumdar, A. S. (2013). Some approaches to improve ventilation system in underground coal mines environment–A computational fluid dynamic study. Tunneling and Underground Space Technology, 34, 82-95.

Schmal, D., Duyzer, J. H., & van Heuven, J. W. (1985). A model for the spontaneous heating of coal. Fuel, 64(7), 963-972.

Schultz, M. J., Beiter, D. A., Watkins, T. R., & Baran, J. N. (1993). Face Ventilation Investigation: Clark Elkorn Coal Company. Pittsburgh Safety and Health Technology Center, Ventilation Division. Investigative Report No. P385-V286.

Schwarzkopf, J. D., Sommerfeld, M., Crowe, C. T., & Tsuji, Y. (2011). Multiphase flows with droplets and particles. CRC press.

Sensogut, C., Kaufmann, M., & Petit, E. (2002). An approach to the modeling of spontaneous combustion in the goaf. JOURNAL-SOUTH AFRICAN INSTITUTE OF MINING AND METALLURGY, 102(5), 311-314.

Shah SD, Cocker DR III, Johnson KC (2007). Reduction of particulate matter emissions from diesel backup generators equipped with four different after treatment devices. Environ Sci Technol 41:5070–5076.

Silvester, S. A., Lowndes, I. S., & Kingman, S. W. (2004). The ventilation of an underground crushing plant. Mining Technology, 113(4), 201-214.

Silvester, S. A., Lowndes, I. S., Kingman, S. W., & Arroussi, A. (2007). Improved dust capture methods for crushing plant. Applied mathematical modeling, 31(2), 311-331.

Singh, R.V.K. (2013). Spontaneous heating and fire in coal mine. Procedia Engineering, vol. 62. pp. 78-90.

Sojoudi, A., Afshin, H., Farhanieh, B., & Saha, S. C. (2012). Large eddy simulation of smoke flow in a real road tunnel fire using FDS. In Proceedings of the 4th International Conference on Computational Methods (ICCM2012).

Sondreal, E. A., & Ellman, R. C. (1974). Laboratory determination of factors affecting storage of North Dakota lignite: computer simulation of spontaneous heating.[28 refs; graphs] (No. BM-RI-7887). Bureau of Mines, Grand Forks, N. Dak. (USA). Grand Forks Energy Research Lab.

Srinivasa, R., Baafi, E., Aziz, N., & Singh, R. (1993). Three-dimensional modeling of air velocities and dust control techniques in a longwall face. In Proceeding of the 6th US Mine Ventilation Symposium (pp. 287-292).

Stewart, C. M. (2014). Practical prediction of blast fume clearance and workplace re-entry times in development headings. In 10th International Mine Ventilation Congress.

Steyn C. (2013). Underground mine workers' respiratory exposure to selected gasses after the blasting process in a platinum mine (Masters thesis).

Su, J., Tsai, C. C., & Sung, W. T. (2012). Area temperature system monitoring and computing based on adaptive fuzzy logic in wireless sensor networks. Applied Soft Computing, 12(5), 1532-1541.

Sullivan, P., & Van Heerden, J. (1993). Simulation of environmental conditions in continuous miner developments using computational fluid dynamics. Journal of the Mine Ventilation Society of South Africa, 46(1), 2-11.

Taraba, B., & Michalec, Z. (2011). Effect of longwall face advance rate on spontaneous heating process in the gob area–CFD modeling. Fuel, 90(8), 2790-2797.

Taraba, B., Peter, R., Slovák, V., & Janek, J. (2005). Coal oxidation process in view of critical (threshold) temperature. Coal–Ores–Geol Survey, 12(12), 26-30.

Taylor, K. (2015). Small Scale Study of the Role of The Muckpile in the Blasting Fumes of Commercial Explosives (Doctoral dissertation).

Taylor, M. (2018). Mining Dangers. Pulse.com.gh.

Tennekes, H., Lumley, J. L., & Lumley, J. L. (1972). A first course in turbulence. MIT press.

Thiruvengadam, M., Zheng, Y., & Tien, J. C. (2016). DPM simulation in an underground entry: Comparison between particle and species models. International Journal of Mining Science and Technology, 26(3), 487-494.

Thuc, K. X., & Insoo, K. (2011). A collaborative event detection scheme using fuzzy logic in clustered wireless sensor networks. AEU-International Journal of Electronics and Communications, 65(5), 485-488.

Tien, J.C. (1999). Mine ventilation systems. Proceedings of the 8th US Mine Ventilation Symposium.

Ting, F. C., & Kirby, J. T. (1996). Dynamics of surf-zone turbulence in a spilling breaker. Coastal Engineering, 27(3-4), 131-160.

Torano, J. A., Rodriguez, R., Diego, I., Rivas, J. M., & Pelegry, A. (2007). Influence of the pile shape on wind erosion CFD emission simulation. Applied mathematical modeling, 31(11), 2487-2502.

Toraño, J., Torno, S., Menéndez, M., & Gent, M. (2011). Auxiliary ventilation in mining roadways driven with roadheaders: validated CFD modeling of dust behavior. Tunnelling and Underground Space Technology, 26(1), 201-210.

Toraño, J., Torno, S., Menendez, M., Gent, M., & Velasco, J. (2009). Models of methane behavior in auxiliary ventilation of underground coal mining. International Journal of Coal Geology, 80(1), 35-43.

Torno, S., Toraño, J., Menéndez, M., & Gent, M. (2011). CFD simulation of blasting dust for the design of physical barriers. Environmental Earth Sciences, 64(1), 73-83.

Torno, S., Toraño, J., Ulecia, M., & Allende, C. (2013). Conventional and numerical models of blasting gas behavior in auxiliary ventilation of mining headings. Tunnelling and Underground Space Technology, 34, 73-81.

Versteeg, H. K., & Malalasekera, W. (2007). An introduction to computational fluid dynamics: the finite volume method. Pearson Education.

Vidmar, P., & Petelin, S. (2007). Application of CFD Method for risk assessment in road tunnels. Engineering Applications of Computational Fluid Mechanics, 1(4), 273-287.

Wade JF III, Newman LS (1993) Diesel asthma: reactive airways disease following overexposure to locomotive exhaust. J Occup Med 35:149–154.

Wala AM, Vytla S, Huang G (2007) Mine face ventilation: a comparison against benchmark experiments for the CFD code validation. Min Eng 59:49–55.

Wala, A. M., Vytla, S., Huang, G., & Taylor, C. D. (2008). Study on the effects of scrubber operation on the face ventilation. In Proceedings of the 12th US/North American Mine Ventilation Symposium (Vol. 12, pp. 281-286).

Wala, A., Jacob, J., Brown, J., & Huang, G. (2003). New approaches to mine-face ventilation. Mining engineering, 55(3), 25-30.

Wan, R. (2016).Facts About Coal and Minerals. National Mining Association (NMA), pp.3.

Wang, D., Dou, G., Zhong, X., Xin, H., and Qin, B. (2014). An experimental approach to selecting chemical inhibitors to retard the spontaneous combustion of coal. Fuel, vol. 117. pp. 218-223.

Wang, H. Y. (2012). Numerical and theoretical evaluations of the propagation of smoke and fire in a full-scale tunnel. Fire Safety Journal, 49, 10-21.

Wang, H., Dlugogorski, B.Z., and Kennedy, E.M. (1999). Theoretical analysis of reaction regimes in low-temperature oxidation of coal. Fuel, vol. 78. pp. 1073-1081.

Wang, Z., & Ren, T. (2013). Investigation of airflow and respirable dust flow behavior above an underground bin. Powder Technology, 250, 103-114.

Wang, Z., Ren, T., Ma, L., & Zhang, J. (2018). Investigations of Ventilation Airflow Characteristics on a Longwall Face-A Computational Approach. Energies, 11(6), 1564.

Wei, N., Zhongan, J., & Dongmei, T. (2011). Numerical simulation of the factors influencing dust in drilling tunnels: its application. Mining Science and Technology (China), 21(1), 11-15.

Whittles, D. N., Lowndes, I. S., Kingman, S. W., Yates, C., & Jobling, S. (2006). Influence of geotechnical factors on gas flow experienced in a UK longwall coal mine panel. International Journal of Rock Mechanics and Mining Sciences, 43(3), 369-387.

Winn, D. (2002). Blast Fumes and Re-entry Times in Underground Metalliferous Mines.

Xu G, Luxbacher KD, Ragab S (2013). Development of a remote analysis method for underground ventilation systems using tracer gas and CFD in a simplified laboratory apparatus. Tunn Undergr Space Tech 33:1–11.

Xu, G., Chang, P., Mullins, B., Zhou, F., & Hu, S. (2018). Numerical study of diesel particulate matter distribution in an underground mine isolated zone. Powder Technology, 339, 947-957.

Xu, G., Luxbacher, K. D., Ragab, S., Xu, J., & Ding, X. (2017). Computational fluid dynamics applied to mining engineering: a review. International Journal of Mining, Reclamation and Environment, 31(4), 251-275.

Yildirim, O.S., Sensogut, C., and Gokay, M.K. (2006). Effects of electrical resistance on spontaneous combustion tendency of coal and interaction matrix concept. Journal of University of Science and Technology Beijing, vol. 13. pp. 1-7.

Yuan, L., & Smith, A. C. (2007). Computational fluid dynamics modeling of spontaneous heating in longwall gob areas. Transactions-society for mining metallurgy and exploration incorporated, 322, 37.

Yuan, L., & Smith, A. C. (2008). Numerical study on the effects of coal properties on spontaneous heating in longwall gob areas. Fuel, 87(15-16), 3409-3419.

Yuan, L., & Smith, A. C. (2009). CFD modeling of spontaneous heating in a large-scale coal chamber. Journal of Loss Prevention in the Process Industries, 22(4), 426-433.

Yuan, L., & Smith, A. C. (2010). Effect of longwall face advance on spontaneous heating in longwall gob area. Mining Engineering, 62(3), 46.

Zannis, T. C., Hountalas, D. T., Papagiannakis, R. G., & Levendis, Y. A. (2009). Effect of fuel chemical structure and properties on diesel engine performance and pollutant emissions: review of the results of four European research programs. SAE International journal of fuels and lubricants, 1(1), 384-419.

Zeng-hua, L., Ya-li, W., Na, S., Yong-liang, Y., & Yu-jing, Y. (2009). Experiment study of model compound oxidation on spontaneous combustion of coal. Procedia Earth and Planetary Science, 1(1), 123-129.

Zhang, Q., Zhou, G., Qian, X., Yuan, M., Sun, Y., & Wang, D. (2018). Diffuse pollution characteristics of respirable dust in fully-mechanized mining face under various velocities based on CFD investigation. Journal of Cleaner Production, 184, 239-250.

Zheng, Y. (2011). Diesel particulate matter dispersion analysis in underground metal/nonmetal mines using computational fluid dynamics.

Zheng, Y., & Tien, J. C. (2008). DPM dispersion study using CFD for underground metal/nonmetal mines. In Proceedings of the 12th US/North America mine ventilation symposium, Reno (pp. 487-493).

Zheng, Y., Li, Y., Thiruvengadam, M., Lan, H., & Tien, J. C. (2017). DPM dispersion inside a single straight entry using dynamic mesh model. International journal of coal science & technology, 4(3), 234-244.

Zheng, Y., Thiruvengadam, M., Lan, H., & Tien, C. J. (2015). Effect of auxiliary ventilations on diesel particulate matter dispersion inside a dead-end entry. International Journal of Mining Science and Technology, 25(6), 927-932.

Zheng, Y., Thiruvengadam, M., Lan, H., & Tien, J. (2015). Simulation of DPM distribution in a long single entry with buoyancy effect. International Journal of Mining Science and Technology, 25(1), 47-52.

Zheng, Y., Thiruvengadam, M., Lan, H., & Tien, J. C. (2015). Design of push–pull system to control diesel particular matter inside a dead-end entry. International journal of coal science & technology, 2(3), 237-244.

Zhou, G., Feng, B., Yin, W., & Wang, J. (2018). Numerical simulations on airflow-dust diffusion rules with the use of coal cutter dust removal fans and related engineering applications in a fully-mechanized coal mining face. Powder Technology.

Zhou, G., Zhang, Q., Bai, R., Fan, T., & Wang, G. (2017). The diffusion behavior law of respirable dust at fully mechanized caving face in coal mine: CFD numerical simulation and engineering application. Process Safety and Environmental Protection, 106, 117-128.

Zhou, L., & Smith, A. C. (2012). Improvement of a mine fire simulation program-incorporation of smoke rollback into MFIRE 3.0. Journal of fire sciences, 30(1), 29-39.

VITA

Raymond Ninnang Tiile was born in Upper West Region, Ghana. He holds BS and MS degrees, both in mining engineering, from University of Mines and Technology and Missouri University of Science and Technology, respectively. After successfully attaining his bachelors and prior to joining Missouri S&T, he gathered extensive training and experience working with explosive, surface, and underground metal mines in Ghana, namely: Strategic Mining Support services (SMiSS), AngloGold Ashanti Obuasi mine, Maxam Explosive Limited, and Perseus Mining Limited (Edikan mine).

At Missouri S&T, he took relevant graduate courses to help in his research. He was a Graduate Research and Teaching Assistant in the Department of Mining and Nuclear Engineering. He has been an active member of different professional organizations including the Society for Mining, Metallurgy and Exploration (SME), and Canadian Institute of Mining, Metallurgy and Petroleum (CIM).

Raymond received his Ph.D. in mining engineering from Missouri University of Science and Technology in May, 2019.